Deciphering the Details of Recent Interactions in the Magellanic Clouds

A Thesis
Submitted for the degree of

Doctor of Philosophy

in

The Department of Physics,
Pondicherry University,
Puducherry - 605 014, India

by

Sipra Hota
Indian Institute of Astrophysics,
Bengaluru - 560 034, India

September 2025

Deciphering the Details of Recent Interactions in the Magellanic Clouds

Sipra Hota
Indian Institute of Astrophysics

Indian Institute of Astrophysics
Bengaluru - 560 034, India

Thesis title : **Deciphering the Details of Recent Interactions in the Magellanic Clouds**

Author : **Sipra Hota**

Address : Indian Institute of Astrophysics
II Block, Koramangala
Bengaluru - 560 034, India

Email : sipra.hota@iiap.res.in, siprahota1997@gmail.com

Supervisor : **Prof. Annapurni Subramaniam**

Address : Indian Institute of Astrophysics
II Block, Koramangala
Bengaluru - 560 034, India

Email : purni@iiap.res.in

Declaration of Authorship

I hereby declare that the research contained in this thesis is the result of the investigations carried out by me at the Indian Institute of Astrophysics, Bengaluru, under the supervision of **Prof. Annapurni Subramaniam**. This work has not been submitted for the awarding of a degree or any other qualification either in this university or any other institution.

Sipra Hota
Ph.D. Student, IIA,
Bengaluru-560 034, India

Signed: ______________________________

Date: ______________________________

Certificate

This is to certify that the thesis titled **"Deciphering the Details of Recent Interactions in the Magellanic Clouds"** submitted to Pondicherry University by Ms. Sipra Hota for the award of the degree of Doctor of Philosophy, is based on the results of the investigations carried out by her under my supervision and guidance, at the Indian Institute of Astrophysics. This thesis has not been submitted to any other university or institute for the award of any degree, diploma, fellowship, etc.

Prof. Annapurni Subramaniam
Thesis Supervisor,
Indian Institute of Astrophysics,
Bengaluru-560 034, India

Signed: ______________________________

Date: ______________________________

Acknowledgements

A Ph.D. is more than a degree—it is a transformative journey of challenges, discoveries, and growth that has shaped me both academically and personally. This work would not have been possible without the support, encouragement, and kindness of many, to whom I extend my heartfelt gratitude. ❀

First and foremost, I am profoundly grateful to my supervisor, *Prof. Annapurni Subramaniam*, whose unwavering support, patience, and wisdom have guided me through every stage of this journey. Her trust in my potential—especially in moments of self-doubt—has meant more than words can convey. I could always rely on her guidance, regardless of time or circumstance, and that steady presence gave me strength. Her insightful feedback, thoughtful encouragement, and dedicated mentorship have not only shaped the course of this research but also profoundly influenced the researcher and individual I have grown to be. ❀

I sincerely thank my collaborators—*Dr. Smitha Subramanian, Prof. M.-R. L. Cioni, Prof. Richard de Grijs, Dr. Prasant Kumar Nayak, Dr. Vikrant V. Jadhav, and S. R. Dhanush*—for their generous support and valuable scientific input throughout this work. I am especially grateful to Dr. Smitha Subramanian for her encouragement and insightful suggestions, and to Dr. Prasant Kumar Nayak for his friendly guidance and practical advice. I am deeply indebted to Prof. Richard de Grijs from Macquarie University, Sydney, for his exceptional guidance during my collaborative visit. I deeply appreciate the time and effort he devoted to mentoring me, both during my visit and thereafter. ❀

I am grateful to my Doctoral Committee members, *Dr. Sudhanshu Barway* and *Dr. V. V. Ravi Kanth Kumar* for their valuable insights and guidance in keeping this work on track, as well as my comprehensive examiners, *Prof. Mousumi Das* and *Dr. Seetha Somasundaram.* I also extend my sincere thanks to IIA for providing this wonderful opportunity and for their continuous support throughout my doctoral journey. I am especially thankful to the Director, the Dean, the BGS Chair, and the BGS office for ensuring that all processes remained smooth and well-coordinated. ❀

I sincerely appreciate all my group-mates—*Sharmila, Deepthi, Anju, Amogha, Aravind, Sneha, Gaurav Singh, Gourav, Chayan and Geeta*—for their valuable advice, critical comments, and constant encouragement. Their support made this journey both enriching and memorable. ❀

Many thanks to the staff at the *Bhaskara* who made the living comfortable during this half-decade. I further thank my batchmates, seniors and juniors for making this journey a very pleasant one by indulging in many festivals, events, games, etc. namely my seniors *Shejila, Raghu, Priya, Deepak, Partha, Swastik, Sujay, Rishabh, Manika, Soumya, Komal, Jyoti, Archita, Radhika, Saraswathi* and *Vishnu*; my batchmates *Soumyaranjan, Neeraj, Parvathy, Judhajeet, Anisha, Payel,* and *Shubhangi*; and my juniors *Rupesh, Sunit, Khushbu, Shivani, Saili, Renu, Chandan, Saurabh, Ajay, Rakshit, Shashank, Shatakshi, Swagata, Puja, Abhisheka, Gurwinder, Nitish, Savitha* and *Ayushi.* Among them, I especially appreciate Soumyaranjan, who has been with me since the very first day of my Ph.D., sharing both highs and lows with unfailing support; Neeraj, whose companionship added many memorable moments; Parvathy, my roommate, whose warmth brightened daily life; and Judhajeet, for our many discussions that broadened my perspectives. Khushbu, my officemate, made the long working hours lighter with her cheerful company and easy camaraderie. ❀

My heartfelt gratitude to the incredible team behind IIA's student e-Magazine, *DOOT*, for offering me the wonderful opportunity to contribute to science outreach. Being part of the *DOOT* family for over four enriching years—across various roles—has been nothing short of inspiring. One of my most cherished experiences remains serving as *DOOT's 'Co-Chief Editor'* in 2024. ❀

I would like to thank Prof. Maheswar Gopinathan, along with all the staff and interns at VBO, for their support in making my thesis writing smoother—especially *Venketesh, Rajesh, Shreya, Akinchan, Smruti, Nirmal, Megha, Debraj, Nivedha, and Somashree.* ❀

I sincerely thank all my teachers and professors, from school through university, especially *Mr. Ashoka, Mr. Premananda, Dr. Ajith, Dr. Rajat*, and *Dr. Sidharth*, who have consistently supported me throughout my academic journey and helped make my career path smoother. I am deeply grateful to my dear friends-turned-family—*Chiki, Chitaranjan, Pinky, Subhasmita, Subhransu, Subhrakanta*, and *Kartik*—whose unwavering support, especially beyond academics, with love, laughter, and endless encouragement. I also cherish the friendships formed during conferences and schools with *Abinaya, Geetika, Akhila, Amit, Vaibhav, Dibya, Dipali, Sunayana*, and *Ayushi*, as well as at Macquarie University with *Deepak, Meghna, Aashique, Jahang, Pradosh, Sri*, and *Swayam*, whose warmth and camaraderie made those experiences both memorable and enriching. ❀

I owe everything I am to my parents, *Smt. Padmabati Hota* and *Mr. Rajendra Hota*, whose love, sacrifices, and unwavering belief in me have shaped every step of my journey. My heartfelt gratitude also goes to my elder brother, *Mr. Paresh Hota*, whose constant care and affection have been a quiet pillar of strength. I am equally grateful to the people of Barikpur, whose blessings have always guided me. To those whose names I may have inadvertently missed, please know that your presence, kindness, and support have been deeply felt and truly valued—you matter. ❀

– Sipra Hota

To my beloved Maa and Bapa,

(All that I am and aspire to be comes from the values and dreams you have instilled.)

& the people of Barikpur.

(This work is as much yours as it is mine.)

♡ ⋆

List of Publications

A). Refereed Journal Publications

1. **"UVIT Study of the MAgellanic Clouds (U-SMAC) - I. Recent star formation history and kinematics of the Shell region in the north-eastern Small Magellanic Cloud"**; **Sipra Hota**, Annapurni Subramaniam, S. R. Dhanush, M.-R. L. Cioni, & Smitha Subramanian, *Monthly Notices of the Royal Astronomical Society, vol. 532, no. 1, pp. 322–335, Jul. 2024.* doi:10.1093/mnras/stae1438
2. **"UVIT Study of the MAgellanic Clouds (U-SMAC). II. A Far-UV Catalog of the Small Magellanic Cloud: Morphology and Kinematics of Young Stellar Population"**; **Sipra Hota**, Annapurni Subramaniam, Prasant Kumar Nayak, & Smitha Subramanian, *the Astronomical Journal, vol. 168, no. 6, 255, Dec. 2024.* doi:10.3847/1538-3881/ad7de2
3. **"UVIT Study of the MAgellanic Clouds (U-SMAC) III. Hierarchical Star Formation in the Small Magellanic Cloud Regulated by Turbulence"**; **Sipra Hota**, Richard de Grijs & Annapurni Subramaniam, *the Astrophysical Journal, vol. 989, no. 2, 216, Aug. 2025* doi:10.3847/1538-4357/adec84
4. **"UVIT Study of the MAgellanic Clouds (U-SMAC) IV. Characterizing Young Massive Stars in the Northeastern Outskirts of the Small Magellanic Cloud"**; **Sipra Hota**, Annapurni Subramaniam & Vikrant V. Jadhav, *(Submitted)*

B). Conference Proceedings

1. **"Visiting the North-Eastern outskirts of the Small Magellanic Cloud: Exploring star formation history and Kinematics"**; **Sipra Hota**, Annapurni Subramaniam, S. R. Dhanush, & M.-R. L. Cioni, *Dynamical Masses of Local Group Galaxies, Proceedings of the International Astronomical Union, held 20-24 March 2023 in Potsdam, Germany.*

Conferences

1. **Contributed talk (online)** given on "***UVIT's Window into the SMC: Unveiling the Morphology and Kinematics of Young massive stars***" in *XMC II: Clouds over Yellowstone* held at Bozeman, Montana in *22–28 May 2025*
2. **Invited talk** given on "***Kinematics and Morphology of Young Population in the Small Magellanic Cloud: Insights from UVIT***" in *Space-based Astrophysics in the Ultraviolet* held at ISSI, Beijing, China in *18–21 Mar 2025*
3. **Poster** presented on "***Morphology, Star Formation, and Kinematics of the Small Magellanic Cloud: Unveiling Insights from UVIT Observations***" in *Young Astronomers Meet* held at TIFR, Mumbai, India in *18–21 Mar 2025*
4. **Poster** presented on "***Morphology and kinematics of young population in the Small Magellanic Cloud: Insights from UVIT/AstroSat***" in *Annual meeting of the Astronomical Society of India* held at NIT Rourkela, India in *15–19 Feb 2025*
5. **Contributed talk (online)** given on "***Morphology and Kinematics of Young stellar population of the Small Magellanic Cloud with UVIT/AstroSat and Gaia***" in *NUVA e-meeting 2024: Initial Program* organized virtually in *15–17 Oct 2024*
6. **Contributed talk (online)** given on "***Unravelling of the hierarchical star formation in the SMC main body using UVIT/AstroSat***" in *Raising the veil on star formation near and far* held at Kavli Institute for Cosmology, Cambridge, UK, organized in hybrid mode in *22–26 Apr 2024*
7. **Contributed talk** given on "***Venturing into the SMC Main Body with UVIT/AstroSat Expedition***" in *Young Astronomers Meet* held at Christ, Deemed to be University, Bengaluru, India, in *6–9 Mar 2024*

8. **Contributed talk** given on "***Deciphering the hierarchical star formation within the Small Magellanic Cloud using the UVIT/AstroSat***", in the *National Space Science Symposium* held at Goa University, Goa, India in *26 Feb–1 Mar 2024*.

9. **Poster** presented on "***Delving into the SMC Main Body with UVIT/AstroSat Exploratio***" in *Annual meeting of the Astronomical Society of India* organized at *IISc, Bengaluru, India* in *31 Jan–4 Feb 2024*

10. **Participant** in *Resolving the Extragalactic Universe with ALMA and JWST* organized virtually held at *Tokyo, Japan* in *6–10 Nov 2023*

11. **Contributed talk (online)** given on "***Journey into the North-Eastern Outskirts of the Small Magellanic Cloud with UVIT/AstroSat***" in *NUVA e-meeting 2023: Initial Program* organized virtually in *24–26 Oct 2023*

12. **Poster** presented on "***Multiband study of Shell region in the North-Eastern Small Magellanic Cloud using UVIT/AstroSat and Gaia***" in *IAUS379: Dynamical Masses of Local Group Galaxies* conference organized by *AIP, Germany* in *20–24 Mar 2023*

13. **Poster** presented on "***Shell region in the North-Eastern Small Magellanic Cloud: Star formation history and kinematics using UVIT/AstroSat and Gaia***" in *Annual meeting of the Astronomical Society of India* conference organized by *IIT Indore, Indore, India* in *1-5 Mar 2023*

14. **Poster** presented on "***UV study of tidally interacting region in the North-East Small Magellanic Cloud using UVIT/ AstroSat***" in *Two-day meeting to celebrate the 7 years of AstroSat in orbit* organized by *Indian Space Research Organization, Bangalore* in *28–29 Sep 2022*

15. **Participant** in *Gaia Symposium: DR3 and beyond* held at *IIA, Bengaluru, India* in *11–15 Jul 2022*

16. **Poster (online)** presented on "***Tidal signatures in the outer Small Magellanic Cloud using AstroSat/UVIT***" in *Annual meeting of the Astronomical Society of India* organized by *IIT Roorkee, Roorkee, India* in *25–29 Mar 2022*

Workshops and Schools

1. **Participant** in *The Physics of Star Formation School* organized virtually held at *Les Houches, France* in *12–23 Feb 2024*
2. **Participant** in *First UVEX Community Workshop* organized virtually at *Caltech, USA* in *13–15 Mar 2023*
3. **Participant** in *Advanced AstroSat data analysis workshop* held at *Goa University, Goa, India* in *9–15 Jan 2023*
4. **Participant** in *Southern African Large Telescope (SALT) workshop* organized virtually in *13–15 Mar 2023*

Software usage

Data: In this thesis work, we have used the data from the AstroSat mission of the ISRO, archived at the Indian Space Science Data Centre (ISSDC; https://astrobrowse.issdc.gov.in/astro_archive/archive/Home.jsp). The optical and PM data utilized in this work have been obtained from the European Space Agency (ESA) space mission (https://www.cosmos.esa.int/gaia), Gaia. We are grateful to the Gaia Data Processing and Analysis Consortium (DPAC, https://www.cosmos.esa.int/web/gaia/dpac/consortium) for their ongoing efforts in processing Gaia data. The DPAC's work is made possible through funding provided by national institutions, with a special acknowledgement to the institutions participating in the Gaia MultiLateral Agreement (MLA). This work includes deep optical data based on observations at Cerro Tololo Inter-American Observatory, NSF's National Optical-Infrared Astronomy Research Laboratory (NOAO Prop. ID: 2013A-0411 and 2013B-0440; PI: Nidever). Infra-red data are created from observations collected at the European Organisation for Astronomical Research in the Southern Hemisphere under ESO programme 179.B-2003.

Data Reduction and photmetry: For data reduction of UVIT level 1 data, CCDLAB was used (Postma & Leahy 2017, 2021). Photometry was performed using IRAF/DAOPHOT (Stetson 1987).

Spectra Energy Distribution: This thesis makes use of VOSA, developed under the Spanish Virtual Observatory (https://svo2.cab.inta-csic.es/theory/vosa/) project funded by MCIN/AEI/10.13039/501100011033/ through grant PID2020-112949GB-I00.

Analysis: For most of the analysis and figures presented in this thesis, various *Python* libraries have been used. Some of the key packages are: *astropy* (Astropy Collaboration et al. 2013, 2018, 2022), *matplotlib* (Hunter 2007), *numpy* (Harris et al. 2020), *pandas* (Wes McKinney 2010; pandas development team 2020), *scipy* (Virtanen et al. 2020), *seaborn* (Waskom 2021). Other tools such as TOPCAT (Taylor 2011), Aladin (Bonnarel et al. 2000), ds9 (Smithsonian Astrophysical Observatory 2000) and SVO filters (Rodrigo & Solano 2020).

Abstract

The Small Magellanic Cloud (SMC), a dwarf galaxy in the local neighborhood, offers an accessible laboratory for exploring star formation processes in a metal-poor environment. The SMC's structure, stellar populations, and kinematics bear clear evidence of its recent dynamical encounters with the Large Magellanic Cloud (LMC) and the Milky Way. In particular, the young massive stars formed in these disturbed conditions serve as crucial tracers of galaxy interactions, stellar feedback, and hierarchical star formation. However, until recently, the far-ultraviolet (FUV) view of the SMC has been limited by spatial resolution and incomplete coverage. In this thesis, we employ data from the Ultra Violet Imaging Telescope (UVIT) onboard *AstroSat* together with complementary optical and near-infrared surveys (Gaia, SMASH, VMC) to present the most comprehensive FUV-based study of young stellar populations in the SMC to date.

As the first step, we constructed a catalog of ∼76,800 SMC FUV stars, of which ∼62,900 are identified as probable SMC main body members. This catalog includes UV, optical, and IR fluxes, enabling the study of stellar populations across multiple evolutionary stages. Based on the Gaia optical color–magnitude diagram (CMD), FUV stars were classified into four young populations: Young 1, Young 2, Young 3, and Blue Loop. Their spatial distribution reveals a highly irregular and clumpy morphology, with structures such as a broken bar, a shell-like feature, and the inner Wing. The Young 1, Young 2, and Young 3 populations are concentrated in the eastern and northeastern SMC, while the Blue Loop, Young 2 and Young 3 dominate the southwest. Proper motion analysis demonstrates that stars younger than ∼150 Myr show evidence of east–west kinematic stretching, consistent with signatures of the recent LMC–SMC encounter, while no strong perturbation is seen along declination.

To probe star formation closely, we analyzed clustering of stars with ages below 150 Myr, identifying 236 stellar structures whose sizes span from two parsecs to three hundred parsecs. Their irregular morphologies, perimeter-area dimension ($D_p = 1.46 \pm 0.04$), fractal dimensions ($D_2 \sim 1.3$–1.6), and log-normal surface density distribution closely resemble the properties of a turbulent interstellar medium. These results provide strong evidence that star formation in the SMC is hierarchical in nature and regulated by supersonic turbulence, with galaxy interactions supplying the driving mechanism for this turbulent regime.

Expanding the analysis to the northeastern SMC Shell region, we combined UVIT data with Gaia EDR3 to create an FUV–optical catalog of ~14,400 stars. Overlaying isochrones on FUV–optical CMD reveals multiple star formation episodes, most notably at ~260 Myr, linked to the last close LMC–SMC encounter, and at ~60 Myr, associated with the SMC's close approach to the Milky Way. The FUV stellar surface density, together with the dispersion in proper motion, indicates that the inner SMC extends northeastward to about 2.2°. In the FUV stellar density map, we identify arm-like and arc-like features whose kinematics are comparable to those of its main body. These outer extensions represent spatial overdensities of stars formed during multiple episodes of star formation, but they do not exhibit any clear kinematic distinction. The median proper motion and velocity dispersion are comparable to those of the SMC main body, suggesting that this region has not undergone significant tidal influence.

Finally, to characterize the properties of the SMC's young stars, we choose a sample region within the Shell where multifilter UVIT data are available for robustness. We constructed spectral energy distributions (SEDs) for 1348 stars in the Shell region, spanning 18 photometric bands from UV to IR. Using single- and double-component fits, we derived effective temperatures, luminosities, and radii, identifying 1242 single systems which are mainly main sequence B- and A-type stars (10,000–30,000 K, 3–8 $M_\odot$) and 85 systems which are double systems. These double systems include

18 stripped star binary systems, 9 subgiant-giant binary systems, and 20 candidate binaries. We also found 38 double systems, which could be non-contact binary or a star with a circumstellar disk or line-of-sight projections within the SMC. The characterized single and double systems include known eclipsing binaries, emission line stars, photometric variables, and pulsating variables.

Taken together, the results presented in this thesis deliver the most extensive FUV catalog of the SMC to date and provide a detailed view of the distribution, clustering, kinematics, and properties of its young stars. Our findings establish that the morphology and dynamics of massive stars are strongly shaped by LMC–SMC interactions, while their spatial substructure reflects turbulence-driven hierarchical star formation. By identifying binary systems and stripped stars, this work also lays critical groundwork for spectroscopic follow-up studies, which are essential to fully constrain the role of binarity and feedback in metal-poor environments. Looking forward, future UV missions such as UVEX and INSIST will further expand upon these results, offering deeper insight into how massive stars regulate the galaxies' evolution in the early Universe.

Contents

List of Figures

List of Tables

Abbreviations

μ	Proper Motion (PM)
$\mu_\alpha cos\delta$	Proper Motion in RA (PMRA)
μ_δ	Proper Motion in Dec (PMDec)
Å	Angstrom
$L_\odot$	Solar luminosity
$M_\odot$	Solar mass
$R_\odot$	Solar radius
$Z_\odot$	Solar metallicity
2MASS	**T**wo **M**icron **A**ll **S**ky **S**urvey
4MOST	**4**-metre **M**ulti **O**bject **S**pectroscopic **T**elescope
AST	**A**rtificial **S**tar **T**est
CF	**C**ompleteness **F**actor
CMD	**C**olor **M**agnitude **D**iagram
FUV	**F**ar **U**ltra **V**iolet
FWHM	**F**ull **W**idth at **H**alf **M**aximum
GALEX	**Gal**axy **E**volution E**x**plorer
HST	**H**ubble **S**pace **T**elescope
IRAF	**I**mage **R**eduction and **A**nalysis **F**acility
ISM	**I**nter **S**tellar **M**edium
KDE	**K**ernel **D**ensity **E**stimation
LA	**L**eading **A**rm

LMC	**L**arge **M**agellanic **C**loud
LSST	**L**arge **S**ynoptic **S**urvey **T**elescope
MCs	**M**agellanic **C**louds
MCPS	**M**agellanic **C**louds **P**hotometric **S**urvey
MS	**M**agellanic **S**stream
MW	**M**ilky **W**ay
NE	**N**orth **E**ast
NIR	**N**ear **I**nfra **R**ed
PSF	**P**oint **S**pread **F**unction
RA	**R**ight **A**scension
RUWE	**R**enormalised **U**nit **W**eight **E**rror
SED	**S**pectral **E**nergy **D**istribution
S/N	**S**ignal-to-**N**oise ratio
SMASH	**S**urvey of the **MA**gellanic **S**tellar **H**istory
SMC	**S**mall **M**agellanic **C**loud
UV	**U**ltra **V**iolet
UIT	**U**ltraviolet **I**maging **T**elescope
UVIT	**U**ltra **V**iolet **I**maging **T**elescope
UVOT	**U**ltra **V**iolet and **O**ptical **T**elescope
VMC	**V**ISTA survey of **M**agellanic **C**louds system
VPD	**V**ector **P**oint **D**iagram
ZAMS	**Z**ero **A**ge **M**ain **S**equence

Chapter 1

Introduction

> *“Earth is a small town with many neighborhoods in a very big universe.”*
> — Ron Garan

The Lambda Cold Dark Matter (ΛCDM or LCDM) framework suggests that the formation of galaxies and the large-scale structure of the Universe is a hierarchical process (Bower et al. 2006). In this paradigm, structure formation proceeds in small-to-large manner, where smaller systems form first within dark matter halos and later merge to build larger structures, as shown in Figure 1.1. Dwarf galaxies occupy a central role in this framework: they are among the first galaxies to form and act as key building blocks for the growth of more massive galaxies. These galaxies are either accreted as satellites or merge with more massive systems, such as the Milky Way (MW), contributing stars and gas to their halos and disks. These interactions leave behind observable signatures, including stellar streams, tidal bridges, and other substructures. This hierarchical assembly process is still ongoing and is observable in both nearby and more distant systems (e.g., Ibata et al. 1995; Bullock & Johnston 2005). In the Local Group, it can be examined in exceptional detail, offering a unique window into the physical mechanisms that govern galaxy growth and transformation. Studying nearby interacting systems, therefore, provides crucial insights into galaxy formation and evolution. One of the most prominent and accessible examples in our vicinity is the Magellanic System.

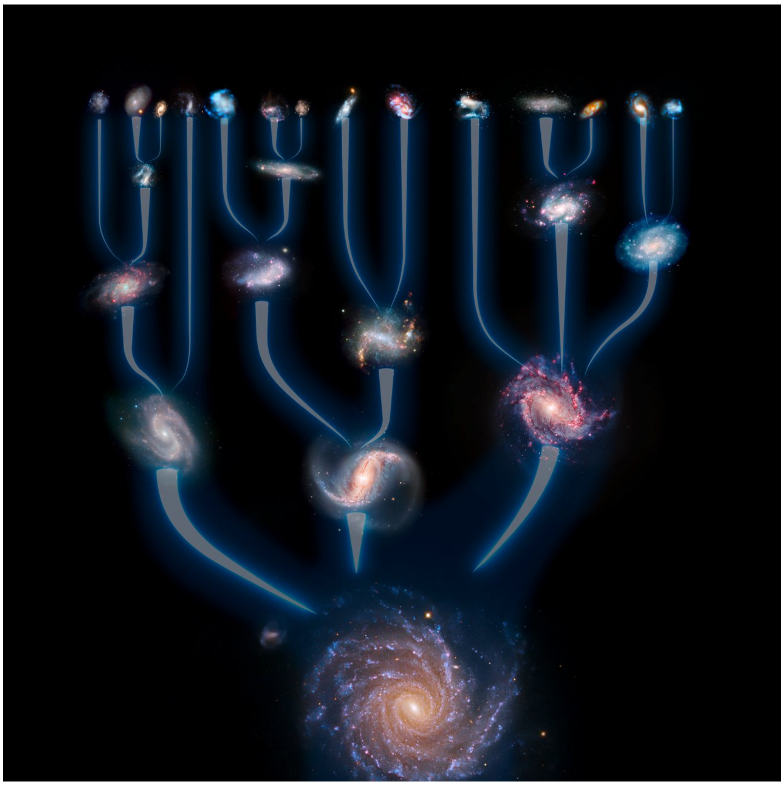

FIGURE 1.1: The hierarchical model of galaxy formation: small galactic building blocks form first and gradually merge over cosmic time to create large and massive galaxies. Credits: ESO/L. Calçada

1.1 The Neighboring System

The Magellanic System, as shown in Figure 1.2, is located in the immediate locality of the MW and comprises an actively interacting group of galaxies and provides an unparalleled laboratory for studying galaxy interactions in detail (D'Onghia & Fox 2016). Its primary components are two gas-rich, irregular dwarf galaxies, the

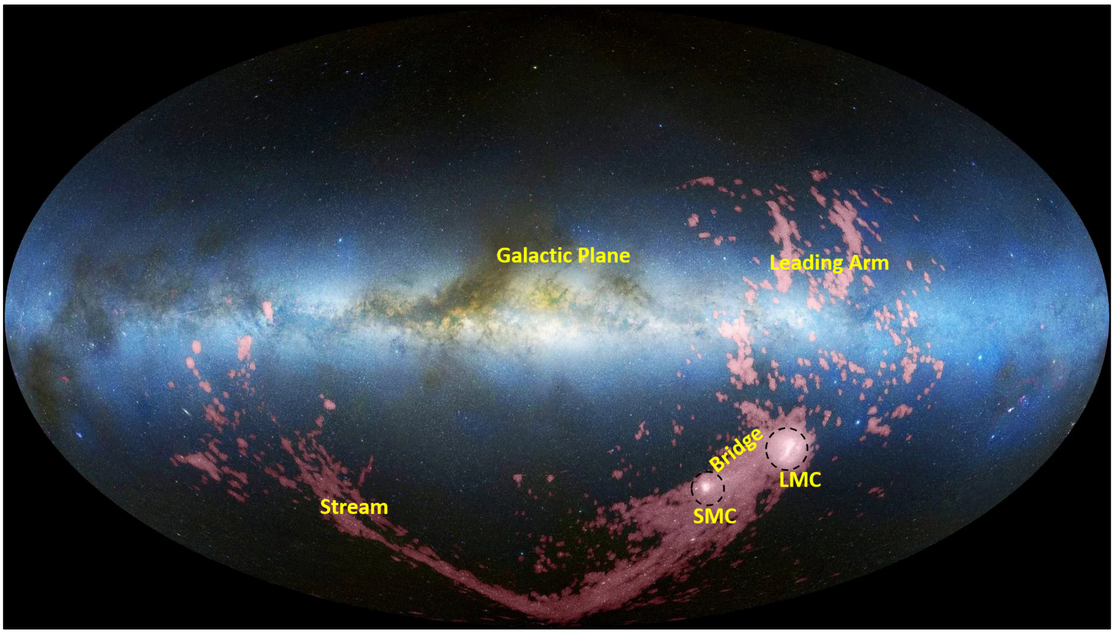

FIGURE 1.2: Composite map of the sky combining radio and optical data. Neutral hydrogen (H I) emission is shown in pink and overlaid on an optical all-sky image (blue, white, and brown) from Mellinger (2009). The map is displayed in an Aitoff projection, centered on the Galactic center. The MCs are visible as bright white patches within the dashed circles. Credits: Nidever et al. (2010).

Large and *Small Magellanic Clouds* abbreviated as LMC and SMC respectively, collectively known as the *Magellanic Clouds*, referred to as MCs. Their ongoing interaction, between the Clouds and with our Galaxy, has given rise to a complex network of gaseous and stellar features that trace the system's dynamical history. Three major signatures of these interactions are observed in the form of extended gaseous and/or stellar structures: (1) *the Magellanic Stream* (MS) — a gaseous structure trailing behind, covering over 200 degrees across the sky (Liu 1992; Gardiner et al. 1994), (2) *the Leading Arm* (LA) — a counterpart feature ahead of the Clouds in their orbit (Putman et al. 1998) and (3) *the Magellanic Bridge* (MB) — a dense gaseous and stellar connection between the LMC and SMC (Hindman et al. 1963; Gardiner et al. 1994; Muller & Bekki 2007; Zivick et al. 2019). These structures reflect both past and ongoing tidal and hydrodynamic interactions and serve as powerful probes of the orbital history and internal dynamics of the Clouds.

1.1.1 The Magellanic Clouds

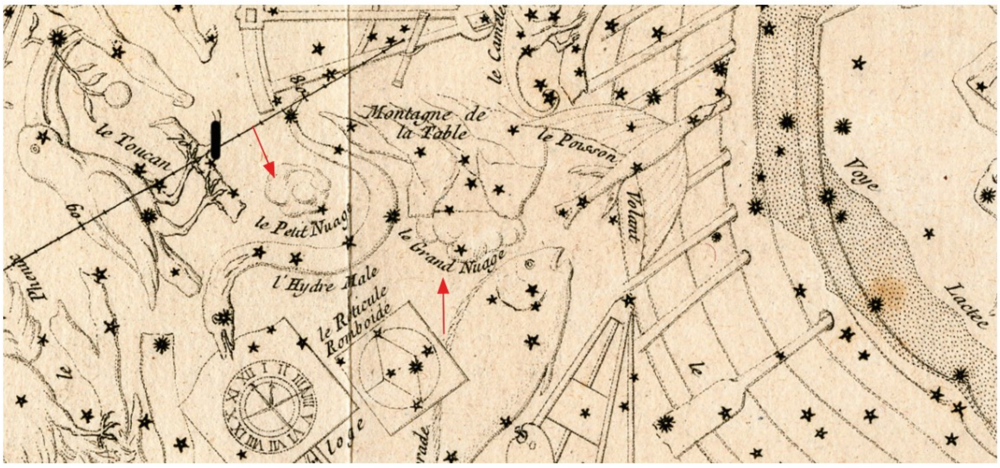

FIGURE 1.3: Enlarged view of La Caille's 1752 map, with the two Clouds marked by red arrows. Credits: Paris Observatory, Dennefeld (2020).

FIGURE 1.4: Left panel: Ground-based wide-field image of the LMC, taken by astrophotographer Eckhard Slawik, covering approximately 10° × 10°. The prominent red region slightly left of center marks 30 Doradus (the Tarantula Nebula), the most active star-forming region in the Local Group. The H II region N11B appears in the upper right portion of the LMC. Credits: Eckhard Slawik. Right panel: Two-colour image of the full SMC, constructed from Digitized Sky Survey 2 (DSS2) data. The field of view spans just over 3.5°. Credits: ESA/Hubble and DSS2 and Davide De Martin.

The MCs stand out in the southern sky and have captured human curiosity for centuries. Their visibility to the naked eye ensured that they were well known to Indigenous populations in the southern hemisphere long before the advent of Western astronomy (Dennefeld 2020). Cultural interpretations by communities

Table 1.1: Basic properties of the MCs: morphological type, distances, masses, spherical coordinates, and proper motions. S – Spiral, B – Barred, (s) – without ring, m – Magellanic, and p – peculiar. [1]Pietrzyński et al. (2019), [2]Graczyk et al. (2020), [3]Besla (2015, and references therein), and [4]de Vaucouleurs & Freeman (1972, hereafter V1972), [5]Gaia Collaboration et al. (2021a).

Property		**LMC**	**SMC**
Morphological Type		SB(s)m	SB(s)mp
Distance D [kpc]		[1]49.59 ± 0.09	[2]62.44 ± 0.47
[3]Mass [M$_\odot$]	Stellar	2.7×10^9	3.1×10^8
	Gas	5.0×10^8	4.2×10^8
	Dynamical	$(1.7 - 2.25) \times 10^{10}$	$(1.4 - 5.1) \times 10^9$
Center [RA, Dec]	[4]Optical	$05^h19^m38^s$, $-69°27'05''.2$	$00^h52^m12^s.5$, $-72°49'43''$
[5]Proper Motion μ [mas/yr]	$\mu_\alpha \cos\delta$	1.7608 ± 0.4472	0.7321 ± 0.3728
	μ_δ	0.3038 ± 0.6375	−1.2256 ± 0.2992

such as the Mapuche and Tupi-Guarani often associated these diffuse celestial objects with natural phenomena like water sources, describing them as fountains or ponds. Early visual depictions, including petroglyphs from northern Chile, provide some of the earliest surviving references to these galaxies. Mentions also appear in early Islamic texts, although much of the knowledge from precolonial societies was transmitted orally and has not survived in written form. The first documented Western observations are attributed to the age of maritime exploration. Amerigo Vespucci, during his voyage in 1501–1502, likely provided the earliest European description of the Clouds. Subsequent explorers, including Andrea Corsali (circa 1515) and members of Ferdinand Magellan's expedition (1519–1522), offered more detailed accounts. The latter, especially through Antonio Pigafetta's travel writings, introduced the Clouds to a broader European audience. Nevertheless, their diffuse nature meant they were often overlooked in navigation charts in favor of more practical asterisms like the Southern Cross. Over time, sailors began informally referring to them as the "Magellanic Clouds," a name that eventually gained scientific acceptance, most notably through John Herschel's usage in the mid-19th century. Despite their long-standing visibility, systematic scientific studies of the Clouds only began in earnest in the mid-20th century. The seminal work of Gérard de Vaucouleurs during the 1950s marked a significant milestone, offering surprisingly accurate insights into their morphology, dimensions, and distance (de

Vaucouleurs 1954a,b, 1955a,b, 1957). From being cultural icons to key objects in modern astrophysics, the MCs have evolved into essential targets for understanding galactic dynamics and evolution.

The LMC and the SMC are located at a distance of ∼50,000 pc (de Grijs et al. 2014; Pietrzyński et al. 2019) and ∼62,000 pc (de Grijs & Bono 2015; Graczyk et al. 2020, hereafter G2015 and G2020 respectively) away from our Solar System. These two satellite galaxies are irregular gas-rich dwarf galaxies, gravitationally bound and currently interacting with each other and the MW. These interactions have led to significant tidal and hydrodynamic effects, shaping the morphology, kinematics, and star formation histories of these galaxies. The LMC is the more massive and more structured of the two, displaying a prominent off-centered bar (Zaritsky 2004) and spiral arm-like features (Gardiner et al. 1998) (left panel of Figure 1.4). 30 Doradus in the LMC is the most active region of stellar formation within the Local Group (Elmegreen & Elmegreen 1980; Gallagher & Hunter 1984). In contrast, the SMC exhibits a more disturbed and irregular morphology (see the right panel of Figure 1.4), with a central bar and extended wing-like structure (Shapley 1940) pointing towards the LMC. The stellar and gas components of both the Clouds show evidence of distortion and displacement, supporting the view that they have experienced repeated close encounters (Harris & Zaritsky 2009; Rubele et al. 2018; Massana et al. 2022; Dhanush et al. 2024). Until approximately two decades ago, it was accepted that the MCs orbit our Galaxy and the episodic star formation was attributed to the perigalactic passages and/or the corresponding tidal effects of the MW-LMC-SMC interactions (Lin et al. 1995; Harris & Zaritsky 2004). Subsequently, observational studies using the ground telescopes, the *Hubble Space Telescope* (HST) (Kallivayalil et al. 2006) and dynamical simulation (Besla et al. 2007; Chandra et al. 2023) found that the MCs are on their orbital encounter with the MW. Vasiliev (2023) proposed that the MCs are on their second passage. A summary of the basic characteristics of the LMC and the SMC is presented in Table 1.1.

1.1.2 The Magellanic Stream and the Leading Arm

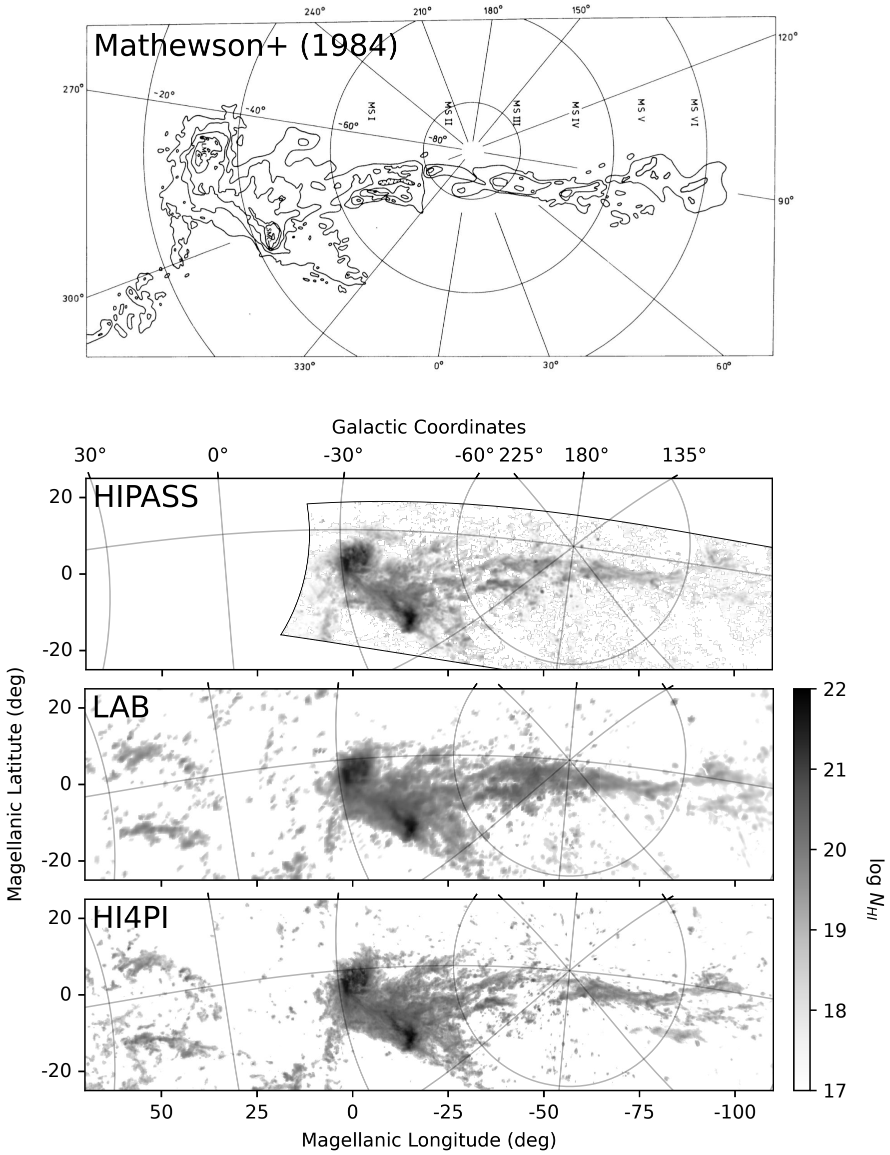

FIGURE 1.5: H I projections of the MCs and their surrounding environment from multiple surveys. Top panel: Original identification of the six high-density knots (MS I–VI) along the MS (Mathewson & Ford 1984). Upper middle panel: Reprocessed HIPASS data (Putman et al. 2003), presented in Magellanic Coordinates as defined by Nidever et al. (2008). Lower middle panel: LAB survey map highlighting gas associated with the MCs, separated from Galactic emission using Gaussian decomposition (Nidever et al. 2008). Bottom panel: HI4PI survey map displaying high-velocity gas (Westmeier 2018). Galactic coordinates are indicated in all panels. Credits: Lucchini (2024).

Among the most prominent components of the Magellanic System is the MS, a massive trailing structure of neutral hydrogen (H I) that arcs across more than 200 degrees of the sky. First identified in 21-cm surveys by Mathewson et al. (1974), the Stream is devoid of significant stellar content and is believed to have originated from the outer gas-rich regions of the LMC and the SMC. The Stream's filamentary morphology, high radial velocities, and low metallicity offer essential clues to its origin and evolution. Kinematic studies have shown that the gas in the Stream is moving at high velocities consistent with material stripped during dynamical interactions, either between the Clouds themselves or with the MW (Nidever et al. 2008). Its chemical composition (Fox et al. 2014)—particularly the detection of low metallicity and alpha-element enhancement—suggests a predominant origin in the SMC, with possible contributions from the LMC as well. An alternative scenario proposes that the Stream is formed via ram-pressure stripping during the Magellanic System's last passage through the MW's extended ionized disk. This interaction likely stripped loosely bound H I gas, creating the observed trailing structure (Mastropietro et al. 2004; Hammer et al. 2015). The Stream is therefore not just a product of galactic interactions but also a laboratory to study the mechanisms of gas removal in dwarf galaxies and their impact on the circumgalactic medium around massive galaxies. A view of the Stream as found in different H I surveys is shown in Figure 1.5.

The LA, first identified by its velocity components lying ahead of the MCs in their orbit (Figure 1.6; Putman et al. 1998), consists of LA I, II, and III. LA I is physically and kinematically connected to the LMC (Nidever et al. 2010), whereas LA III lies farthest away. Though limited absorption spectroscopy data exist for a few sightlines, metallicity measurements remain poorly constrained (Fox et al. 2018), and low O/H values have ruled out an LMC origin for LA III. Estimated distances to the LA ($\sim$20 kpc) are supported by stellar population detections, interactions with the MW disk, and Hα emission (Casetti-Dinescu et al. 2014; McClure-Griffiths et al. 2008; Antwi-Danso et al. 2020). While initially viewed as

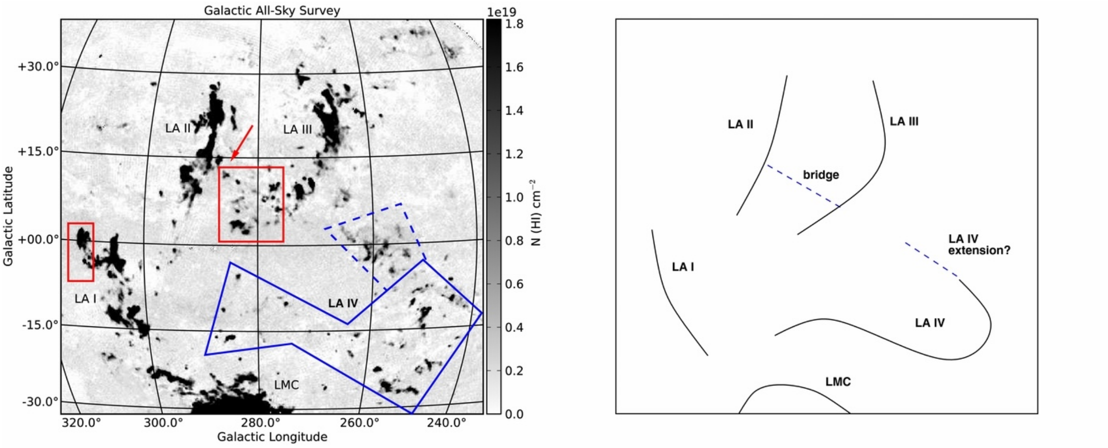

FIGURE 1.6: Newly detected components of the LA as revealed by the GASS survey. Left panel: Integrated H I column density map, where red boxes highlight newly identified extended features within the LA complexes. The arrow indicates a potential bridge connecting LA II and LA III. A previously unidentified complex, designated as LA IV, is enclosed within the blue box, with a possible extension marked by the dashed blue box. Right panel: Schematic illustration of the LA structures (For et al. 2013). Credits: Lucchini (2024).

strong evidence for a tidal origin, more recent studies show that even tidal models struggle to fully explain the presence of the LA (Tepper-García et al. 2019). Ram-pressure exerted by the MW's circumgalactic medium may disrupt or displace the leading gas (Bustard & Gronke 2022), and alternative scenarios suggest it may contain gas removed from dwarf galaxies leading the Clouds during their infall (Hammer et al. 2015). However, definitive remnants of such dwarfs remain unidentified.

1.1.3 The Magellanic Bridge

The MB represents a prominent stellar and gaseous connection between the SMC and LMC. It was initially thought to consist mainly of neutral hydrogen and young stars (Putman et al. 2003; Harris 2007). Later Belokurov et al. (2017) revealed a second branch, the Southern Bridge, the Southern Bridge, which is not aligned with the LMC and contains older stars traced by RR Lyrae variables. More

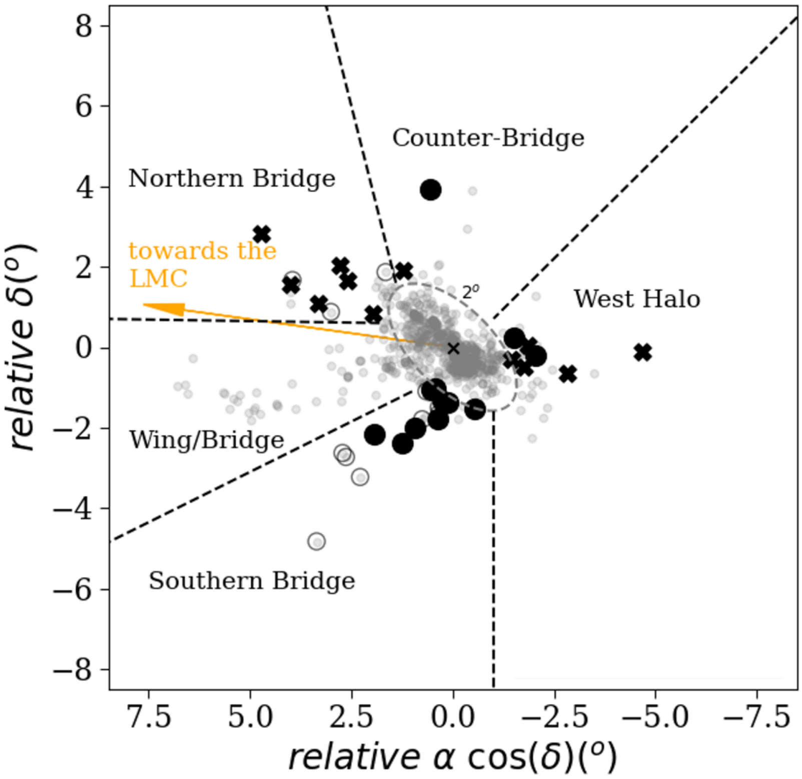

FIGURE 1.7: Spatial distribution of star clusters in the SMC. Small gray circles represent clusters from the catalog by Bica et al. (2020). Black circles mark clusters studied by Parisi et al. (2023), while black crosses indicate clusters analysed in the VISCACHA studies by Dias et al. (2021, 2022). Clusters with CaT-based metallicities available in the literature are shown as larger gray circles. The ellipse traces the projected extent of the SMC main body. Thick dashed lines demarcate the outer regions into distinct two-dimensional structural components of the SMC, following the definitions of Dias et al. (2014, 2016). Credits: Parisi et al. (2023).

recently, Dias et al. (2021) uncovered a third component, the Northern Bridge, supported by earlier indications (Nidever et al. 2013). This structure appears to contain star clusters, possibly stripped from the SMC and moving toward the LMC. Figure 1.7 shows the projected locations of the main bridge (extension of the Wing), Southern, Northern, and Counter Bridges (in terms of clusters), and southwest halo (discussed in section 1.2.1). Diaz & Bekki (2012) used N-body simulations to predict a tidal structure associated with the MB, the Counter-Bridge, which originated roughly 250 Myr ago. Dias et al. (2021) identified the first star cluster associated with this structure. Further evidence from the VISCACHA survey (Oliveira et al. 2023) identified two cluster populations in the Bridge region: a young population formed in situ, and an older population likely stripped from the SMC.

1.2 The Small Magellanic Cloud

The SMC is one of the largest satellites of the MW and a metal-poor galaxy with an average metallicity of $Z \approx 0.2\ \mathrm{Z}_{\odot}$ (Russell & Dopita 1990; Trundle et al. 2007; Hunter et al. 2009; Hocdé et al. 2023). It is currently undergoing active star formation, particularly concentrated in the central and eastern regions (Gonidakis et al. 2007), (El Youssoufi et al. 2019, hereafter DL2019). The SMC has likely experienced multiple interactions with its more massive companion, the LMC, with the most recent close passage occurring approximately 150–300 Myr ago (as inferred from dynamical modelling, cluster formation histories, and star formation histories, Harris & Zaritsky 2009; Rubele et al. 2018; Massana et al. 2022; Dhanush et al. 2024). These interactions have triggered bursts of star formation and significantly influenced the galaxy's morphology and internal dynamics. With a dynamical mass of $(1.4\text{–}5.1) \times 10^9, M_{\odot}$, the SMC is about an order of magnitude less massive than the LMC ($DM_{MW} = (1.7 - 2.25) \times 10^{10}\ M_{\odot}$; Stanimirović et al. 2004; van der Marel & Kallivayalil 2014; Besla 2015) and nearly two orders of magnitude less massive than the MW ($DM_{MW} = (0.75\text{–}2.25) \times 10^{12}\ M_{\odot}$, Cautun et al. 2020). This large mass disparity renders the SMC highly susceptible to tidal forces and ram pressure effects, resulting in pronounced structural asymmetries and the development of prominent tidal features such as the MB, the Stream (Putman et al. 1998; Tatton et al. 2021), (Massana et al. 2020, hereafter MS2020) and substructures in the outskirts (Dias et al. 2016, 2021, 2022; Parisi et al. 2023).

The SMC serves as a critical laboratory for understanding dwarf galaxy evolution in an interacting environment. Its immediate vicinity (≈62,000 pc; G2015; G2020) allows the resolution of individual stars across its extent, enabling detailed studies of stellar populations and kinematics. Moreover, its position in the sky avoids the crowded central regions of the MW, minimizing foreground contamination and allowing high-fidelity mapping of its structure and dynamics. *In this thesis, the recent evolutionary history of the SMC is examined, with particular attention given to its morphology, kinematics, star formation, and properties of its young massive stars.* This section presents a comprehensive overview of these aspects, which will serve as the foundation for the subsequent chapters.

1.2.1 Morphology

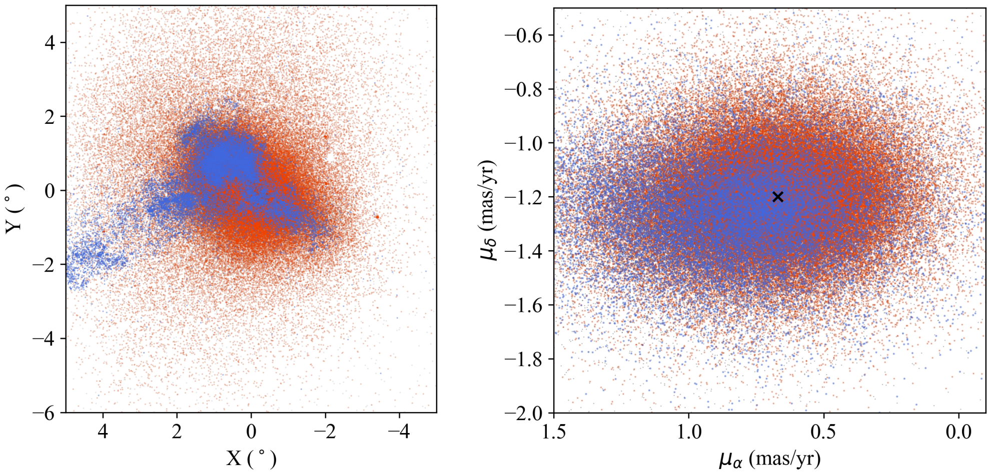

FIGURE 1.8: Distributions of main sequence (blue) and red giant (red) stars of the SMC in XY- (left panel; spatial) and proper motion (right panel; VPD) plane. The black “×” marks the proper motion center of the red giants. Credits: Zivick et al. (2021).

The appearance of the SMC, i.e. its morphology, is complex and varies with its stellar population (e.g. Bot et al. 2004), (Gaia Collaboration et al. 2021a, hereafter G2021). The young population in the SMC is distributed asymmetrically, concentrated primarily in the central body and extending eastward into the SMC

Wing, a region that connects to the MB (see the distribution of the blue points, the main sequence stars, left panel, Figure 1.8; Indu & Subramaniam 2011; Rubele et al. 2015; Zivick et al. 2021). In contrast, the older stellar population, traced by red giant (RG) stars, appears more uniformly distributed, i.e., spheroidal or ellipsoidal configuration (see distribution of the red points, the RG stars, left panel, Figure 1.8; Zaritsky et al. 2000; Stanimirović et al. 2004; Rubele et al. 2015; Zivick et al. 2021). Recent study by DL2019 recently found that its young stars exhibit a bar with a noticeable break, indicating a density discontinuity, while intermediate-age stars extend towards the MB, probably as a consequence of tidal effects from the LMC ∼200 Myr ago. Additionally, irregular features seen in the central area suggest that the inner SMC has also been significantly shaped by these past gravitational encounters.

The 3D structure of the SMC reveals considerable complexity, particularly along the viewing direction. Depth estimates vary significantly across different regions. Cepheids, which trace younger stellar populations, have been shown to follow a bimodal age distribution, with younger Cepheids generally located closer to the observer compared to older ones (Subramanian & Subramaniam 2015; Ripepi et al. 2017). According to Scowcroft et al. (2016), the galaxy extends as much as ∼20 kpc along the northeast-southwest (NE–SW) axis, with the northeastern side being the nearer end. Furthermore, the SMC bar has been identified as being significantly stretched along the observer's line of sight (Gardiner & Noguchi 1996),with eastern areas showing greater depth, sometimes extending to 23 kpc (Nidever et al. 2013). Investigations using red clump (RC) stars also support this geometry. Subramanian & Subramaniam (2012) concluded that the SMC is elongated along the northeast–southwest direction, with a tidal extent estimated between 7 and 12 kpc. Subramanian et al. (2017) reported a bi-modal distance distribution among a foreground population of RC stars, suggesting tidal stripping that may be linked to the formation of the MB. According to Sakowska et al. (2024, hearafter SW2024), the northeastern portion of the SMC extends about 7 kpc along the observer's line of sight. Dhanush et al. (2025) found that the SMC exhibits a line-of-sight extent of roughly 30 kpc, reflecting significant elongation along the radial direction.

1.2.2 Substructures

The SMC's peripheral regions host a range of stellar substructures, providing clues to its complex dynamical interactions with the LMC and the MW. Several studies have identified distinct spatial and kinematic features tracing signatures of past tidal interactions and localized star formation events (Belokurov & Erkal 2019), (MS2020). One such feature is the northeastern SMC-Shell, estimated to be younger than 500 Myr, and studied extensively (Albers et al. 1987; Zaritsky et al. 2000), (Martínez-Delgado et al. 2019, hearafter MD2019), (SW2024). According to MD2019, the Shell may have originated in the latest phase of star formation, potentially driven by interactions with the LMC or MW, but a tidal formation scenario remains unconfirmed. Piatti (2022) analyzed 20 star clusters in this region and found that the region shows a significant depth of ∼13 kpc, exceeding earlier estimates. SW2024 found that the northeastern Shell is dominated by young stars, with episodes of enhanced stellar activity at ∼250 and ∼450 Myr.

On the western side of the SMC, a distinct feature known as the West Halo (Figure 1.7) has been reported in both photometric and kinematic studies (Dias et al. 2016, 2022; Zivick et al. 2018; Saroon et al. 2023). This structure appears to be receding from the SMC and likely represents tidally stripped material. In the southern outskirts, Cullinane et al. (2023) reported the presence of two distinct stellar populations: one consistent with the SMC outskirts and another appearing as debris removed from the SMC through interactions with the LMC. Similarly, Omkumar et al. (2021) detected a foreground stellar population in the eastern outskirts, which they associated with the stellar counterpart of the MB. A prominent overdensity known as SMCNOD was discovered 8° from the SMC centre by Pieres et al. (2017) using Dark Energy Survey (DES) data. Based on color–magnitude diagram (CMD) analysis with theoretical isochrones, this structure primarily comprises intermediate-age stars around 6 Gyr old, with a smaller number of younger stars with an age of ∼1 Gyr, and is likely a tidal remnant stripped from the SMC disc. Follow-up observations with the Magellanic Satellites Survey (MagLiteS) confirmed that SMCNOD lies at a similar distance as the SMC, reinforcing its tidal origin. Another substructure, termed Northern Substructure 2, was reported by El Youssoufi et al. (2021) near the SMCNOD, around 7° northeast of the SMC's centre. This feature, composed mainly of intermediate-age stars, may be linked to the SMC's ellipsoidal shape rather than an external interaction. In addition, a recently discovered diffuse feature located approximately 14° from the SMC centre was discovered by MS2020 using the *Survey of the MAgellanic Stellar History* (SMASH) (Nidever et al. 2017, 2021, hearafter N2017 and N2021, respectively) data. The significant separation points to a potential association with a distant and ancient component.

1.2.3 Kinematics

The kinematic structure of the SMC exhibits significant variation depending on the stellar population (see Figure 1.8). Using the Australia Telescope Compact Array (ATCA) observations, Stanimirović et al. (2004) revealed that the H I gas in the SMC exhibits differential rotation, characterized by a velocity gradient extending from southwest to northeast." Intermediate-age RGB stars also show kinematically complex behavior. In particular, Dobbie et al. (2014a) found a pronounced velocity gradient, with lower line-of-sight velocities towards the Wing and higher values towards the southwestern end of the bar. These features were interpreted as kinematic evidence of tidal debris—the former possibly representing stars drawn into the MB and the latter linked to the so-called Counter-Bridge.

Proper motion measurements by Zivick et al. (2018), based on HST observations across 43 SMC fields, suggested that the SMC lacks strong internal rotation. According to their orbital study, the LMC and SMC experienced a close, head-on encounter around 147 Myr ago. In another study, De Leo et al. (2020) identified signs of tidal disruption in the RG population, particularly through tangential velocity anisotropy, further supporting the scenario of tidal influence from the LMC. More recently, Niederhofer et al. (2021) used data from the *VISTA survey of the Magellanic Clouds system* (VMC) (Cioni et al. 2011, hereafter C2011) to examine proper motions across different stellar ages. Their results indicated that the SMC's outer regions are being stretched outward. Notably, younger stars exhibited larger proper motions toward the MB, while older populations showed coherent motion toward the region associated with the older bridge.

El Youssoufi et al. (2023) revealed that young stars in the bar exhibit systematically higher radial velocities than supergiants, likely due to their formation from gas already perturbed by tidal forces during a star formation episode ∼40 Myr ago. Moreover, stars originating in the northern bar during a significant burst about 25 Myr ago show greater radial velocities relative to stars in the southern bar. This north–south kinematic asymmetry is also evident among giant stars. These stellar patterns, supported by analyses of cold gas along with transverse motion data, provide strong evidence for tidal stretching and stripping of the SMC induced by its recent interactions with the LMC. More recent work by Dhanush et al. (2025) reveals that young populations (<400 Myr) form a rotation-supported disk with high elongation, moderate velocity dispersion (∼11 kms^{-1}), and an estimated asymptotic rotation velocity of ∼49–89 kms^{-1} over a ∼6–9 kpc scale radius. In contrast, the older stellar components exhibit little to no rotation and instead trace a more spheroidal or flattened elliptical morphology.

1.2.4 Star Formation

The galaxy's stellar formation history characterizes how its star formation(SF) rate has varied over cosmic time, offering insights into the processes governing stellar mass assembly. It reflects the efficiency and timing of SF events, which are influenced by mechanisms such as gas accretion, galaxy interaction/mergers, internal feedback, and external environmental factors. Numerous studies have explored the SMC's temporal evolution of SF using various tracers.

Using UBVI photometry from the *Magellanic Clouds Photometric Survey* (MCPS), and StarFISH analysis software (Harris & Zaritsky 2001), Harris & Zaritsky (2004) derived the spatially resolved SF and chemical enrichment history of the central region of the SMC. Their study revealed that nearly half of all stars in the SMC formed more than 8.4 Gyr ago,with additional episodes of SF around 0.06, 0.4 and 2.5 Gyr, closely coinciding with past perigalactic interactions with the MW. Sabbi et al. (2009) revealed that SF began around 12 Gyr ago in the SMC based on the oldest main sequence turn off (MSTO) from HST/ACS CMDs, though it remained low for the first few Gyr. A radial metallicity gradient is observed, with lower metallicity in the outskirts. SF persisted until ∼2–3 Gyr ago and re-ignited around 500 Myr ago, especially in the bar and wing. The patchy spatial arrangement of young stars suggests that recent SF is localized. Indu & Subramaniam (2011) traced the last star-formation event in the SMC over the past 500 Myr using the MSTO identified from optical CMDs based on OGLE III and MCPS data. They detected young star-forming concentrations near the center and wing, with notable activity at 0–10 Myr and 50–60 Myr. A systematic shift in the centroid of young populations was observed towards the LMC, suggesting recent SF was triggered by the LMC's gravitational influence combined with the MW's perigalactic passage. Rubele et al. (2018) using CMD reconstruction method found that the SMC built up approximately 5.3×10^8 $M_\odot$ in stars, with nearly 67% of that mass remaining in stars and remnants today. Roughly half of the stellar content originated more than 6.3 Gyr ago, while 80% was in place between 8 and 3.5 Gyr ago. This pattern suggests that SF was most vigorous in the galaxy's earlier stages, tapering off in more recent times. Joshi & Panchal (2019) reported a noticeable increase in the Cepheid population around 200 Myr ago, likely triggered by a close interaction between the Clouds. SW2024 analyzed a Shell-like structure in the northeastern SMC using deep SMASH photometry and CMD fitting. They found young SF enhancements at ∼1 Gyr, ∼650 Myr, ∼450 Myr, ∼200 Myr, and ∼150 Myr with evidence of synchronization with the LMC's northern arm over the past ∼2.8 Gyr. The formation of star clusters in the SMC has been closely associated with episodes of SF (e.g., Glatt et al. 2010; Nayak et al. 2018; Dhanush et al. 2024), indicating that periods of enhanced SF are often accompanied by increased cluster formation activity. Massana et al. (2022) used THESTROM (Tracing tHe Evolution of the STar fOrmation Rate and Metallicity) software (Bernard et al. 2015, 2018) to obtain the best-fitting star formation history (SFH) solution for each Voronoi bin of the SMC via a Poisson-adapted χ^2 that fits synthetic single stellar populations to the observed CMD. They identified five major SF peaks in the SMC over the past 3.5 Gyr, occurring around 3, 2, 1.1, 0.45 Gyr ago and one presently. They found a striking synchronicity between the SMC and LMC SF histories, implying that their repeated tidal interactions have significantly influenced their recent evolution.

1.2.5 Hierarchical Star Formation

Stars can be observed either as isolated field stars or as members of larger groups, including clusters, stellar associations, or even widespread complexes that span galaxy-scale regions. It is well-established that SF begins when pockets of gas and dust within molecular clouds collapse under their own gravity (Lada & Lada 2003; Larson 2003; Duchêne et al. 2004). The interstellar medium (ISM) exhibits

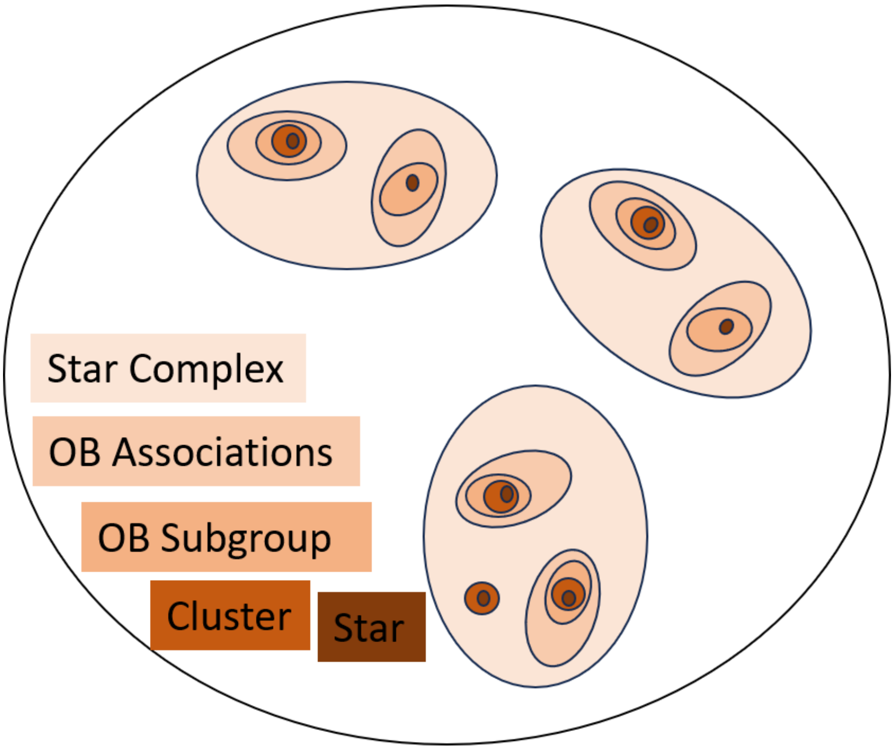

Figure 1.9: Schematic representation of hierarchical star formation, following Elmegreen et al. (2014).

structures which are hierarchical across various spatial scales (e.g., Elmegreen 1993), where large-scale features like giant molecular clouds consist of progressively smaller and denser substructures. These nested formations continue down to the smallest scales, forming a fractal-like pattern. Elmegreen & Efremov (1996) found that this organization within the ISM is largely shaped by turbulence, magnetic fields, and gravitational forces. Young stars, particularly those younger than 100 Myr, display a spatial arrangement (see Figure 1.9) that mirrors the hierarchical structure of the gas in the ISM (e.g., Gouliermis et al. 2015). Both observational studies and simulations indicate that young stellar groupings emerge following the ISM's fractal distribution (Vázquez-Semadeni et al. 2017; Elmegreen & Elmegreen 2001). This pattern of formation is commonly referred to as 'hierarchical,' 'fractal,' or 'scale-free' SF (Bate et al. 1998; Larson 1995).

According to Hodge (1985), the SMC has 70 associations of stars, averaging 77 pc in size, similar to associations observed in the LMC (Lucke & Hodge 1970) but smaller than typical associations in the MW, M31, or M33. Using the spatial distribution of OB stars, Battinelli (1991) identified associations in the SMC with a comparable mean size of 90 pc. In M33, Bastian et al. (2007) demonstrated that the typical size of young structures can vary depending on the detection criteria, such as the adopted breaking scale or minimum number of stars. Gieles et al. (2008), analyzing MCPS data and using two-point correlation function and spanning trees, reported prominent substructures among ∼10 Myr old stars that fade by ∼75 Myr. Similarly, Bonatto & Bica (2010) reported that clusters of young stars in the SMC and LMC display strong spatial self-correlation and a power-law size distribution, consistent with hierarchical star formation. However, their analysis relied on Bica et al. (2008)'s catalog, which may suffer from selection biases. More recently, Sun et al. (2018, hereafter S2018), using VMC near-infrared (NIR) data, found that the SMC's structures of young stars are non-uniformly arranged but their size and mass follow power-law distributions, likely driven by the ISM's supersonic turbulence.

1.2.6 Massive Stars

Massive stars, despite their relatively short lifetimes, play a pivotal role in driving galactic evolution. Through their intense ionizing radiation, powerful stellar winds, and eventual core-collapse supernovae, they act as primary sources of mechanical feedback and the chemical enrichment of the ISM (Zinnecker & Yorke 2007). By dispersing heavy elements and injecting large amounts of energy into their surroundings, they regulate SF on local and galactic scales, shape the structure and dynamics of the ISM, and set the conditions for subsequent generations of stars and planetary systems (Bally & Zinnecker 2005; Kennicutt 2005; Kennicutt & Evans 2012; Goswami et al. 2022). Their influence extends beyond individual star-forming regions, profoundly affecting the physical, chemical, and morphological evolution of galaxies across cosmic time.

The SMC, with its proximity and low line-of-sight extinction, offers an exceptional laboratory to study individual massive stars in a low-metallicity environment ($\sim$0.2 $Z_\odot$; Russell & Dopita 1990; Trundle et al. 2007; Hunter et al. 2009; Choudhury et al. 2018). Its metallicity is comparable to that of galaxies at intermediate redshifts, making it a valuable local analog for conditions in the early Universe. Bonanos et al. (2010) created a catalog of 5,324 massive stars with photometry for 3,654 of them and revealed systematic differences in properties in the infrared between the SMC and the LMC. These differences were attributed to the reduced dust content and lower mass-loss rates at low metallicity, which affect the infrared excesses of evolved massive stars. Schootemeijer et al. (2021) reported a notable scarcity of luminous, very young massive stars in the SMC. They argued that many such stars may remain deeply embedded in their natal molecular clouds due to the lower dust content, making them harder to detect in optical and NIR surveys. On the other extreme, properties of young massive stars in the UV are also significant in the low metallicity environment. Bouret et al. (2021), using high-resolution UV and optical spectra, found evidence of stronger chemical evolution signatures—particularly nitrogen enrichment—in evolved O-type stars. Their results suggested that rotational mixing and mass-loss processes operate differently in the low-metallicity regime of the SMC, when compared to the MW. More recently, Cakırlı et al. (2023) identified five candidate slowly pulsating B-type stars in binary systems with component masses ranging from 2–25 $M_\odot$. Nakano et al. (2025) recently identified 7,426 massive stars with $M \geq 8$ $M_\odot$ using Gaia data (Gaia Collaboration et al. 2023, hereafter G2023), providing the most extensive and homogeneous catalog to date for exploring the demographics and evolutionary pathways of massive stars. To probe binarity in such low-metallicity environments—analogous to the early Universe—the *Binarity at Low Metallicity* (BLOeM) survey was launched (Shenar et al. 2024a). BLOeM is monitoring 929 massive stars across 25 spectroscopic epochs and has already yielded results on Be/Oe stars, BAF-type supergiants, and OB-type populations in the SMC (Bodensteiner et al. 2025; Patrick et al. 2025; Britavskiy et al. 2025).

1.3 Multiwavelength Study of the SMC

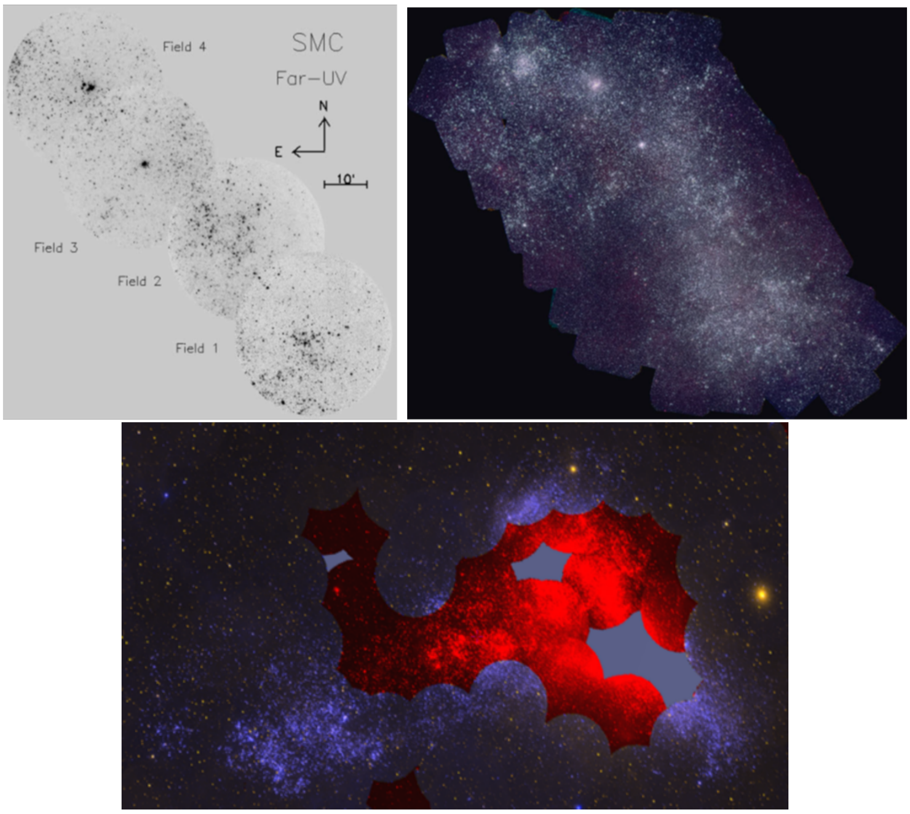

FIGURE 1.10: Top left panel: Four FUV fields observed by UIT (Cornett et al. 1997). Top right panel: Field observed by Swift/UVOT (Gehrels et al. 2004). Bottom panel: Combined FUV (blue) and NUV (red) coverage of the SMC by GALEX DR6 and DR7 data (Simons et al. 2014; Bianchi et al. 2017).

Observations of the SMC across multiple wavelengths are crucial for tracing its morphology (see section 1.2.1) as a function of stellar population, thereby providing insights into its evolutionary history. In the NIR wavelength, surveys such as the 2MASS (Cohen et al. 2003) and the VMC (C2011) have traced the older stellar populations and the galaxy's underlying structure. In the mid- and far-infrared (FIR), the *Spitzer* has provided a detailed census of dust emission and SF regions (Gordon et al. 2011). At optical wavelengths, Gaia has delivered high-precision astrometry and photometry, enabling unprecedented studies of stellar kinematics and populations (Gaia Collaboration et al. 2016),(G2021; G2023), (Gaia Collaboration et al. 2021b), while the SMASH survey (N2017; N2021) has contributed to the deep imaging for studying the SF history.

Far-UV (FUV) observations are particularly valuable for studying the properties and spatial distribution of young stellar populations, since young massive stars emit the majority of their radiation at these wavelengths (Cornett et al. 1997), (Devaraj et al. 2023, hereafter D23). While the HST provides high-resolution FUV imaging, its narrow field of view restricts coverage to localized regions. Wider-field instruments, such as the *Ultraviolet Imaging Telescope* (UIT) (Cornett et al. 1994, 1997) and *UltraViolet and Optical Telescope* (UVOT) (Gehrels et al. 2004), have observed parts of the SMC, but with spatial resolutions $\geq 2''$. The *Galaxy Evolution Explorer* (GALEX) (Simons et al. 2014) extended this effort by mapping large areas of the SMC in both FUV and near-UV (NUV) at a spatial resolution of approximately $5''$, but leaving gaps in coverage. Complete and contiguous FUV mapping is therefore crucial to fully resolve the young stellar distribution, constrain the recent SF history, and identify interaction-driven substructures. The footprints of UIT, UVOT, and GALEX observations across the SMC are shown in Figure 1.10.

1.4 Rationale and Goals of the Thesis

The SMC has long served as a natural laboratory for exploring stellar populations in a low-metallicity environment. Previous studies have investigated a wide range of stellar types, such as X-ray binaries, Classical Cepheids, and Wolf–Rayet stars, yielding valuable insights into their evolutionary pathways, feedback processes, and demographics in a metal-poor regime (Shtykovskiy & Gilfanov 2005; Haberl & Sturm 2016; Neugent et al. 2018). Optical and infrared surveys have largely focused on young, low-mass stellar populations, revealing substructures associated with the SMC's past interactions (MD2019; DL2019; MS2020). Large-scale catalogs of massive stars have also expanded significantly, with ∼5,000 candidates identified by Bonanos et al. (2010) and more than 7,000 stars with $M \geq 8$ M$_\odot$ reported by Nakano et al. (2025). These datasets provide an essential statistical foundation for population-wide studies.

Despite these advances, significant gaps remain. Most investigations have concentrated on particular stellar subgroups or localized fields or young low mass stars, whereas a comprehensive, galaxy-wide characterization of young massive stars is still lacking. This omission leaves a significant gap because massive stars are short-lived and highly sensitive to environmental conditions, making them excellent tracers of recent SF and dynamical processes. Moreover, their strong radiative and mechanical feedback profoundly affects the ISM, influencing subsequent star and planet formation, and regulating galactic chemical enrichment. Understanding the spatial distribution, kinematics, SF, and physical properties of the young massive stars in the SMC therefore offers direct clues to how interactions with the LMC and MW have shaped the SMC's recent evolution.

Acknowledging the above gap, this thesis focuses on the detection of young massive stars and their role in tracing the SMC's recent dynamical and SF history. A key component of this effort is the use of UV data from the *Ultra Violet Imaging Telescope* (UVIT) (Tandon et al. 2017a), whose superior resolution (about 1.4$''$) with respect to GALEX, UIT, and UVOT enables contiguous, better-resolution FUV coverage of the SMC for the first time. Through a multiwavelength approach that combines UV, optical, and NIR, this work provides a detailed view of the spatio-temporal distribution, kinematics, and physical properties of young massive stars, thereby highlighting their role as tracers of recent SF and as key agents of feedback in a dynamically evolving, low-metallicity galaxy.

The scientific goals of this thesis are:

- Spatial distribution: Determine how young massive stars are distributed across the SMC and assess whether their large-scale patterns carry signatures of tidal interactions.
- Kinematics: Characterize the motions of massive stars using astrometric data, and evaluate how these kinematic properties reflect the SMC's dynamical history.
- Star formation hierarchy: Investigate whether massive stars form in hierarchical structures, and assess how these structures are generated.
- Physical properties: Constrain the fundamental stellar parameters (e.g., luminosities, temperatures, size) of young massive stars using multiwavelength photometry, linking their properties to their evolutionary processes.

A sample of young massive stars in the SMC is created to meet the scientific goals mentioned above.

1.5 Thesis Chapter Arrangement

To address the objectives of this thesis, it is organized into seven chapters, each building toward a comprehensive understanding of the young massive stellar populations in the SMC and their role in galaxy evolution:

- Chapter 1: This chapter sets the foundation for the thesis by reviewing the scientific background, with a particular focus on the morphology, kinematics, SF history, and young massive stars of the SMC, and by outlining the underlying motivation and goals of this study.

- Chapter 2: This chapter describes the multiwavelength datasets employed in this study, spanning the UV, optical, and NIR regimes. It details the UVIT observed fields, data reduction procedures, and source extraction techniques. Furthermore, the chapter outlines the methodology for deriving stellar parameters, including the use of different theoretical models to interpret the data.

- Chapter 3: This chapter presents a FUV catalog of the SMC main body and inner wing, and examines the morphology and kinematics of FUV-detected stars across different young stellar populations. This chapter is based on our published work Hota et al. (2024b, hereafter, H24b).

- Chapter 4: This chapter investigates the clustering properties of young massive stars in the SMC, examining how these clusters are spatially organized (i.e., hierarchical star formation) and exploring the underlying mechanisms that drive the arrangement. The content of this chapter is drawn from our study Hota et al. (2025, hereafter, H25).

- Chapter 5: This chapter focuses on the study of the SMC's northeastern outskirts, a region likely influenced by tidal interactions. It examines the morphology, kinematics, and SF history of this area and compares the findings with those of the SMC main body to assess the impact of interactions on its evolution. This chapter presents results from our published work Hota et al. (2024a, hereafter, H24a).

- Chapter 6: This chapter focuses on investigating the fundamental properties of young massive stars of a sample region in the SMC, including their multiplicity, effective temperatures, sizes, and luminosities. By characterizing these parameters, the chapter aims to link stellar properties with their evolutionary status and the underlying SMC's low-metallicity environment. The content of this chapter is drawn from work submitted to a journal (Hota et al.).

- Chapter 7: This chapter summarizes the thesis's main results and highlights pathways for future research on the SMC's young massive stars and beyond.

Chapter 2

Data and Methods

> *"Telescopes are in some ways like time machines."* — Martin Rees

In the previous chapter, we discussed the basic characteristics of the SMC and its significance in understanding the evolution of dwarf galaxies within an interacting environment. Particular emphasis was placed on the importance of studying young massive stars in the SMC, a nearby, metal-poor galaxy that offers a unique laboratory for stellar population studies. Since these massive stars emit the majority of their energy in the ultraviolet (UV) range, observations in the UV band are essential to probe their physical properties. In addition to UV data, proper motion (PM) measurements are crucial for tracing their kinematics within the SMC. A comprehensive understanding also requires multiwavelength data, spanning optical to near-infrared (NIR) bands. A summary of the wavelength ranges considered in this thesis and the corresponding telescopes and surveys is presented in Figure 2.1. This chapter presents the data used in this thesis and their organization across sections: section 2.1 describes UV observations and the steps taken for their processing. Section 2.2 outlines the photometry procedure used to derive FUV magnitudes, along with completeness estimates based on ASTs. Section 2.3

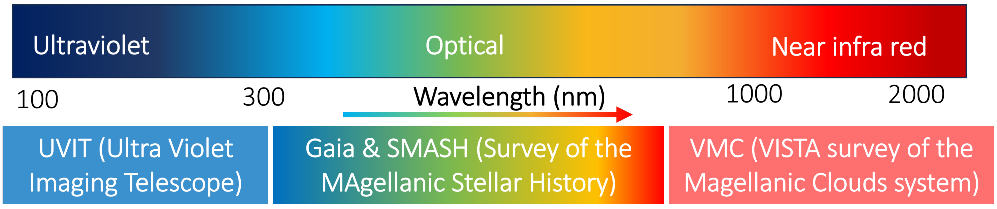

FIGURE 2.1: Multiwavelength datasets employed in this study, spanning from the ultraviolet (UVIT) to the optical (Gaia, SMASH) and near-infrared (VMC).

details the archival optical and NIR datasets used in this study, followed by the methods used to detect single and double systems in section 2.4. A brief discussion on different theoretical models is provided in section 2.5.

2.1 UV data

As discussed in the previous chapter, the SMC has been observed in the UV band by several space-based missions, including the Ultraviolet Imaging Telescope (UIT), Swift's Ultraviolet/Optical Telescope (UVOT), and the Galaxy Evolution Explorer (GALEX), as shown in Figure 1.10. While these missions have provided valuable images/data, they suffer from limitations in spatial resolution and partial coverage in the FUV regime. Although the HST offers superior spatial resolution, its limited field of view restricts large-scale studies of the SMC. Therefore, there is a critical need for FUV observations of the SMC that combine better spatial resolution with wide-area coverage, surpassing what was previously achieved by UIT, UVOT, and GALEX. Here, the UVIT fills the gap.

2.1.1 UVIT Observation

The UVIT, a key payload onboard AstroSat, India's first space observatory, offers better-resolution imaging capabilities across UV and optical wavelengths. A

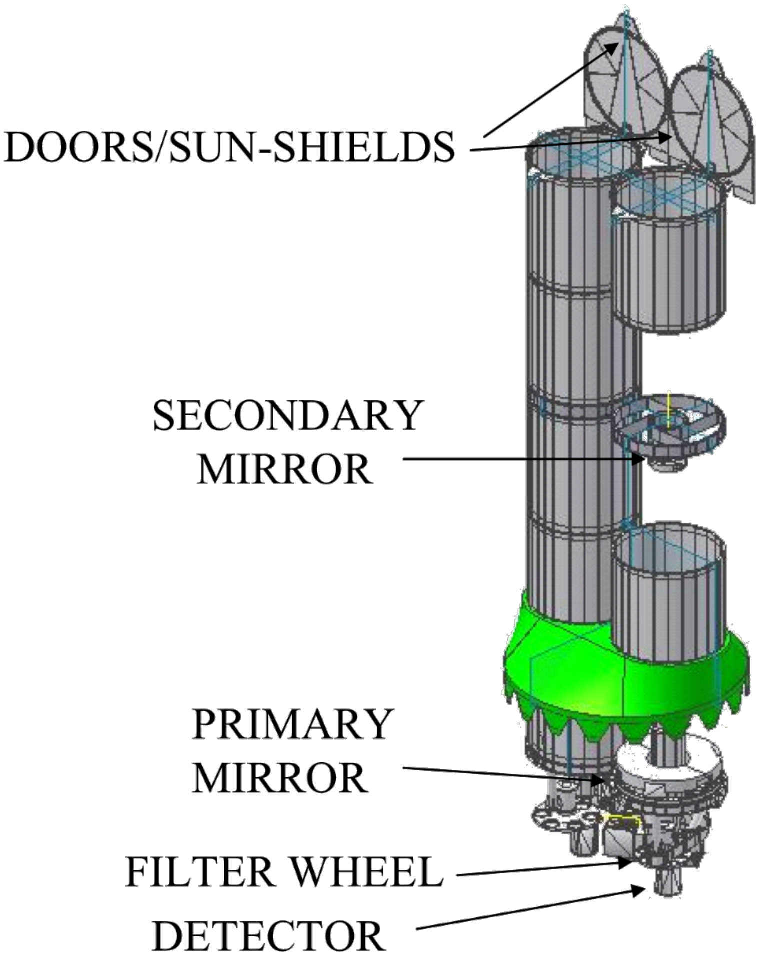

Figure 2.2: Illustration of the twin UVIT telescopes mounted on AstroSat, India's inaugural space observatory. Credits: IIA and ISRO

schematic diagram of the instrument is shown in Figure 2.2. It consists of a pair of Ritchey–Chretien telescopes mounted in a co-aligned configuration, each with a 38 cm aperture. One telescope is designated exclusively for the FUV (130–180 nm) channel, while the second is designed to handle both the NUV (200–300 nm) and visible (VIS; 350–550 nm) channels. Each channel is equipped with a suite of filters that enable multi-band imaging, facilitating a broad range of astrophysical investigations (Tandon et al. 2020). UVIT provides a wide circular field of view of approximately $28'$, with a spatial resolution of around $1''.4$, significantly improving upon previous UV missions such as GALEX, UVOT, and UIT (Tandon et al. 2017a).The technical specifications and calibration of UVIT are discussed extensively in Postma et al. (2011); Subramaniam et al. (2016a); Kumar et al. (2012).

Due to the inherently low photon flux in the UV domain, UVIT utilizes photon-counting detectors for both the UV channels. These intensified CMOS detectors register the arrival of individual photons rather than collecting integrated flux. When a UV photon strikes the photocathode, it releases a photoelectron, which is then propelled into a microchannel plate that amplifies the signal by a factor of about 10^7. This amplified electron cascade hits a phosphor screen, producing light, which is transmitted through a fiber-optic taper to a 512×512 pixel CMOS sensor. A centroiding algorithm is employed to pinpoint the position of each photon event with sub-pixel precision, typically reaching an accuracy of about 1/8 of a pixel (Postma et al. 2011; Hutchings et al. 2007).

The final image resolution is primarily determined by the intrinsic spread of photoelectrons at the detector, about 1 arcsecond, and by spacecraft jitter, roughly half an arcsecond. The typical readout speed of the CMOS detector is about 29 frames per second in full-frame mode, with the option to increase this to around 200 frames per second in subarray mode for faster readouts. The VIS channel, which operates in the integration mode due to the presence of large flux in the optical wavelength, is primarily used to track and correct for drift due to spacecraft motion during exposures. Since AstroSat orbits the Earth every 90 minutes and observations are limited to the dark portion of each orbit, UVIT typically obtains useful exposures < 25 minutes for a single orbit. Therefore, the total integration time is accumulated over several orbits. The spacecraft initially downlinks Level 0 (L0) data to the ISSDC, ISRO, which are then processed by incorporating spacecraft-related metadata to generate Level 1 (L1) data. The L1 data, formatted as FITS files, contain time-stamped photon centroid events along with essential observational and spacecraft metadata.

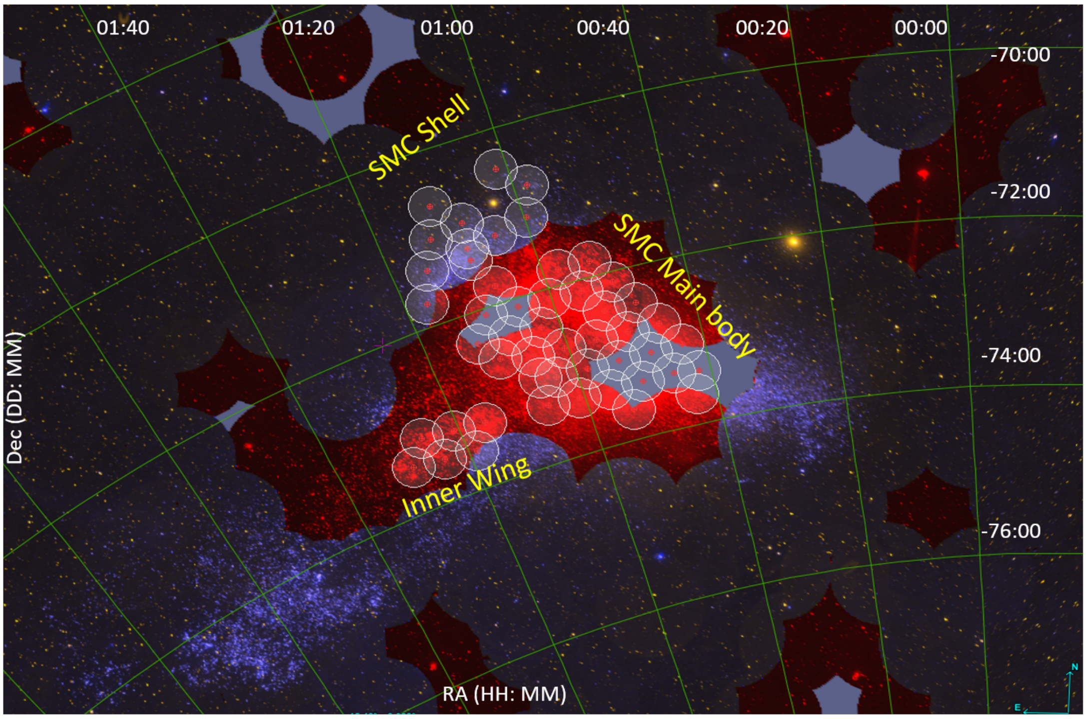

FIGURE 2.3: The UVIT-observed fields of the SMC are marked by white circles, overlaid on a GALEX background image (Bianchi et al. 2017). This background is a two-color composite, with blue indicating FUV data and red representing NUV data, incorporating both GR6 and GR7 releases.

In this thesis, we employed 39 UVIT pointings using the medium-band filter F172M (silica: 1717±125 Å; Tandon et al. 2020), covering the SMC's main body and its Wing (Figure 2.3). Additionally, we used 11 UVIT fields observed in the broad-band filter F148W (1481±250 Å; Tandon et al. 2020), targeting the SMC Shell region, as shown in Figure 2.3. The L1 data for all the UVIT fields used in this study are publicly accessible [*] and the details of the UVIT observed SMC fields are provided in Table 2.1. The data processing workflow, including reduction, photometry, and completeness, is summarized in Figure 2.4 and described in detail in the subsequent sections.

---

[*] https://astrobrowse.issdc.gov.in/astro_archive/archive/Home.jsp

Table 2.1: Details of the UVIT observed SMC fields. RA and Dec indicate the central coordinates, and t_{exp} denotes the exposure time in seconds of each field.

SMC Main Body and Wing			
Observed Field	**RA [deg]**	**Dec [deg]**	**t_{exp} [sec]**
SMC-02	10.47	−73.38	153.0
SMC-03	10.84	−73.03	954.2
SMC-04	11.49	−72.73	953.9
SMC-05	12.11	−72.43	954.9
SMC-06	12.72	−72.13	445.3
SMC-07	13.30	−71.82	955.1
SMC-08	10.76	−73.64	954.6
SMC-09	11.43	−73.34	954.3
SMC-10	12.08	−73.04	954.8
SMC-11	12.70	−72.74	954.9
SMC-12	13.31	−72.43	954.4
SMC-13	13.90	−72.13	951.6
SMC-14	14.46	−71.82	951.7
SMC-17	12.69	−73.35	1022.3
SMC-18	13.32	−73.04	965.3
SMC-19	13.92	−72.74	957.2
SMC-21	15.07	−72.12	955.8
SMC-23	13.32	−73.65	952.7
SMC-24	13.95	−73.35	951.0
SMC-25	14.55	−73.04	952.6
SMC-26	15.14	−72.73	634.3
SMC-27	15.70	−72.42	952.0
SMC-28	16.24	−72.10	953.7
SMC-29	16.77	−71.79	953.9
SMC-31	15.21	−73.34	951.3
SMC-32	15.79	−73.03	951.3
SMC-33	16.35	−72.71	825.8
SMC-34	16.89	−72.40	472.0
SMC-35	17.42	−72.08	485.3
SMC-37	16.46	−73.32	377.0
SMC-38	16.37	−72.98	371.0
SMC-39	17.54	−72.62	395.4
SMC-40	18.08	−72.37	471.8
SMC-42	18.97	−73.27	187.8
SMC-43	19.71	−73.55	951.7
SMC-44	20.21	−73.23	951.6
SMC-45	20.97	−73.51	470.6
SMC-46	21.45	−73.18	472.0
SMC-47	22.23	−73.46	471.5

Continued on next page

SMC-Shell Region			
Observed Field	**RA [deg]**	**Dec [deg]**	**t_{exp} [sec]**
Field 1	14.55	−70.76	2406.4
Field 2	14.94	−71.12	2405.7
Field 3	15.37	−70.48	2373.2
Field 4	16.16	−71.22	2371.3
Field 5	17.05	−70.96	2366.2
Field 6	17.87	−70.66	2208.1
Field 7	18.26	−71.03	1533.6
Field 8	18.79	−71.36	2373.7
Field 9	19.25	−71.73	2375.1
Field 10	17.22	−71.27	1903.6
Field 11	17.22	−71.41	1902.5

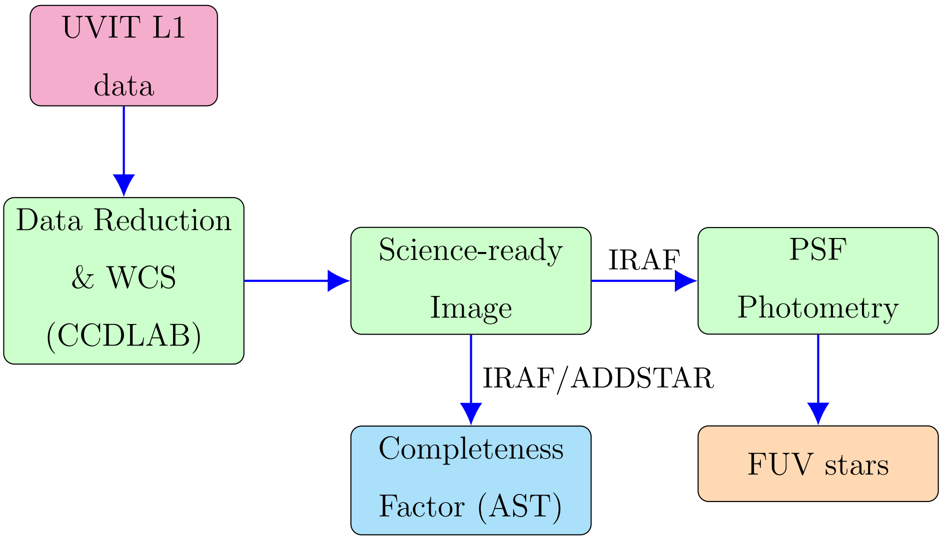

Figure 2.4: Flowchart presenting the UVIT data process.

2.1.2 Data Reduction

The L1 data obtained from UVIT observations of the SMC fields were processed using CCDLAB, an automated data reduction pipeline developed specifically for UVIT data (Postma & Leahy 2017, 2021; Ranasinghe & Leahy 2025). This pipeline systematically applies several necessary corrections, including flat-fielding, fixed pattern noise removal, and correction for spacecraft drift, to generate calibrated UV images.

Astrometric calibration is performed within the same pipeline using reference stars from the Gaia DR3 catalog (G2023), enabling the construction of an accurate World Coordinate System (WCS) solution for each field. The final output comprises science-ready UV images of the SMC fields, each with reliable astrometric accuracy and suitable for further photometric analyses.

2.2 Photometry

Photometry is the process of determining the amount of light/flux emitted by a celestial object. To measure the stars' UV fluxes in the UVIT science-ready images of the SMC, we performed PSF photometry, which is particularly suitable for crowded stellar fields like those in the SMC. Unlike aperture photometry, which can suffer from flux contamination due to nearby stars, PSF photometry models the intrinsic shape of a point source and fits this model to all detected stars in the image, enabling more accurate flux estimation even in dense regions.

We used the *DAOPHOT* package within the Image Reduction and Analysis Facility (IRAF) environment (Tody 1986, 1993; Stetson 1987) for the photometric analysis. The process began with an initial estimation of the image background (σ) and source FWHM using the *imexam* routine. Source detection was then performed using *daofind*, typically employing a threshold of five times the background noise (σ).

Following source identification, preliminary aperture photometry was carried out using the *phot* task. A subset of bright, isolated stars was selected using *pstselect* to build an empirical PSF model with the *psf* task. This model was then fit to all detected sources using *allstar*, which iteratively refines source magnitudes by simultaneously fitting overlapping stellar profiles.

To convert PSF-fitted magnitudes into instrumental magnitudes, we computed the mean offset between the PSF magnitudes and aperture magnitudes for common bright stars. This PSF correction was then applied uniformly to all sources. Subsequently, an aperture correction was applied based on the curve of growth method to account for flux loss outside the chosen aperture radius. A comprehensive explanation of both aperture and PSF photometry methods is described in W. E. Harris's manual [†].

The final instrumental magnitudes were calibrated to the AB magnitude system using the relation:

$$m_{\mathrm{AB}} = -2.5\log(\mathrm{CPS}) + ZP \tag{2.1}$$

where CPS is the counts per second, and ZP is the zero-point given by

$$ZP = \left(-2.5\log(UC)\cdot(\lambda_{\mathrm{mean}})^2\right) - 2.407 \tag{2.2}$$

Here, UC is the unit conversion for the filter. For the FUV filter, the zero point adopted was from Tandon et al. (2020). Given that FUV and NUV channels of UVIT operate in photon-counting mode, we also applied saturation corrections following the method provided by Tandon et al. (2017b). This correction is essential for bright stars, where multiple photons may arrive within a single frame. This photometric approach ensures homogeneous magnitude estimation across UVIT's fields of view, particularly in the crowded regions of the SMC. To avoid the edge effect, sources within a $\sim 1'$ annulus near the edges of the observed fields are excluded.

[†] `https://physics.mcmaster.ca/~harris/daophot_irafmanual.txt`

Completeness Factor

In photometry, completeness refers to the fraction of sources of a given brightness that are successfully detected in an observational image. Due to factors such as detector sensitivity, background noise, and crowding, particularly in dense regions like the SMC, some faint sources may go undetected. This effect becomes more significant as one moves toward the detection limit of the image. Therefore, assessing the completeness of a dataset is essential when deriving statistically robust conclusions about stellar populations, such as the surface density or star formation history. One way to infer the completeness of a field is by examining the distribution of measured magnitudes. Typically, the number of detected stars increases with fainter magnitudes up to a certain peak, beyond which it declines due to observational incompleteness. This peak acts as an indicator of the onset of incompleteness in the data (Leahy et al. 2020), (D23).

To quantify this effect across our observed fields, we performed ASTs using the DAOPHOT package within IRAF, a widely used software environment for photometric analysis. ASTs involve injecting synthetic stars of known brightness into science images and then attempting to recover them using the same photometric pipeline as used for real sources. The CF is estimated as the ratio of recovered artificial stars to the total number of added stars:

$$\mathrm{CF} = \frac{N_{\mathrm{recovered}}}{N_{\mathrm{added}}} \tag{2.3}$$

To assess the CF of an observed field in our study, artificial stars were added using the *addstar* task in IRAF. We added stars amounting to ∼10–15% of the total detected stars to avoid artificially increasing the crowding. The magnitudes of added stars ranged from 12 to 21 mag. These stars were uniformly distributed in position and magnitude. The addstar task utilizes a model PSF (created by the psf task in DAOPHOT) to insert artificial stars into the original image. It scales the pixel intensity of the artificial stars based on their magnitudes and the reference PSF, and adds appropriate Poisson noise, taking into account the detector gain (stored in the datapars file). If no manual photometry file is provided, addstar can randomly generate positions and magnitudes for a specified number of stars using the parameters minmag, maxmag, and nstar. Following the injection, PSF photometry was applied to the modified images using the procedure outlined in section 2.2. The recovered stars were then cross-matched with the input artificial star list to determine the number of matches. To improve the statistical robustness of our completeness estimates, we repeated ASTs for each field multiple times. Specifically, we conducted tests twice over the full magnitude range (12–21 mag), and three times within narrower intervals: 15–21 mag, 18–21 mag, 19–21 mag, and 20–21 mag. The final CF for a field was obtained by averaging the results across these tests, and the corresponding completeness percentage was computed accordingly.

2.3 Archival Data

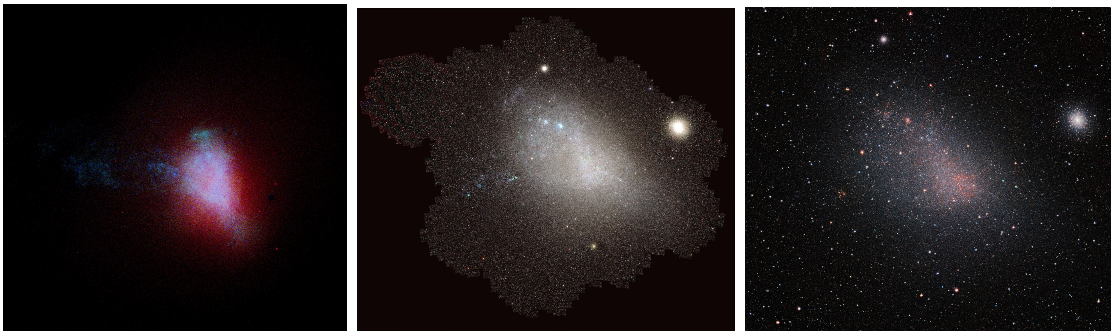

Figure 2.5: left to right: The SMC as observed by Gaia (Credits: ESA/Gaia/DPAC), SMASH (Credits: `https://datalab.noirlab.edu/data/smash`), and the VMC survey (Credits: ESO/VISTA VMC).

To characterize the identified stellar sources, we combined UVIT ultraviolet observations with optical (Gaia, SMASH) and NIR (VMC) datasets. The spatial coverage of the optical and NIR surveys across the SMC is presented in Figure 2.5.

2.3.1 Gaia Data

The Gaia mission, launched by the European Space Agency (ESA) on 19 December 2013, is dedicated to astrometry, the precise measurement of positions, parallaxes, and motions of celestial objects. Gaia carries two telescopes, each equipped with a primary mirror measuring 1.45×0.5 m^2, fixed at an angular separation of $106^\circ.5$, enabling it to observe two regions of the sky simultaneously with an exceptional spatial resolution of about $\sim 0''.4$. Gaia's instrument suite includes:

- An astrometric instrument for measuring stellar positions and motions,
- Photometers that observe in three bands, G (330–1050 nm), $\mathrm{G_{BP}}$ (330–680 nm), and $\mathrm{G_{RP}}$ (640–1050 nm),
- A spectrometer for measuring radial velocities.

Gaia surveyed the SMC within a circular region of radius 11°, centred on the optical coordinates defined by Cioni et al. (2000). To retrieve the complete Gaia dataset covering this region, we executed an ADQL query (G2021) using the Gaia Archive[‡]. The query selected all sources within the specified area that have valid parallax measurements and G-band magnitudes brighter than 20.5 mag:

```
"SELECT * FROM user_edr3int4.gaia_source AS g
WHERE 1 = CONTAINS(POINT('ICRS', g.ra, g.dec),
```

[‡] https://gea.esac.esa.int/archive

```
                  CIRCLE(’ICRS’, 12.80, -73.15, 11))
AND g.parallax IS NOT NULL
AND g.phot_g_mean_mag < 20.5"
```

Following the execution of the query (G2021), we obtained 4,709,622 Gaia sources.

2.3.2 SMASH Data

The SMASH (N2017; N2021) is a deep optical imaging survey designed to trace the MCs’ extended stellar structures, including their stellar halos, tidally removed stars, and other low surface brightness features. The survey covers a total of 480 square degrees to a depth of approximately 24th magnitude in the u, g, r, i, and z filters, enabling the detection of faint and diffuse stellar populations. Although the survey design targeted a sparse tiling pattern over a larger region of about 2400 square degrees, the actual imaging was conducted in discrete, strategically chosen fields. The first public data release (DR1; N2017) provided photometric measurements for around 100 million sources from 61 observed fields. The more recent and comprehensive data release (DR2; N2021) includes measurements for nearly 360 million sources across 197 fields, making it one of the most extensive datasets available for studying the stellar content and structure of the MCs and their surroundings. Data from SMASH DR2 can be accessed via several tools provided by the NOIRLab Data Lab:

- **TAP (Table Access Protocol):** Users can connect to the TAP service at `https://datalab.noirlab.edu/tap` using TAP-compatible clients such as `TOPCAT`. The database `SMASH DR2` contains the full set of tables and metadata that can be browsed and queried.

- **Data Lab Query Client:** This Python-based interface allows direct access to the SMASH catalog using SQL queries. It supports both synchronous and asynchronous modes, and can be used locally or through the Jupyter notebook environment provided by NOIRLab. Tutorials and example notebooks are available at `https://github.com/astro-datalab/notebooks-latest`.

For this study, we accessed SMASH DR2 using a structured SQL query through the NOIRLab Data Lab interface, and this enabled us to extract objects located within the SMC region relevant to our analysis.

2.3.3 VMC Data

The VMC (C2011) is a deep NIR imaging survey designed to explore the star formation history and three-dimensional geometry of the Magellanic system. The VMC survey covers a total sky area of approximately 170 square degrees, including ∼105 deg^2 in the LMC, 42 deg^2 in the SMC, 21 deg^2 in the MB, and 3 deg^2 in the MS region. The survey area is segmented into VISTA tiles, comprising 68 tiles for the LMC, 27 for the SMC, 13 for the MB, and 2 for the MS. Each tile spans an area of ∼1.5×1.18 deg^2 and includes slight overlaps (0.1 deg vertically and 0.016 deg horizontally) to ensure uniform coverage. Observations are conducted in three NIR bands: Y, J, and K_s. The survey achieves 10σ detection limits of 21.1, 21.3, and 20.7 mag in the Y, J, and K_s bands (Vega system), enabling sensitive observations of a wide variety of stellar populations, from old main sequence turn-off stars to evolved giants. The bright-end limits, set by detector linearity, are roughly 12.9, 12.7, and 11.4 mag in the same bands.

The VMC data products, including images, source catalogs, and confidence maps, are publicly available via the ESO Science Archive and the VISTA Science Archive

(VSA). For this work we used PSF photometry catalog of the SMC in NIR band as part of the VMC, from the ESO archive [§].

2.4 Spectral Energy Distribution

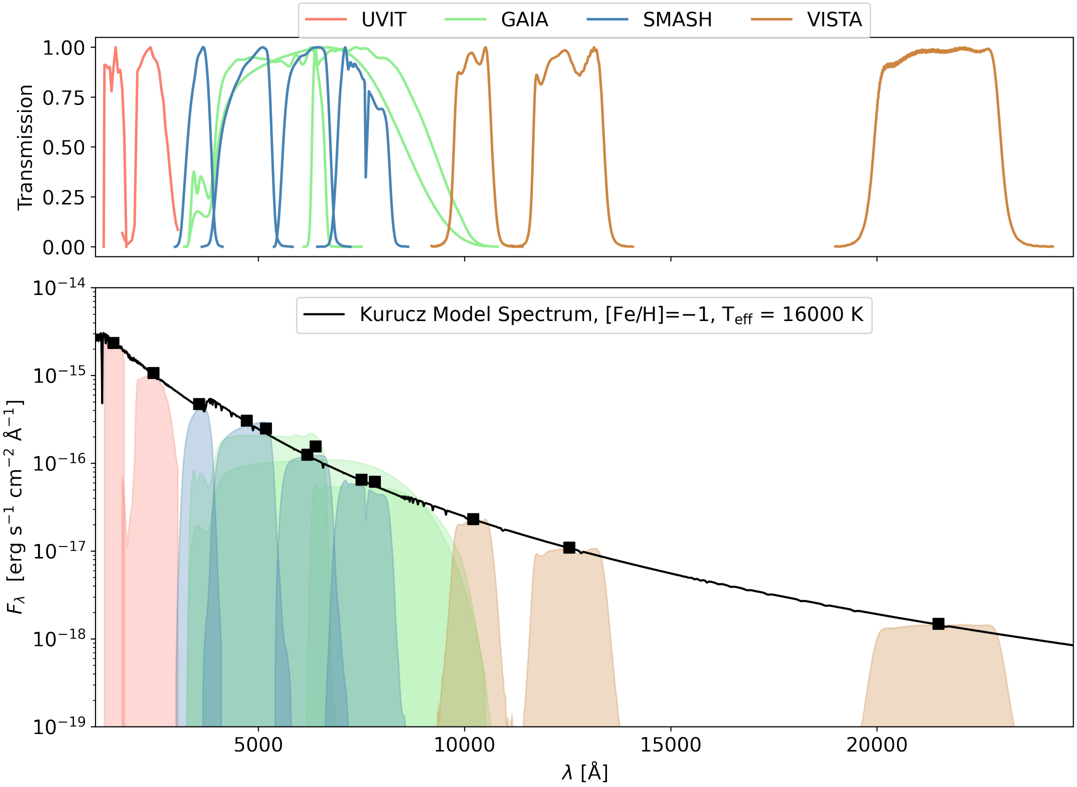

FIGURE 2.6: The top panel displays the transmission profiles of filters from UVIT, Gaia, SMASH, and VMC. In the lower panel, schematic SED of a model star with an effective temperature of 16,000 K is shown. The Kurucz synthetic spectrum is plotted in black and the colored regions indicate the portions of the spectrum sampled by each filter, while the black square symbols mark the corresponding integrated fluxes. Plotting these integrated fluxes against the filters' effective wavelengths yields the constructed SED.

By analyzing the radiation emitted by stars across various wavelengths, we can infer their physical characteristics. One powerful approach for doing this is SED fitting, which utilizes broadband photometric data across different filters to estimate parameters such as the effective temperature ($T_{\rm eff}$), stellar radius (R), and

---

[§] "https://archive.eso.org/cms.html"

luminosity (L). An SED is a representation of the observed flux of a source plotted against wavelength or frequency. The shape of this distribution carries information about the underlying physics of the object. Compared to spectroscopy, which offers high-resolution data but requires significant telescope time and can be difficult for faint objects, SED fitting using photometry is an efficient alternative. It provides an approximate, low-resolution spectral profile constructed from multi-band observations.

In our last project work of this thesis (Hota et al. submitted) , we compiled photometric data covering a wide wavelength range, from the UV to the NIR, using filters from UVIT, Gaia, SMASH, and VMC surveys. These magnitudes were converted to fluxes and corrected for extinction. The Milky Way foreground extinction toward the SMC is low (Schlegel et al. 1998; Schlafly & Finkbeiner 2011). For extinction correction, we adopted the extinction law, from Cardelli et al. (1989); Gordon et al. (2024), R_V value of 3.1 (Gordon et al. 2024) and a color excess of $E(B-V) = 0.05$ mag (mean value; Haschke et al. 2011). The extinction in each band was estimated using the filter transmission curves and extinction coefficients provided by the Spanish Virtual Observatory (SVO) Filter Profile Service [¶].

To perform the SED fitting, we used the Virtual Observatory SED Analyzer (VOSA; Bayo et al. 2008), a web-based tool developed by the SVO. Figure 2.6 presents an example of a synthetic stellar model with an effective temperature of 16,000 K, assuming the observed fluxes from UVIT, Gaia, SMASH, and VMC. VOSA offers access to several theoretical model libraries and enables comparison between observed data and model-predicted fluxes through synthetic photometry. This is achieved by convolving the model spectra with the filter response functions.

[¶] "https://svo2.cab.inta-csic.es/theory/fps/"

The fitting process in VOSA is based on minimizing the reduced chi-squared statistic:

$$\chi^2_{\text{red}} = \frac{1}{N - N_f} \sum_{i=1}^{N} \left(\frac{F_{\text{obs},i} - M_d F_{\text{mod},i}}{\sigma_{\text{obs},i}} \right)^2, \tag{2.4}$$

where:

- N is the number of photometric data points,
- N_f is the number of free parameters,
- $F_{\text{obs},i}$ is the observed flux in the i^{th} band,
- $\sigma_{\text{obs},i}$ is its corresponding uncertainty,
- $F_{\text{mod},i}$ is the model flux, and
- $M_d = \left(\frac{R}{D}\right)^2$ is the scaling factor, which scales the model to the observed data, incorporating the stellar radius R and distance D.

From the best-fit model, the stellar radius can be derived as:

$$R = \sqrt{M_d} \cdot D, \tag{2.5}$$

and the luminosity is computed using the Stefan–Boltzmann law:

$$L = 4\pi R^2 \sigma_{\text{SB}} T_{\text{eff}}^4, \tag{2.6}$$

where σ_{SB} is the Stefan–Boltzmann constant.

In addition to the standard χ^2, VOSA calculates two extra parameters, vgf and vgf_b, as estimates of the visual goodness of fit. These parameters account for cases where a fit looks satisfactory by eye but yields a large χ^2 due to underestimated observational errors. Vgf is a modified χ_r^2 obtained by imposing a minimum error of 2% of the observed flux ($F_{o,i}$), while vgf$_\mathrm{b}$ is similarly defined but with a minimum error of 10%. These parameters help evaluate how well the model matches the observations and are especially valuable when the photometric uncertainties in any catalog used to construct the SED are smaller than the actual. VOSA also provides error estimates using a Markov Chain Monte Carlo (MCMC) method that generates multiple realizations of the best-fit solution. The uncertainty in T_eff is typically taken as half the grid step unless the MCMC-derived error is larger.

Fitting of two-component SEDs

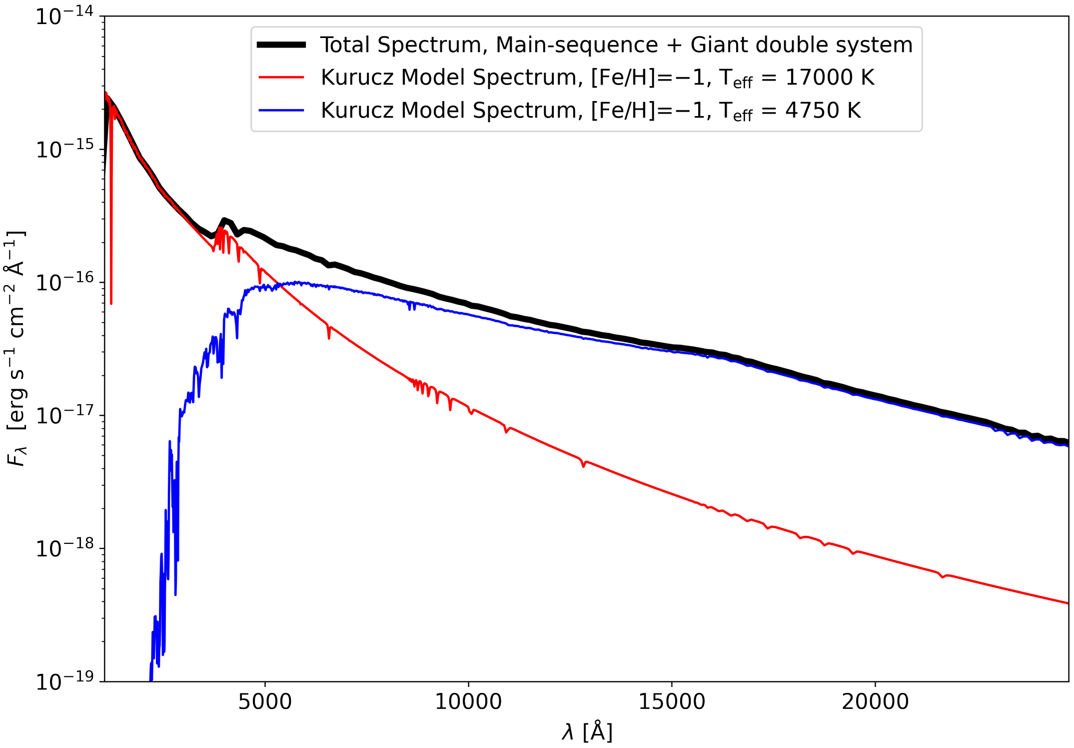

FIGURE 2.7: Schematic composite SEDs of a main sequence–giant double system. Kurucz synthetic spectra are shown for the main sequence star (T_eff = 17000 K, red) and the giant star (T_eff = 4750 K, blue), with their combined spectrum plotted in black.

During the SED analysis, we encountered several stars whose observed SEDs could not be adequately reproduced by a single stellar atmosphere model. These cases typically exhibited notable UV excess or abnormally high values of the goodness-of-fit parameter (vgf$_b$ values in VOSA), indicating possible complexities in their spectral contributions. UV excess in stellar SEDs may arise due to various physical mechanisms, including enhanced chromospheric activity, the presence of a hot unresolved companion, or differences in metallicity. To investigate the possibility of binarity/doubles, we employed the double fitting functionality available within the VOSA tool. This method enables the modelling of a composite SED using the weighted sum of two different stellar spectra, each characterised by distinct effective temperatures. By fitting the combined observed SED with two-component models simultaneously, we were able to better match the observed UV flux and overall SED shape. This approach is particularly useful when the individual stars in a binary system contribute significantly different fluxes across the wavelength range, allowing us to disentangle the physical properties of both components. Figure 2.7 shows an example of double SED fitting for a system composed of a main sequence star and a giant, with effective temperatures of 17,000 K and 4,750 K, respectively.

2.5 Theoretical Models

In this study, we employed theoretical isochrones to infer the age distribution and star formation history, evolutionary tracks to understand stellar development, and synthetic SED models to derive the physical parameters of individual stars. The specific models and their applications are outlined below.

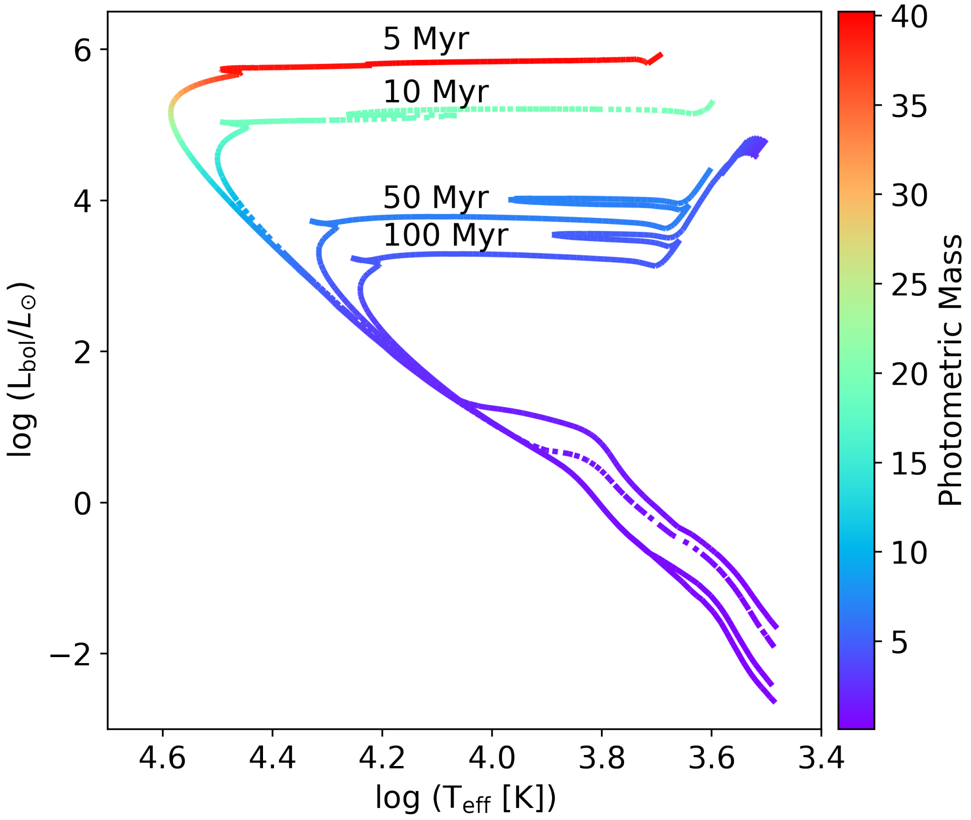

Figure 2.8: Padova–PARSEC isochrones with ages of 5, 10, 50, and 100 Myr for $Z = 0.002$. The color bar indicates the photometric mass.

Isochrones

Isochrones represent the theoretical loci of stars that formed at the same time and possess the same metallicity but span a range of initial stellar masses as shown in Figure 2.8. When plotted on a CMD, these models provide a snapshot of stellar evolution at a given age. They are particularly useful for deriving the age distribution of stellar populations in galaxies, where stars exist in various evolutionary stages and mass ranges.

In this work, we used Padova-PARSEC isochrones (Bressan et al. 2012) to estimate the age range of stars identified in our study region. These isochrones were generated assuming a Kroupa initial mass function (Kroupa 2001, 2002). The PARSEC models assume non-rotating stars, include mass loss during the red giant branch phase, and do not account for the thermally pulsing asymptotic giant branch (TP-AGB) or post-AGB phases. The initial point of each isochrone is the $0.1\,M_\odot$ model on the lower main sequence. The terminal stage of the isochrones is either the beginning of the TP-AGB for low- and intermediate-mass stars ($M \leq M_{\rm IM}$, ages $\gtrsim 10^8$ yr) or carbon ignition for more massive stars. For extinction corrections, we applied the reddening law described by Cardelli et al. (1989) and refined by O'Donnell (1994) and we followed the metallicity of the SMC of $Z = 0.002$ (Lemasle et al. 2017). This approach enabled us to compare the theoretical isochrones with observed CMDs.

Evolutionary tracks

An evolutionary track traces the predicted changes in the physical properties of a single star—such as its luminosity, effective temperature, and radius—over time as it evolves from one stage to another, as presented in Figure 2.9. These tracks are plotted on the CMD, and they represent the life path of a star of a given initial mass and metallicity. Unlike isochrones, which show the positions of stars of different masses at a fixed age, evolutionary tracks follow the time-dependent behavior of individual stars.

To understand the evolutionary status of our sources, we used stellar models from the MESA Isochrones and Stellar Tracks (MIST) project (version 1.2; Paxton et al. 2010; Dotter 2016; Choi et al. 2016). Built on the MESA stellar evolution code, these models offer detailed predictions for a wide range of stellar parameters and evolutionary stages, from the pre-main sequence to the end stages of stellar

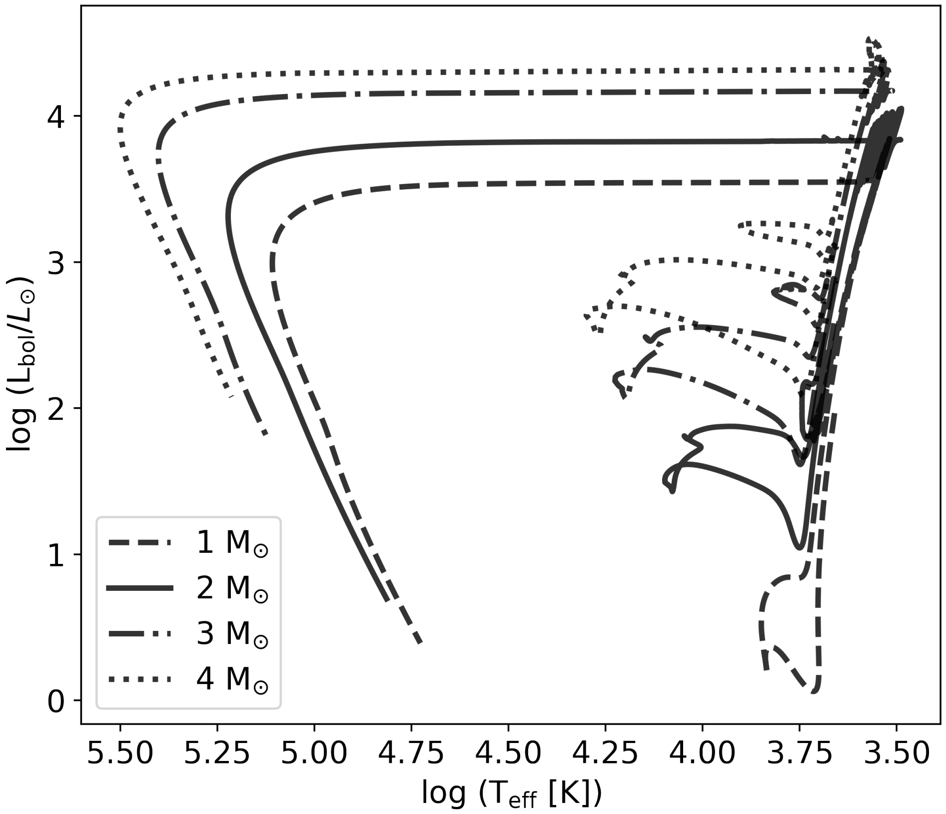

FIGURE 2.9: MIST evolutionary tracks for stellar masses between 1 and 4 $M_\odot$ at metallicity $Z = 0.002$.

evolution. The MIST models adopt the solar abundance scale, scaled to the SMC metallicity. Convection is treated using the mixing-length theory with $\alpha_{\rm MLT} = 1.82$, and overshoot is implemented as time-dependent and diffusive with $f_{\rm ov,core} = 0.0160$ and $f_{\rm ov,env} = 0.0174$. Mass loss follows prescriptions for low-mass stars on the RGB or AGB and for high-mass stars.

Spectral models

To interpret the observed SEDs of stars in our study, we adopted synthetic stellar atmosphere models developed by Castelli & Kurucz (see Figure 2.6 and Figure 2.7;

2003). These models simulate the emergent flux from stellar atmospheres under the assumptions of local thermodynamic equilibrium and hydrostatic equilibrium, and are generated using the ATLAS9 code (Kurucz 1993; Castelli et al. 1997; Castelli & Kurucz 2003). The Kurucz model grid spans a broad parameter space, including effective temperatures ($T_{\rm eff}$) from 3,500 K to 50,000 K, surface gravities ($\log g$) from 0.0 to 5.0 dex, and metallicities ([Fe/H]) ranging from –2.5 to +0.5 dex.

The Kurucz models provide flux predictions across a wide wavelength coverage—from the ultraviolet to the infrared—making them highly suitable for multi-band SED fitting. In this work, we employed these models to estimate stellar parameters such as effective temperature, radius, and luminosity for both single and binary stellar systems.

It is important to note that the Kurucz models assume local thermodynamic equilibrium (LTE) and a plane-parallel geometry. These assumptions are generally valid for stars with effective temperatures below $\sim$30,000 K and for atmospheres that are not significantly extended by stellar winds. For hotter stars or those with strong mass loss, however, non-LTE effects and spherical geometry become important, and alternative model atmospheres such as TLUSTY (Hubeny & Lanz 2011) or CMFGEN (Hillier & Miller 1998) would be more appropriate. The stellar sample analyzed in this study primarily consists of stars in the temperature regime where the LTE plane-parallel approximation is sufficient, justifying the use of Kurucz models for our analysis.

Chapter 3

FUV catalog, Morphology and Kinematics of young stellar population in the SMC[*]

"The cosmos is within us. We are made of star-stuff. We are a way for the universe to know itself." — Carl Sagan

3.1 Introduction

The SMC is known to have undergone episodes of recent star formation and therefore hosts massive stars. The first step in carrying out a systematic study of massive stars is to create a catalog. The UV band is a good tracer to map massive stars, particularly in a low-metallicity environment, as these stars have high effective temperatures and emit the bulk of their radiation in the ultraviolet. In

---

[*] This chapter is based on the work published in *The Astronomical Journal*, **168**, 255 (2024), Hota et al., 10.3847/1538-3881/ad7de2

addition, reduced metal-line blanketing and lower dust content at low metallicity result in less attenuation, making UV observations especially effective in tracing young massive stellar populations. Also, to derive the characteristics and properties, it is essential that the catalog should have multi-wavelength data of massive stars. The addition of kinematic information, such as proper motion, will add additional value to understanding the massive star kinematics within the SMC.

Here, we present a point source catalog of the SMC in the FUV band based on the UVIT images of the SMC main body and the Wing. The catalog is cross-matched with the VMC and Gaia DR3 (G2023) catalogs to provide the corresponding IDs. We also present the morphology and kinematics of various young populations of the SMC that are detected in the FUV. In this chapter, section 3.2 covers the data used in this work and their analysis. We show the location of different types of populations on the UV–optical and IR CMDs in section 3.3. Section 3.4 and section 3.5 explore their morphology and kinematics, respectively. Discussion is in section 3.6 and the summary and conclusions are in section 3.7.

3.2 Data and Analysis

3.2.1 UV data

In this work, we utilized FUV images of thirty-nine (39) UVIT pointings in the medium passband filter; F172M (silica: 1717±125 Å; Tandon et al. 2020). The observational details of the SMC fields are provided in Table 2.1. We note from Table 2.1 that out of 39 SMC fields, 25 SMC fields have exposure time > 900 sec, 9 fields have exposure time between 400–830 sec, while 3 fields have exposure time between 300 to 400 sec. Two SMC fields, SMC-02 and SMC-42, exhibit shorter exposure time (< 200 sec). SMC-02 is situated on the periphery of the SMC's

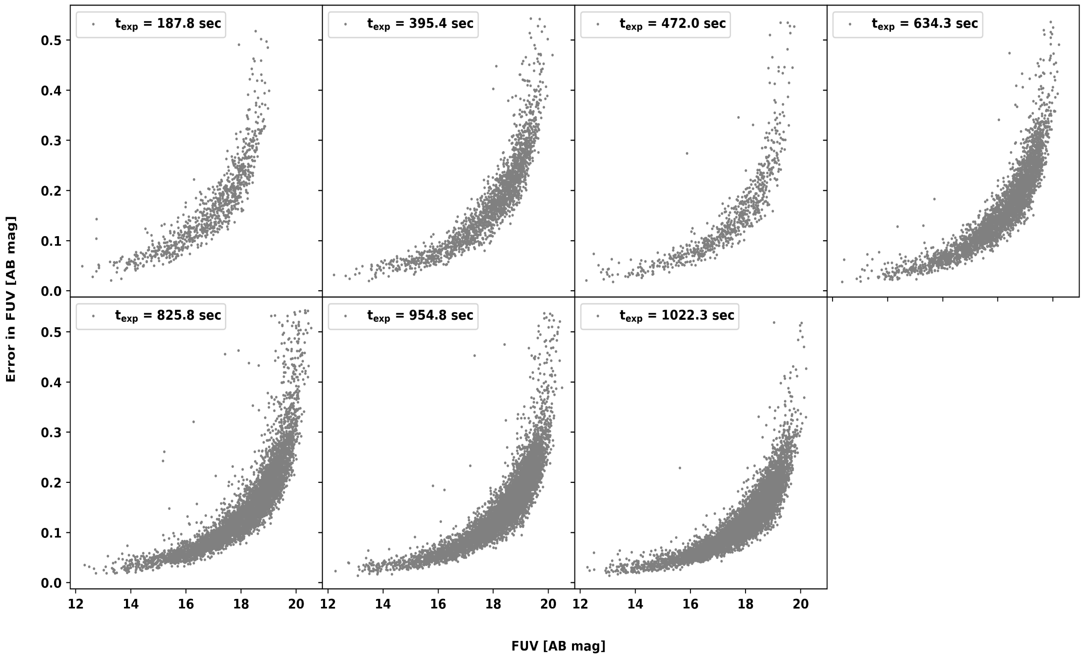

FIGURE 3.1: FUV magnitude vs error in magnitude (PSF fit error) for various fields of the SMC with different exposure times.

main body, whereas SMC-42 is located within the inner region of the SMC Wing. We processed UVIT L1 data of 39 observed fields and performed PSF photometry as described in Chapter 2. The variation of PSF fit error with the obtained FUV magnitude and exposure time is shown in Figure 3.1 using seven sample SMC fields: SMC-42 (187.8 sec), SMC-39 (395.4 sec), SMC-46 (472.0 sec), SMC-26 (634.3 sec), SMC-33 (825.8 sec), SMC-10 (954.8 sec), and SMC-17 (1022.3 sec). Other observed fields of the SMC exhibit a similar trend.

3.2.2 Completeness factor

The peak of the magnitude distribution of an observed field is a pointer to the completeness in the data (Leahy et al. 2020), (D23). In Figure 3.2(a), we have shown the distribution of FUV magnitude of SMC fields with seven different exposure times (same SMC fields as in Figure 3.1). The distribution shows peaks in magnitudes between 17.5 and 19.5 mag, and we note a sudden drop in the number

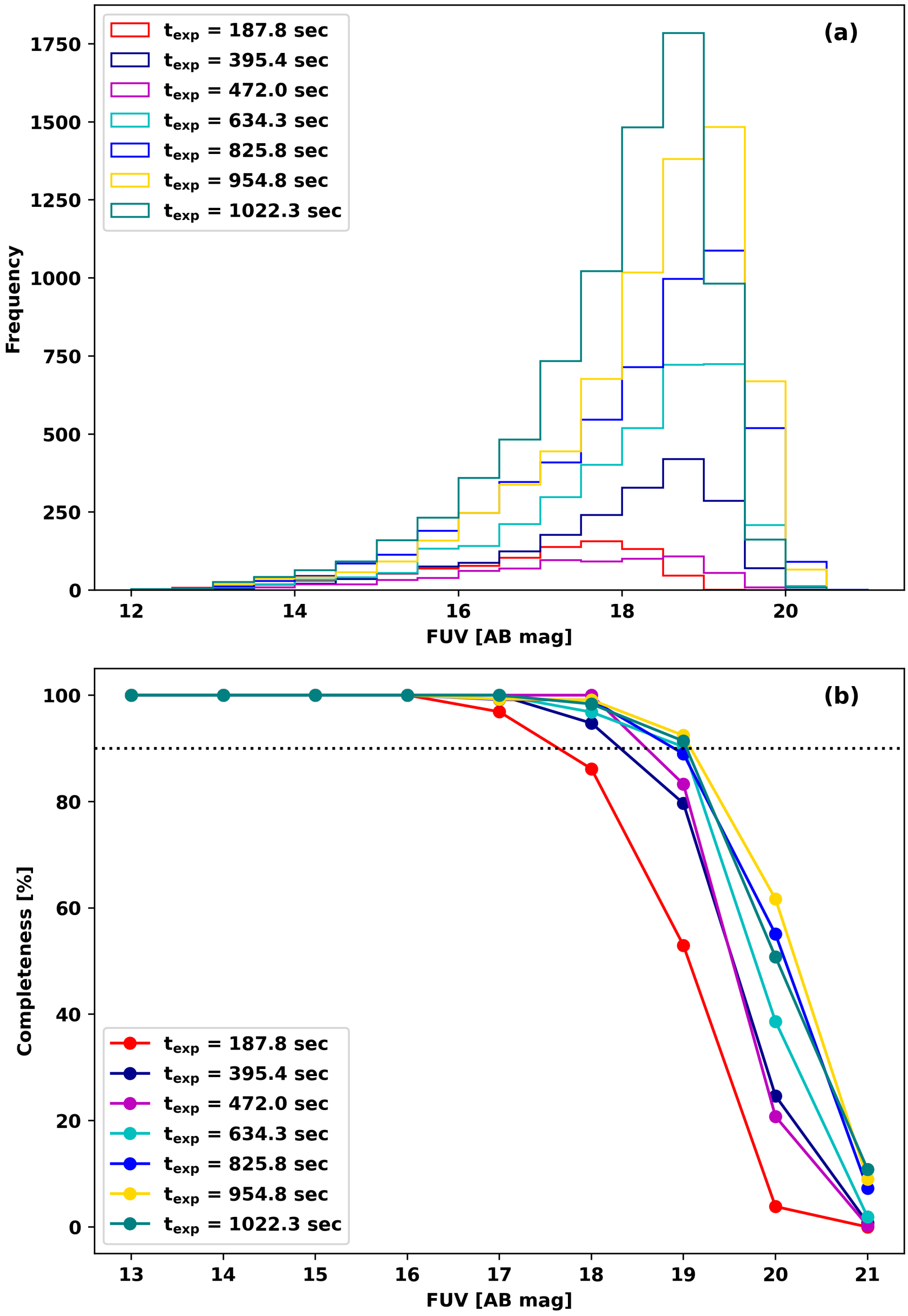

FIGURE 3.2: (a) The FUV magnitude distribution and (b) completeness in percentage for seven UVIT observed SMC fields with different exposure times. The black dotted line represents 90% of completeness.

of fainter stars along with an increase in the FUV magnitude error, as shown in Figure 3.1. This points to a range in incompleteness in the observed fields that need to be quantified.

In order to quantitatively estimate the incompleteness in the data across the observed fields, we conducted ASTs on the above mentioned seven fields to determine the CF. We followed the AST as mentioned in Chapter 2. The same procedure of AST is followed for all the images. Figure 3.2(b) shows the variation of completeness with the FUV magnitude for seven SMC fields. Extending these CFs to all fields, we conclude that the observed fields exhibit 100% completeness at ∼16 mag, and beyond which the completeness starts to reduce. For artificial stars up to 18 mag, all considered images (with different exposures and crowding) show a recovery rate of around 90%. Therefore, we consider a completeness of 90% or more at ∼18 mag (FUV) for all the observed SMC fields.

For context, previous FUV surveys of the SMC exhibit significant incompleteness beyond approximate limits of ∼14 Vega mag for UIT (Cornett et al. 1997) and ∼18 AB mag for Swift/UVOT (Ludwig et al. 2026) based on their magnitude distributions. For GALEX (Morrissey et al. 2007), we find significant incompleteness beyond ∼20 AB mag from its published calibration. These are indicative thresholds rather than precise quantifications. Our UVIT observations achieve 90% completeness at ∼18 AB mag, representing a significant improvement over UIT and comparable depth to Swift/UVOT, while GALEX provides deeper coverage across a larger area.

Table 3.1: FUV catalog of the sources detected in the direction of the SMC. Columns 1 to 8 of the catalog table present UVIT_ID, spatial coordinates, magnitude in the F172M filter, corresponding fit error in magnitude, VMC_PSF_Source_ID, Gaia_DR3_Source_ID, and probable SMC member (PSM), respectively. The complete table is accessible as supplementary online material in H24b.

UVIT_ID	RA [deg]	Dec [deg]	FUV [AB mag]	Error [AB mag]	VMC_PSF_Source_ID	Gaia_DR3_Source_ID	PSM
UVIT00000	10.315324	−73.277606	16.116	0.098	558371534268	4688850813948992896	Y
UVIT00001	09.940444	−73.294990	16.586	0.163	558371499893	4688862942940210304	Y
UVIT00002	10.548706	−73.303662	17.022	0.154	558371482809	4688848855413218688	Y
UVIT00003	10.034966	−73.309045	16.083	0.129	558371472160	4688851054467630464	Y
UVIT00004	10.368390	−73.330106	17.078	0.134	558371430415	4688847446664173568	N

Note. Total detected FUV stars: ∼76,800; cross-matched with Gaia: 73,395; with VMC: 72,790; with both: ∼70,900; not matched with Gaia or VMC: 1,456. PSMs are identified by truncated optimal NN with RUWE < 1.4 (62,901 sources). In the last column, Y = Yes, N = No.

3.2.3 FUV catalog and Cross-matching

To produce the FUV catalog, we combined the photometric data of all 39 UVIT observed fields. The presence of data duplication in the overlapping regions is addressed by considering the source with the better S/N and/or photometric error. For the catalog, we selected FUV sources with a magnitude error of $\leq$0.2 mag (for S/N $\geq$5) and an FUV magnitude >13.2 mag as the FUV sources brighter than ∼13.2 mag may be saturated (Tandon et al. 2017b). With the above criteria, a catalog with ∼76800 FUV sources are listed in Table 3.1. Though this catalog covers the inner SMC, we point out the presence of a gap in the observed area, centered around the coordinates (α,δ):(14°, −72.5°) (see Figure 3.8 and Figure 2.3).

To better characterize the detected FUV sources in the SMC, we cross-matched these FUV sources with IR and optical data. We obtained the Gaia DR3 data (Gaia Collaboration et al. 2023) of the SMC with ADQL query in the Gaia archive[†] as mentioned in G2021, (see also Chapter 2, section 2.3.1). The number of cross-matched UVIT-Gaia sources within a search radius of $1''$ is 73395, and their corresponding Gaia_DR3_Source_IDs are listed in the seventh column of Table 3.1.

[†] `https://gea.esac.esa.int/archive/`

The PSF photometry catalog of the SMC in IR band (Rubele et al. 2018) as part of the VMC, from the European Southern Observatory (ESO) archive [‡] is cross-matched with the detected FUV sources within a search radius of 1″ to obtain 72790 UVIT-VMC cross-matched sources (VMC_PSF_Source_ID is listed in 6th column of Table 3.1). We note that ∼70900 FUV sources have both optical (Gaia) and IR (VMC) data, while ∼1450 FUV sources do not have either Gaia or VMC cross-matches. For Gaia and VMC data, a uniform search radius of 1″ was adopted for cross-matching, based on the positional uncertainty and spatial resolution of the UVIT data (∼1.2–1.5″). Given the significantly higher astrometric precision of Gaia and VMC, the matching radius is primarily governed by the UVIT positional uncertainties. This radius represents a balance between minimizing false associations and maximizing the recovery of true counterparts, particularly in the crowded regions of the SMC.

We performed a cross-match of the FUV catalog (see Table 3.1) with the SIMBAD database using a search radius of 1″. This analysis revealed that 9133 stars were matched with the SIMBAD database, and we note that ∼30% of cross-matched sources are eclipsing binaries, and another ∼30% are classified as ”star” (no spectral classification). We also found some UVIT-SIMBAD stars are classified as supergiants (∼200), white dwarfs (∼200), Be stars (∼650), and high mass X-ray binaries (∼100). We also cross-matched our catalog with the catalog of 5324 massive stars in the SMC by Bonanos et al. (2010), using a search radius of 1″ (UVIT observed fields cover only 65% of the catalog), and 2388 stars were identified. The majority of these cross-matched stars are of OB type (O-type: ∼132, B-type: ∼2000). We cross-matched the UVIT catalog with major spectroscopic surveys of massive stars in the SMC. We find 96 sources in common with the VLT-FLAMES survey (Evans et al. 2006) and 32 sources with the RIOTS4 catalog (Lamb et al. 2016). For the BLOeM dataset, Patrick et al. (2025) report 754 sources in common with the UVIT catalog.

[‡] `https://archive.eso.org/cms.html`

3.2.4 Most Probable FUV sources of the SMC

TABLE 3.2: Number of probable FUV member sources of the SMC and the MW obtained using different classification methods. *Jiménez-Arranz et al. (2023)

Method	SMC	MW	SMC (RUWE < 1.4)	MW (RUWE < 1.4)
3σ clipping to $\langle\mu_\alpha \cos\delta\rangle$, $\langle\mu_\delta\rangle$, $\langle$Plx$\rangle$	69,389	4,006	61,624	2,141
NN complete*	70,319	3,076	63,444	321
Optimal NN*	68,621	4,774	62,980	785
Truncated-Optimal NN*	68,540	4,855	62,901	864

To find the most probable FUV sources in the SMC, we considered only those FUV sources that have Gaia counterparts. The spherical coordinates of the SMC are projected onto the XY-plane using the zenithal equidistant projection method, where we followed the X and Y conversion as defined in van der Marel & Cioni (2001, hereafter M2001). For this, we considered the optical center of the SMC at $\alpha_{\text{SMC}} = 00^{\text{h}}52^{\text{m}}12^{\text{s}}.5$ and $\delta_{\text{SMC}} = -72^\circ\ 49'\ 43''$ (J2000; V1972). Here, we followed two criteria for selecting the most probable SMC sources: (1) We implemented a 3σ cut-off around the mean value of the parallax (Plx $= 0.014$ mas) and proper motion (PM) in both RA and Declination (Dec) ($\mu_\alpha \cos\delta = 0.74$ mas yr^{-1}, $\mu_\delta = -1.25$ mas yr^{-1}) for the detected FUV sources. The resulting number of the most probable FUV sources of the SMC is 69389. Still, there is a possibility that these FUV sources may be contaminated with the background galaxies; (2) We cross-matched the FUV sources with the Gaia probability catalog of the SMC sources provided by Jiménez-Arranz et al. (2023). They obtained three samples of the SMC based on probability (P_{cut}) and G mag cut-off. We followed the same cut-offs to obtain three samples of the most probable SMC stars: (i) NN complete ($\text{P}_{\text{cut}} = 0.01$): 70,319 FUV sources, (ii) NN optimal ($\text{P}_{\text{cut}} = 0.31$): 68,621 FUV sources and (iii) NN truncated-optimal sample ($\text{P}_{\text{cut}} = 0.31$ and G < 19.5 mag): 68,540 FUV sources (see Table 3.2). The spatial distribution of the SMC and MW sources, obtained from different methods, are shown in Figure 3.3. We note that the MW FUV stars show a similar spatial distribution as the SMC.

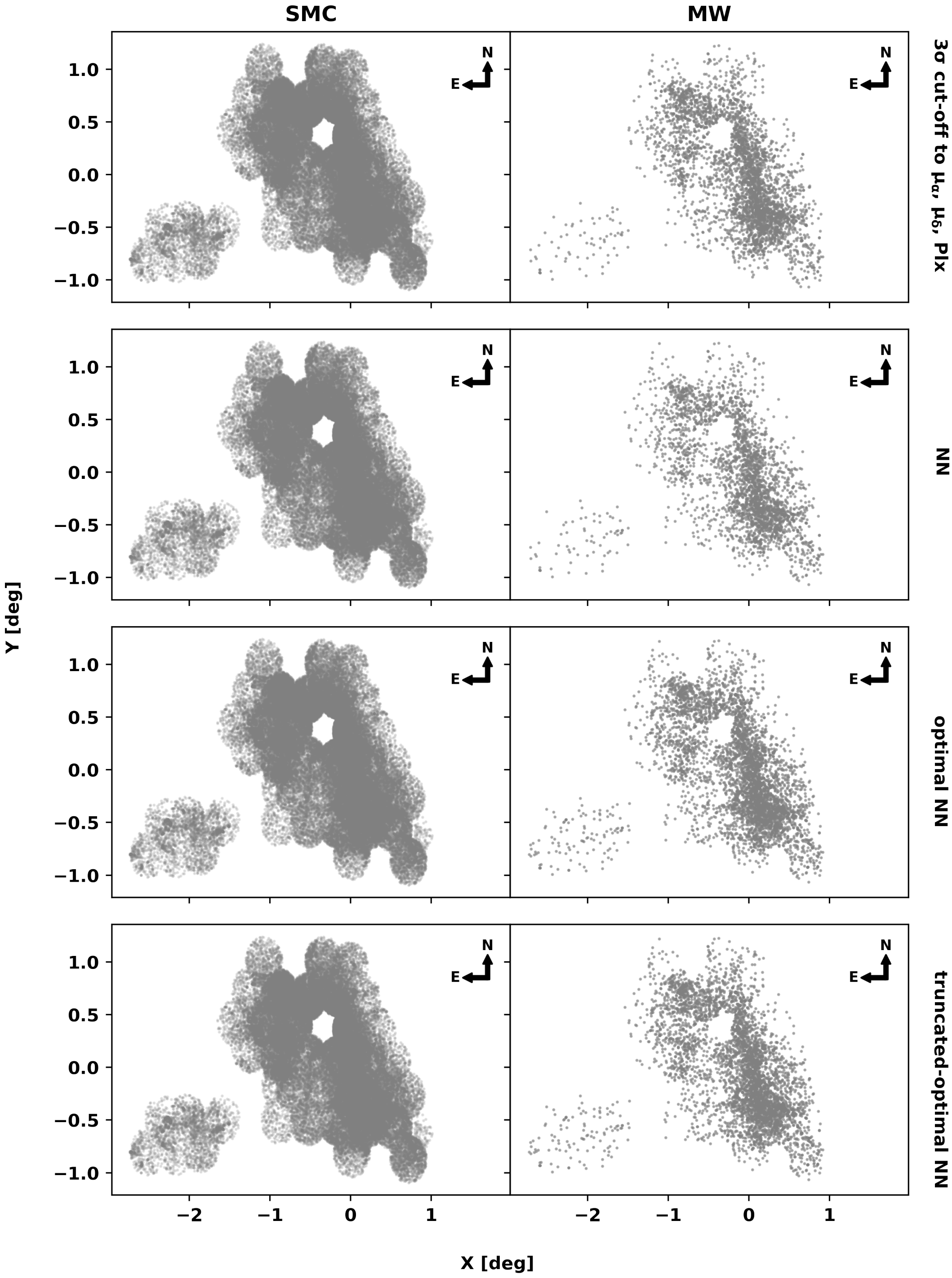

Figure 3.3: The spatial distribution of probable FUV stars of the SMC and the MW obtained from different methods without RUWE constraints.

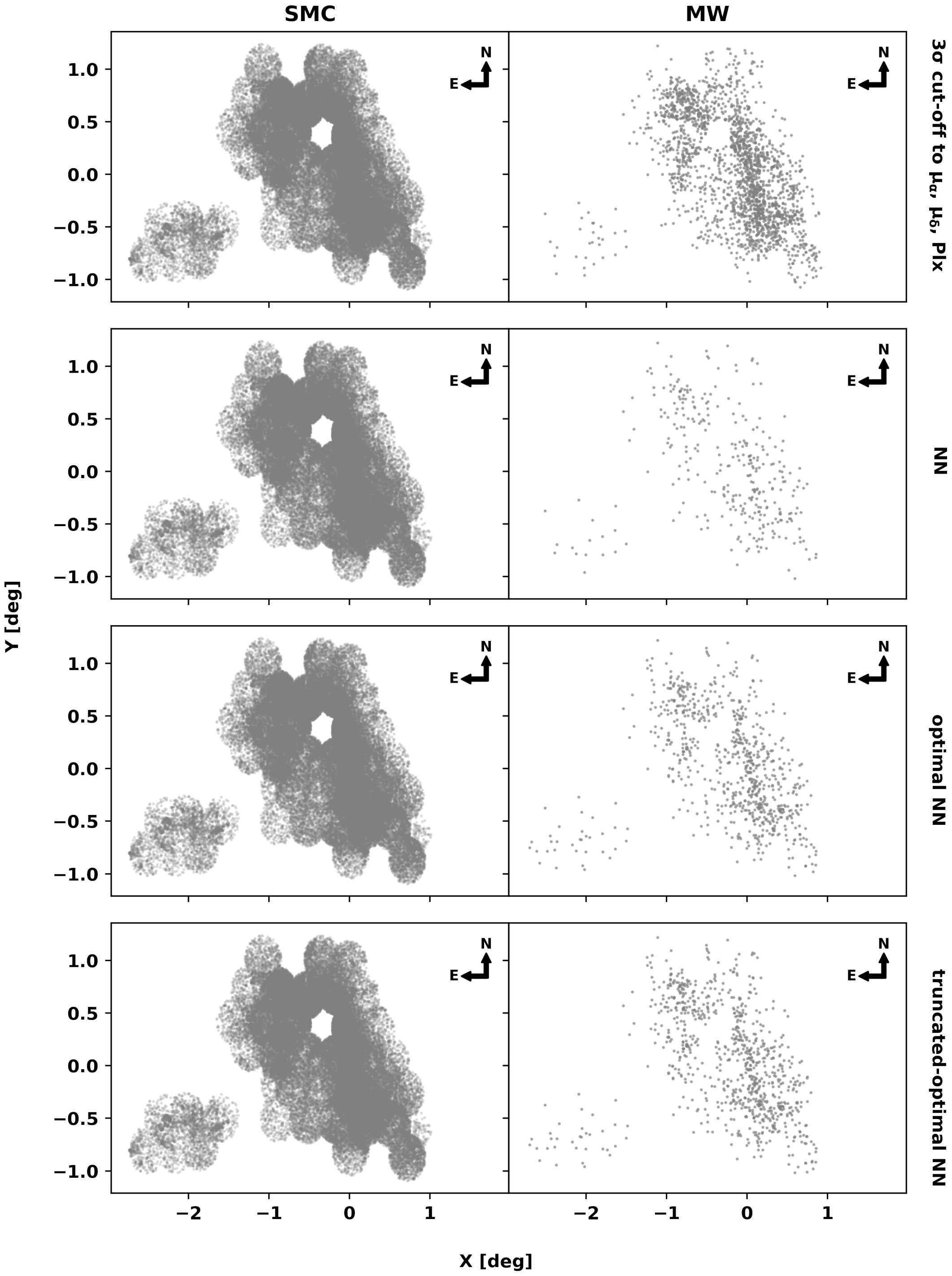

Figure 3.4: The spatial distribution of probable FUV stars of the SMC and the MW obtained from different methods with a RUWE < 1.4.

There is a possibility that Gaia sources are non-single or problematic for astrometric solutions (Lindegren et al. 2018). To identify and remove such UVIT–Gaia sources (see Table 3.1), we applied a constraint on the renormalized unit weight error (RUWE), which quantifies the goodness of fit of the astrometric solution. Values near 1.0 indicate a well-behaved single-star solution, while values above 1.4 typically suggest binarity or astrometric issues. We therefore selected sources with RUWE < 1.4 (Lindegren et al. 2018). Then, we followed again all the above two criteria for selecting the most probable SMC stars (see Table 3.2). In Figure 3.4, we note that the MW stars obtained using only the first criteria (3σ cut-off to the means of Plx: 0.013 mas, $\mu_{\alpha cos\delta}$: 0.74 mas yr^{-1} and μ_{δ}: -1.25 mas yr^{-1}) show a spatial distribution like the SMC even after RUWE constraint. But the MW stars obtained based on probability and/or G mag cutoff (Jiménez-Arranz et al. 2023) show more or less uniform distribution, which is the expected spatial distribution of the foreground stars. The numbers of most probable stars obtained after the RUWE constraint in NN complete (63444), optimal NN (62980), and truncated-optimal NN (62901) samples are similar. Hereafter, we consider truncated-optimal NN samples (i.e., Gaia cross-matched FUV stars with probability $> 31\%$, G < 19.5 mag, and RUWE < 1.4, and listed as probable SMC members (PSMs) in the 8th column of Table 3.1) for further analysis.

3.3 Color-Magnitude Diagrams

A CMD is a useful tool to trace the evolutionary paths of different stellar populations. Our goal is to identify various stellar populations within the SMC based on their location in the FUV–optical CMD. As the FUV is in AB magnitude, we converted G mag from the Vega magnitude system to the AB magnitude system[§] to create the FUV–optical CMD, as shown in Figure 3.5(a). To identify various

---

[§] https://gea.esac.esa.int/archive/documentation/GDR2/Data_processing/chap_cu5pho/sec_cu5pho_calibr/ssec_cu5pho_calibr_extern.html

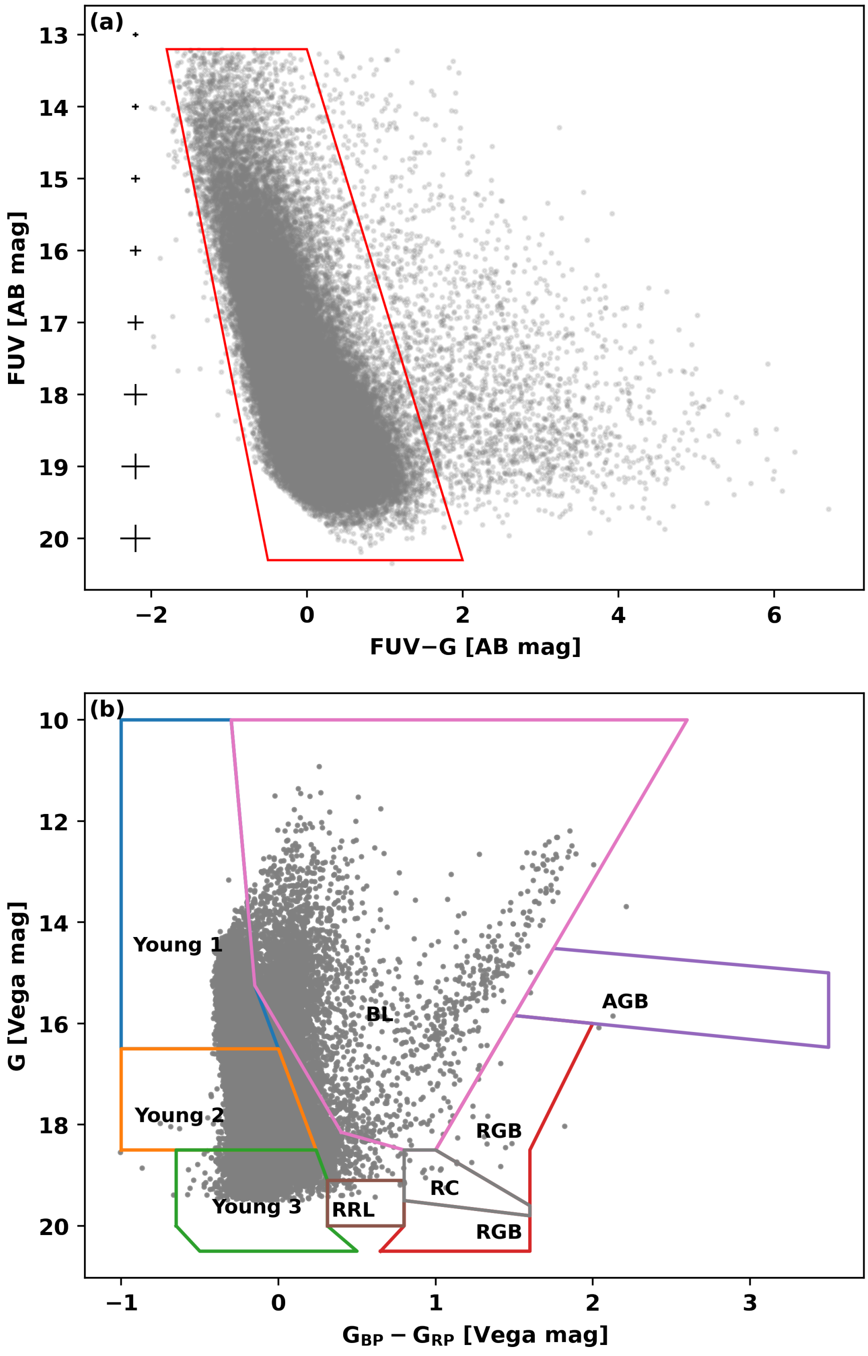

FIGURE 3.5: (a) FUV–optical CMD of the SMC sources. The main sequence branch is shown within a red polygon. The error bars (median value) for FUV magnitude and FUV–optical color are shown in black. (b) Polygons on the optical CMD of the SMC sources representing different populations of the SMC (G2021, see right panel of their Fig. 2).

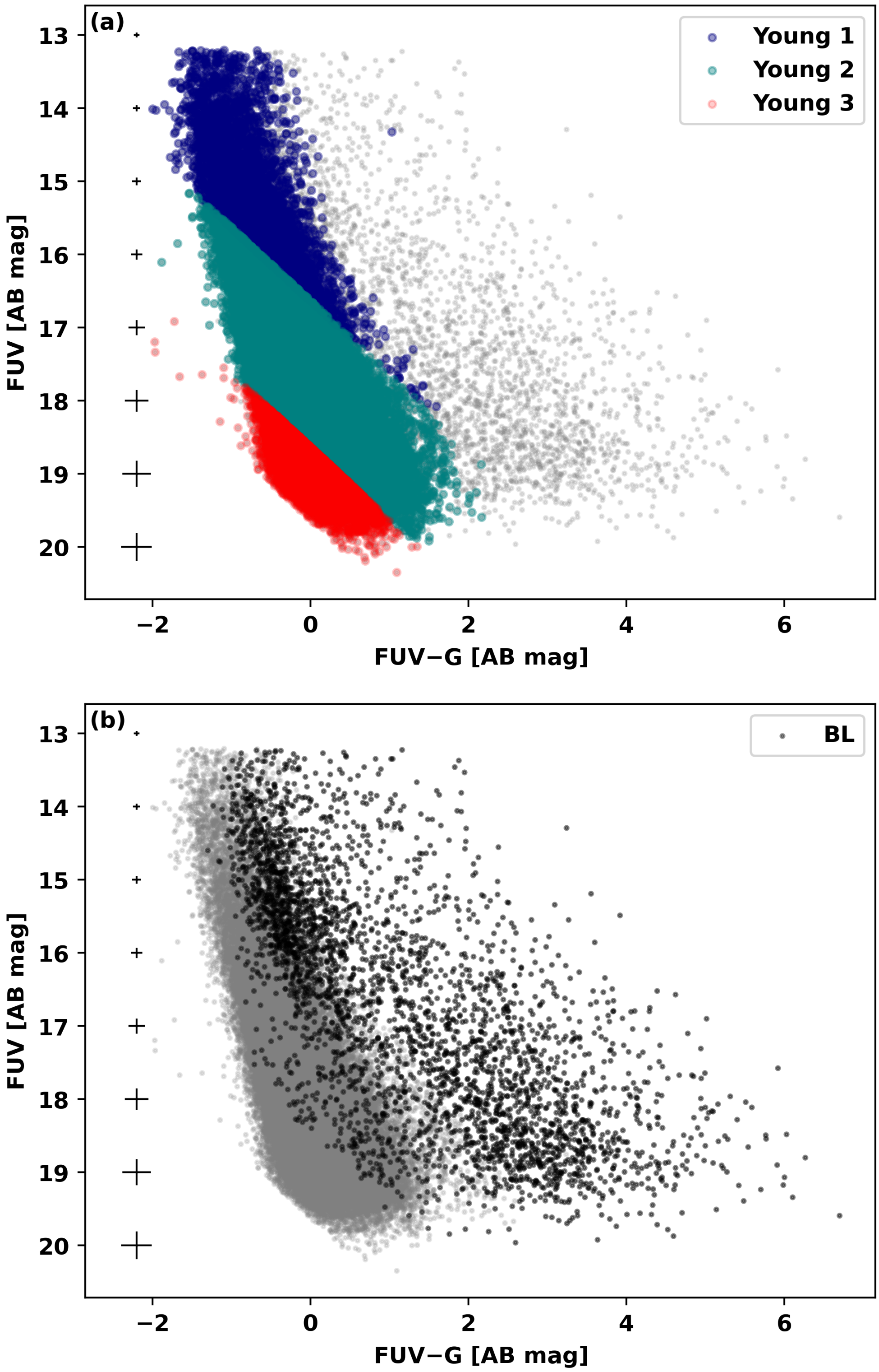

FIGURE 3.6: The locations of Y1, Y2, Y3 and BL stars on FUV–optical CMDs are shown in (a) and (b), respectively. The error bars (median value) for FUV magnitude and FUV–optical color are shown in black. Gray points are the SMC FUV sources.

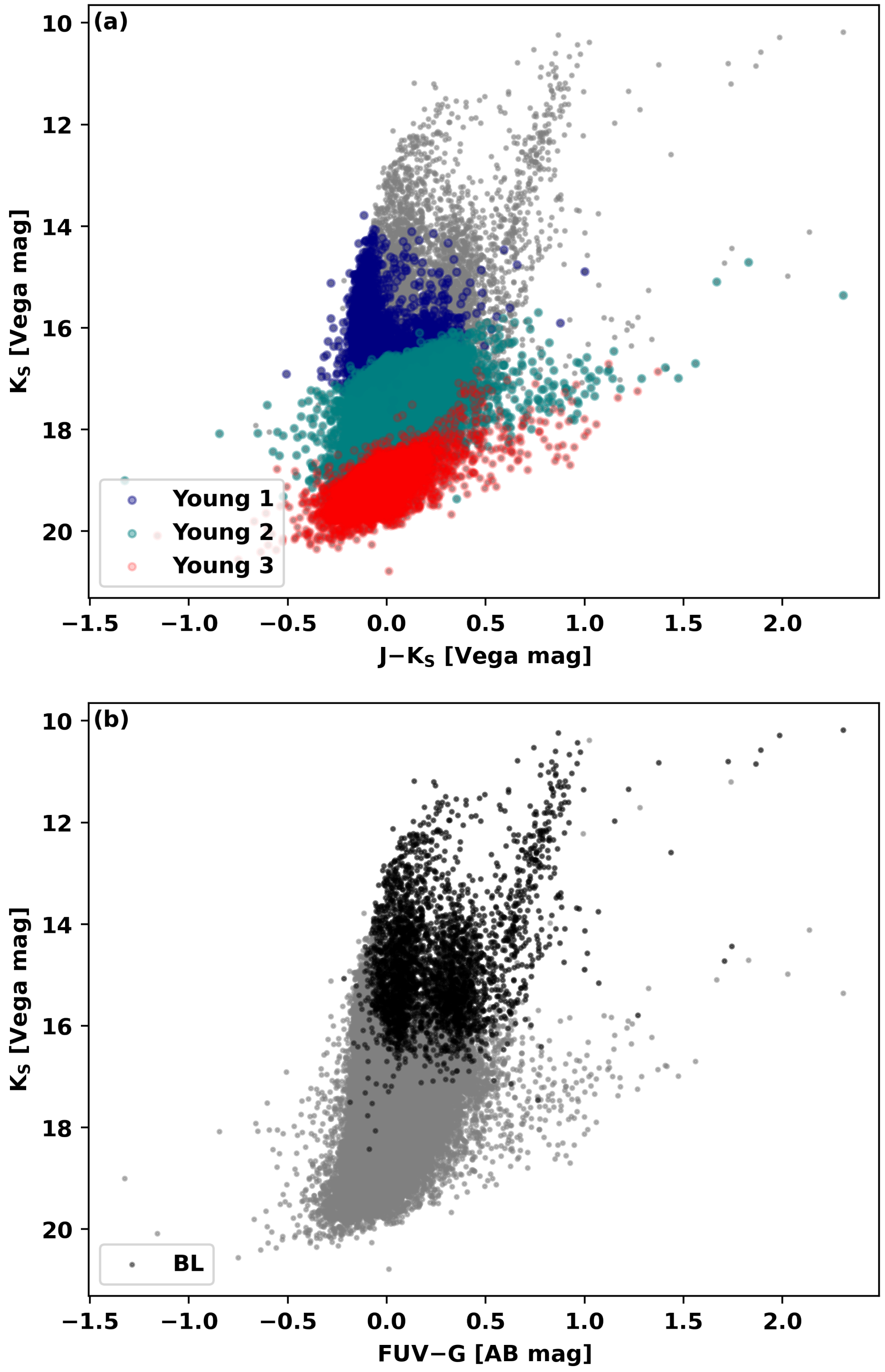

FIGURE 3.7: The locations of Y1, Y2, Y3, and BL stars on IR CMDs are shown in (a) and (b), respectively. Gray points are the SMC FUV sources.

populations, we plotted the Gaia optical CMD (G vs. $G_{BP} - G_{RP}$) for the 62901 probable SMC FUV members (see section 3.2.4) as shown in Figure 3.5(b) and identified different populations as described by G2021. Here, we considered only the young populations (Young 1 (Y1), Young 2 (Y2), Young 3 (Y3), Blue Loop (BL)) as they are detected in large numbers (see Figure 3.5(b)), as listed in Table 3.3. As the detected number of RGB, AGB, RC, and RR-Lyrae (RRL) are significantly low, we did not consider them for further analysis. Figure 3.6(a) and (b) show the position of the Y1, Y2, Y3, and BL stars on the FUV–optical CMDs of the SMC. We note that Y1, Y2, and Y3 have distinct locations on the main sequence branch with an increasing FUV mag (Figure 3.6(a)), whereas BL stars majorly fall on the redder part of the FUV–optical CMD, with some located on the main sequence branch (Figure 3.6(b)).

The young populations defined from Gaia optical CMD (Figure 3.5(b)) are also plotted in the IR CMDs (K_s vs. J–K_s) as shown in Figure 3.7(a) and (b), after restricting sources with a maximum photometric error of 0.2 mag in the two IR filters. We compared the positions of the populations in the IR CMD with a similar study by DL2019, (see Figure 1 in their paper). Our analysis revealed that the BL stars align with the positions of supergiant and giant stars, while the Y1, Y2, and Y3 populations are mainly located on the main sequence and subgiant branches. Therefore, we conclude that the detected SMC FUV stars primarily belong to the main sequence and supergiant/giant stars.

TABLE 3.3: Description and star count of four young populations in our catalog.

Population	Description*	N
Young 1	Very young main sequence (ages $<$ 50 Myr)	4924
Young 2	Young main sequence (50 $<$ age $<$ 400 Myr)	40484
Young 3	Intermediate-age main sequence population (mixed ages reaching up to 1–2 Gyr)	11885
BL	Blue loop (including classical Cepheids)	3584

Note. *The descriptions of the populations are taken from G2021.

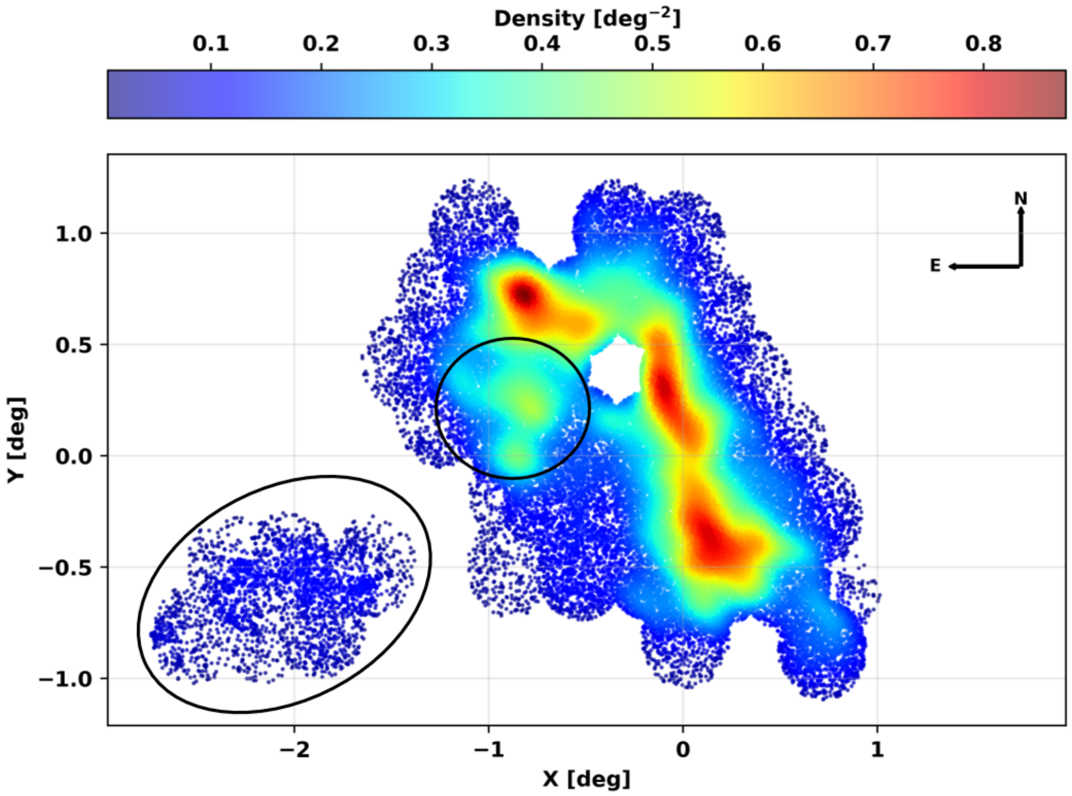

FIGURE 3.8: Surface density distribution (KDE; kernel width = 0.1 deg) of the SMC. The color bar represents the density in the unit of deg^{-2}. The black ellipse and circle represent the inner SMC Wing and shell-like structure, respectively.

3.4 Spatial distribution

The morphological features of the young population in the SMC are examined using the spatial distribution of the FUV stars. It is important to note that the SMC fields exhibit a range of completeness with the FUV magnitude, based on their exposure times and crowding from Figure 3.2(b). Except two, all fields show their peak FUV magnitude around 19 mag before declining (Figure 3.2(a)) where completeness is more than ∼90%. This suggests that the impact of incompleteness in the morphology based on the FUV stellar density is negligible. The surface stellar density of the SMC is shown in Figure 3.8, based on a KDE with a kernel width of 0.1 deg, which is sufficient to identify the dense regions. The distribution as seen in Figure 3.8 is irregular, with an asymmetric young bar i.e. the stellar density along the bar is not the same, DL2019, (see their Figure 6) and an eastern extension, the inner SMC Wing at ($-2.75 < \Delta\alpha < -1.25$, $-1 < \Delta\delta < -0.25$) deg. The young bar has a relatively higher density segregated into three distinct regions in the inner SMC. When there is a continuity between the SW high-density region to the central high-density region, we note a discontinuity in density at $\sim(-0.5, 0.5)$ deg in the NE direction. This stellar density in the young bar is broken (i.e. density is not distributed continuously throughout the SMC bar) and bends towards the east direction. A shell-like structure (previously detected a clump of stars; Maragoudaki et al. 2001) is detected at ($-$ 0.75, 0.25) deg in the east direction towards the SMC Wing.

In order to trace the morphology, the KDE map of the stellar surface density of Y1, Y2, Y3, and BL stars are shown in Figure 3.9. These show 4 distinct dense regions; visually identified and marked as east, NE, center, and SW on the basis of direction, as shown in Figure 3.9. The relative density in each region varies with population and the Y2 population is found to closely resemble the overall density map as shown in Figure 3.8. The maximum range in stellar surface density is seen for the Y1, whereas the other 3 populations have a reduced but similar range of stellar density values. The densest region of the Y1 population is in the NE of the bar (Figure 3.9(a)), whereas the densest BL population is found in the SW (Figure 3.9(d)) of the bar. The broken bar and the shell-like features are predominantly seen in Y2 population(see Figure 3.9(b)). The densest regions of Y3 are found in the NE as well as at the central part of the bar (see Figure 3.9(c)).

3.5 Kinematics

As the SMC is disturbed due to interactions, the imprint of interactions could be traceable in the motion of the young stars through a kinematic analysis. We

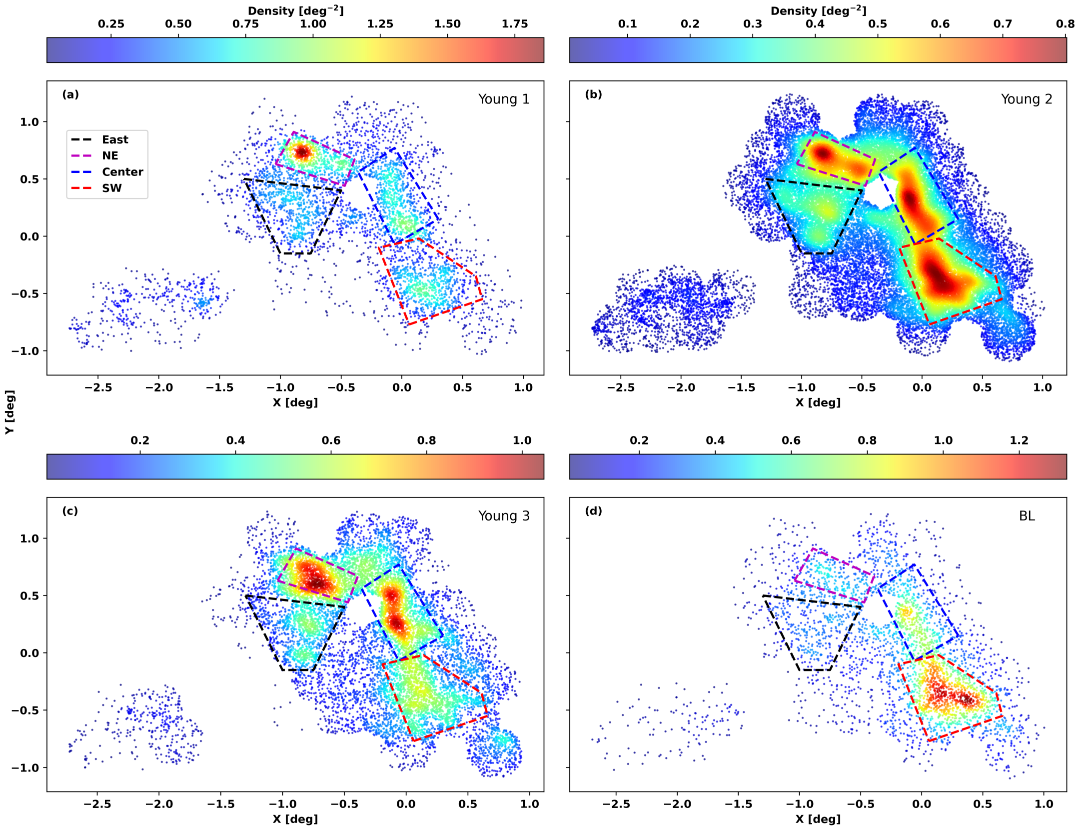

FIGURE 3.9: Surface density distribution (KDE; kernel width = 0.1 deg) of Y1, Y2, Y3, and BL populations in (a), (b), (c), and (d), respectively. The color bar represents the density in units of deg^{-2}. Dashed polygons mark four distinct dense regions named east, NE, center, and SW. The labeling in panel (a) is consistent across all panels.

performed a 2-D kinematic analysis of 4 populations as well as the 5 regions using their PM values, and the results are presented here.

The PM distribution of all four populations and the fitted Gaussian curves are shown in Figure 3.10. The fit parameters, such as the peak and standard deviation values, along with their corresponding errors from the covariance matrix, are listed in Table 3.4. All the PM distributions had to be fitted with two Gaussian profiles. The Gaussian profiles fitted to Y1 and BL have slightly differing peaks and widths, whereas those fitted to the Y2 and Y3 populations have significantly differing widths. The width of the Y2 and Y3 populations suggest that there is a cool component corresponding to a PM distribution with reduced dispersion and a hot component corresponding to a PM distribution with a relatively large dispersion. Interestingly, the two sub-populations of BL and Y1 exhibit relatively less widths, when compared to both the widths of Y2 and Y3 profiles. Next, we set out to check if both components of the transverse motion (PM) are contributing to the above-observed differences.

We transformed ($\mu_\alpha cos\delta$, μ_δ) into the Cartesian plane (μ_x, μ_y) using the conversion equation as defined by G2021, (Equation 2). After this transformation, we conducted further analysis on the kinematics using the obtained PM values on the X-Y plane, with μ_x and μ_y representing PMRA and PMDec, respectively. Then, we created vector point diagrams (VPDs) for four populations as shown in Figure 3.11. VPDs of Y1 and BL stars (Figure 3.11) show a spread in PMRA, whereas the PMDec distributions do not. The distributions of Y2 and Y3 populations have broad profiles in both PMRA and PMDec distributions. Double Gaussians are well-fitted for the PMRA distributions of Y1 and BL, while the single Gaussian curves are well-fitted for the rest. The peak and standard deviation values of these Gaussian fits, along with their corresponding errors obtained from the covariance matrix, are listed in Table 3.4 (4th to 6th column). The peak PMRA and PMDec values of all the populations are similar to each other. The PMRA distribution widths of the Y1 and BL populations are dissimilar with the broad distribution showing about thrice the width of the narrow one. We note an increasing width of the PMRA and PMDec distribution from Y2 to Y3, which are even larger than the width of the PMRA distribution of Y1 population and BL stars. We checked the spatial distribution of PMRA for these four populations as shown in Figure 3.12. We observed a noticeable PMRA gradient, increasing towards the east and NE direction for the Y1 population, in contrast to Y2 and Y3. The spatial distribution of PMRA for the BL stars also indicates a similar, though less pronounced, gradient compared to Y1 population. We note a distinct pocket of relatively high PMRA in the eastern part of the SMC in the case of the Y1 population, near the shell-like structure and the inner SMC wing.

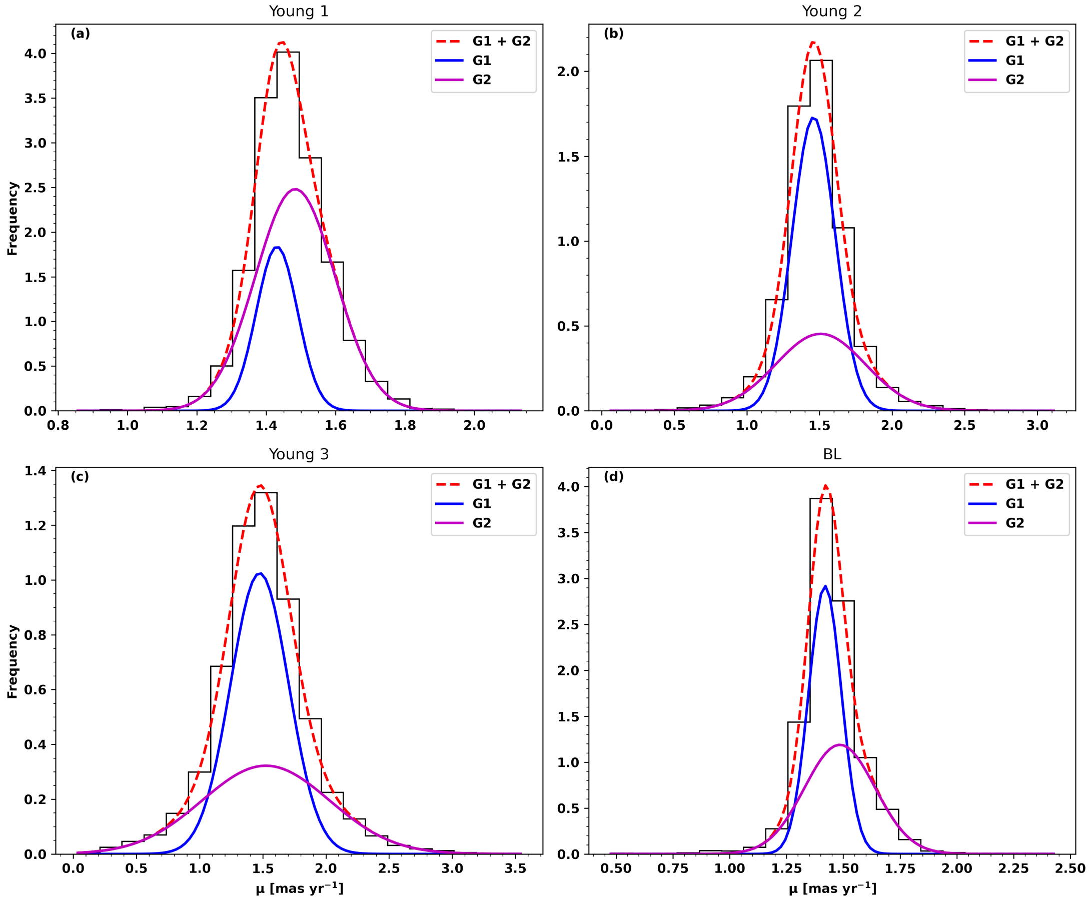

FIGURE 3.10: PM distribution of four young populations. Gaussian 1 (G1), Gaussian 2 (G2), and their sum (G1 + G2) curves are shown in blue, magenta, and red, respectively.

We have found two sub-populations in BL and Y1 based on PMRA distribution (see Figure 3.11). It is quite interesting to examine whether the sub-populations are located all over the observed SMC or confined to a specific region. To do so, we plotted their VPDs separately for four dense regions and the inner Wing region, as depicted in Figure 3.13. We clearly see that there are two peaks of PMRA distribution of BL in the east and NE parts of the SMC, although BL stars are more concentrated in the SW part. In the case of the Y1 population, two possible peaks of PMRA distribution are in the east and NE direction. We note a higher PMRA value in the inner Wing region for both Y1 and BL populations. We conclude that the two sub-populations with differing PMRA distribution found for 1 and BL are mainly located in the east, i.e., the shell-like structure and inner

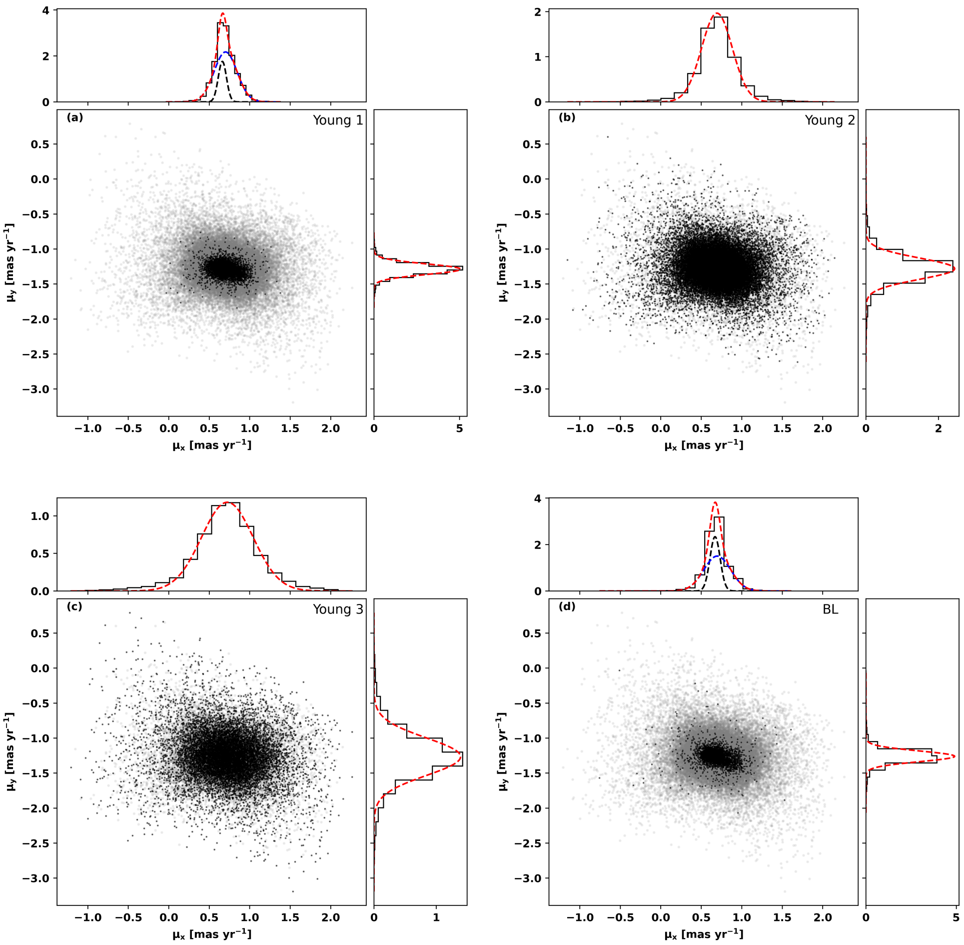

Figure 3.11: VPDs of four young populations. Distributions of PMRA and PMDec are shown at the top and right. Gaussian (sum) is shown in red for all panels, while Gaussian 1 and Gaussian 2 are shown in black and blue, respectively, in (a) and (d). Gray points represent the SMC FUV stars.

Table 3.4: Peak and standard deviation values (in units of mas yr^{-1}) of Gaussian curve fits on PM, PMRA, and PMDec distributions, along with fit errors, for different young populations.

Population	Gaussian 1 (PM)		Gaussian 2 (PM)		Gaussian 1 (PMRA)		Gaussian 2 (PMRA)		Gaussian (PMDec)	
	Peak	Std	Peak	Std	Peak	Std	Peak	Std	Peak	Std
Y1	1.431±0.002	0.060±0.002	1.483±0.003	0.115±0.002	0.662±0.001	0.051±0.002	0.701±0.002	0.142±0.002	−1.288±0.001	0.076±0.001
Y2	1.460±0.002	0.148±0.004	1.508±0.012	0.308±0.019	0.693±0.004	0.190±0.004	–	–	−1.281±0.003	0.152±0.003
Y3	1.475±0.002	0.230±0.005	1.525±0.011	0.504±0.021	0.723±0.006	0.318±0.006	–	–	−1.266±0.006	0.268±0.006
BL	1.420±0.001	0.072±0.001	1.485±0.003	0.155±0.002	0.670±0.003	0.063±0.006	0.697±0.008	0.166±0.013	−1.261±0.002	0.076±0.002

SMC wing. In summary, the analysis points to kinematic differences in PMRA for the young population in the east and NE, without any noticeable difference in PMDec.

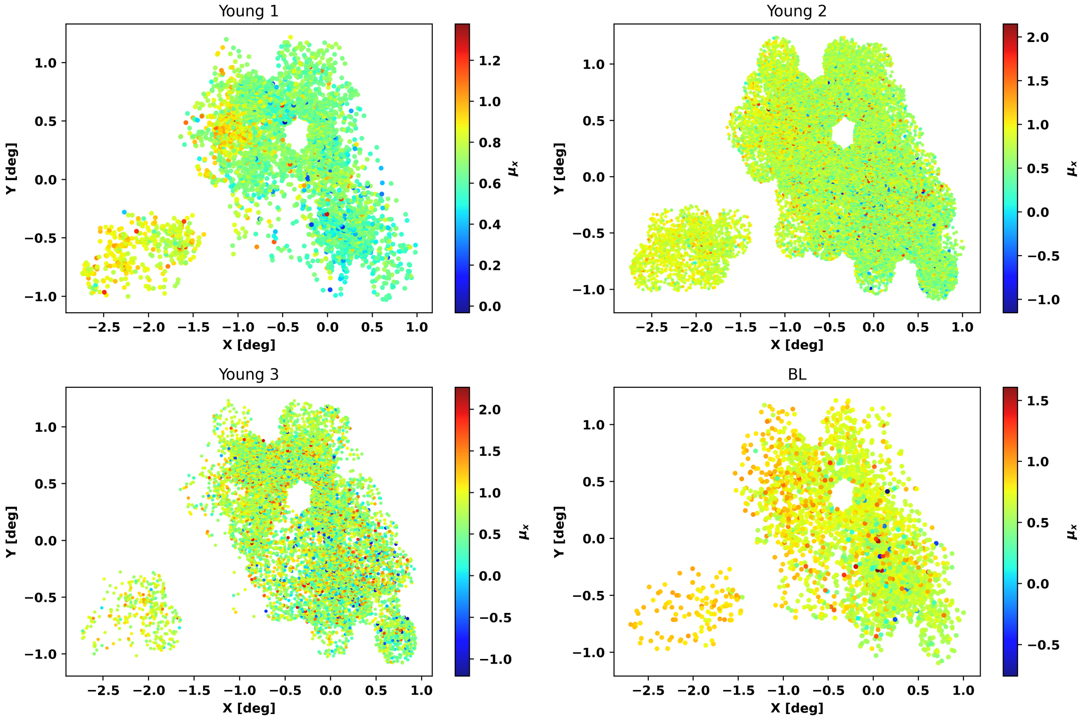

FIGURE 3.12: Spatial distribution of PMRA of four young populations.

3.6 Discussion

TABLE 3.5: Peak and standard deviation values of Gaussian curve fits on PMRA distributions, along with fit errors, for different BL populations.

BL Population	Gaussian 1		Gaussian 2		Gaussian 3	
	Peak [mas yr^{-1}]	Std [mas yr^{-1}]	Peak [mas yr^{-1}]	Std [mas yr^{-1}]	Peak [mas yr^{-1}]	Std [mas yr^{-1}]
Age ≤150 Myr	0.588±0.013	0.053±0.008	0.688±0.004	0.045±0.002	0.736±0.008	0.148±0.004
Age > 150 Myr	0.688±0.023	0.283±0.036	0.647±0.010	0.120±0.018	–	–

The interactions of the SMC with the LMC play a vital role in shaping the morphology of the SMC. In this study, we created an FUV catalog of the SMC obtained from UVIT observations and examined the spatial distribution and kinematics. We found an irregular and clumpy surface density distribution of the young population of the SMC, which is consistent with the previous studies (e.g. Zaritsky et al. 2000; Cioni et al. 2000), (DL2019).

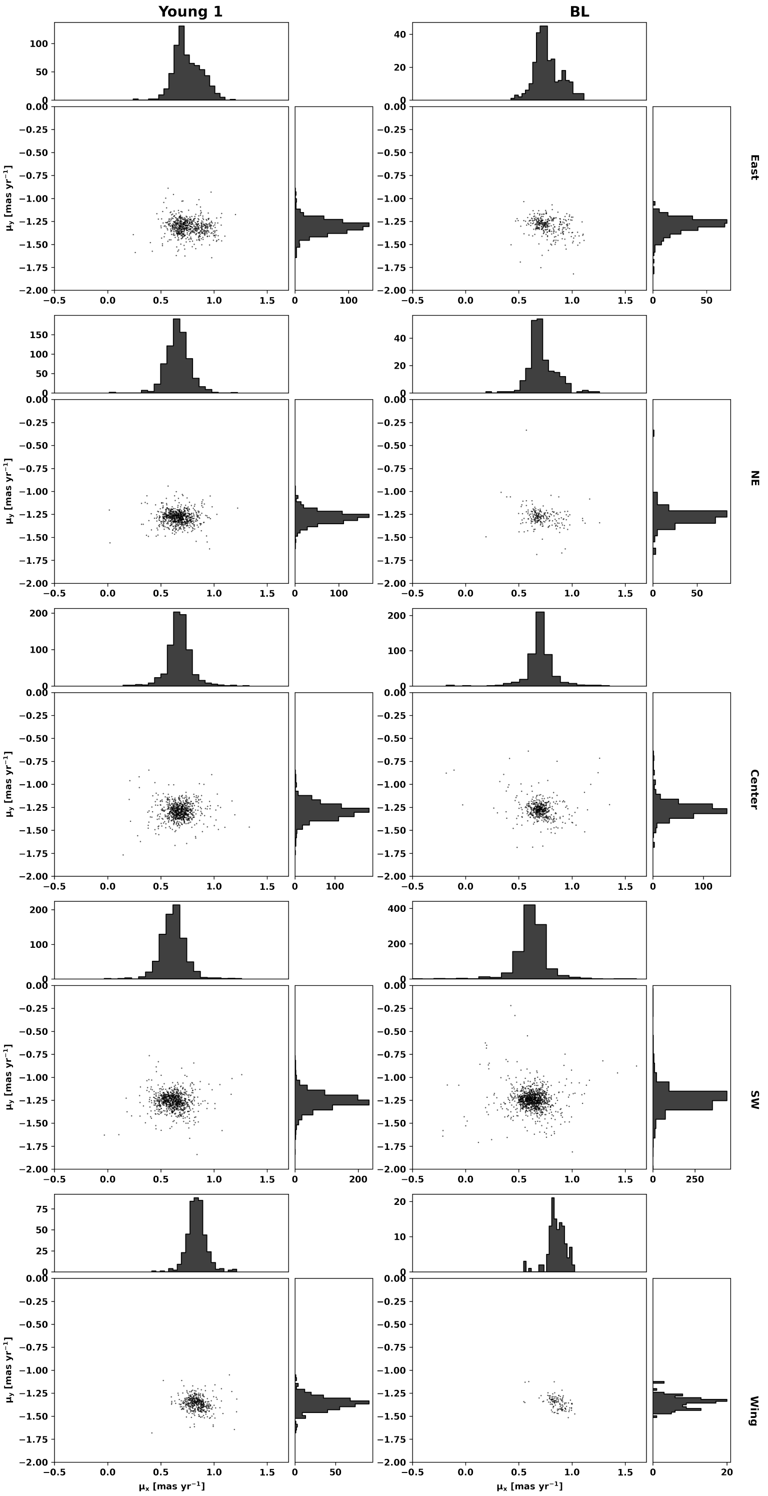

FIGURE 3.13: VPDs of four dense and inner Wing regions of Young 1 and BL stars. Distributions of PMRA and PMDec are shown at the top and right, respectively.

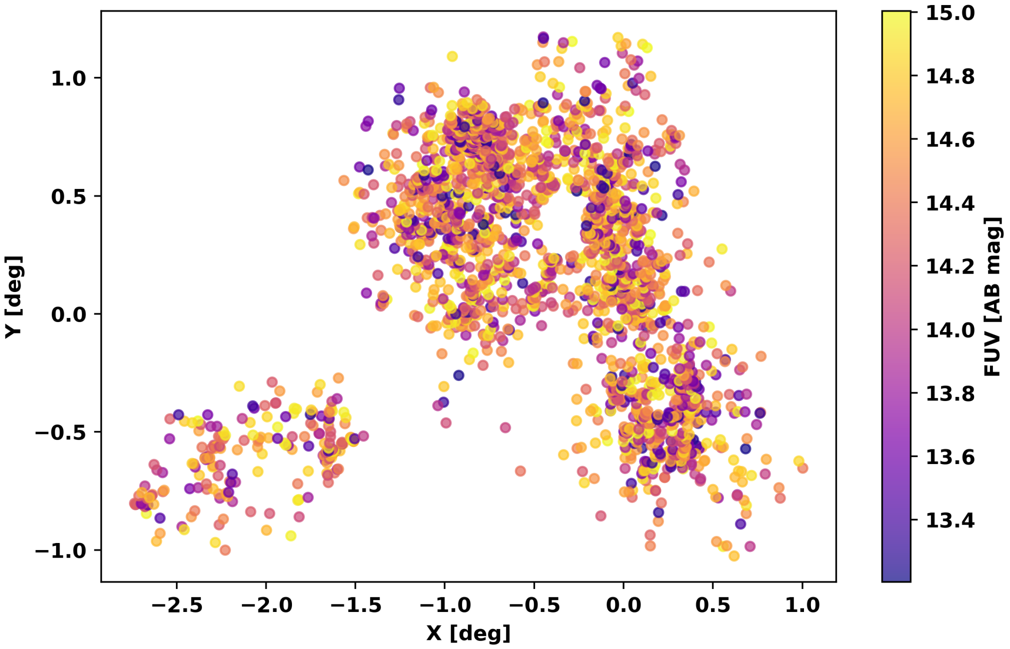

Figure 3.14: Spatial distribution of the SMC FUV stars brighter than 15 magnitude corresponding to a photometric mass $> 8M_{\odot}$.

Patrick et al. (2022) studied the binary systems that contain red supergiant (RSG) stars of the SMC based on FUV data of 88 red supergiants from UVIT. We found a cross-match of 61 FUV sources from our catalog (Table 3.1) with their RSGs (see their appendix, Table A2), and the FUV magnitudes of these cross-matched sources are within the error. The RSGs, which are not cross-matched, are either found to be faint or associated with larger errors in FUV magnitude (the cutoff error in FUV magnitude in this study is $\leq$0.2 mag).

Maragoudaki et al. (2001) investigated the spatial distribution of different populations of the SMC. They found that the young population exhibited an asymmetric distribution, unlike the old population. They attributed this irregularity to the recent interaction between the LMC and the SMC at $\sim$0.2 – 0.4 Gyr ago. Gonidakis et al. (2009) mapped the spatial distribution of four age groups of the SMC stellar populations and provided the isopleth contour maps using 2MASS data. The spatial distribution of their B and A-type stars are similar to the distribution of

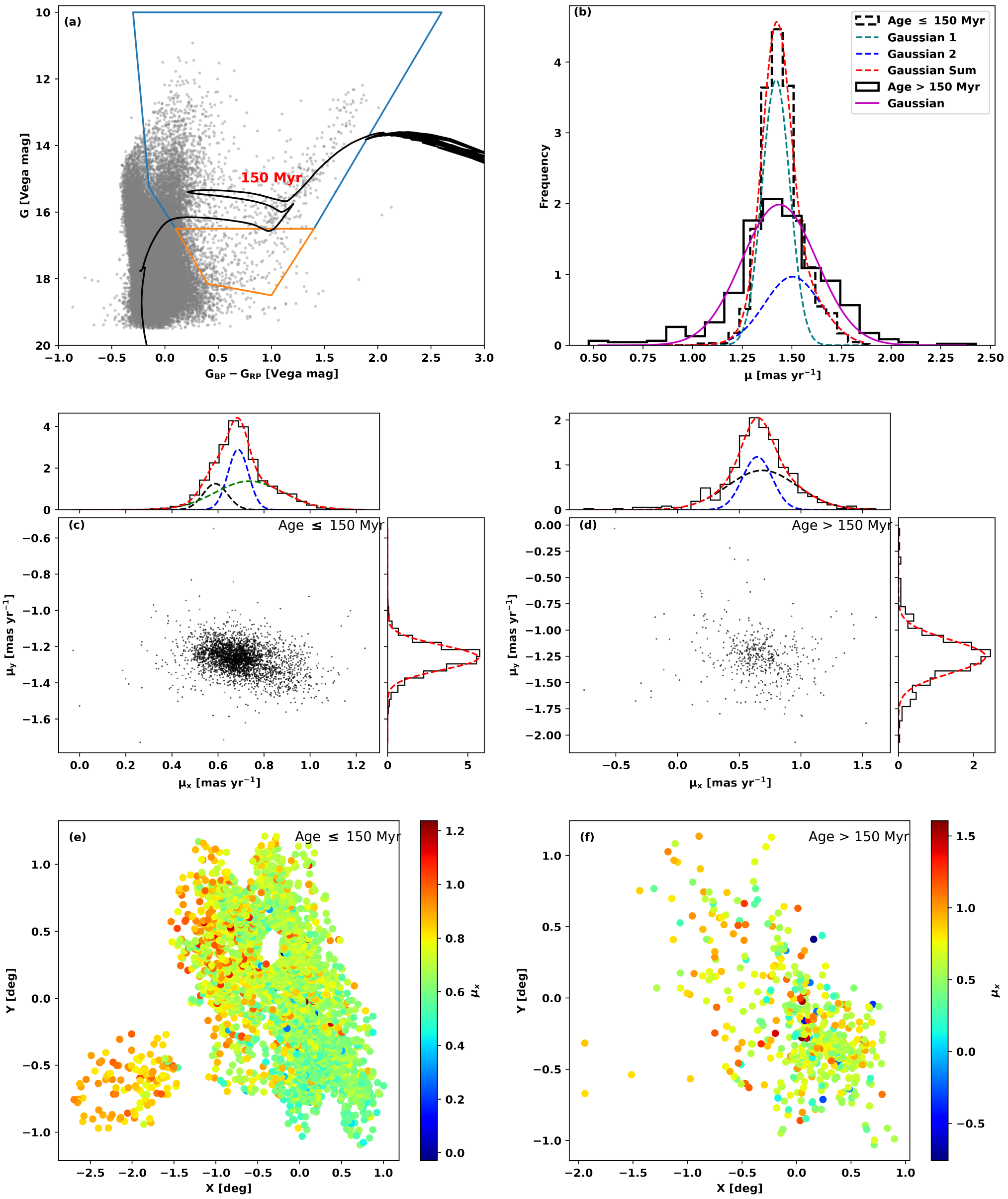

FIGURE 3.15: (a) BL stars on the optical CMD. Blue and orange polygons denote the BL stars with age ≤ 150 Myr and > 150 Myr, respectively. (b) Gaussian curve fits the PM distribution. (c) and (d) VPDs with PMRA and PMDec distribution at the top and right, respectively. (e) and (f) present the spatial distribution of PMRA of two BL sub-populations (age ≤150 Myr and > 150 Myr)

the Y2 population. In a study by Belcheva et al. (2011), iso-density contour maps were used to analyze the morphology of different populations of the MCs. Their spatial distribution for the young stars (see their Figure 4) of the SMC is similar to our result. We also note a shell-like structure at $\sim(-0.8, 0.25)$ deg towards the SMC Wing (Figure 3.8) that is already mentioned by Maragoudaki et al. (2001).

The surface density of the SMC, as well as that of all four young populations, depict a broken young bar which shows a discontinuity in density at $\sim(-0.5, 0.5)$ deg (see Figure 3.8 & 3.9). The presence of the broken bar has previously been reported by DL2019, (see their Figure 6) and they mention the bending of the bar by about ∼30 deg to the east. In the density distribution of the BL stars, we note a denser region towards the SW of the bar, which is also found in the density distribution of the supergiant and giant stars by DL2019. Cioni et al. (2000) also found an asymmetric distribution of the younger populations (main sequence and supergiant stars) with protuberance.

In this study, we find that the eastern region and the northeastern regions are mainly populated by Y1, Y2, and Y3. The central region predominantly has the Y2 and Y3 populations, whereas the SW has BL stars, Y2 and Y3. These can be used to trace the recent star formation history of these regions (age $<$ 400 Myr) and study stars of various mass, age, and evolutionary phases.

This catalog has stars up to a mass of ∼30 to 45 $M_\odot$ (photometric mass obtained from a 1 Myr Padova-PARSEC isochrone (Bressan et al. 2012) using a distance modulus of $m-M = 18.96$, (G2015) and a metallicity of $Z = 0.002$ dex (Lemasle et al. 2017)) corresponding to an FUV magnitude of ∼13.2. Here, we have used the extinction law from Cardelli et al. (1989); Gordon et al. (2024), R_V value of 3.13 (Gordon et al. 2024) and a range of color excess values; $E(B-V) = 0.05$ (mean value; Haschke et al. 2011) and 0.1 (a higher value around OB stars; Gordon et al. 2024). As massive stars ($M > 8\ M_\odot$) are likely progenitors of supernovae, we show the spatial distribution of stars brighter than 15 mag in FUV corresponding to a mass of ∼8 $M_\odot$ as shown in Figure 3.14. The spatial distribution of these massive stars (∼2200) is similar to the distribution of Hα of the SMC (Gaustad et al. 2001; McClure-Griffiths et al. 2018). These are the sites of high-mass star formation in the inner SMC. These FUV bright stars, as well as their location, will be of interest to various ongoing studies such as binary at low metallicity by Shenar et al. (2024b), B-type supergiants by Parsons et al. (2024) and many other studies of massive stars.

The PMRA and PMDec values estimated for the young populations are well-matched with the previous studies (Costa et al. 2009; van der Marel & Sahlmann 2016; Zivick et al. 2018; Niederhofer et al. 2021). From the PMRA distribution, we found that Y1 and BL stars have two types of sub-populations, which are mainly located in the east and NE direction of the SMC (see Figure 3.11, 3.13). However, the width of the PM distribution of both populations are relatively low, indicating that these sub-populations are relatively undisturbed (as seen in Figure 3.10 and Table 3.4). We also note an increase in PMRA (not found in PMDec) for BL and Y1 populations in the eastern SMC. A similar pattern in the PM of young stars in the SMC was reported by Niederhofer et al. (2021). However, our findings confirm that this stretching in PM is predominantly due to the motion of young stars in the RA direction. Additionally, De Leo et al. (2020), in their analysis (see Figure 10), also observed increased PMRA values for RGB stars in the eastern region of the SMC. Murray et al. (2019) identified a similar gradient in the residual PM of 143 massive stars, whose radial velocities are aligned with HI gas peaks. A recent study by Almeida et al. (2024) found a similar pattern in the radial velocity and proper motion of RGB stars. The study suggests that stars located on the eastern side of the SMC are part of material pulled out from the central SMC due to its tidal interaction with the LMC. However, these higher PMRA values are found within the 2 deg of the SMC, and hence unlikely to be connected to the foreground population found by Omkumar et al. (2021) and James et al. (2021) (using RC and RGB tracers, respectively) in the east of the SMC beyond 2 deg from the SMC center. Overall, our result, the PMRA gradient observed in the Y1 and BL populations, indicates that stars younger than 250 Myr are being stretched towards the LMC, likely as a consequence of the recent LMC-SMC interaction.

In order to check whether we can trace the impact of the recent LMC-SMC interaction at 150–300 Myr ago (Irwin et al. 1985; Besla et al. 2012; Choi et al. 2022) in the motion of the young population, we overlaid a 150 Myr Padova-PARSEC isochrone (Bressan et al. 2012) considering a distance modulus of m−M = 18.96 (G2015) on the Gaia optical CMD as shown in Figure 3.15(a), to separate populations born before and after the interaction. We can see that BL stars have both types of populations: (1) before interaction (age $\leq$150 Myr) and (2) during/after the interaction (age $>$ 150 Myr). From the Gaussian curve fit to the PM distribution of these two populations of BL stars as shown in Figure 3.15(b), we determined the peak and sigma values as follows: for the BL population with age $\leq$150 Myr, (μ_1, σ_1) = (1.420±0.002, 0.070±0.003) and (μ_2, σ_2) = (1.504±0.024, 0.142±0.011) and for the BL population with age $>$ 150 Myr, (μ, σ) = (1.436±0.010, 0.189±0.010). BL stars with age $\leq$150 Myr show a peaked narrow distribution that has contributions from two populations with different transverse motions. The broader distribution of the above two appears to be similar to that of BL population with age $>$150 Myr. Since the number of stars of the older BL population is not statistically significant, we will not discuss this population further but provide its VPD as shown in Figure 3.15(d). Peak and standard deviation of PMDec distribution for the two BL populations with age $\leq$150 Myr and $>$ 150 Myr are (−1.260±0.002, 0.067±0.002) and (−1.252±0.006, 0.157±0.006), respectively. The Gaussian curve fits for PMRA distribution to these are listed in Table 3.5. We note from PMRA distribution as shown in Figure 3.15(c) that BL stars younger than 150 Myr have three sub-populations with slightly different peaks and widths in PMRA (Table 3.5). We checked the spatial distribution of PMRA of the BL stars (age $\leq$150 Myr and $>$150 Myr) as shown in Figure 3.15(e) & (f). We found that there is a gradient in PMRA for the BL stars with age ≤150 Myr, unlike the older BL stars. The gradient in PMRA is in the direction from SW to NE and east. We already found that the Y1 population that is also formed after the recent interaction shows a very similar kinematic signature. We conclude that the younger sub-population of BL stars and the Y1 population bear the kinematic signature of the recent LMC-SMC interaction. This signature is in the PMRA distribution and we do not detect any perturbation in the PMDec distribution. This is an important pointer that can constrain the models of LMC-SMC interaction.

Four regions of the SMC (bar) were observed by the UIT[¶] (Cornett et al. 1997). We have cross-matched the UVIT catalog with the UIT catalog (FUV: 1620 Å) of the SMC with search radii of 2″ and 1″(spatial resolution of UIT is 3″) and found ∼1700 and ∼550 common sources, respectively. Figure 3.16 shows the relation between the UVIT (AB magnitude) and UIT (Vega magnitude), and their fluxes are found to be well matched in a study by Subramaniam et al. (2016b). Cross-matching the common sources with the SIMBAD database revealed that many of these sources are eclipsing binaries, emission line stars etc., and are marked in Figure 3.16. Differences in the magnitudes between the two catalogs arise mainly from the magnitude system, along with variations in filter wavelengths and widths, the spatial resolution of UVIT and UIT, and the variable nature of some sources. In addition, we cross-matched the UVIT catalog with the Swift/UVOT catalog (Ludwig et al. 2026) and identified ∼52,253 sources in common. Comparing the UVIT FUV magnitudes with the UVOT UVW2 (192.8 nm) magnitudes in the AB system, we find a small offset of ∼0.2 mag, which is likely to be due to a difference in the effective area for this filter between the two systems and lies within the photometric uncertainties, indicating good agreement between the two datasets.

The SMC FUV sources are younger than 400 Myr (H24a). Various studies have indicated that massive stars are often found in binary or higher multiple systems

---

[¶] Of the four UIT fields, three overlap with UVIT fields, while one lies in a gap within the UVIT observed area.

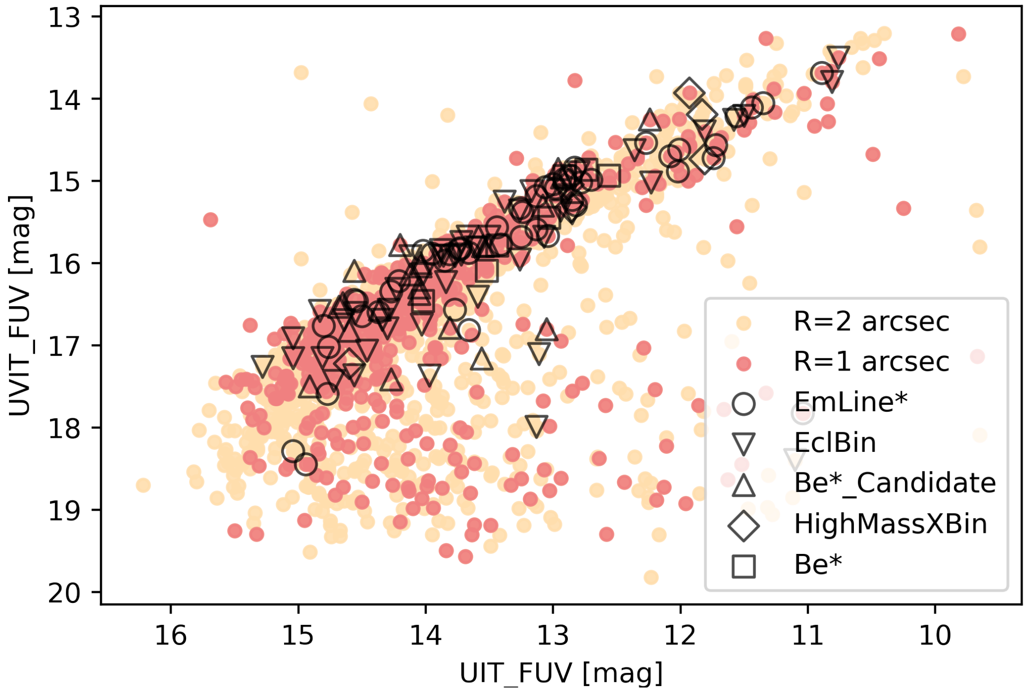

Figure 3.16: UVIT and UIT FUV magnitudes of common sources (for search radii of 2″ and 1″). Different markers represent UVIT-UIT-SIMBAD stars classified as emission-line stars, eclipsing binaries, Be star candidates, high-mass X-ray binaries, and Be stars.

(Mason et al. 1998; García & Mermilliod 2001; Sana et al. 2014; Moe & Di Stefano 2017). It is estimated that approximately 70% of close binary systems (Sana et al. 2012; Kobulnicky et al. 2014) are likely to interact, impacting stellar evolution, apart from leading to the end stages of a massive star, such as a supernova explosion (Podsiadlowski et al. 1992; de Mink et al. 2013; De Marco & Izzard 2017). They also have the potential to form double compact object binaries (Marchant et al. 2017). In our future work, we plan to identify binaries through multi-band photometry and characterize them, apart from estimating the properties of single stars. The catalog presented in this work will be a very useful resource to study the FUV properties of various exotic populations such as the high-mass X-ray binaries, Wolf-Rayet stars, O/B emission line stars, Be-X ray binaries, etc. This photometric catalog will also be quite a useful resource to plan photometric/spectroscopic observations of future space-based observatories, such as UVEX

(Ultraviolet Explorer; Kulkarni et al. 2021) and INSIST (INdian Spectroscopic and Imaging Space Telescope; Subramaniam 2022; Sriram et al. 2023).

3.7 Summary and Conclusions

In this study, we present a FUV catalog of the SMC obtained using the UVIT/ AstroSat, based on observations of 39 pointings of UVIT in the filter F172M. The catalog contains ∼76800 sources along with their IDs in Gaia and VMC. This catalog will be an excellent resource for various studies of young and massive stellar populations in the SMC. We also provide the data completeness as a function of magnitude for the observed regions.

Applying different classification methods to get the most probable SMC stars, we found that RUWE constraint is required for better MW decontamination. We adopt the Truncated-Optimal NN of Jiménez-Arranz et al. (2023) and RUWE<1.4 cutoff to identify the probable SMC population consisting of 62901 stars. The spatial as well as kinematical properties of this population, as found in this study, are summarized below:

- FUV stars in the catalog are mainly main sequence, giant, and subgiant stars as found from the CMDs (Gaia optical, FUV–optical, and VMC IR CMDs).
- There are about ∼2200 stars that are brighter than 15 mag in FUV, corresponding to a photometric mass of $M > 8M_{\odot}$. The catalog is therefore an important resource to study massive stars in low metallicity environments.
- Stellar surface density distribution is found to be clumpy. The distribution traces three morphological features such as the inner SMC Wing, a broken

bar, and a shell-like structure. We also find a high concentration of FUV stars in the SW of the bar.

- The morphology as a function of stellar population is studied through KDE plots. From the KDE plots of Y1, Y2, Y3, and BL stars, we find that the morphology varies with population. The density distribution of Y2 has a close resemblance to the overall density while Y1 and BL stars are concentrated at the NE and SW of the bar, respectively. The densest regions of Y3 are located in the northeast and at the central part of the bar.

- The kinematic properties of the above population suggest that all populations show two kinematically distinct sub-populations. The Y2 and Y3 show a kinematically cool, less dispersed (with a narrower width in the PM distribution) and a hot, highly dispersed (with a broad PM distribution) sub-populations, whereas the Y1 and BL stars show kinematically distinct two cool populations.

- The VPDs suggest that the kinematically distinct sub-populations of Y1 and BL stars differ in PMRA, but have similar PMDec distribution. The spatial distribution of PMRA of Y1 and BL stars show a gradient with increasing towards the eastern SMC, mainly located in the shell-like structure (east) and the NE part of the bar.

- The kinematic analysis of this study points to a specific disturbance for stars younger than ∼150 Myr in the PMRA, with no significant disturbance in the PMDec. This can place strong constraints on the details of the recent LMC-SMC interaction.

- The probable SMC members (∼62900) with FUV magnitudes will be very useful to the study of massive young stars in the low metallicity and kinematically perturbed environment of the SMC.

Chapter 4

Turbulence Regulated Hierarchical Star Formation in the SMC*

"Do not look at stars as bright spots only. Try to take in the vastness of the universe." — Maria Mitchell

4.1 Introduction

Star formation across different scales in galaxies reveals a remarkable structural pattern. Rather than forming solely in isolated environments, stars often emerge in a wide range of configurations—from bound clusters and loose associations to extensive complexes that span kiloparsec scales. Particularly, young stars (ages $\lesssim$100 Myr) tend to trace spatial distributions that mirror the fractal structures

---

*This chapter is based on the work published in *The Astrophysical Journal*, **989**, 216 (2025), Hota et al., 10.3847/1538-4357/adec84 of the ISM (e.g., Gouliermis et al. 2015), (S2018),(Miller et al. 2022, hereafter M2022). Both observations and numerical simulations consistently support the idea that the morphology of young stellar populations reflects the underlying turbulent gas from which they form (Elmegreen & Falgarone 1996; Elmegreen & Elmegreen 2001; Vázquez-Semadeni et al. 2017).

In the SMC, early studies identified tens of stellar associations with typical sizes around 70–90 pc (e.g., Hodge 1985; Battinelli 1991), comparable to those in the LMC but smaller than those in larger spiral galaxies like the MW or M31. Subsequent studies employing statistical tools, such as the two-point correlation function and minimum spanning trees, have revealed that younger populations in the SMC ($\lesssim$10–30 Myr) show significant substructure, which gradually becomes smoother with age (Gieles et al. 2008). This age-dependent erasure of structure is consistent with hierarchical star formation regulated by dynamical evolution and turbulence-driven fragmentation of the ISM (Bonatto & Bica 2010), (S2018; M2022). These works collectively support a picture where supersonic turbulence plays a dominant role in shaping the star-forming structures across scales, leading to mass and size distributions that follow power laws, indicating scale-free processes. More recently, Miller et al. (2024) developed a novel automated technique for detecting and characterizing semi-resolved star clusters, where the PSF is smaller than the cluster size but larger than typical stellar separations. This method is well-suited for studying resolved structures in nearby galaxies. Applying it to a 1.77 deg^2 area in the LMC, they identified 682 cluster candidates.

In this chapter, we analyze the hierarchical distribution of young massive stellar populations in the SMC using the FUV catalog developed as discussed in Chapter 3. To identify overdensities associated with young stars, we apply a contour-based surface density map analysis developed by Gouliermis et al. (2015, 2017), which allows us to trace structures across a range of significance levels. Throughout this study, we refer to all identified groupings, whether clusters, associations, or larger complexes, collectively as young stellar structures, without distinguishing between their subtypes. The primary goal is to characterize the clustering properties, spatial distribution, and structural hierarchy of young massive stars in the SMC and explore how these relate to large-scale star formation processes. The chosen sample for this work and methods of detecting young stellar structures are detailed in section 4.2. section 4.3 focuses on the properties of the identified structures, including their sizes, perimeters, areas, stellar content, and surface densities. In section 4.4, we interpret the results in the context of hierarchical star formation and compare them with findings from other galaxies and the caveats of this study. Concluding remarks are provided in section 4.5.

4.2 Sample and Methodology

4.2.1 Sample

In our study, we use the UV point-source catalog of the SMC compiled in the previous Chapter (see Table 3.1), obtained from 39 fields across the SMC observed by the UVIT (Tandon et al. 2017a) onboard AstroSat. We have considered only the ∼62,900 most probable SMC FUV stars (see the final column of Table 3.1) with Gaia DR3 counterparts that meet the following criteria: (i) RUWE < 1.4 (Lindegren et al. 2018), (ii) a classification probability greater than 31%, which indicates the likelihood that a source is a member of the SMC, and (iii) $G < 19.5$ mag (criteria (ii) and (iii) were obtained from Jiménez-Arranz et al. 2023). These criteria were adopted to exclude foreground stars. Detailed information regarding foreground decontamination can be found in section 3.2.4.

Since our method for identifying young structures depends on their surface density, a high completeness level of our sample of FUV stars is essential. In Chapter 3,

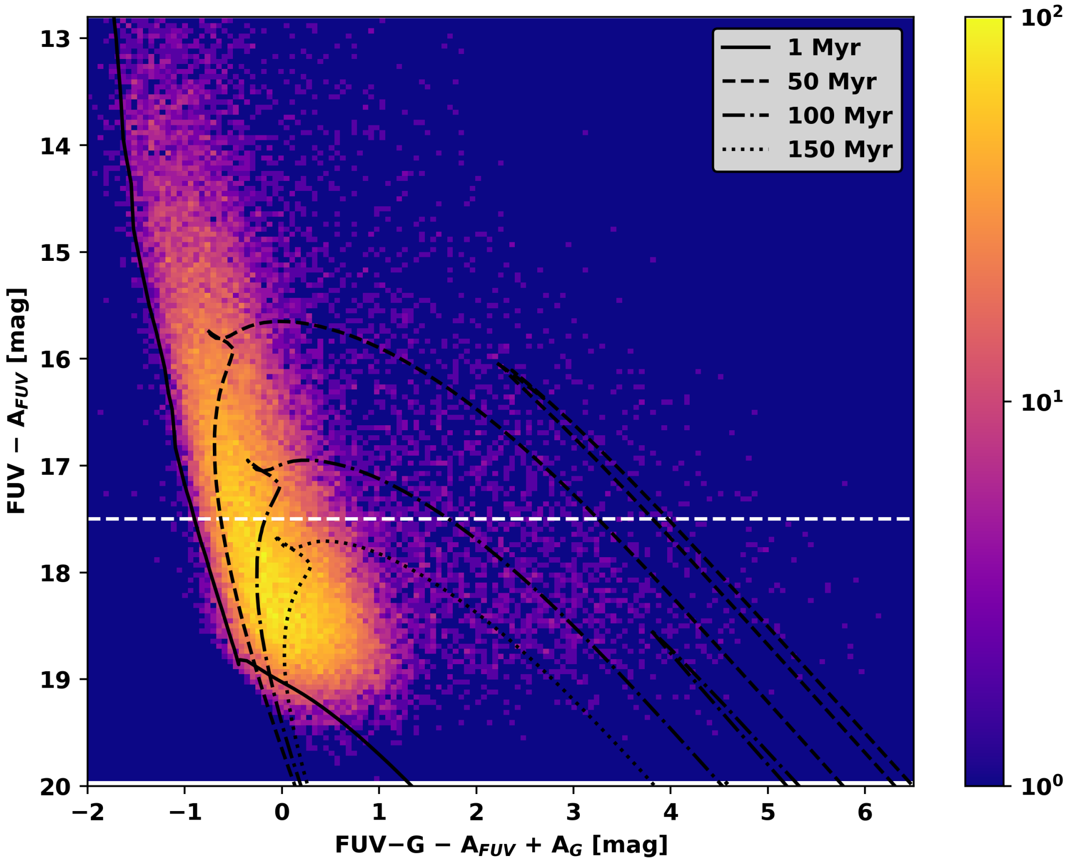

FIGURE 4.1: FUV–optical color–magnitude Hess diagram of the most probable FUV stars (∼62,900) in the SMC. The color bar represents the number of stars in each color–magnitude bin. The white dashed line represents our FUV magnitude cut-off at 17.5 mag.

we performed an FUV completeness check of the catalog by conducting ASTs. We achieved a recovery rate of approximately 90% for stars with FUV magnitudes up to 18 mag, increasing to 100% completeness at 16 mag (refer to Figure 3.2). In this work, we selected FUV stars brighter than 17.5 mag, a limit at which the completeness exceeds 90%, resulting in a sample of about $N \simeq 20,800$ stars. We verified the results using different magnitude cut-offs from 16.0 to 18.0 mag, in steps of 0.5 mag: see section 4.4. The mass range extends from 5 to 40 $M_{\odot}$, corresponding to FUV magnitudes between 18 and 13.3 mag, as derived from isochrone-based photometric mass estimates.

Figure 4.1 shows the FUV—optical CMD for about 62,900 SMC FUV stars. The

FUV and G magnitudes have been corrected for extinction using an average color excess of $E(B-V) = 0.05$ mag (Haschke et al. 2011; Skowron et al. 2021), adopting the extinction laws of Cardelli et al. (1989) and O'Donnell (1994), and $R_V = 3.1$ (Girardi et al. 2008; Gordon et al. 2024). The Padova group's PARSEC isochrones (v2.0; Bressan et al. 2012) for ages of 1, 50, 100, and 150 Myr, assuming a distance modulus of $m - M = 18.96$ mag (G2015) and a metallicity of $Z = 0.002$ (Lemasle et al. 2017) are overlaid on the FUV–optical CMD. We note that FUV stars brighter than 18 mag are younger than 150 Myr, and these stars are primarily O- and B-type main sequence stars, as well as giants. Therefore, the stars selected for this study with FUV magnitudes brighter than 17.5 mag are younger than 150 Myr.

4.2.2 Surface density distribution

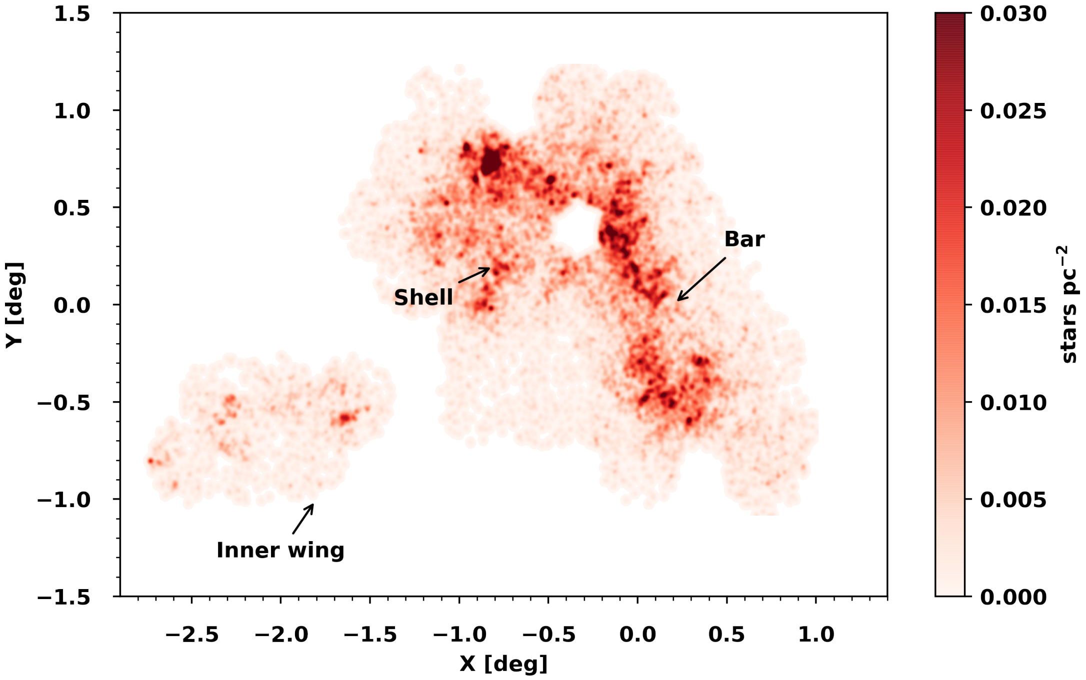

FIGURE 4.2: Surface density map (KDE) of the SMC. The color bar represents the number of stars pc^{-2}. The bar, shell, and inner wing of the SMC are marked with black arrows. XY are the projected coordinates, with the optical center at $\alpha_{\rm SMC} = 00^{\rm h}52^{\rm m}12^{\rm s}.5$, $\delta_{\rm SMC} = -72°49'43''$ (J2000; V1972).

The SMC's spherical coordinates were projected onto the XY plane using the zenithal equidistant projection method, adopting the X and Y conversions given by M2001. The optical center of the SMC was taken at $\alpha_{\mathrm{SMC}} = 00^{\mathrm{h}}52^{\mathrm{m}}12^{\mathrm{s}}.5$ and $\delta_{\mathrm{SMC}} = -72°49'43''$ (J2000; V1972). To analyze the surface density distribution of our selected sample (FUV magnitudes < 17.5 mag), we employed KDE. This method entails creating a two-dimensional binned map of the selected sample by smoothing the positions of stars with a Gaussian kernel. The kernel width was selected according to the spatial scale of interest. While a narrow kernel highlights finer structures at the expense of increased noise, a broader kernel suppresses noise but smooths out details. We experimented with kernel widths ranging from 5 to 15 pc and found that 10 pc offers an optimal balance between noise reduction and structural preservation. Further justification for adopting a kernel width of 10 pc is provided in section 4.4.4. The same kernel size has been used in previous studies of the MCs (Sun et al. 2017a,b), (S2018; M2022). In the KDE map, there is a gap at $(\alpha,\delta) \equiv (14°, -72.5°)$ where UVIT data are unavailable (H24b).

From the KDE map of the selected sample (age $\leq$150 Myr; Figure 4.2), we note the broken bar, which extends in the northeast–southwest direction across the SMC (H24b; Sewiło et al. 2013), (DL2019), a shell-like structure (Maragoudaki et al. 2001, H24b), and the inner SMC Wing (Zaritsky et al. 2000; Cioni et al. 2000; Sewiło et al. 2013; Oliveira et al. 2023). The overall surface density distribution of the selected SMC sample is irregular and clumpy (e.g., Zaritsky et al. 2000; Cioni et al. 2000; Sewiło et al. 2013, H24b, H24a), (DL2019). The median, mean, and standard deviation of the KDE surface density are 0.00008 stars pc^{-2}, 0.002 stars pc^{-2}, and 0.005 stars pc^{-2}, respectively. These values are consistent with those found by S2018 and M2022 for the SMC and LMC, respectively, using VMC data. Our identification and analysis of young structures is based on this surface density map.

4.2.3 Detection of young stellar structures and their parameters

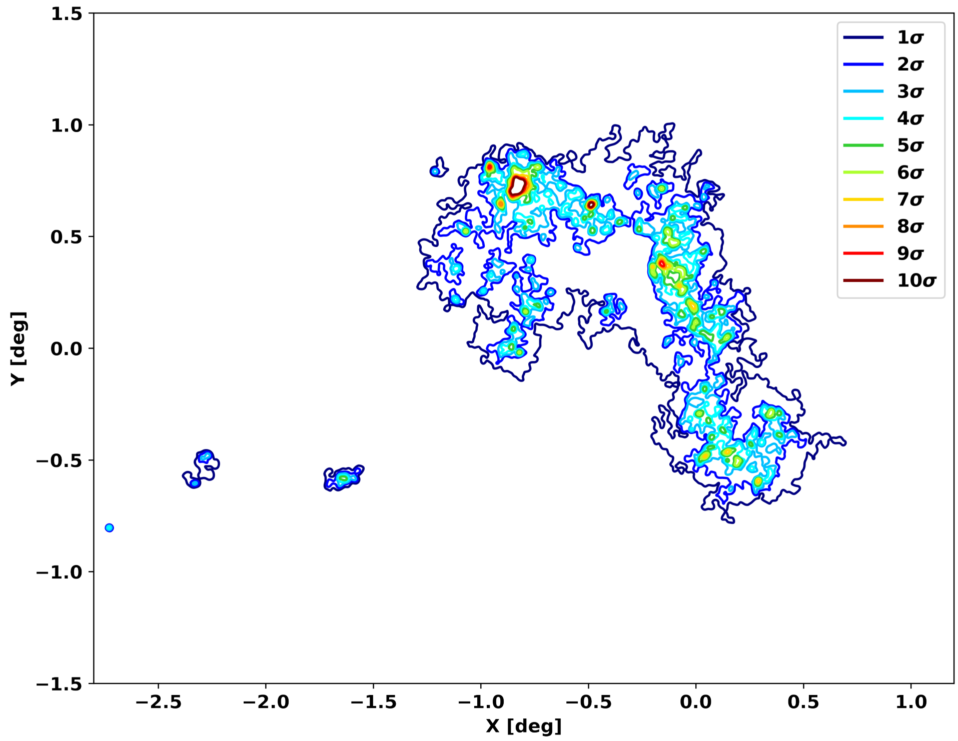

FIGURE 4.3: Detected young stellar structures colored by their significance levels.

To identify young stellar structures (hereafter YS structures) in the SMC's surface density map (Figure 4.2), we applied a contour map-based technique (Gouliermis et al. 2015, 2017). This technique uses estimates of surface overdensities across a range of significance levels (n times the standard deviation of the surface density from the KDE map, σ, where n is an integer) to detect YS structures. In our work, a range of significance levels, from 1σ + the median value of the KDE density to 10σ + the median value of the KDE density, in equal steps of 1σ (where $\sigma = 0.005$ stars pc^{-2}) was used to obtain the isodensity contours in the KDE map. Note that the median value of the KDE map is significantly smaller than the standard deviation in all less populous regions. At each significance level, any isodensity contour enclosing an overdensity is classified as a candidate young stellar structure, with the contours delineating their projected boundaries. Using this method, we detected approximately 370 YS structures of all kinds.

In the next step, we estimated the physical parameters of the detected YS structures. The radius of a stellar structure (R) was determined by the radius attained by a circular area equivalent to the projected boundary. The total number of stars within a structure was estimated by the number of stars of the selected sample (N) within the boundary. The surface density of a structure was estimated by computing the ratio of the number of stars within its boundary to the area of the structure, using $\Sigma = \frac{N}{\pi R^2}$.

There is a possibility that some of the structures identified may be spurious detections. To address this potential concern, we applied two additional criteria adopted from previous studies (S2018; M2022): (1) a genuine structure must contain a minimum number of stars ($N_{\rm min}$), and (2) structures at the 1σ and 2σ significance levels must enclose the contours of structures at higher significance levels (3σ to 10σ). The choice of $N_{\rm min}$ is arbitrary; a higher value helps to reject most unreliable structures but may also remove genuine ones, whereas a lower value may result in more unreliable detections. Therefore, we adopted $N_{\rm min} = 5$, following previous studies (Bastian et al. 2007, 2009; Gouliermis et al. 2017; Sun et al. 2018; Miller et al. 2022), to reduce contamination by spurious structures while retaining physically meaningful groupings. We also tested the robustness of our results for $N_{\rm min} = 3$ and 4, as discussed in Section 4.4.1 Following application of these two criteria, we retained a total of 236 YS structures: see Figure 4.3. This shows the non-uniform and hierarchical pattern of the detected YS structures in the SMC, which is similar to those in many star-forming regions and entire galaxies (Gouliermis et al. 2010, 2015; Gusev 2014; Sun et al. 2017b,a), (S2018; M2022). We emphasized the hierarchical pattern of the detected structures. Table 4.1 lists the details of individual structures across a range of significance levels; Table 4.2 summarizes the demographic data for the detected YS structures as a function of significance level.

TABLE 4.1: Details of the detected young stellar structures.

ID	Level (σ)	X (deg)	Y (deg)	RA (deg; J2000)	Dec (deg; J2000)	N	R (pc)	Σ (stars pc^{-2})
1	1	−2.345	−0.591	21.35	−73.26	31	17.06	0.034
2	1	−2.277	−0.520	21.09	−73.20	93	29.67	0.034
3	1	−1.643	−0.580	18.92	−73.33	152	34.64	0.040
4	1	−0.336	0.228	14.31	−72.59	15424	366.07	0.037

Note. This table includes the identification number (ID), significance level (σ), central projected coordinates (X and Y in degrees), celestial coordinates (RA and Dec in degrees; J2000), the number of stars (N) in each structure, radius (R in parsecs), and the surface density (Σ in stars pc^{-2}). Only the first four records are shown here as an example. Projected XY coordinates of the SMC are defined with respect to the galaxy's optical center at $\alpha_{\rm SMC} = 00^{\rm h}52^{\rm m}12^{\rm s}.5$, $\delta_{\rm SMC} = -72^\circ 49' 43''$ (J2000, V1972). The full table is available in MRT format at H25.

TABLE 4.2: Demographics of the detected young stellar structures at each significance level.

Level	$N_{\rm str}$ (No. structures)	$R_{\rm min}$ (pc)	$\langle R \rangle$ (pc)	$R_{\rm median}$ (pc)	$R_{\rm max}$ (pc)	$N_{\rm sum}$ (No. stars)	$\langle \Sigma \rangle$ (stars pc^{-2})
1	5	17.06	93.17	29.67	366.07	15734	0.035
2	19	8.33	35.14	19.00	175.37	10607	0.056
3	59	3.55	13.71	8.19	98.97	7275	0.083
4	60	2.46	11.52	8.49	47.96	4138	0.109
5	47	3.07	8.76	6.14	37.86	2258	0.140
6	24	2.34	8.23	7.59	31.51	1170	0.180
7	11	2.27	7.72	5.95	26.88	626	0.222
8	5	3.63	9.82	8.13	23.68	447	0.224
9	4	3.14	9.03	6.01	20.95	342	0.259
10	2	5.62	12.13	12.13	18.64	267	0.269

Note. This table presents the significance level (column 1), number of structures ($N_{\rm str}$), minimum size ($R_{\rm min}$), average size ($\langle R \rangle$), median size ($R_{\rm median}$), maximum size ($R_{\rm max}$), number of stars ($N_{\rm sum}$), and the average surface density ($\langle \Sigma \rangle$) of the detected YS structures at each significance level (columns 1 to 8).

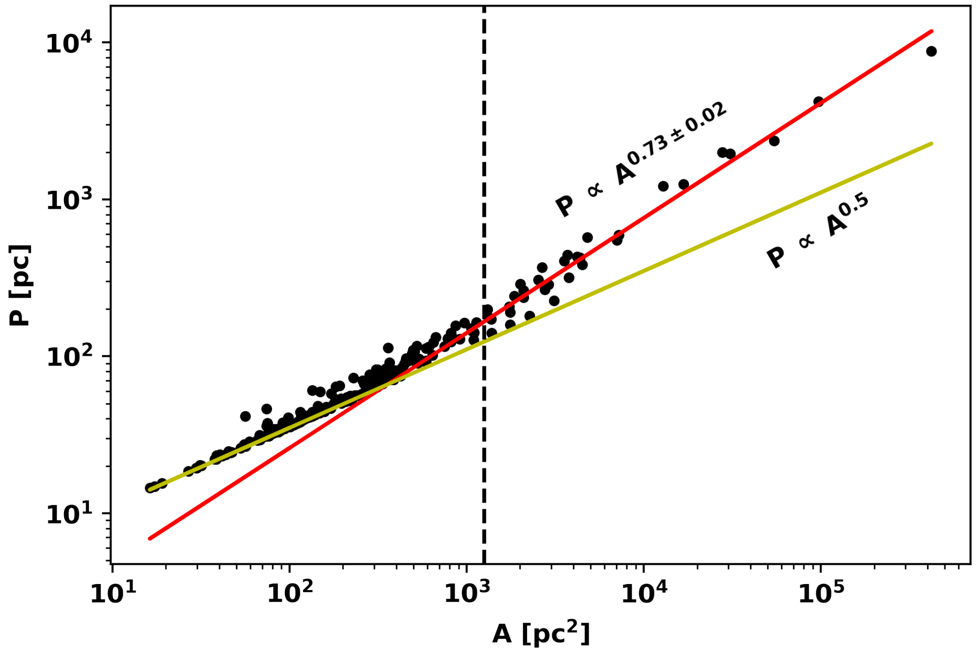

FIGURE 4.4: Perimeter vs. area of the detected young stellar structures. The black dashed line represents the area cut-off, $A_{20} \approx 1.3 \times 10^3$ pc^2, which corresponds to a size of $R = 20$ pc. For areas beyond this cut-off radius, the data is fitted with a single power-law function as indicated by the red solid line.

4.3 Results

4.3.1 Perimeter–Area relation

From the contour plot (Figure 4.3), we note that the boundaries of the detected YS structures are irregular. These irregularities in the morphology of the detected structures can be quantified by a perimeter–area relation. Figure 4.4 shows the perimeter (P) versus area (A) of the projected boundaries of the detected YS structures. Circular structures follow the perimeter–area relationship, $P \propto A^{0.5}$. We consider the area threshold A_{20} at $R = 20$ pc to be greater than the resolution of the KDE map (Figure 4.2), so that resolution effects become negligible. For an area $\leq$ the area at $R = 20$ pc ($A_{20} \approx 1.3 \times 10^3$ pc^2), the detected structures follow the circular perimeter–area relation shown by the yellow solid line in Figure 4.4. The data points above this cut-off ($> A_{20}$) follow the perimeter–area relation with a power-law slope of $\alpha = 0.73 \pm 0.02$ (the power-law slope was found by means of least-squares fitting) shown as the red solid line, while the area threshold, A_{20}, is represented by the dashed black line. The perimeter–area dimension, D_p, can be estimated using $P \propto A^{D_p/2}$ defined by Falgarone et al. (1991) for molecular clouds. For the observed YS structures, the perimeter–area dimension is $D_p = 2 \times \alpha = 1.46 \pm 0.04$. This value is considerably higher than the perimeter–area dimension of a circular (smooth) structure, which therefore quantitatively reflects the irregular shapes of the detected YS structures with R > 20 pc.

4.3.2 Number–Size relation

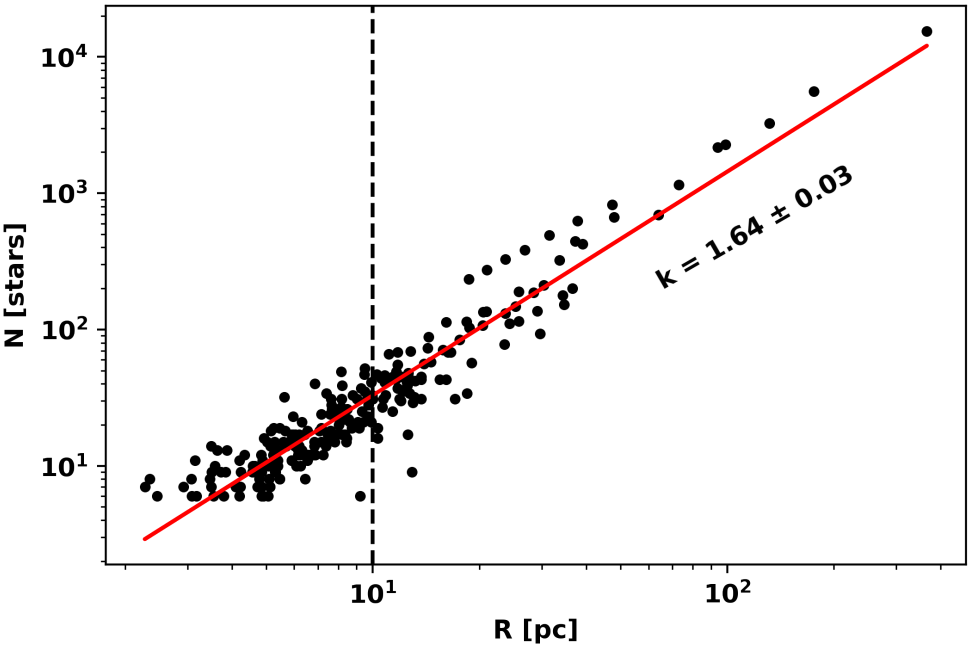

FIGURE 4.5: Number–size relation of the detected young stellar structures. The dashed line indicates the spatial resolution of the KDE (see Figure 4.2). The solid red line represents the best single power-law fit.

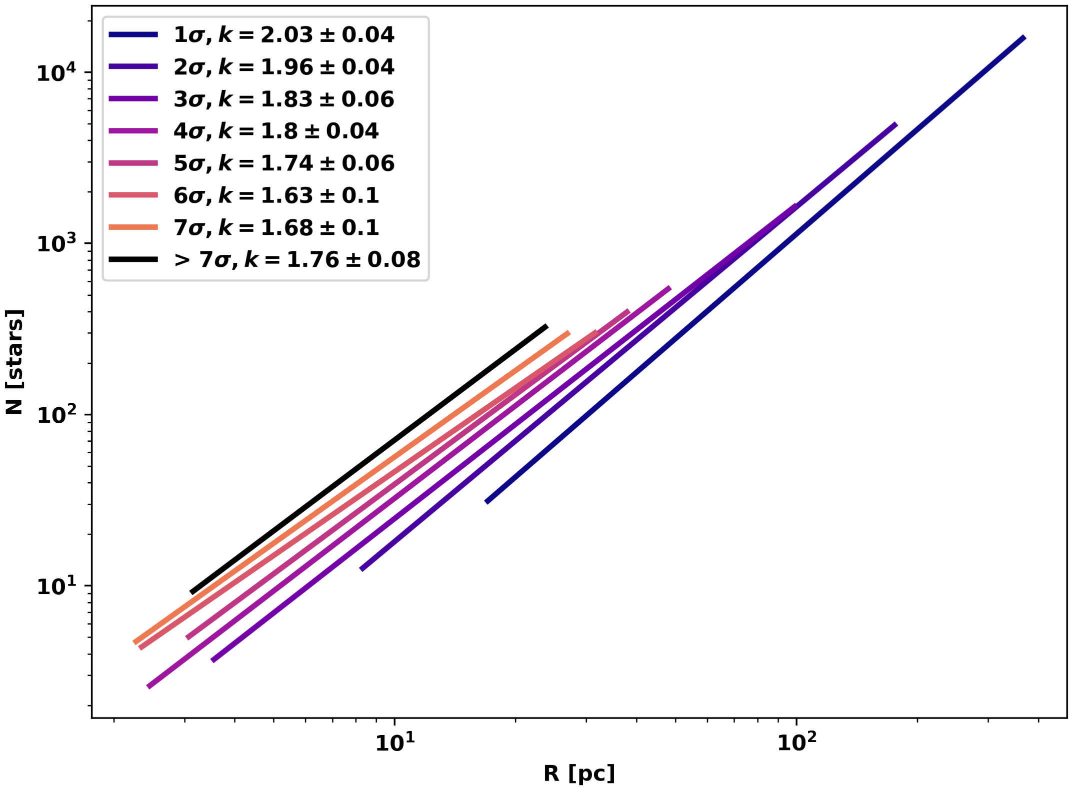

FIGURE 4.6: Power-law fits to the relationship between the numbers and sizes of the detected YS structures at different significance levels. Since the number of data points at significance levels $> 7\sigma$ is small, we combined all data points for significance levels 8–10σ.

Figure 4.5 shows the variation of the numbers of stars within the structures (N) as a function of the size of the detected YS structures. We estimate the best-fitting slope, using a least-squares fit, of $k = 1.64 \pm 0.03$. While UV observations are biased in favor of detecting young, massive stars, and the stellar initial mass function (IMF) is not fully sampled at this wavelength range, the number–size relation can still serve as a reliable proxy for the mass–size relation. This is because the mass—size relation of structures estimated using massive stars is expected to exhibit a similar slope to the mass—size relation derived for the total stellar population within the structures.

The mass–size relation for masses that are hierarchically clustered follows the relationship $M \propto R^{D_2}$ as given by Mandelbrot (1983). Here we want to mention that the 2D fractal dimension, D_2, is not the same as the perimeter–area dimension, D_p, and it does not explicitly depend on R, but rather reflects the scaling behavior of the spatial distribution of stellar structures across a range of sizes. Values of $D_2 < 2$ reflect a clumpy, self-similar distribution, while values approaching 2 correspond to a more uniform spatial distribution. The projected fractal dimension of the detected YS structures in this work is $D_2 = k = 1.64 \pm 0.03$. We have estimated the 2D fractal dimension by calculating the slopes of least-squares fits to structures at different significance levels: see Figure 4.6. In this figure, we display only the power-law fits. Because the number of points is limited to five or fewer, we used a single power law to describe the number–size relation for all structures with significance levels $> 7\sigma$ (i.e. 8σ to 10σ). Note that the slopes of the best fits, and consequently the fractal dimensions of the structures, vary from $D_2 = 1.6$ to 2.0 across significance levels. Feitzinger & Galinski (1987) showed that uniform artificial distributions, such as rhombic and quadratic patterns, exhibit fractal dimensions close to 2. In contrast, star-forming regions typically display lower fractal dimensions, ranging from 1.4 to 1.9. This implies that stellar structures with a fractal dimension near 2 have a uniform surface density, while those with lower fractal dimensions are marked by irregular, patchy distributions. The derived D_2 values, computed at various significance levels and for the entire sample, suggest that the structures exhibit non-uniform, clumpy distributions.

4.3.3 Size distribution

Figure 4.7 shows the distribution of the size of the detected YS structures. We note that the peak, mean, and median of the size distribution are at 5.6 pc, 14.6 pc, and 8.2 pc, respectively. As noted in section 4.2.2, structures with sizes smaller than 10 pc are not resolved, and statistical noise is evident in the size distribution,

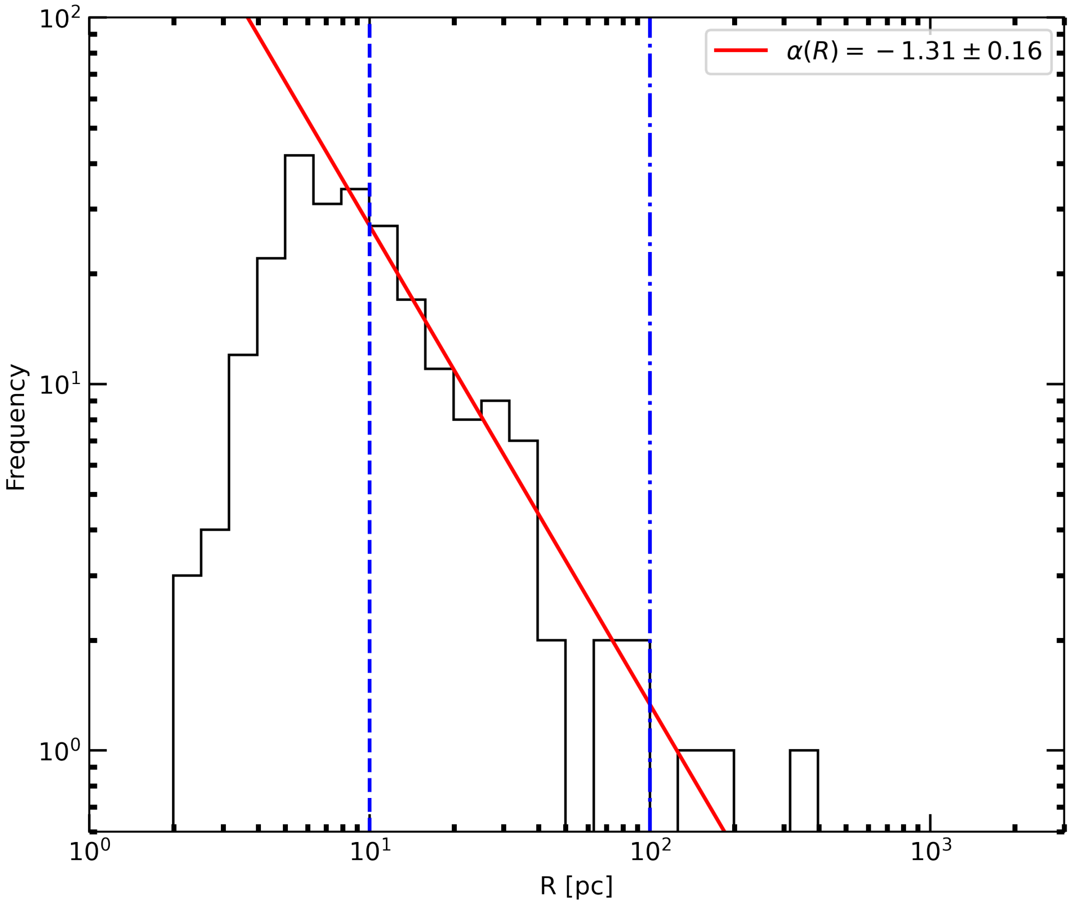

FIGURE 4.7: Distributions of size for the identified young stellar structures. The blue dashed lines indicate the range of data points used for power-law fitting, with the slope of the fit denoted by α.

particularly for larger sizes. Therefore, to fit a single power law, we selected the range from 10 pc to 100 pc in the size distribution of the detected YS structures. We performed a fit to the data within the range 10–100 pc, as shown by the red solid line in Figure 4.7, and estimated the best-fitting slope, $\alpha(R) = -1.31 \pm 0.16$. Substructures within a hierarchical system follow a cumulative size distribution,

$$N(> R) \propto R^{-D_2}, \tag{4.1}$$

where D_2 is the 2D fractal dimension (Mandelbrot 1983; Sun et al. 2017b,a), (S2018; M2022). Since Equation 4.1 represents a single power law, it is mathematically equivalent to a differential size distribution,

$$\frac{\mathrm{d}N}{\mathrm{d}\log R} \propto R^{-D_2}. \tag{4.2}$$

Equation 4.2 has the same functional form as the size distribution of the identified YS structures (Figure 4.7) within the size range of 10–100 pc. Consequently, these structures align with a 2D fractal dimension of $D_2 = -\alpha(R) = 1.31 \pm 0.16$, similar within 2σ to the D_2 value derived from the number–size relation (i.e. 1.64 ± 0.03, as discussed in section 4.3.2). We note that there are three structures with sizes of $100 < R < 400$ pc. We found their linear scales to be comparable to that of the main body of the SMC, consistent with S2018. This suggests that the spatial extent of the larger structures composed of young massive stars (5–40 $M_\odot$) identified in our study is similar to that of large-scale structures traced by low-mass young stellar populations (S2018). Structures located in the inner region of the SMC are less affected by external galactic processes—such as tidal forces and interactions with neighboring galaxies—compared with those in the outermost regions (De Leo et al. 2020; Dias et al. 2022). Hence, the larger, outer structures are more affected by such global processes, which likely contributes to their deviation from the power-law size distribution.

4.3.4 Number distributions

Figure 4.8 shows the number distribution of the detected YS structures. Here, we confirm that the number distribution is incomplete for smaller values (i.e. smaller numbers of stars). Based on Figure 4.5, we note that for $N \gtrsim 30$, the sizes correspond to $R > 10$ pc, i.e. there is a negligible effect of incompleteness in detecting YS structures for $N \gtrsim 30$. For $N > 1000$, we note the increased

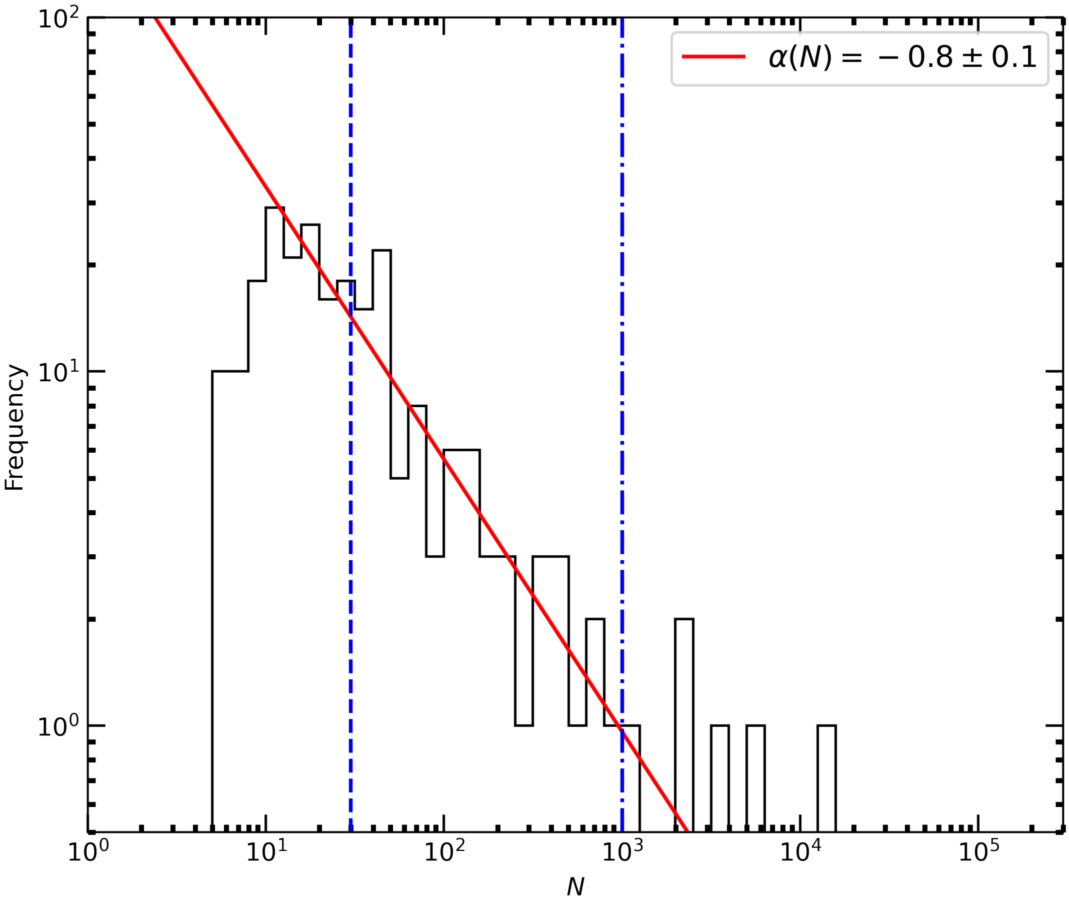

FIGURE 4.8: Distributions of numbers for the identified young stellar structures. The blue dashed lines indicate the range of data points used for power-law fitting, with the slope of the fit denoted by α.

statistical noise in the number distribution. That is the reason why we have fitted only a single power law in the range encompassing 30–1000 in the number distribution of the detected structures. If masses are arranged in a hierarchical pattern, their mass distribution will follow a single power law with a slope of -1 (Elmegreen & Falgarone 1996), (S2018; M2022). Similarly to section 4.3.2, the slope of the number distribution can serve as a reliable proxy for the slope of the mass distribution. From the best fits, we found a power-law slope of $\alpha(N) = -0.8 \pm 0.1$, which is close to the expected theoretical value. Five structures have $N > 1000$; they are not well-represented by the same power-law slope. Note that the two structures with the highest and second-highest N values have projected

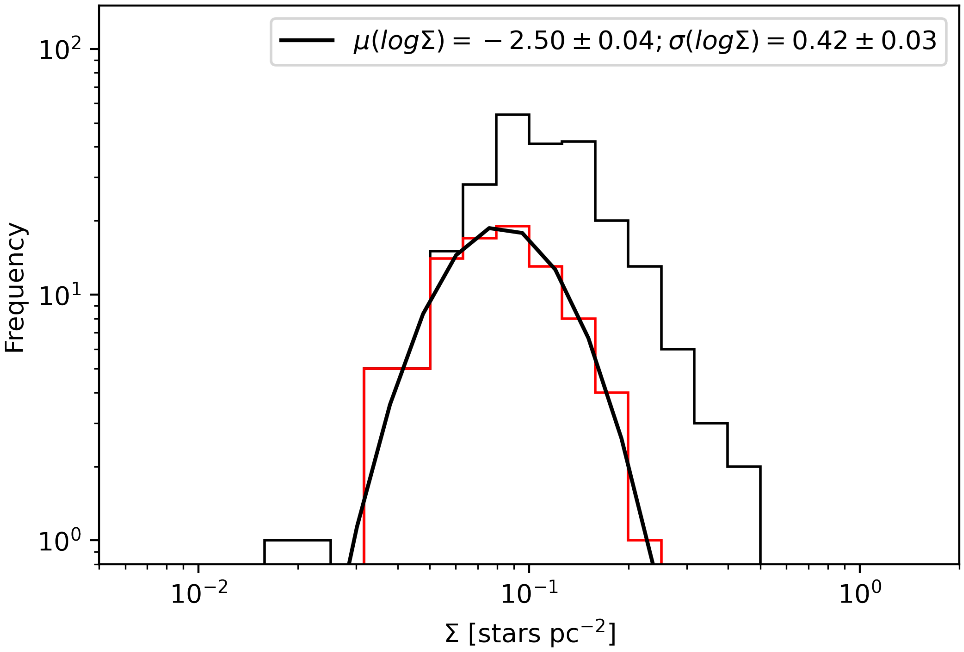

Figure 4.9: The surface density distribution, where the black histogram includes all data points, and the red histogram represents the distribution after applying constraints.

boundaries comparable in extent with that of the main body of the SMC, while the remaining three structures have sizes of nearly 100 pc. These two high-N structures are, therefore, more likely associated with galactic-scale processes rather than with sub-galactic hierarchical star formation (De Leo et al. 2020; Dias et al. 2022).

4.3.5 Surface density distributions

Figure 4.9 shows the distribution of the surface density of all detected YS structures, represented by the black histogram. Note that there are two structures with very low surface densities (below 0.03 stars pc^{-2}), which introduce statistical noise into the distribution. For this analysis, therefore, these two structures, along with those having a size of $R \leq 10$ pc, have been excluded. The distribution of the surface density for the remaining structures is shown as the red histogram in Figure 4.9. The structures considered follow a log-normal distribution in surface density, as shown by the solid black curve. The mean and standard deviation of the logarithm of the surface density are $\mu(\log\Sigma) = -2.50 \pm 0.04$ (stars pc^{-2}) and $\sigma(\log\Sigma) = 0.42 \pm 0.03$ (stars pc^{-2}).

4.4 Discussion

4.4.1 Impact of different constraints on the results

In this study, we compare the outcomes under varying conditions, such as for different magnitude cut-offs (which affect data completeness), populations characterized by different ages, and different number cut-offs for structure detection, with the results obtained for the sample with an FUV magnitude cut-off of 17.5 and $N_{\rm min}$. Figure 4.10 shows the slopes of the power-law relations obtained via least-squares fitting of the number distribution, size distributions, the perimeter–area and the number–size relationships, as detailed in sections 4.3.1, 4.3.2, 4.3.3, 4.3.4 and 4.3.5 under varying conditions. It also includes literature values for the LMC (M2022) and the SMC (S2018), as discussed in section 4.4.3. The dashed lines indicate the slopes derived for the sample in this study, using an FUV magnitude cut-off of 17.5 and a minimum count of $N_{\rm min} = 5$.

We first examined the impact of incompleteness by applying different magnitude cut-offs, ranging from 16 to 18 mag in steps of 0.5 mag, while retaining a constant number cut-off ($N_{\rm min} = 5$) for identifying YS structures. Here each FUV magnitude cut-off corresponds to a cumulative age threshold, with brighter limits selecting progressively younger populations. These cut-offs were primarily used to assess the effects of photometric incompleteness on the structure identification

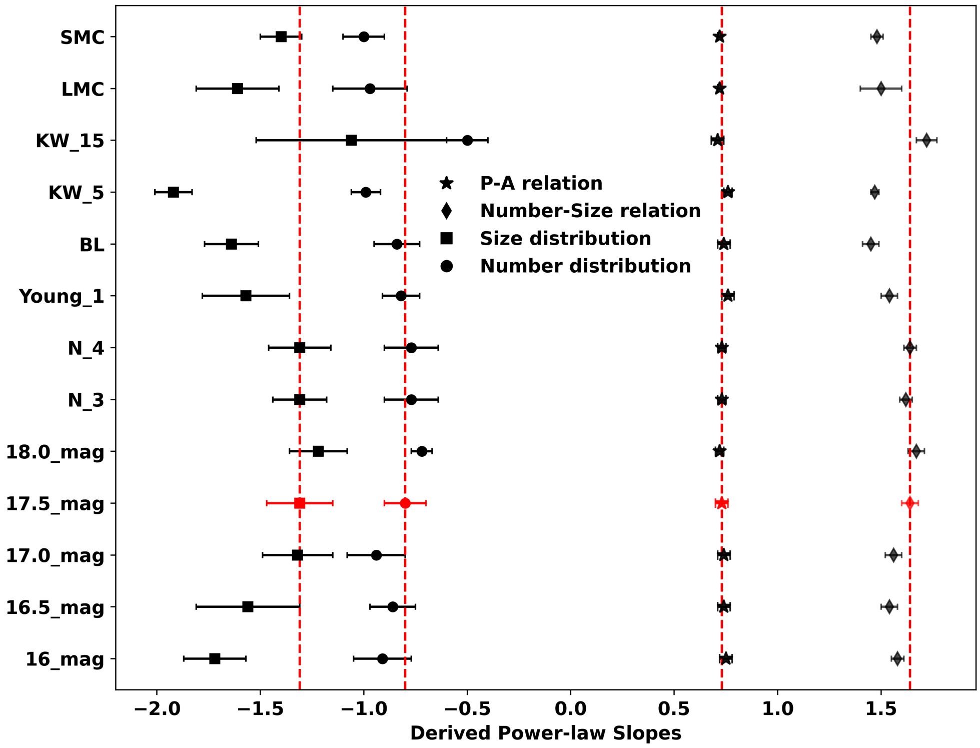

Figure 4.10: Comparison of the derived power-law slopes from the number–size, perimeter–area, and number–size relationships under varying constraints of kernel width (KW), N_{min}, magnitude cut-off, and different stellar populations. The x-axis represents the derived power-law slopes, while the labels 'LMC' and 'SMC' along the Y axis correspond to values from the literature; see M2022 and S2018, respectively. The red markers and red dashed lines both represent the slopes obtained for the adopted sample (FUV magnitude cut-off of 17.5 and $N_{\mathrm{min}} = 5$), shown for visual reference.

process. As shown in Figure 4.10, the slopes derived from the perimeter–area relations remain consistent within the uncertainties, and the slopes obtained from the size distributions, number distributions, and number–size relations all fall within the 2σ range of the slopes for the entire sample. These findings indicate that within a data completeness range of 90–100%, the hierarchical nature of the YS structures remains unaffected.

To eliminate spurious detections of YS structures, we established a minimum cut-off for the number of stars, denoted by N_{min}. A structure is considered genuine if it contains at least N_{min} stars. We set $N_{\mathrm{min}} = 5$. To explore the effects of a lower N_{min} value, which could introduce more noise, we also examined results with cut-offs of $N_{\mathrm{min}} = 3$ and 4, while keeping a magnitude cut-off of 17.5 mag. Our results, shown in Figure 4.10, demonstrate that the slopes of various relations and distributions remain consistent, indicating that $N_{\mathrm{min}} = 3$ is acceptable, since the effect of noise on the final results is negligible.

To examine how the fractal nature of young populations evolves with age, we analyzed two young stellar populations (Young 1 and Blue Loop; BL) spanning different age groups, identified from the G vs. $(G_{\mathrm{BP}} - G_{\mathrm{RP}})$ CMDs of G2021 and Chapter 3 (Figure 3.5(b)). Here, we did not consider the Young 2 and Young 3 populations, given that the majority of those stars are fainter than 17.5 mag. We note that the BL, younger than 200 Myr and Young 1 (age $\leq$ 50 Myr) populations include some stars with FUV magnitudes fainter than 18 mag; however, we have presented results for them without accounting for incompleteness effects. The derived slopes from the perimeter–area relation and number distribution fall within the uncertainties of our earlier results, as shown in Figure 4.10. Additionally, the fractal dimensions of the hierarchical structures derived from the number–size relation and the size distribution remain within the 2σ range. The Young 1 and BL stars show irregular morphologies and fractal characteristics. This indicates that the fractal nature of star formation remains present in the SMC for populations with mean ages as old as 200 Myr.

4.4.2 Similarities between the ISM and Young stellar structures

The YS structures and the ISM exhibit many notable similarities. The gas exhibits a hierarchical, self-similar morphology spanning a wide range of scales, from 0.1 pc to 1 kpc (Elmegreen & Scalo 2004; Bergin & Tafalla 2007; Sánchez & Alfaro 2008). The largest gas structures are comparable in size with the parent galaxy itself (Elmegreen 2000). In our case, the sizes of the YS structures range from a few parsecs to several hundred parsecs (see section 4.3.3 and Figure 4.5). The gas substructures exhibit irregular morphologies. The projected boundaries of these structures have been studied extensively using perimeter–area relations, including by Beech (1987); Falgarone et al. (1991); Vogelaar & Wakker (1994); Lee et al. (2016). The perimeter–area dimension (D_p) typically falls between 1.3 and 1.6 (Dickman et al. 1990; Hetem & Lepine 1993; Roman-Duval et al. 2010), and the value derived here, $D_p = 1.46 \pm 0.04$ (see section 4.3.1), also lies within this range.The D_p values obtained under different conditions, as discussed in section 4.4.1, also fall within the range found in the literature.

Turbulence significantly affects the hierarchical substructures within the ISM, acting as a key driver for the fragmentation of the ISM into increasingly smaller substructures and the formation of stars (Elmegreen & Scalo 2004; Pingel et al. 2018). Turbulence forms across a wide range of spatial scales and cascades down to the smallest scales, as evidenced by the fractal nature of the ISM (Elmegreen et al. 2001). On larger scales, turbulence is likely initiated by the accretion of circumgalactic material and gravitational instabilities (Krumholz & Burkhart 2016), whereas on smaller scales, energy is likely injected by stellar feedback mechanisms such as outflows and supernova explosions (Padoan et al. 2016). The HI gas in both MCs exhibits a fractal structure on galactic scales (Stanimirovic et al. 1999; Kim et al. 2003; Nestingen-Palm et al. 2017). Stanimirović & Lazarian (2001) analyzed HI data from the Australia Telescope Compact Array and the Parkes Telescope/Murriyang, examining the spectrum of intensity fluctuations in relation to the velocity slice thickness. Their results were consistent with the theoretical predictions of turbulence in the SMC by Lazarian & Pogosyan (2000). Thus, the pronounced density fluctuations of HI in the SMC result from active turbulence. Stanimirovic et al. (1999, 2000) estimated projected fractal dimensions of $D_2 = 1.4$–1.5 for the gas and dust in the SMC. These values are consistent with the fractal dimensions of our detected YS structures: $D_2 = 1.64 \pm 0.03$ from the number–size relation and $D_2 = 1.31 \pm 0.16$ from the size distribution (see Figure 4.5 and Figure 4.7). This study, therefore, supports a scenario of hierarchical star formation within a turbulent ISM, where the properties of the ISM are imprinted onto the youngest stellar structures across the scale. The striking similarities between the ISM and these stellar structures further indicate that dynamical evolutionary effects between the two are likely minimal. Hierarchical structures result from both top-down (fragmentation of molecular clouds) and bottom-up (energy injection from stellar winds and supernovae) mechanisms (M2022). Smaller structures reflect the fractal nature of molecular clouds, while larger ones align with the large-scale ISM shaped by supersonic turbulence.

The impact of turbulence aligns with the observed surface density distribution. Studies of molecular clouds reveal that those exhibiting a log-normal surface density distribution are primarily governed by supersonic turbulence (Padoan & Nordlund 2002; Elmegreen 2011; Gouliermis et al. 2017). Log-normal distributions have been identified in the column and volume densities of molecular clouds (Lombardi et al. 2010; Konstandin et al. 2012) as well as in simulations of turbulent gas (Klessen 2000; Federrath et al. 2010; Konstandin et al. 2012). Since star formation follows the gas distribution, YS structures are expected to exhibit a log-normal surface density distribution, consistent with our results discussed in section 4.3.5 and shown in Figure 4.10. In contrast, molecular clouds with a surface density distribution that exhibits a power-law tail are more strongly affected by self-gravity

(Klessen 2000; Federrath et al. 2010). However, note that the lack of a power-law tail in our size distribution may be caused by the limitations of our study, specifically by the minimum spatial resolution of our KDE map of 10 pc. This resolution limit might prevent us from detecting the effects of self-gravity, given that we are unable to resolve the smallest and densest structures (S2018; M2022).

4.4.3 Hierarchy in galaxies

Our analysis has shown that hierarchical substructures among young stellar populations in the SMC are preserved up to ages of ∼200 Myr (section 4.4.1), thus clearly extending the previously reported upper limit of ∼75 Myr by Gieles et al. (2008). This suggests a more prolonged dispersal timescale of stellar structures in the SMC than previously inferred. In our study, the size distribution yields a fractal dimension of $D_2 = 1.31 \pm 0.16$. This is consistent with the values reported for young clusters in the MCs by Bonatto & Bica (2010). Gouliermis et al. (2014) derived a fractal dimension of $D_2 = 1.2$–1.4 for NGC 346, a local star-forming region within the SMC, based on simulations, which is broadly consistent with our global estimate for the entire SMC.

S2018 applied a contour-based method to investigate the fractal nature of YS structures in the SMC using VMC data. They selected bright main sequence stars, 98% of which are younger than 200 Myr, and identified 556 structures—approximately twice the number detected in our analysis. This discrepancy primarily reflects the larger SMC area covered in their VMC-based study. Nevertheless, the slopes of the perimeter–area relation and the number distribution are consistent within the uncertainties, and the derived fractal dimension (D_2) lies within 1.5σ of our measurement, as shown in Figure 4.10. The main distinction is that our sample consists exclusively of massive stars, whereas their selection likely included bright red giants that are not necessarily young or massive. While the FUV is particularly effective for isolating the youngest stellar populations, the NIR encompasses a broader age range (though this does not affect the comparison presented here). Despite differences in the stellar populations traced by UV and IR data, the results remain consistent in terms of age.

The fractal dimensions derived in our study, as well as those of S2018 for the SMC, are smaller than the value of $D_2 = 1.8$ reported by Bastian et al. (2009) for the LMC. The latter authors used fractured minimum spanning trees, the Q parameter, and two-point correlation functions, methods known to involve considerable uncertainties (Cartwright & Whitworth 2004). In contrast, our results are consistent within the prevailing uncertainties with the fractal dimensions of the LMC Bar ($D_2 = 1.5 \pm 0.1$) and 30 Doradus ($D_2 = 1.6 \pm 0.3$) obtained using similar contour-based techniques (Sun et al. 2017a,b). When we compare our findings with those obtained for the entire LMC by M2022, we observe that the YS structures in the LMC exhibit comparable power-law relations and distributions to those identified in the SMC (see Figure 4.10). Overall, the comparison of fractal dimensions and parameter distributions indicates that, despite differences in galactic environments—such as metallicity and the spatial extent of the surveyed regions (e.g., 30 Dor, LMC Bar, entire LMC and SMC)—YS structures in both the LMC and SMC consistently display a hierarchical spatial pattern.

Tobias & Santiago (2020) estimated the three-dimensional fractal dimension ($D_3 = D_2 + 1$) for three Milky Way star-forming regions using the box-counting method. They found D_3 values of 2.468 for M16 ($D_2 = 1.468$), 2.126 for the Orion Nebula ($D_2 = 1.126$), and 2.435 for RCW 38 ($D_2 = 1.435$). These values are consistent with the uncertainties in our derived D_2 measurements. Additionally, our D_2 value aligns well with that of open clusters younger than 100 Myr in the Milky Way (Qin et al. 2025). This suggests that galaxies of different ordered masses, such as the Milky Way, LMC, and SMC, exhibit hierarchical star formation characterized by a similar fractal dimension.

Menon et al. (2021) investigated the hierarchical spatial distribution of young star clusters in 12 nearby galaxies using data from the LEGUS survey (Calzetti et al. 2015), reporting a wide range of fractal dimensions (D_2) from 0.5 to 1.9, reflecting substantial galaxy-to-galaxy variation in cluster hierarchy. More recently, Shashank et al. (2025) analyzed hierarchical star formation in four nearby galaxies with UVIT observations, finding D_2 values ranging from 1.05 to 1.50. The D_2 values obtained in our study fall within this observed range, supporting the consistency of our results. Using deep UV data from the Hubble GULP survey (Sabbi et al. 2026), Meena et al. (2025) studied the hierarchical distribution of young stellar structures in dwarf starburst galaxy NGC 4449. They found that clustering strength decreases with age, with the power-law slope of the two-point correlation function declining from $\alpha \sim 0.65$ for stars < 5 Myr to $\alpha \sim 0.4$ for stars older than 50 Myr, likely driven by internal stellar motions. These findings are consistent with the hierarchical evolution of stellar structures and complement our analysis of the SMC.

In this study, the sizes of the YS structures in the SMC range from a few parsecs to several hundred parsecs. Similar size ranges have been observed in six nearby (3–15 Mpc) star-forming galaxies (50–150 pc; Grasha et al. 2017), IC 2574 (15–285 pc; Mondal et al. 2019), NGC 7793 (12–70 pc; Mondal et al. 2021b), the Wolf–Lundmark–Melotte galaxy (7–30 pc; Mondal et al. 2021a), and the LMC (10–700 pc; Miller et al. 2022).

By comparing findings from the MW, LMC, SMC, and other galaxies discussed in this section, we assess whether the hierarchical properties of star formation are influenced by factors such as metallicity or environmental conditions (e.g., starburst activity, galaxy interactions). The results suggest that there is no clear dependence on any of these parameters. This indicates that, irrespective of large-scale galactic dynamics or small-scale microphysical processes, the clustering of star formation across scales from stellar clusters to entire galaxies appears to be governed universally by turbulence-driven hierarchical star formation.

4.4.4 Caveats

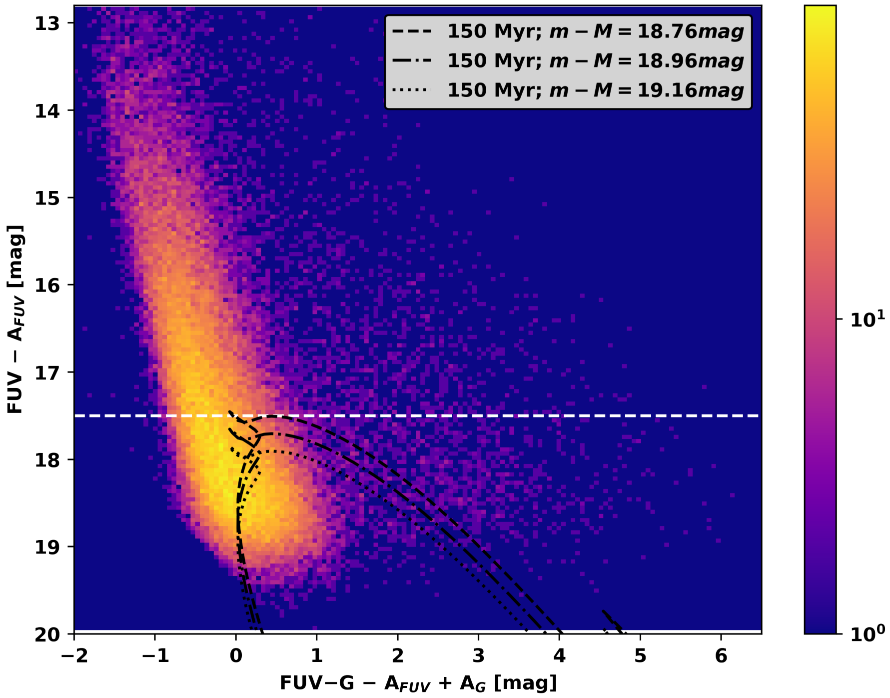

FIGURE 4.11: Same as Figure 3.1. Overplotted are 150 Myr Padova PARSEC isochrones with varying distance moduli.

The SMC has a line-of-sight depth of ∼10 kpc (see section 1.2.1), corresponding to $\Delta m_{\mathrm{FUV}} \sim 0.4$ mag. To evaluate its impact, we examined the UV–optical CMD using different distance moduli. We find that stars brighter than 17.5 mag are younger than 150 Myr (see Figure 4.11), and the effect of depth is minimal. Similarly, as shown in Figure 4.10, varying the limiting magnitude between 18.0

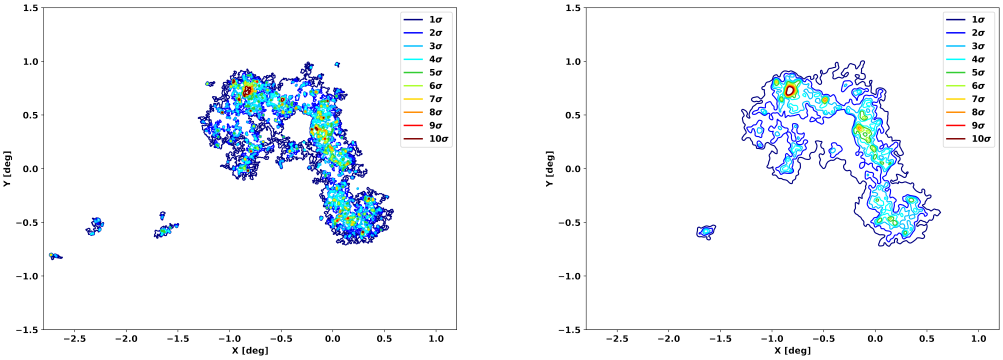

FIGURE 4.12: Left and right panels: young stellar structures detected at different significance levels for kernel widths of 5 pc and 15 pc, respectively.

and 17.0 mag (a shift of 0.5 mag) produces no significant differences. Hence, both depth and extinction effects are negligible for our sample.

As discussed in section 4.2.2, we tested a range of kernel widths to assess their influence on the detection of YS structures. The final kernel width was chosen to balance noise suppression with the retention of genuine structures. Figure 4.12 illustrates the outcomes for kernel widths of 5 pc and 15 pc. At 5 pc, spurious detections are more likely, whereas at 15 pc many genuine structures are missed; thus, a kernel width of 10 pc represents a suitable compromise.

In Figure 4.10, we further compare results for kernel widths of 5 pc and 15 pc. The perimeter–area relation remains consistent, and the D_2 values from the mass—size relation lie within 2σ of our adopted value. The main differences occur in the number and size distributions: for 15 pc, the slope of the number distribution is significantly lower due to the omission of small, dense structures, while for 5 pc the slope of the size distribution (D_2) is steeper, reflecting the inclusion of numerous small structures. These comparisons confirm that a kernel width of 10 pc provides an optimal balance between minimizing noise and preserving genuine structures.

Overall, while both the SMC line-of-sight depth and the choice of kernel width affect the detection of YS structures, our results remain robust and are not significantly impacted by these factors.

4.5 Summary and Conclusions

We present the first FUV study of hierarchical star formation in the SMC to date. Our results and conclusions can be summarized as follows:

- We have detected 236 YS structures composed of FUV stars with magnitudes brighter than 17.5 mag and a completeness level greater than 90%.
- We have calculated the key parameters of the detected YS structures, such as their sizes, areas, perimeters, surface densities, and the number of stars within a given structure.
- The sizes of the structures vary from a few parsecs to a few hundred pc.
- From the perimeter–area relation, the estimated perimeter–area dimension is $D_p = 1.46 \pm 0.04$.
- The 2D fractal dimensions obtained from the number–size relation and the size distributions are $D_2 = 1.64 \pm 0.03$ and $D_2 = 1.31 \pm 0.16$, respectively. These two values are equivalent within their 2σ errors.
- From the best fit to the number distribution between 30 and 1000, we estimated a slope of -0.8 ± 0.1, which is close to the theoretically expected value of -1.
- The surface density distribution of the detected young structures follows a log-normal distribution.

- We have tested our results under various conditions, including the imposition of a magnitude cut-off, a number cut-off, and age limits, and found that all results remain consistent within the 2σ range of the values obtained for the sample.
- We trace the fractal nature of star formation in populations up to an age of 200 Myr.

Our results for the stellar distributions and fractal dimensions D_p and D_2 are consistent with those observed in the SMC, the LMC, the MW and other galaxies, highlighting strong similarities in both the fractal dimensions and the surface density distributions of stellar structures. These characteristics mirror those seen in the ISM based on both observations and numerical simulations, suggesting that the stellar structures we identified have inherited their fractal nature from the ISM. This supports the idea that supersonic turbulence plays a key role in shaping the hierarchical architecture of these structures. Our results align with the broader theory of turbulence-driven hierarchical star formation observed within different galactic environments.

Chapter 5

Recent star formation history and kinematics of the SMC Shell region*

"The universe is like a safe to which there is a combination, but the combination is locked up in the safe." — Peter de Vries

5.1 Introduction

The SMC Shell region is located in the northeastern outskirts of the SMC and shows signatures of recent star formation. V1972 found that this region is the part of the outer arm B . Brueck & Marsoglu (1978), using photographic plates in the B and V bands, found three young (∼60 Myr old) star clusters, suggesting that this arm may be formed due to a recent burst of star formation. Albers et al. (1987)

---

*This chapter is based on the work published in *the Monthly Notices of the Royal Astronomical Society*, **532**, 322-335 (2024), Hota et al., 10.1093/mnras/stae1438 also identified the SMC Shell region associated with the faint outer arm in the NE part of the SMC, using a plate-scanning mechanism on the photographic plates. Using the MCPS data, Zaritsky et al. (2000) found that the SMC Shell region is dominated by upper main sequence stars aged about 200 Myr. MD2019 combined the deep optical data of the SMASH (N2017; N2021) and the proper motion (PM) data from the Gaia DR2 (Gaia Collaboration et al. 2018a) to probe the SMC Shell region. Using clusters and classical Cepheids, they estimated that this region has stars with age $\leq$ 150 Myr. They concluded that the origin of the SMC Shell region is most likely due to the hydrodynamic interaction of the SMC with the LMC or the MW but discarded the possibility of a tidal origin. Piatti (2022) studied 20 star clusters of the SMC Shell region using the SMASH data. According to his work, four of the studied objects could not be confirmed as genuine clusters, while the rest were identified as either young ($\sim$30–200 Myr) or intermediate-age ($\sim$1.7–2.8 Gyr) systems. His analysis revealed that the intermediate-age clusters, along with some of the young ones, are situated within the SMC main body, whereas the remaining young clusters are located at a distance of roughly 13 kpc farther out. An age-dependent trend was also detected, showing that clusters farther from the SMC tend to be younger, relatively more metal-rich, less massive, and subject to slightly higher reddening compared to the older clusters. These results imply that the Shell-like overdensity may correspond to a tidal structure or an additional stellar structure in the SMC, likely shaped by the interactions with either the LMC or the MW. SW2024 reported that the northeastern Shell of the SMC predominantly consists of stars younger than 500 Myr, with notable peaks in star formation occurring roughly 250 Myr and 450 Myr ago. These younger populations largely define the Shell's morphology. Their analysis revealed a temporal correspondence between the star formation history of this Shell and that of the LMC's northern arm, which we link to the past 500 Myr of interactions among the SMC, LMC, and MW. The findings emphasize the combined effects of ram pressure stripping and the MW's circumgalactic medium in shaping the northeastern Shell's structure.

In this Chapter, we explore the distribution, kinematics and star formation history of young massive stars in the outskirts of the SMC and how it is similar or dissimilar to the main body/inner SMC. In this work, we have used 11 UV images from the UVIT (Tandon et al. 2017a, ; details in Chapter 2). In addition, we have also used the optical and PM data from Gaia Early Data Release 3, EDR3 (G2021), which are the same with respect to the data in Gaia DR3 (Gaia Collaboration et al. 2022), (G2023). We have used a UV–optical stellar map of the SMC Shell region to decipher its recent star formation history, kinematics and probe the details of two structures found in this region. In section 5.2, we describe the observations and data used in this analysis. Section 5.3 and section 5.4 describe the age estimation and spatial distribution of the FUV stellar population, respectively. Section 5.5 presents the kinematics of the young population. The distribution of age and median PM are given in section 5.6 and section 5.7, respectively whereas section 5.8 deals with the properties of two morphological structures found within the SMC Shell region. In section 5.9, we discuss our results, and we summarize and conclude our work in section 5.10.

5.2 FUV catalog

In this work, we have obtained FUV images in the F148W (1481±250 Å) filter for eleven fields of the SMC Shell region. Observation details are given in Table 2.1. Data reduction and photometry were performed as mentioned in Chapter 2. The PSF-fit error as a function of the estimated magnitudes in the F148W filter for all the FUV detected sources is shown in Figure 5.1. For a maximum error of 0.2 mag, we detect sources up to 22 mag, and these are considered for further analysis. We combined all the observed fields to create a catalog of ∼16000 FUV sources in the SMC Shell region after taking care of data duplication of the overlapping fields based on signal-to-noise criteria. We note that stars brighter than 15 mag in

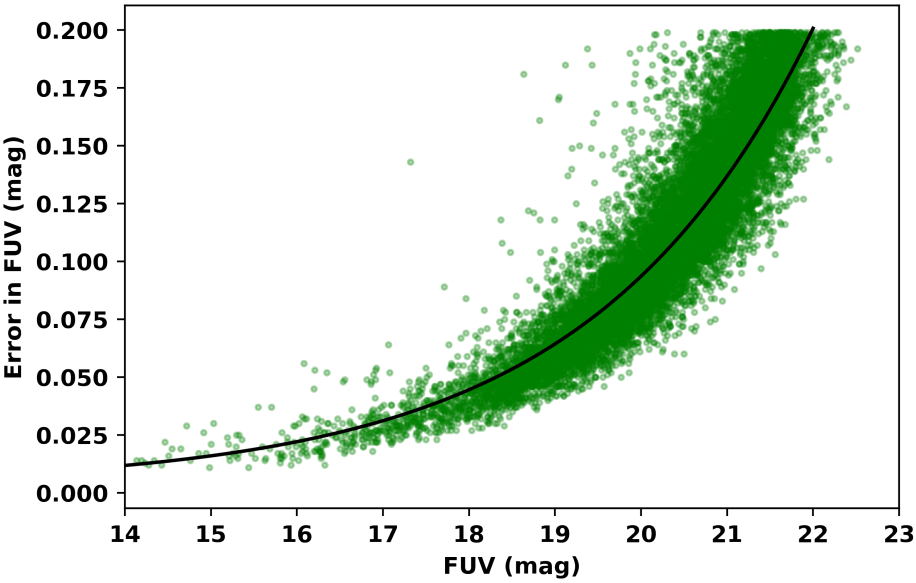

Figure 5.1: The PSF-fit error as a function of the FUV magnitude for the observed sources of the SMC Shell region. The line plot is the median error of the F148W filter.

FUV (∼20 stars) might be affected by uncorrected saturation and therefore might be slightly brighter than the estimated magnitude.

The detected FUV sources were cross-matched with the Gaia EDR3 data (G2021) within a separation of $1''$, and we considered only stars with RUWE < 1.4 (Lindegren et al. 2018). A 3σ cut-off is applied to the mean value of the parallax (parallax = 0.011 mas) and the PM in the RA and the Declination (Dec) ($\mu_{\alpha} cos\delta$ = 0.90 mas yr^{-1}, $\mu_{\delta} = -1.21$ mas yr^{-1}) of the detected FUV stars to obtain the most probable members in the SMC Shell region. The final FUV catalog of the SMC Shell region has ∼14400 stars, along with the optical photometry and the PM values from Gaia EDR3 (Table 5.1).

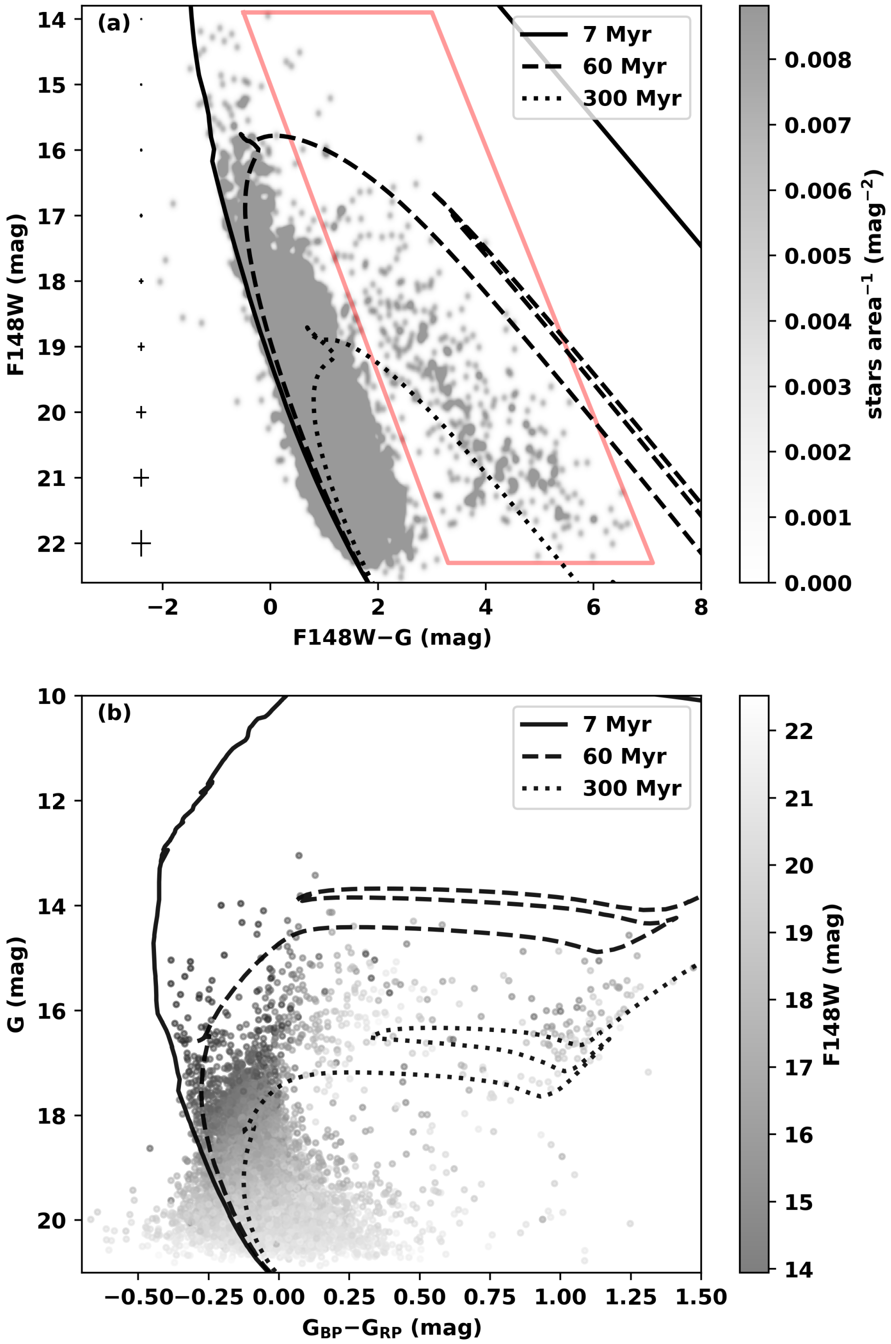

FIGURE 5.2: (a) FUV–optical CMD (KDE with a bandwidth of 0.05 mag) with the error bars (median value) shown in black color on the left side and a red polygon denoting the region of the sub-giant branch. (b) Optical CMD of the SMC Shell region. The color bars of (a) and (b) represent the number of stars area^{-1} (area = 10^{-4} mag^2) and FUV (mag), respectively.

Table 5.1: UV catalog of the SMC Shell region. The Gaia EDR3 source_id, spatial coordinates, and magnitude in the F148W filter, along with the fit error in magnitude, are listed in columns 1 to 5, respectively. The full table is available as online material (H24a).

Gaia EDR3 Source_id	RA [deg]	Dec [deg]	FUV [mag]	error [mag]
4690731730417825920	18.12019792	−70.85794556	19.581	0.081
4690734754072739456	17.84952625	−70.83735222	16.880	0.018
4690734891513810432	17.97096000	−70.83903333	17.787	0.027
4690795742608440192	15.29432708	−71.23031833	21.119	0.106
4690794716120011904	15.36130083	−71.25074083	21.446	0.117

5.3 Color Magnitude Diagram

We used all the stars in the catalog of the SMC Shell region (Table 5.1) to construct the CMD. We used FUV and optical photometric data to create the FUV–optical CMD, i.e. F148W vs (F148W–G) as shown in Figure 5.2(a) and the optical CMD, i.e. G vs G_{BP}–G_{RP} (Figure 5.2(b)). In Figure 5.2(a), we present a KDE applied to the color-magnitude surface. The bandwidth used for this KDE was set to 0.05 mag. This diagram is aimed at helping in identifying the densely populated evolutionary features. We used the Padova-PARSEC isochrones (Bressan et al. 2012) with an age step size of 5 Myr to overlay on the CMDs. We adopt the distance, reddening, and metallicity values previously used by MD2019, which are: a distance modulus of 18.96 mag (G2015), a metallicity of Z = 0.002 (Lemasle et al. 2017) and a mean color excess of $E(B-V) = 0.05$ mag (Haschke et al. 2011). When we overlaid the isochrones in the FUV–optical CMD, we had to reduce the color excess value to 0.03 mag, which is within the error margin of the literature reddening value, to best visually overlay the isochrones onto the data. On the other hand, we adopted the same extinction value as in the literature for the optical CMD. The difference in reddening (0.02 mag) between those adopted in the FUV–optical and the optical CMDs is very small. In the optical CMD, the blue loop stars and the sub-giant stars overlap, resulting in an ambiguous age estimation from the main sequence turnoff. But in the FUV–optical CMD, the large color-magnitude range introduces a sufficient separation between the blue loop and the sub-giant stars. Therefore, the FUV–optical CMD is better suited for estimating the age range of young stars. From Figure 5.2(a) and Figure 5.2(b), the sub-giant branch is clearly seen in the FUV–optical CMD within a red polygon with coordinates at (F148W−G, F148W) = [(−0.5, 13.9), (3, 13.9), (7.1, 22.3), (3.3, 22.3), (−0.5, 13.9)] mag when compared to the optical CMD (at G ≈ [14, 17] mag and G_{BP}–G_{RP} ≈ [0, 1.5] mag. To guide the reader with the stellar evolutionary phases detected in the CMD, we have overlaid a few isochrones to demonstrate the extended turn-off and the sub-giant branch in the FUV magnitude axis. The overlaid isochrones suggest that most of the star formation is likely to have happened between 60–300 Myr ago and a probable recent event at ∼7 Myr. We note that the brightest stars in the CMD may be brighter due to uncorrected saturation, but the younger age estimations are unlikely to be affected by this.

5.4 Surface density map

We have determined zenithal equidistant projection of the SMC Shell region where we followed the X and Y conversion as defined in M2001 with the SMC optical center at $\alpha_{\rm SMC} = 00^{\rm h}52^{\rm m}12^{\rm s}.5$ and $\delta_{\rm SMC} = -72°49'43''$ (J2000; V1972). To understand the spatial distribution of FUV stars in the SMC Shell region, we used KDE, where convolution of stellar distribution with a Gaussian kernel was performed. Using a kernel size of 10 pc, we could identify morphological structures. The same kernel size was considered in previous studies on the MCs by Sun et al. (2017b), S2018; M2022. We have visually identified two structures within this region; one is an arm-like structure, and another is an arc-like structure, shown in Figure 5.3. These two structures were noticed previously by MD2019 using main sequence

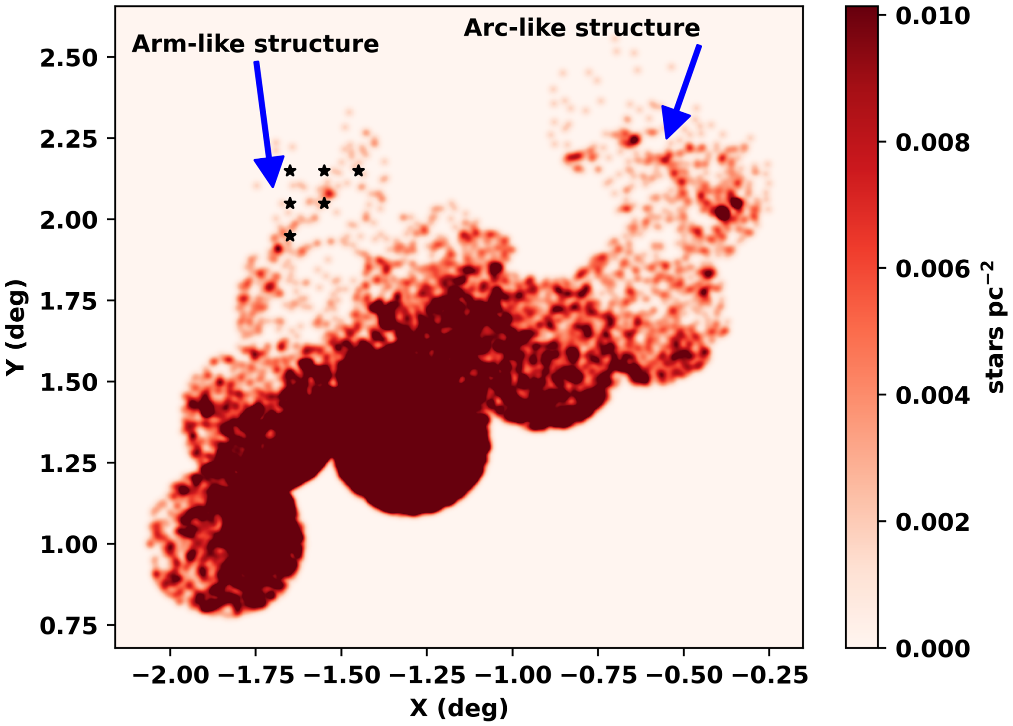

FIGURE 5.3: The surface density plot of the SMC Shell region. The color bar represents the number of stars pc^{-2}. Blue arrows indicate the arm-like and arc-like structures. The six black points are the center of the bins located on the arm-like structure which are shown within the blue polygon in Figure 5.4(b).

stars brighter than 21 mag in the g band (right panel of their Figure 3 and Figure 4) obtained from the SMASH data. The details of these two structures are explained in section 5.8.

We performed a spatial binning with the bin size of 0.1 deg along the X and Y directions and estimated the number of stars per bin. Here, we considered only bins that fully fall within the FUV coverage (118 such bins). The spatial distribution of FUV stars is shown in Figure 5.4(a). In Figure 5.4(a), we identified the densest bin with center at (X, Y) = (−1.45, 1.45) deg where a young cluster HW64 of age ∼30 Myr (Piatti 2022) is located. We identified the positions of clusters within the SMC Shell region, which had been previously examined by Piatti (2022). We observed that these clusters lack a significant population of FUV stars, and

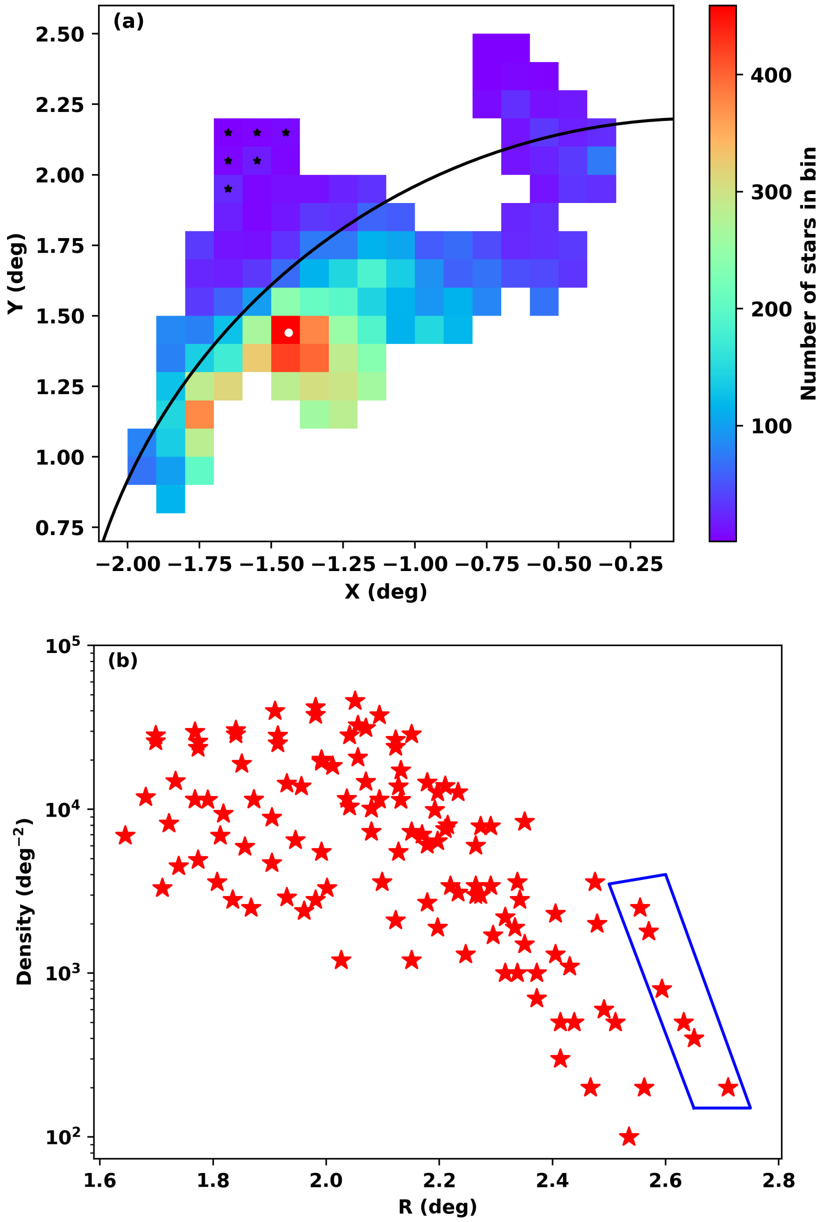

Figure 5.4: (a) The spatial distribution of FUV stars of the SMC Shell region. The color bar shows the number of stars in each bin (area of bin = 0.01 deg^2). The black arc represents a segment of a circle with a radius of 2.2 deg centered at the SMC optical center. The white dot represents the location of star cluster HW64. (b) The radial variation of the number density of FUV stars from the SMC center. The points in the blue polygon in Figure 5.4(b) and marked as stars in Figure 5.4(a) are located on the arm-like structure shown in Figure 5.3.

the FUV–optical CMDs do not offer substantial insights for further investigation. Consequently, we opted not to explore these detected clusters in our study. We note that the spatial distribution of young stars is not uniform, and there is a gradient that decreases radially outward (Figure 5.4(a)).

We calculated the FUV stellar surface density of bins with area of 0.01 deg^2 and their radial distance from the SMC center (Figure 5.4(b)). We note a nearly flat FUV stellar surface density between 1.6 to 2.2 deg, where the density range is found to be between a few thousand to a few tens of thousands of stars deg^{-2} and the same does not occur for all the position angles. This large spread in number density at a given radial distance reflects the inhomogeneous and clumpy distribution of young stellar populations, arising from localized star formation. The variation with position angle further highlights the asymmetric and hierarchical nature of star formation in the SMC. The density starts to decline, from $\sim$2.2 deg and falls below 1000 stars beyond $\sim$2.4 deg. The radius corresponding to 2.2 deg is shown in Figure 5.4(a) as a black curve. This suggests that the area within this radius covers nearly all the higher density regions within the limitation of spatially incomplete observations in the NE of the SMC ($X > -1$ deg) and hence could be considered as an extent of the inner SMC within the limited observed part of the NE SMC. Regions beyond this radius could be considered as the outer SMC because they have a declining stellar density. The six outermost points showing a higher stellar density more than 100 FUV stars deg^{-2} are identified in the arm-like structure and shown in Figure 5.3 and Figure 5.4(a). The arc-like structure appears to start within the inner SMC and extends to the outer SMC, whereas the arm-like structure seems entirely co-located in the outer SMC (Figure 5.4(a)).

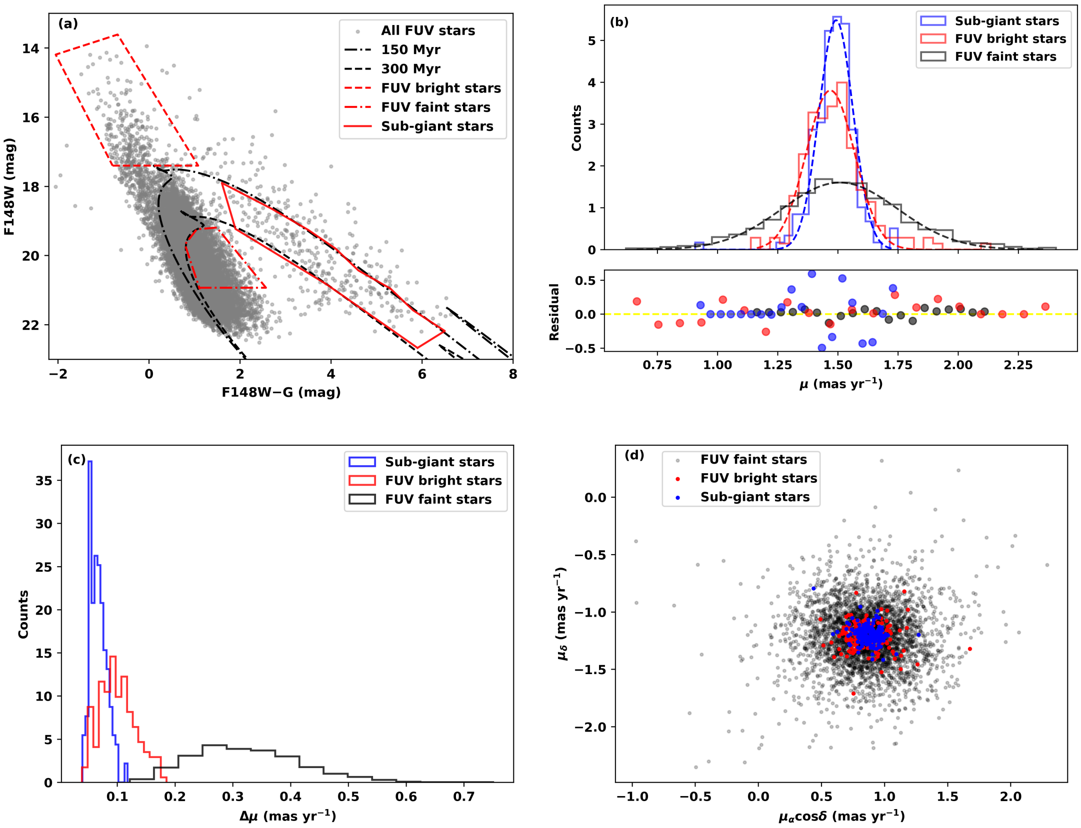

FIGURE 5.5: (a) Selection of different populations using the FUV–optical CMD: FUV bright (red dashed polygon), FUV faint (red dash-dotted polygon), and sub-giant (red solid polygon) stars. (b) the Gaussian fit of the histogram of the PM with residuals, (c) the distribution of measurement error in PM, and (d) the VPD of the three different populations.

5.5 Kinematics of different age groups

As the outer regions are affected more by tidal effects due to the recent interaction between the MCs, it will be interesting to probe the kinematics of stars born before and after the interactions in this part of the SMC. To differentiate the kinematics of FUV stars formed before and after the recent LMC-SMC interaction, we defined three age groups from the FUV–optical CMD as shown in Figure 5.5(a). Stars with FUV magnitudes brighter than 17.4 mag and younger than 150 Myr in the main sequence of the CMD are defined as the FUV bright population, and stars

TABLE 5.2: For each of the three FUV populations listed in column 1, mean and standard deviation values of the PM distribution with their fit error (from the covariance matrix) are listed in columns 2 and 3, respectively. The median values of PM and the median value of error in PM are listed in columns 4 and 5, respectively.

Defined population	μ_{mean} (mas yr^{-1})	σ_μ (mas yr^{-1})	μ_{median} (mas yr^{-1})	$\Delta\mu_{\text{median}}$ (mas yr^{-1})
FUV faint stars	1.508±0.006	0.241±0.006	1.508	0.315
FUV bright stars	1.468±0.003	0.101±0.003	1.471	0.097
Sub-giant stars	1.492±0.003	0.070±0.003	1.490	0.065

with the FUV magnitude between 19 to 21 mag in the main sequence are defined as the FUV faint population, as the majority of this population are stars older than 300 Myr. The third group is the sub-giant stars, aged between 150 to 300 Myr and fainter than 18 mag.

First, we applied a 3σ cut-off to the PM of these populations to remove outliers, then we created the PM distributions (Figure 5.5(b)), which we fitted with Gaussian and estimated the values of mean and standard deviation of the PM distribution, along with median values of PM and median values of error in PM of each group as shown in Table 5.2. The error in PM of each star of these three populations is estimated by using $\Delta\mu_\alpha\cos\delta$ and $\Delta\mu_\delta$ from Gaia, and the distributions of these errors are shown in Figure 5.5(c).

We converted the standard deviation in PM to velocity dispersion using the following formula.

$$V = 4.7\mu D \tag{5.1}$$

where V is the transverse velocity in km s^{-1} and D is the distance in parsec (pc).

We obtained the velocity dispersion of the FUV bright and the sub-giant stars as 29.67±0.88 km s^{-1} and 20.76±0.88 km s^{-1}, respectively. The velocity dispersion of the FUV faint stars is 70.82±1.76 km s^{-1}, which is very large compared to the velocity dispersion of the other two groups. Figure 5.5(d) is a VPD of the three groups. This plot illustrates that the FUV bright and sub-giant stars appear compact when compared to the FUV faint stars. We note that the median value of error in PM, 0.315 mas yr^{-1} is relatively higher than the standard deviation of 0.241 mas yr^{-1} of PM distribution for this population. Therefore, the relatively large velocity dispersion estimated for the age group $>$ 300 Myr is likely to be due to the large measurement error in PM. However, the FUV bright and sub-giant stars have similar peak and standard deviation values in PM, along with a small difference in velocity dispersion. This leads us to conclude that the stars younger than 150 Myr (FUV bright stars) and stars with age between 150–300 Myr (sub-giants) are kinematically similar. As the kinematic dispersion is used as a probe to check for interaction induced by tidal heating of the older stellar population in the outer SMC, a consistent dispersion points to an undetectable tidal heating within the data accuracy.

5.6 Age distribution

In order to assess the age and kinematics of FUV stars comprehensively, we obtained the age range and median PM for each individual spatial bin within the SMC Shell region. We considered the same binning as mentioned in section 5.4 for the age map, but we excluded bins (regions) containing less than 15 FUV stars to get a reliable estimate of the age range. For each of the 126 individual bins, we created FUV–optical CMDs. These CMDs bear the signatures of the episodes of star formation experienced by the region in the form of evolutionary features in the CMD. As these CMDs cannot be considered as originating from a simple star population, we cannot use quantitative isochrone fitting methods to estimate ages. Therefore, we utilize the presence of (1) sub-giants and (2) turn-off features in the

CMDs to identify the dominant population, and Padova-PARSEC isochrones are visually overlaid on them to derive their ages. We did not come across any requirement to alter the assumed values of extinction and distance (section 5.3), as the overlaid isochrones matched the stellar patterns in the CMD well.

In most of the regions, we were able to detect up to three episodes of star formation based on the features in the CMD (for example, Figure 5.9(b) and section 5.8.1). These suggest that in general, the SMC Shell region experienced star formation in episodes. We combined the identified ages of star formation in the individual regions to understand the overall picture of star forming episodes in the SMC Shell region.

As the ages are estimated by a visual overlay of isochrones on the CMD features, we overlaid isochrones with a range in age to identify how much deviation can be detected visually for the age range considered in this study. We found that it is generally not possible to differentiate isochrones with age within the 10% range (see, Figure 5.11 in section 5.9.1). A similar method for estimating the error in age when the fitting was done visually was used by Piatti (2014).

The age distribution, as shown in Figure 5.6, indicates a few peaks in star formation, pointing to the episodic star formation experienced by the region. We used a bin size corresponding to 1-sigma error (20 Myr) at 200 Myr. We note a peak between 40–80 Myr and another between 240–280 Myr. The peak noticed at ∼170 Myr may not be significant and may only suggest a ramping down of star formation between 150–200 Myr. There is a dip between 100–160 Myr, prior to a peak at ∼60 Myr, indicating a recent burst. The peak at ∼390 Myr is not regarded as a significant star formation peak as stars with age ∼390 Myr have a large photometric error. In summary, two noticeable star formation episodes can be traced between 40–300 Myr. The episode of star formation at 240–280 Myr is likely due to the last LMC-SMC interactions (Mathewson 1985; Besla et al. 2012;

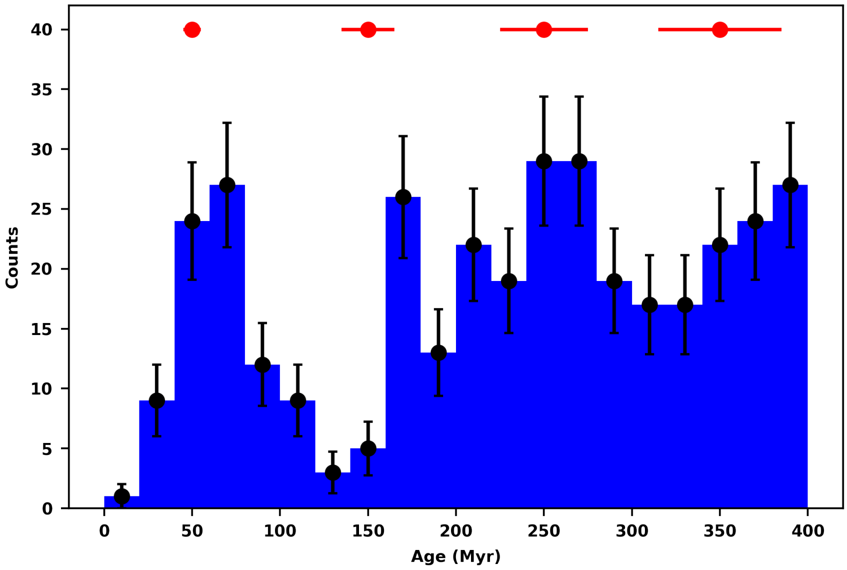

FIGURE 5.6: The histogram of the star formation events of the SMC Shell region. The vertical error bars represent Poissonian errors, while the horizontal error bars at 50 Myr, 150 Myr, 250 Myr, and 350 Myr indicate approximately $\sim 10\%$ errors in the estimated ages.

Choi et al. 2022).

To check for evidence of propagating star formation, we compared the spatial distribution of bins with age groups of < 125 Myr, 125–225 Myr, 225–325 Myr, and 325–400 Myr as shown in the Figure 5.7. There is no noticeable pattern to suggest any propagation of star formation within the SMC Shell region in the considered age range. If we check the youngest group (age < 125 Myr), we notice that the recent star formation happened in the SMC Shell region except region towards at X $\approx [-1.75, -1.25]$ deg, Y $\approx [1.50, 2.25]$ deg including the arm-like feature and in the NE, where observations are spatially incomplete. Figure 5.7 suggests that the arm-like structure is formed in the age range 125–400 Myr. Instead, the arc-like structure appears to be present in all four age ranges.

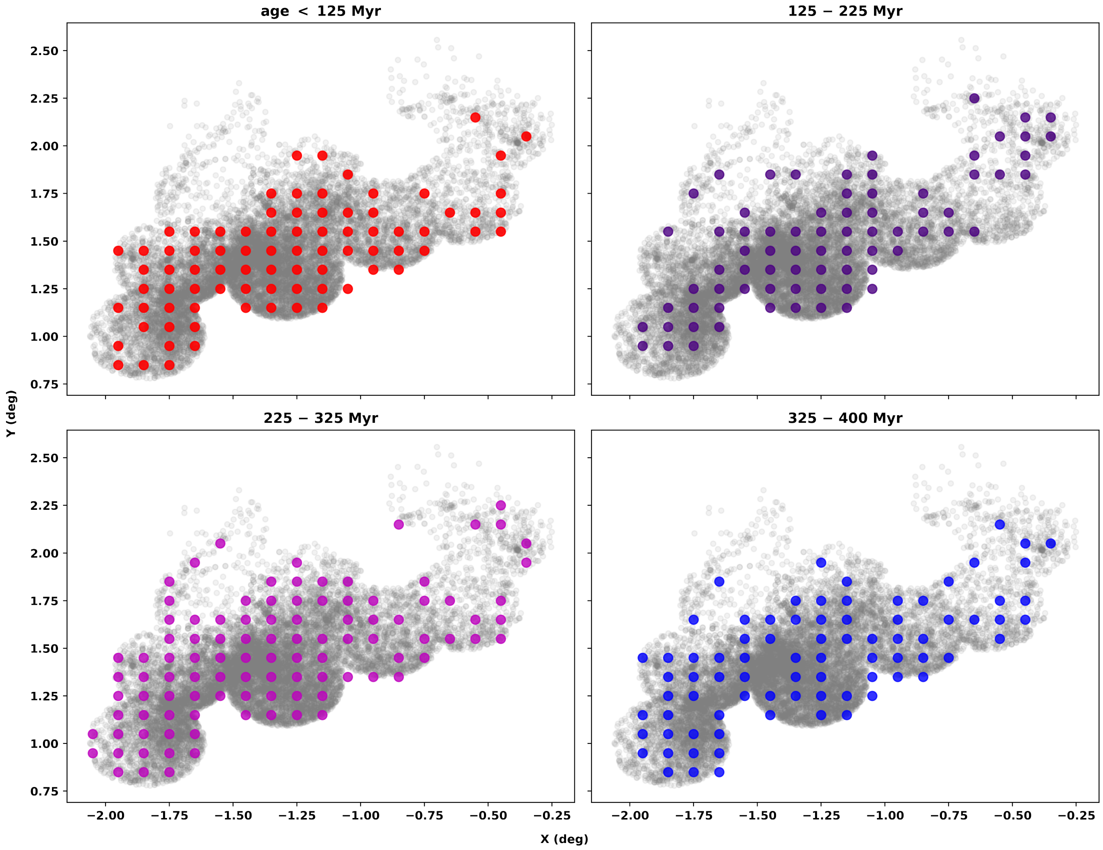

FIGURE 5.7: Spatial distribution of the age of the major star forming events of individual regions, estimated from the FUV–optical CMDs using the same parameters as mentioned in section 5.3. All stars detected in the FUV are shown as gray-colored dots.

5.7 Proper motion distribution

To probe the kinematics of the SMC Shell region, we created the VPD (Figure 5.8(a)), where the median PM vectors of each bin are shown. Most of the vectors are aligned and co-located, with some scatter. The position angle (PA) of the median PM vector (angle of median PM to $\mu_\alpha \cos\delta$) is found to be between −65 deg to −45 deg for the majority of the bins (Figure 5.8(b)). For the spatial distribution of PM, we transformed ($\mu_\alpha cos\delta$, μ_δ) into the Cartesian plane using the conversion equation as defined by G2021, (Eq 2) and estimated the median value of the PM of each bin. Figure 5.8(c) shows the spatial distribution of the median

PM after a 3σ cutoff (three bins were eliminated), which suggests that there is no significant gradient in the median PM within the SMC Shell region. Further, the velocity dispersion of each bin was obtained following the formula shown in Eq 5.1. The spatial map of the velocity dispersion (Figure 5.8(d)) reveals a range in velocity dispersion within the SMC Shell region. Figure 5.8(e) represents the spatial distribution of the residual PM vector, which is calculated by subtracting the systemic PM (Gaia Collaboration et al. 2018b) from the median value of PM of each bin (without considering internal rotation). This plot illustrates that within the SMC Shell region, the western and outer regions are relatively more disturbed than the inner and eastern regions.

In order to check for any radial gradient in the PM value, Figure 5.8(f) shows the median value of the PM of each bin as a function of the radial distance. The error bar for each value indicates the standard error. This plot shows that most of the bins have a similar median value of PM, which coincides with the PM value of the SMC main body (Gaia Collaboration et al. 2018b). Significant scatter is noticed for bins located at a radial distance more than 2.4 deg from the SMC center. We also note that bins that show large variations in the median value of PM do not necessarily have a large PM error. The deviation in the median PM, as shown in Figure 5.8(f), is found to increase after 2.4 deg, whereas the inner regions between 1.6 deg to 2.4 deg are found to have a similar PM. The inner regions are, therefore, likely to be kinematically stable, with the median PM similar to the SMC main body. This supports the finding at section 5.4 that the NE extent of the inner SMC is likely at ∼2.2 deg.

5.8 Morphological structures

In this study, we identified visually two morphological structures from the distribution of FUV stars in the SMC Shell region (Figure 5.3). One is an arm-like

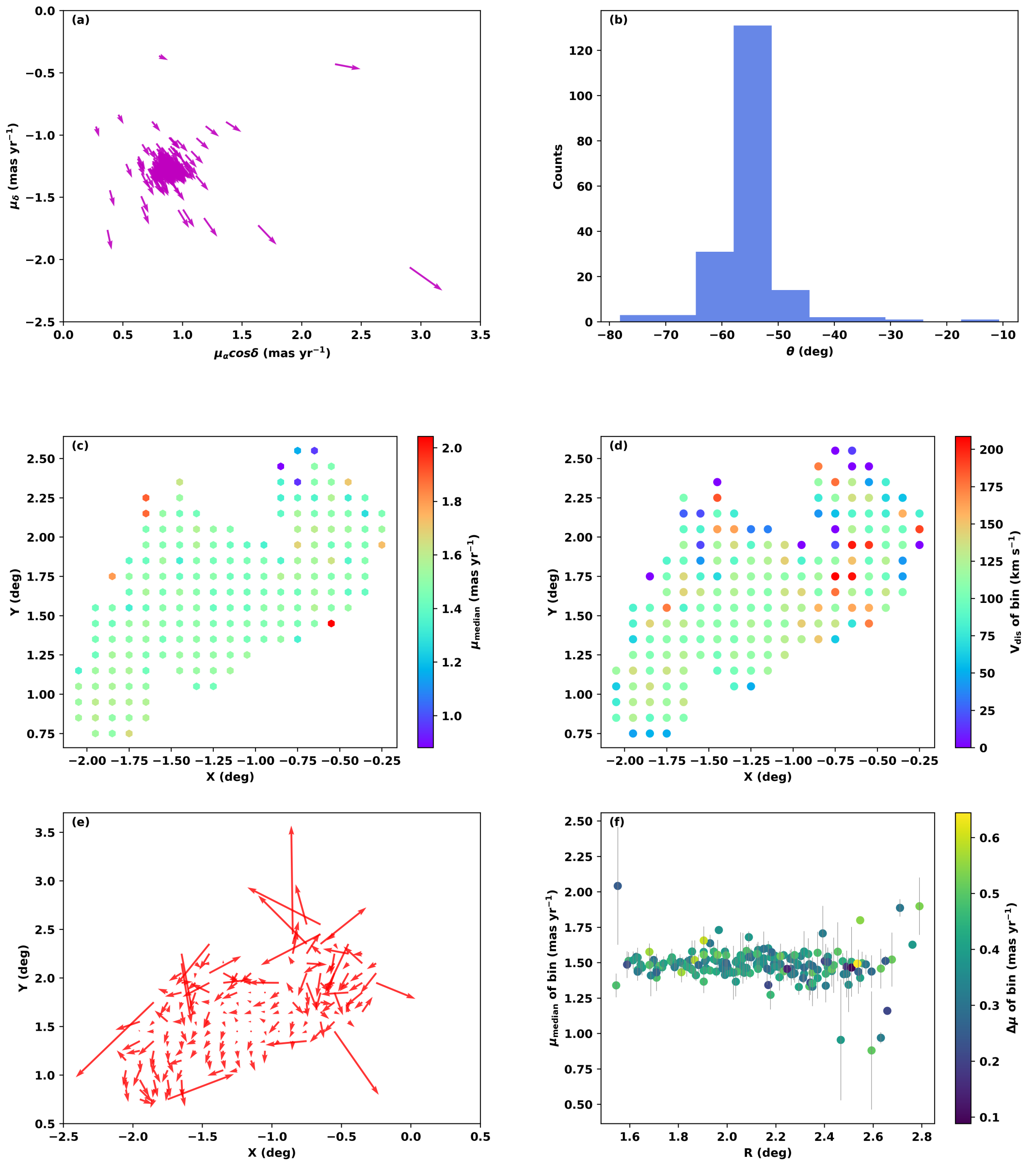

FIGURE 5.8: (a) A plot of the median PM vector of each bin in the SMC Shell region in the $\mu_\alpha \cos\delta$ and μ_δ plane, (b) a histogram of the angle between the median PM vector and the $\mu_\alpha \cos\delta$, (c) the color map of the median PM of each bin in X-Y plane, (d) the color map of the velocity dispersion of each bin in X-Y plane, (e) a plot of the residual PM vector in the X-Y plane, and (f) a plot of the radial variation of the median PM of each bin with an error bar (standard error) where the color bar represents the median value of error in PM within each bin.

structure, and the other is an arc-like structure. To compare the kinematics of these two structures with their nearby region, we define nearby control regions. The polygons for the structures make sure that the feature (arm and arc-like) falls within, and the polygons for the control sample ensure that they are sufficiently close to the structure without contamination and have a similar number of stars. In the following, we discuss these structures in detail.

5.8.1 Arm-like Structure

In Figure 5.9(a), we show the arm-like structure enclosed within a black solid polygon and define a control sample made of stars within the black dashed polygon. To estimate the age range of stars within the arm-like structure, we have plotted the FUV–optical CMD and overlaid the Padova-PARSEC isochrones (Figure 5.9(b)) using the same parameters as mentioned in section 5.3. The isochrones are visually checked to match the evolutionary pattern of stars seen in the CMD. There are only a few stars with age ∼35 Myr. Thus, the arm-like structure does not have much of a contribution from stars younger than 200 Myr. This structure, therefore, shows the enhanced star formation between 220 Myr to 400 Myr ago, either continuous or episodic star formation. There may have been older stars, but here, we do not attempt to estimate older ages due to large photometric errors for stars fainter than 20 mag in FUV.

The PM distribution is fitted with a Gaussian curve to find the peak and standard deviation of the arm-like structure and the control sample (Figure 5.9(c) and 5.9(d)). We found that the values of peak and standard deviation of PM, ($<\mu>$, σ) of the arm-like structure and the control sample are $(<\mu>, \sigma)_{arm\_wide}$= (1.595±0.024, 0.343±0.017) mas yr^{-1}, $(<\mu>, \sigma)_{arm\_narrow}$ = (1.398±0.007, 0.106±0.010) mas yr^{-1}, and $(<\mu>, \sigma)_{cs}$ = (1.501±0.019, 0.225±0.019) mas yr^{-1}, respectively. The narrow and wide PM components of the arm-like structure

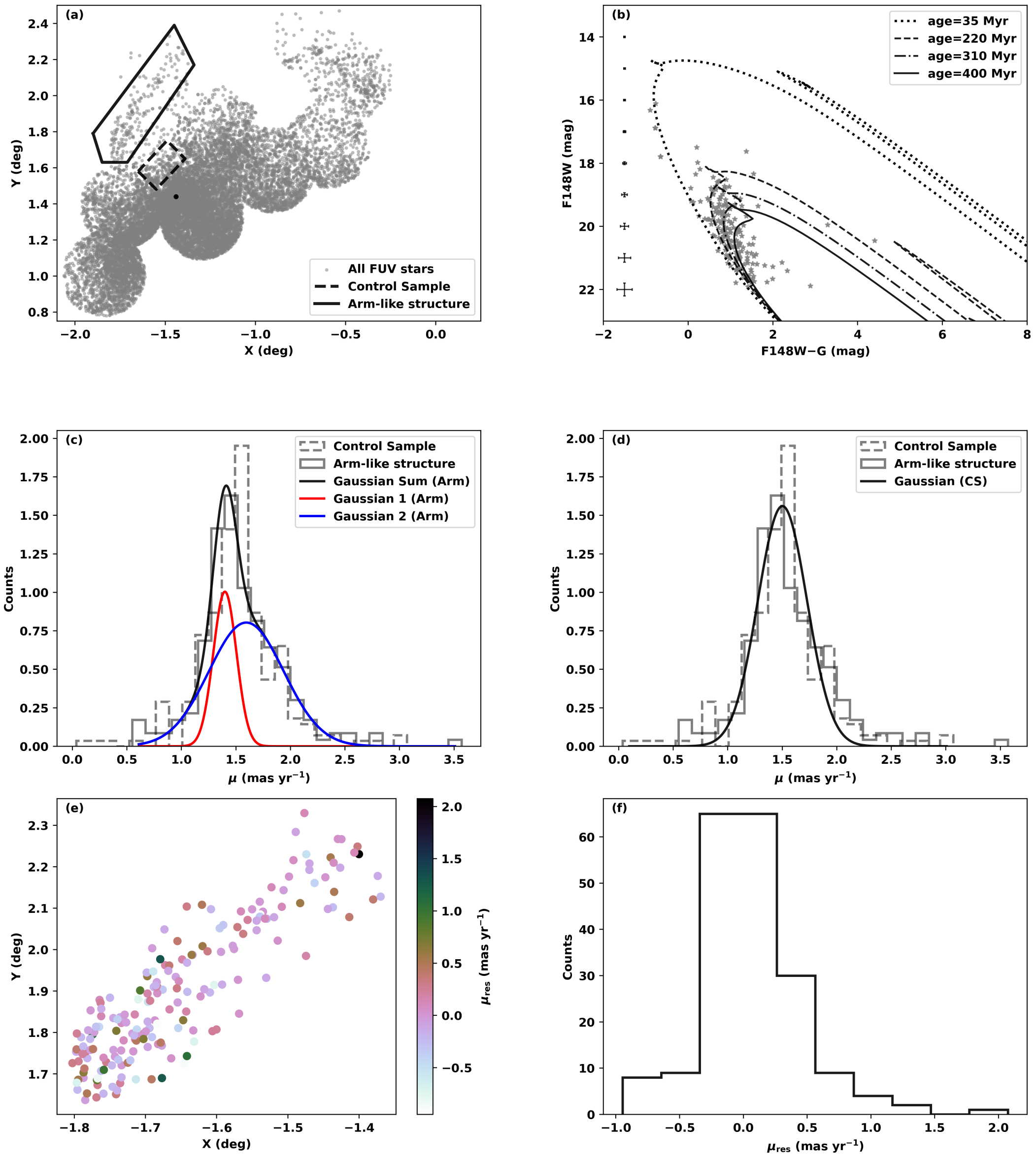

Figure 5.9: Characterization of arm-like structure: (a) Stars inside the black solid polygon are considered as belonging to the arm-like structure, and stars within the black dashed polygon are taken as a control sample for kinematic comparison, and the black dot represents the location of star cluster HW64 for a reference. (b) FUV–optical CMD of stars within the arm-like structure. (c) and (d) show Gaussian fits to the PM histogram of the arm-like structure and control sample, respectively. (e) and (f) present the spatial distribution and histogram of the residual PM of the arm-like structure, respectively.

suggest a two-component population, with the narrow component constituting 28% of the sample. The peak PM values of the narrow and wide components are different, and the difference is statistically significant, suggesting the presence of a population within the arm-like structure with reduced dispersion in PM. However, the peak value of the control sample PM distribution is similar to the peak of the wide component of the arm-like structure. This indicates that 72% of the arm-like structure and the control sample population are kinematically indistinguishable. To estimate the residual PM, we subtracted the median value of PM of the arm-like structure from the PM of each star. Here, the internal rotation is not taken into account. The spatial distribution of residual PM (Figure 5.9(e)) shows that most stars have residual PM close to zero. Figure 5.9(f) shows the residual to peak near zero PM. We infer that the arm-like structure is an over density formed between 220–400 Myr ago with kinematics similar to the underlying part of the SMC.

5.8.2 Arc-like structure

MD2019 detected this separated small arc. In Figure 5.10(a), we have considered the arc-like structure within the black solid polygon and the nearby region within the black dashed polygon as a control sample to study the kinematics. To estimate the age, the FUV–optical CMD (Figure 5.10(b)) is overlaid with the Padova-PARSEC isochrones taking the same parameters as mentioned in section 5.3. We detect a small number of stars with age ∼45 Myr. From Figure 5.10(b), the arc-like structure appears to have a significant contribution from stars aged between 130 to 350 Myr, and the contribution from the FUV stars younger than 130 Myr is very small. This region also shows episodes of star formation like the arm-like structure (Figure 5.9(b)). This region may be formed in several episodes of the star formation, including the last LMC-SMC interaction.

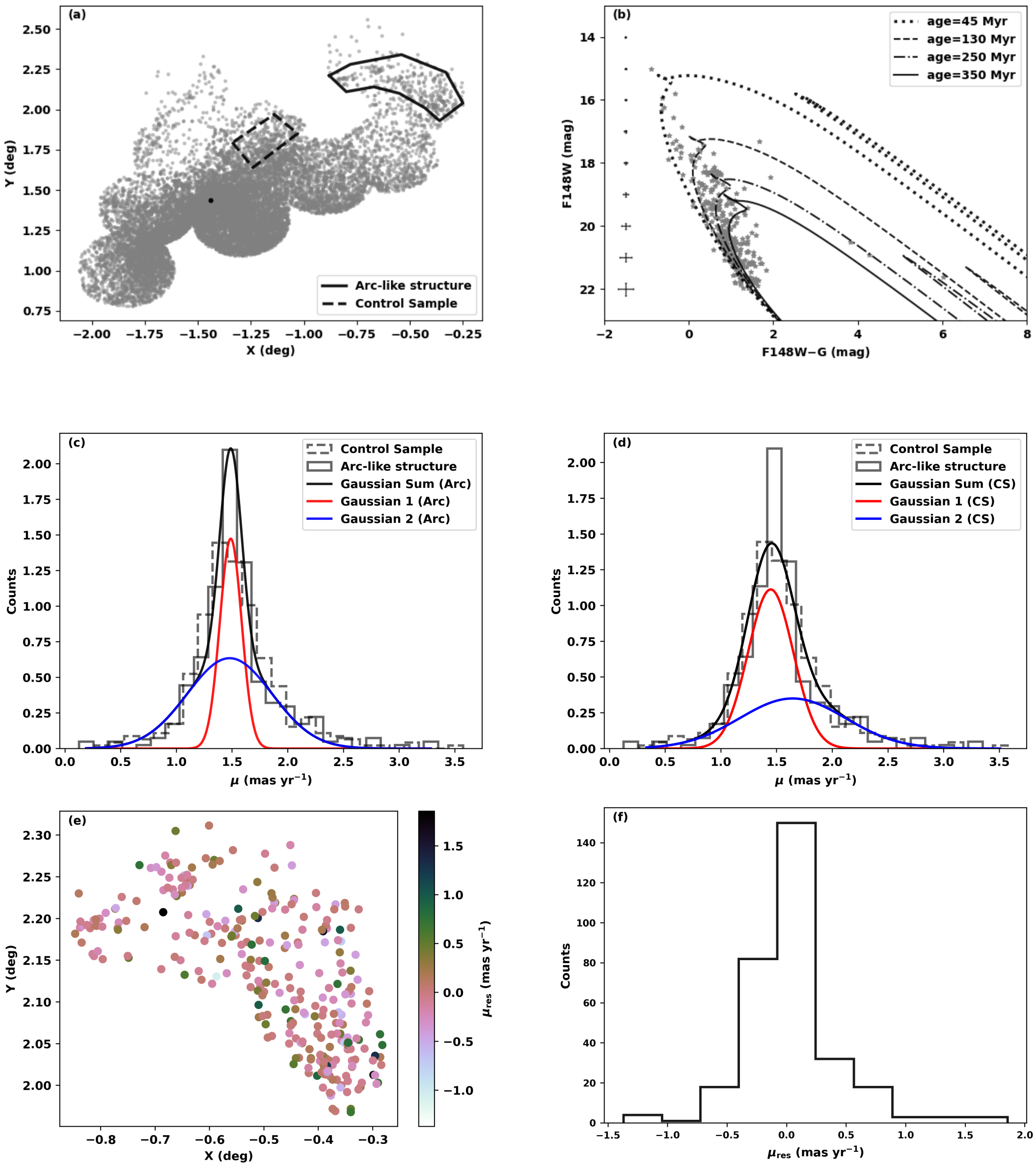

FIGURE 5.10: Characterization of the arc-like structure. (a) Stars inside the black solid polygon belong to the arc-like structure, while stars within the black dashed polygon serve as a control sample for kinematic comparison. The black dot marks the location of the star cluster HW64 for reference. (b) FUV–optical CMD of stars within the arc-like structure, with isochrones of different ages overlaid. (c) and (d) Gaussian fits to the proper motion histograms of the arc-like structure and the control sample, respectively. (e) Spatial distribution of residual proper motions for the arc-like structure, where the color bar indicates the residual proper motion magnitude. (f) Histogram of the residual proper motion for the arc-like structure.

Using the PM values of the FUV stars of the arc-like structure and its control sample, the PM distributions were created and fitted with a Gaussian curve to find the peak and standard deviation of PM of these two regions (Figure 5.10(c) and 5.10(d)). We found that the peak and the standard deviation values of PM of arc-like structure and its control sample are $(<\mu>, \sigma)_{\mathrm{arc\_narrow}}=$ (1.487±0.005, 0.097±0.006) mas yr^{-1} (fraction = 0.37), $(<\mu>, \sigma)_{\mathrm{arc\_wide}}=$ (1.477±0.025, 0.380±0.035) mas yr^{-1}; and $(<\mu>, \sigma)_{\mathrm{cs\_narrow}}=$ (1.446±0.009, 0.203±0.014) mas yr^{-1} (fraction = 0.56), $(<\mu>, \sigma)_{\mathrm{cs\_wide}}=$ (1.644±0.070, 0.475±0.054) mas yr^{-1}. The narrow and wide components of the arc region have similar values of PM with respect to that of the narrow component of the control sample. We note that the control sample has a broad component with significantly different PM values. It appears that there is a stellar population with broad distribution of PM in this region, that is not found in the control region of the arm-like feature, though these are located nearby.

Two components of the arc-like structure have similar peak values of the PM with a different standard deviation. This leads to the conclusion that the arc-like structure may contain two sub-populations. However, the narrow component of the control sample shows a motion similar to that of the arc-like structure, indicating that the arc-like structure is not kinematically distinguishable from its control sample. To measure the residual PM of the arc-like structure, we subtracted the median PM of the arc-like structure from the PM of individual stars within this structure. Here also, the internal rotation is not taken into account. The spatial distribution of residual PM (Figure 5.10(e)) shows that most of the stars have the same PM as their median, as the residual is almost zero (see Figure 5.10(f)).

We noted from the FUV–optical CMD (Figure 5.10(b)) that, though the arc-like structure has stars with age ranging from 45 to 350 Myr, most of the stars have ages in the range 130–350 Myr. If the arc is formed from holes created due to material driven away by OB stars or supernovae, the age range of stars formed from the scooped-up material in the shell of such an arc will not be so large (Efremov 2002). On the other hand, it may be possible that different parts of the arc underwent collapse over a period of time. However, Figure 5.7 suggests that there is no localized age-specific star formation in the arc-like structure. Therefore, this structure is probably a random over density.

5.9 Discussion

This work presents a comprehensive study of the young population residing in the SMC Shell region using FUV observations obtained from the UVIT and optical data from Gaia. This study presents the FUV–optical catalog (Table 5.1) and FUV–optical CMD (Figure 5.2(a)) of the SMC Shell region. From the KDE map (Figure 5.3) of the SMC Shell region, we identify the arm-like and the arc-like structures, which have previously been detected within the SMC Shell region by MD2019.

The density map (Figure 5.3 and Figure 5.4(a)) represents a clumpy distribution of the young stellar population, unlike the older population in the SMC Shell region (Zaritsky et al. 2000; Noël et al. 2007). The FUV number density reduces radially outward (Figure 4, MD2019). Noël et al. (2009) found a similar surface density of the young population of the SMC Wing. Figure 5.4(b) suggests that we are able to trace the extent of the inner SMC in the NE direction at ∼2.2 deg. Also, Figure 5.4(a) reveals that the arm-like structure lies outside of the R = 2.2 deg radius, whereas the arc-like structure starts inside the R = 2.2 deg radius and extends beyond. We suggest that the arm-like and arc-like structures could be equivalent to the faint extended UV features found in external galaxies (Thilker et al. 2007).

Our study indicates that the kinematics of the young stars in the NE SMC is similar to the SMC main body. The median PM spatial map (Figure 5.8(c)) suggests that the NE part of the SMC is likely to be undisturbed (with the limits of this study; see section 5.9.1) and, therefore, unlikely to have experienced significant tidal perturbation in comparison to the wing region, which is extensively disturbed (Niederhofer et al. 2021). A relatively large scatter in median PM is visible in Figure 5.8(f) after 2.4 deg, which implies that the NE extent of the inner SMC is close to the photometric inner edge of ∼2.2 deg and the disk beyond it is tidally disturbed. De Leo et al. (2020) found the tidal radius of the SMC to be at ∼2 kpc, while analyzing the spectra of ∼3000 SMC RGB stars. Dias et al. (2022) studied the star clusters of the SMC West Halo and found the signature of tidal disruption beyond ∼2 kpc. Our result is therefore in good agreement with the above findings. The estimate of a radial distance of ∼2.2 deg as the stable kinematic extent of the SMC in the NE region will be an important input to the LMC-SMC interaction models. More studies of the outer SMC at larger radii than studied here will shed light on the outer SMC properties.

We derive that the FUV bright ($<$ 150 Myr) and sub-giant stars (150–300 Myr) display comparable kinematics. The transverse velocity dispersions obtained from our work for the above ages are similar to the radial velocity dispersion estimated by El Youssoufi et al. (2023) for the main body of the SMC. These indicate that the kinematics of the young stars in the SMC Shell region are not altered by the latest LMC-SMC interaction.

The recent work by SW2024 on the SMC Shell region revealed that it experienced increased star formation within the last few billion years. Our results (Figure 5.2 and Figure 5.6) are in agreement with SW2024, which highlights a significant episode of recent star formation approximately at 250 and 450 Myr ago. Piatti (2022) detected a peak of young cluster formation in the NE SMC Shell region at 30–200 Myr, where we detected a peak of star formation in the same age range. By considering nine young star clusters MD2019 estimated the age of the SMC Shell region as ∼150 Myr, a value within our estimated age range of star formation. The detected episode of star formation at 240–280 Myr is probably linked to the last LMC-SMC interaction (Mathewson 1985; Besla et al. 2012; Choi et al. 2022) happened at 150–300 Myr.

The spatial age map of the SMC Shell reveals that star formation in this region occurred episodically, lacking any distinct pattern of propagation in star formation, with the younger stars being formed slightly inward. The study conducted by Joshi et al. (2016) using classical Cepheids aligns with our findings, as both studies identify that the majority of star formation happened at ∼200–300 Myr. The arm-like feature is likely formed between 220–400 Myr, whereas the arc-like feature is formed between 130–350 Myr. The arc-like structure is probably younger than the arm-like structure. SW2024 highlighted that the formation of the SMC's northeastern shell is driven by the combined effects of ram pressure stripping and interactions with the MW's circumgalactic medium. The study by MD2019 reported that the formation of the SMC Shell region could be attributed to factors other than tidal effects. As this region does not show any evidence of tidal disturbance, we also rule out the tidal origin of the arm-like and arc-like features. The arm-like feature is likely to be an over density created due to multiple star formation events. We rule out any connection to the formation of the arc-like structure with star formation around shells/holes created by massive stars or supernovae.
The youngest episode of star formation, which is relatively more confined to the inner regions, is likely to be triggered by a mechanism other than the interaction with the LMC. Indu & Subramaniam (2011) found a shift of the younger population in the 40–200 Myr towards the NE of the SMC. They also noted that the direction of the line connecting the LMC to the MW is the same as that connecting the SMC to the MW. Compression of the HI gas and star formation as found in the NE of the LMC (Salem et al. 2015) due to the passage of the LMC in the MW halo, is a process that may also be happening in the NE of the SMC owing to the

motion of the LMC-SMC system in the halo of the MW. Zivick et al. (2018) suggested that the recent pericentric passage of the MCs around the MW happened around 50 Myr ago. We suggest that the youngest episode of star formation in the SMC Shell region at 40–80 Myr is probably due to the pericentric passage of the SMC around the MW.

5.9.1 List of Caveats

- In this study, the region around the Galactic globular cluster NGC 362 is excluded as this region is contaminated with the MW stars. We also point out that the UVIT has not observed the SMC Shell at larger radii, which limits our analysis of the NE extent of the inner SMC (the kinematic edge and photometric edge).
- The SMC Shell region shows continuous star formation, and to estimate the age range of star formation, we have visually overlaid isochrones on the FUV–optical CMDs. Even though the quoted age values may be subjective due to the visual overlay of isochrones, one can still notice deviation if the shift in the age of the isochrone is beyond 10% error of the estimated age as shown in Figure 5.11.
- We limit our upper age estimation at 400 Myr as stars older than that have an FUV magnitude fainter than 20 mag, which is associated with the larger photometric error (Figure 5.1 and Figure 5.2(a)).
- Another limitation of this study is the adoption of a uniform distance modulus and reddening for all the FUV sources. We assume a constant reddening value, which is representative of the total extinction towards the SMC. As our analysis primarily focuses on the outer regions of the SMC, where internal extinction is expected to be minimal, this approximation is reasonable. While small-scale spatial variations in reddening may still be present, their

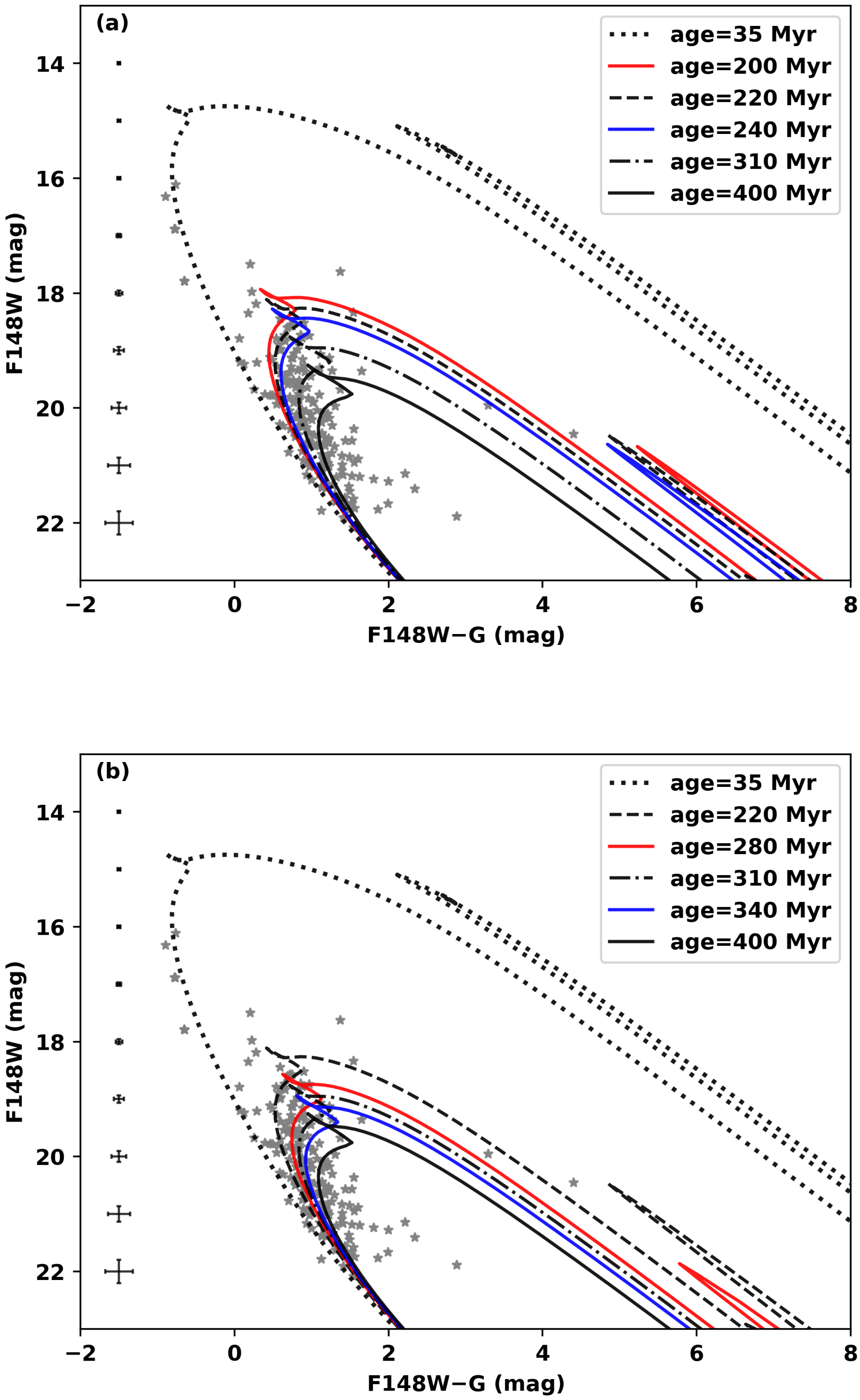

FIGURE 5.11: (a) and (b) show the FUV–optical CMDs of the arm-like structure (Figure 5.9(b)) displaying ∼10% error range for ages 220 Myr and 310 Myr, respectively.

impact on the observed magnitudes and colours is likely to be negligible and does not affect the global trends presented in this work.

5.10 Summary and Conclusions

In this study, we present a FUV map and analysis of the SMC Shell region in the NE outskirts of the SMC. A summary of the results and conclusion are given below:

- We present the first FUV map of the northeastern SMC, based on the images from the UVIT/AstroSat. The UV catalog from this study is combined with the Gaia EDR3 data set to produce an FUV–optical catalog with kinematic data. We present the photometric as well as kinematic study of young stars in this region.
- The ages estimated from the FUV–optical and optical CMDs reveal that this region is populated with a few stars as young as 7 Myr. We find that the majority of star formation happened between 60–300 Myr ago.
- The KDE spatial distribution of the FUV stars traces two distinct structures that were previously suggested: an arm-like structure and an arc-like structure. The distribution of the FUV stars shows an outward radial gradient within the SMC Shell region, and we suggest the extent of the inner SMC to be at a radial distance of ∼2.2 deg. The arm-like structure is located outside this boundary, while the arc-like structure extends from the inner SMC to the outer regions.
- The PM, as well as the velocity dispersion of young FUV stars (computed from the PM dispersion), are found to be similar to that of the SMC main

body. Therefore, we do not find any evidence of tidal perturbation or disruption in this part of the SMC.

- The arm-like and the arc-like features do not show differences in kinematics with respect to the surrounding regions. The arm-like and the arc-like structures are probably stellar over densities, which were formed at a similar period in time.
- In the SMC Shell region, we do not detect any propagation in star formation. Most parts of the SMC Shell experienced two episodes of star formation, ranging between 40 and 400 Myr ago. The episode at $\sim$260 Myr is probably linked to the recent interaction between the MCs, whereas the youngest episode at $\sim$60 Myr could be due to the pericentric passage of the SMC around the MW.

Chapter 6

Characterizing Young Massive Stars in the SMC Shell region

"To confine our attention to terrestrial matters would be to limit the human spirit." — Stephen Hawking

6.1 Introduction

Massive stars are believed to have been key contributors of ionizing radiation and mechanical feedback in galaxies during the early universe, thereby influencing cosmic re-ionization and early galaxy formation (Hopkins et al. 2014). Although direct observations of individual stars in the early universe are currently not feasible, one can consider nearby metal-poor galaxies as their analogs. The recent studies of the starburst region 30 Doradus in the nearby LMC ($Z = 0.5$ $Z_\odot$; Russell & Dopita 1990; Hunter et al. 2009; Choudhury et al. 2021; Hocdé et al. 2023) have revealed an overabundance of very massive stars (Schneider et al. 2018).

Therefore, extending the study of massive stars to the SMC ($Z = 0.2$ $Z_\odot$; Dobbie et al. 2014b; Choudhury et al. 2018; Hocdé et al. 2023) is crucial for advancing our understanding of massive star evolution in metal-poor environments. Bonanos et al. (2010) compiled a catalog of 5,324 massive stars in the SMC and showed metallicity-driven differences in IR colors compared to the LMC. Later studies revealed a dearth of young, bright massive stars, likely still embedded in natal clouds (Schootemeijer et al. 2021), and stronger chemical evolution in evolved O-type giants and supergiants (Bouret et al. 2021). Photometric surveys have expanded the census, identifying ∼2200 massive stars with UV–optical CMDs (H24b) and 7,426 with Gaia DR3 data (Nakano et al. 2025). Massive stars with masses of 5-40 $M_\odot$, younger than 150 Myr, follow a hierarchical distribution shaped by ISM turbulence (H25). Additional discoveries include candidate slowly pulsating B-type binaries (Cakırlı et al. 2023).

Understanding the properties and evolution of massive stars, whether isolated or in binary/multiple systems, is crucial, particularly in low-metallicity environments, as these are the progenitors of supernovae, neutron stars, and black holes. While spectroscopic studies provide detailed insights into stellar characteristics, they are often limited by observational constraints. To address this, we focus on the SMC Shell region, where multi-filter UV data are publicly available, and study massive stars with photometric stellar masses $\geq 2 M_\odot$ (D23) and (H24a). Previous studies have shown that this region experienced two star formation episodes (at ∼60 Myr and ∼260 Myr) with no significant tidal imprint as found in the proper motion values (H24a), while others reported a line-of-sight depth of ∼7 kpc and synchronicity between the Shell's star formation and the LMC's northern arm, linking it to the SMC–LMC–MW interaction history (SW2024). In this work, we employ multi-band photometry (UV–optical–IR) combined with fitting the observed SED with the theoretical models to investigate the intermediate massive stellar population in the Shell region (discussed in Chapter 5). In this pilot study, we explore the physical properties of a UV-selected stellar sample, which is

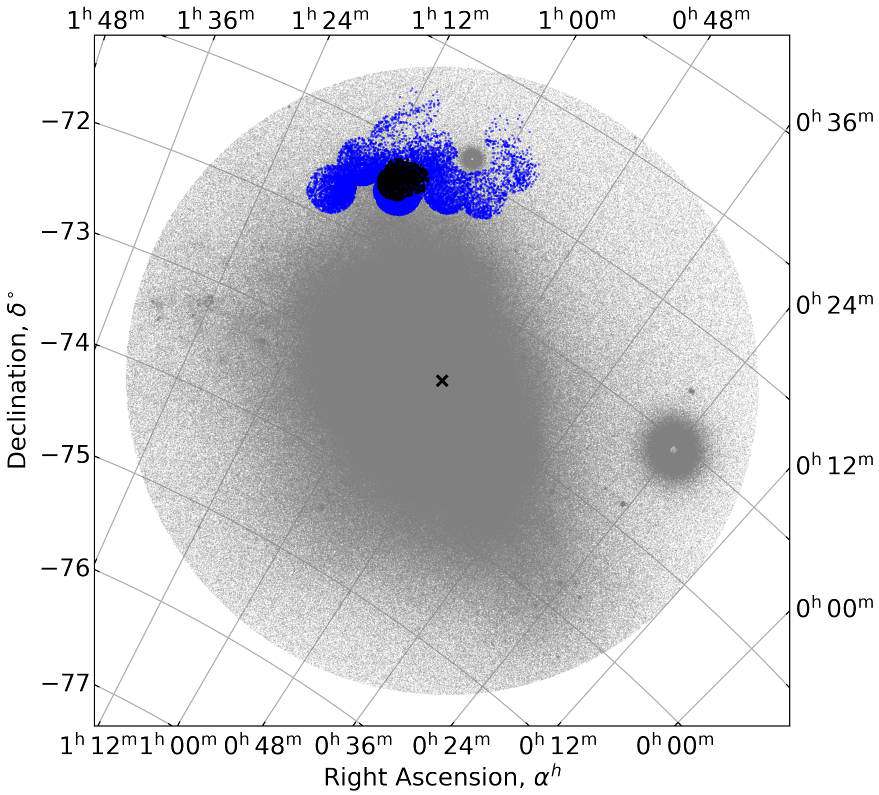

FIGURE 6.1: Gray points indicate Gaia DR3 sources (G2023) located within 3° of the SMC center, shown as the background. The UVIT-observed SMC Shell region from H24a is shown in blue, while black points mark the sample (1348 stars), including data from H24a and D23. "×" mark is the optical center of the SMC at $\alpha_{\rm SMC} = 00^{\rm h}52^{\rm m}12^{\rm s}.5$, $\delta_{\rm SMC} = -72°49'43''$ (J2000; V1972).

dominated by intermediate-mass stars with a smaller contribution from massive stars in Chapter 5. The Chapter is organized as follows: section 6.2 describes the data and sample selection, section 6.3 outlines the SEDs and fitting methodology, section 6.4 presents the results, section 6.5 discusses their implications, and section 6.6 summarizes our conclusions.

6.2 Data and Sample

6.2.1 UV data

Since UV wavelengths trace massive stars effectively, as discussed in previous Chapters, we selected a region in the SMC Shell where multi-filter UV data in the FUV and NUV bands are available. This being a pilot study, the multiple-filter UV data ensures good UV-wavelength coverage in the SED, leading to robust fitting of the SED using models. Figure 6.1 shows the UVIT-observed SMC Shell region in blue (H24a), overlaid on Gaia DR3 sources, gray points (G2023) serving as the background and black points are the stars in the sample (will discuss in section 6.2.2). We obtained the UV data, both FUV and NUV, of the selected region from the catalogs compiled by H24a and D23. Both catalogs were created using the images obtained from the UVIT (Tandon et al. 2017a). We cross-matched H24a and D23 catalogs, and ∼5300 stars are found to be in common. However, not all common UV-detected stars have flux measurements in all eight UVIT filters: four in the FUV (F148W, F154W, F169M, F172M) and four in the NUV (N245M, N263M, N279N, N219M) bands. The characteristics of the UVIT filters are described in detail by Tandon et al. (2020). Therefore, we only considered those stars which have UV fluxes in all four FUV and four NUV filters and applied a UV magnitude cut-off of 20 mag to exclude fainter sources with high photometric uncertainties.

6.2.2 Optical and near Infrared data

We combined UV data from UVIT with optical and NIR data to characterize the detected stars. For optical counterparts, we cross-matched the sources with

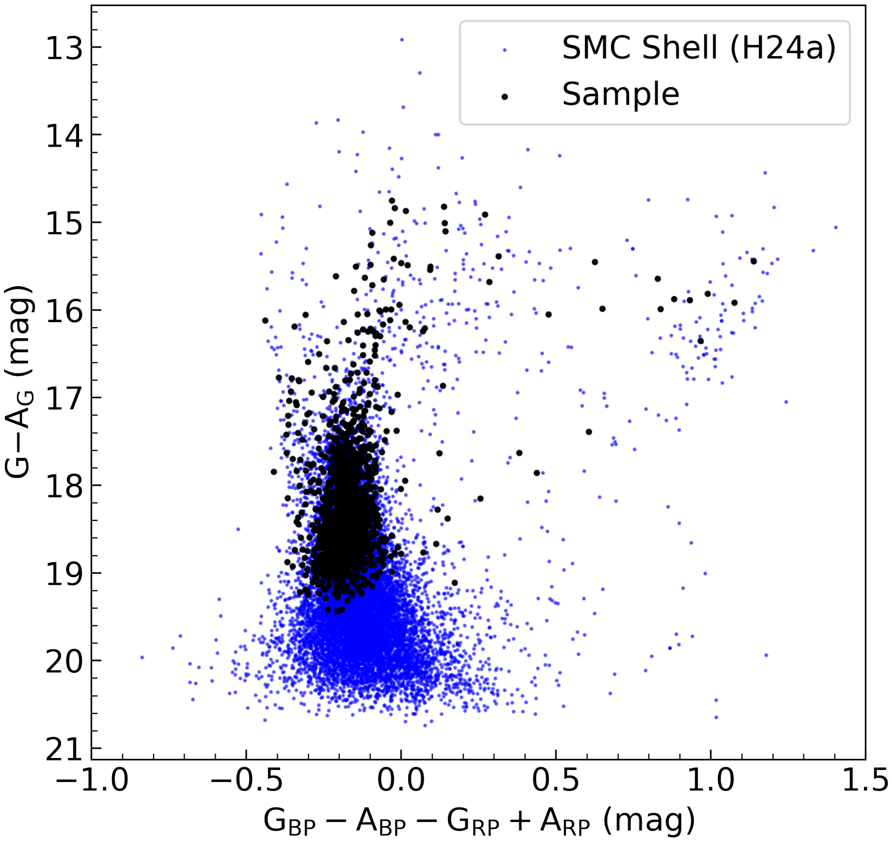

FIGURE 6.2: Extinction-corrected Gaia optical CMD showing sources in the SMC Shell region (blue points) and the selected sample (black points).

Gaia DR3 (G2023, G, G_{BP}, G_{RP}) and the SMASH (N2017; N2021, u, g, r, i). We used the VMC (C2011, Y, J, and K_s) for NIR data. All cross-matching was performed using a searching radius of $1''$. We examined the cross-matching results for duplicate associations and found no cases of multiple matches to a single source. After cross-matching across all datasets, our final sample consists of 1348 stars (black points in Figure 6.1 with flux measurements in all eighteen filters spanning the UV, optical, and NIR wavelengths. From the extinction-corrected Gaia optical CMDs (Figure 6.2) of both the SMC Shell region and our sample, we find that most sample stars are bright main sequence stars in the G-band, with a few located in the bright giant region. Extinction correction was applied

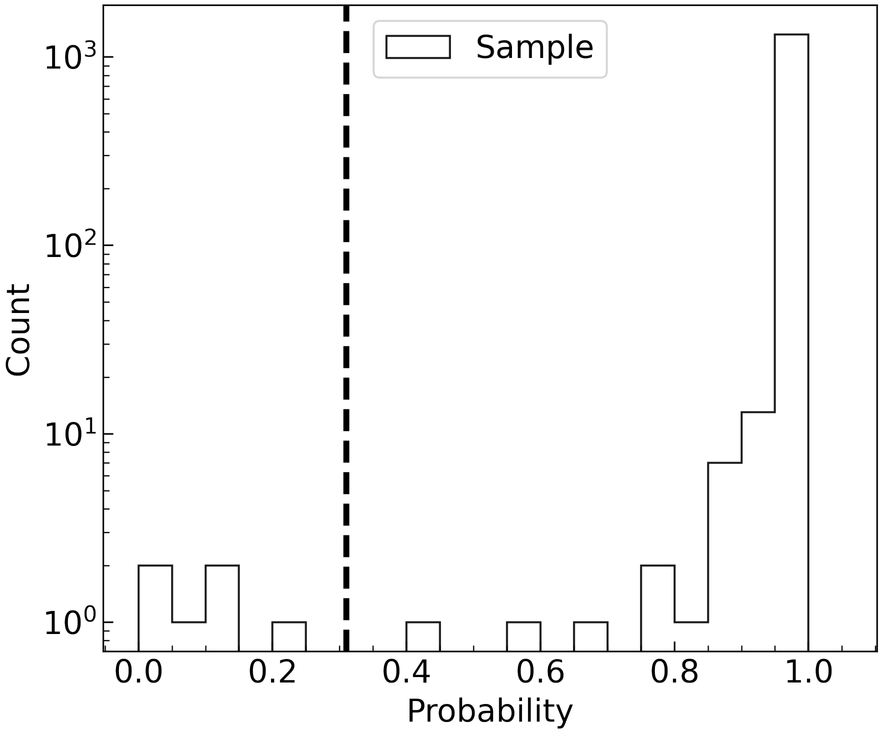

FIGURE 6.3: SMC membership probability distribution of the sample. The dashed line marks the probability threshold (0.31) for the NN-optimal sample, as defined by Jiménez-Arranz et al. (2023).

following the reddening law of Cardelli et al. (1989); O'Donnell (1994), considering $R_V = 3.1$ (Girardi et al. 2008; Gordon et al. 2024) and a mean color excess of $E(B-V) = 0.05$ (Haschke et al. 2011; Skowron et al. 2021).

6.2.3 Milky Way decontamination

H24a (see Chapter 5) performed MW foreground decontamination of the SMC Shell region by applying a 3σ cut-off to parallax, $\mu_\alpha cos\delta$, and μ_δ from Gaia EDR3 (Gaia Collaboration et al. 2021b). So our sample has already been MW decontaminated. However, a recent catalog of probable SMC stars by Jiménez-Arranz et al. (2023) employed a neural network-based classification approach, assigning membership probabilities based on astrometric and photometric properties. Based on their probability thresholds, two samples can be defined: (i) the NN-complete sample (Pcut = 0.01), which includes nearly all potential SMC members but may include MW contaminants, and (ii) the NN-optimal sample (Pcut = 0.31), representing a cleaner subset with higher membership confidence. We cross-matched our sample with this catalog. As shown in Figure 6.3, all the stars have probabilities greater than 0.01, placing them within the NN-complete sample. Moreover, except for six stars, all other stars have probabilities higher than the 0.31 threshold and fall within the NN-optimal (high-probability) sample. This indicates that our sample stars are probable SMC stars. Therefore, we consider all 1348 stars for the analysis.

6.3 Spectral Energy Distribution

In this study, we fitted theoretical SED models to the observed SEDs to estimate the physical parameters of the sample stars, such as effective temperature (T_{eff}), luminosity (L), and radius (R). For this purpose, we used the VOSA (Bayo et al. 2008). The details of single and double component SED fittings using VOSA are provided in section 2.4 of Chapter 2.

Since the multiplicity status (single or binary) of the stars in our sample was initially unknown, we performed single-component SED fitting for all 1348 stars. We adopted a uniform distance of $D = 62,440$ pc for all sources, following G2020. The SMC exhibits a substantial depth, estimated to be about 7 kpc in the Shell (SW2024). Because luminosity depends directly on distance, to quantify the variation in luminosity arising from this depth, we adopted an input distance of $D = 62,440 \pm 3,500$ pc for the SED fitting. The extinction correction was applied using the law from Cardelli et al. (1989), assuming an R_V value of 3.1 (Gordon

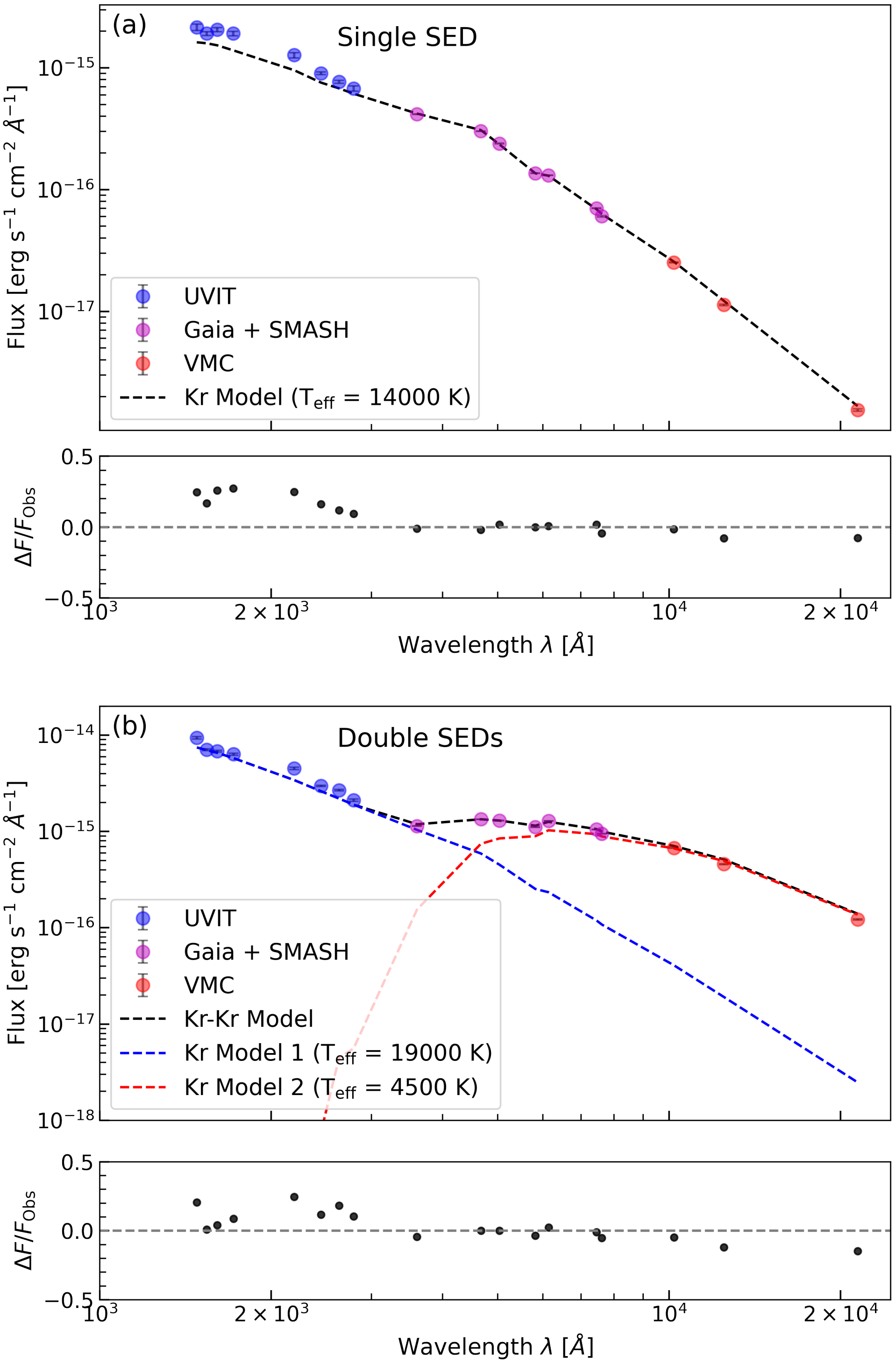

FIGURE 6.4: (a) and (b) show the single- and double-component SED fittings to the observed fluxes from UVIT, SMASH, Gaia, and VMC of sample stars. The corresponding lower panels represent the fractional residuals between the observed and model fluxes.

et al. 2024) and a mean color of $E(B-V) = 0.05$ (mean value; Haschke et al. 2011). We used the Castelli & Kurucz (Kr model; 2003) model a full parameter range with $T_{\rm eff}$ ranging from 3,500 to 50,000 K, log g from 0 to 5 dex, and a metallicity of [Fe/H] = −1, which is close to the metallicity of the SMC (Choudhury et al. 2018).

After performing single-component SED fitting for all 1348 stars, we found that 1256 stars yielded satisfactory fits, both visually and quantitatively, with $\rm vgf_b$ values below 10. An example of a well-fitted single-component SED is shown in Figure 6.4(a), corresponding to a star with an effective temperature of $T_{\rm eff} = 14{,}000$ K, where the model closely matches the observed fluxes across all bands. According to VOSA, SED fits with $\rm vgf_b$ values less than 15 are considered reliable. This criterion has also been adopted in several previous studies (Rebassa-Mansergas et al. 2019, 2021), where $\rm vgf_b < 15$ was used to identify well-fitted SEDs. The remaining stars, which either had $\rm vgf_b \geq 10$ or did not fit well visually, were considered for double SED fitting. Among the 1256 well-fitted stars, we identified 14 stars with UV excess greater than 50%. These stars were also considered for double-component SED fitting.

We performed double-component SED fitting for 106 stars using the model grids from Castelli & Kurucz (2003) for both stellar components (Kr–Kr model), adopting the same values of distance, metallicity, and extinction as used in the single-component fitting and a full parameter range with $T_{\rm eff}$ ranging from 3,500 to 50,000 K and log g from 0 to 5 dex. An example of a successful double-component SED fit is shown in Figure 6.4(b), where the binary system consists of a hot component with $T_{\rm eff} = 19{,}000$ K and a cooler companion with $T_{\rm eff} = 4{,}500$ K. The condition that the source should be detected in all 8 filters is imposed to get reliable fits of the SED and, therefore, to obtain reliable parameters for the double systems. We note that 85 stars yielded satisfactory fits, based on both visual inspection and quantitative evaluation, specifically with $\rm vgf_b$ values below 10. The remaining

21 stars, which did not satisfy these criteria, were excluded from further analysis. The conservative limits applied for detection and SED fits will impact the detected double/binary fraction (BF) in the whole sample.

We assessed the reliability of the double fits following the approach of Jadhav (2025). Each double component was modelled as a blackbody, with uncertainties derived from the observed photometry. Priors on temperature and luminosity were adopted from the SED fitting results. The SED parameters were then recovered analytically over 100 random realizations to obtain their distributions. The differences between the prior and recovered parameters were found to be minimal across all double fits, indicating that, if the systems are indeed doubles, their SED parameters can be considered reliable.

SED fitting based on broadband photometry is subject to degeneracies between effective temperature, extinction, and luminosity, which cannot be fully resolved without spectroscopic diagnostics such as the Balmer jump; moreover, unresolved binary systems—particularly those composed of similar spectral-type stars—can exhibit nearly indistinguishable SEDs, making it difficult to differentiate them from single stars.

6.4 Results

The physical properties (T_{eff}, R, L) of stars in both single and binary systems, along with their positions on the Hertzsprung–Russell (HR) diagram, are presented in the following sections.

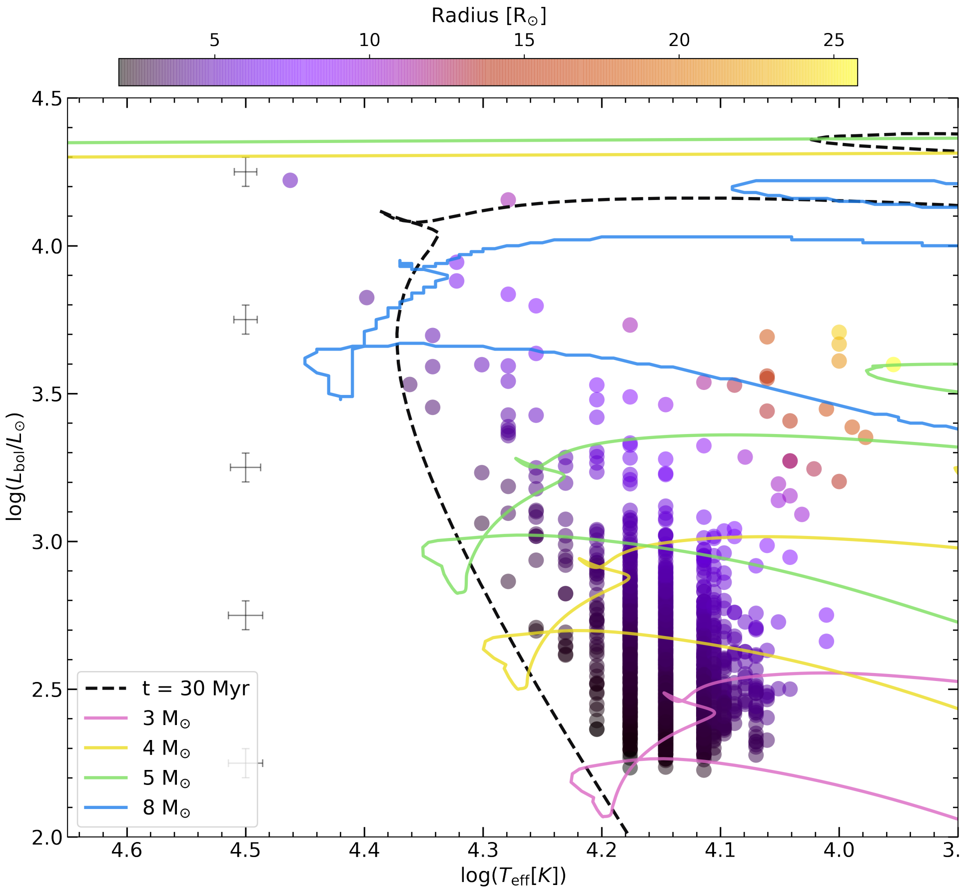

FIGURE 6.5: HR diagram of the single-star sample, showing stellar luminosity versus effective temperature. The overlaid curves include a 30 Myr Padova-PARSEC isochrone, and MIST stellar evolutionary tracks (v1.2) for stellar masses of 3, 4, 5, and 8 M$_\odot$ with a metallicity of $Z = 0.002$. The color bar indicates the stellar radius, increasing from left to right. Error bars indicate the median uncertainty in T$_{\rm eff}$ (x-axis) and the luminosity spread arising from depth effects (y-axis).

TABLE 6.1: Stellar parameters derived from single SED fitting. Columns list the object name, coordinates (RA, Dec), effective temperature ($T_{\rm eff}$), luminosity (L), radius (R), and good fit parameters such as vgf and vgf$_{\rm b}$. The first five lines of the table are shown here; the full version is available in MRT format at drive.

Gaia DR3 ID	RA [deg]	DEC [deg]	$T_{\rm eff}$ [K]	L [L$_\odot$]	R [R$_\odot$]	vgf	vgf$_{\rm b}$
4690561271762049920	17.38501	-71.56226	13000±312	569±64	4.67±0.04	4.81	0.63
4690561306121806592	17.43257	-71.56050	12500±125	594±68	5.14±0.04	3.47	0.48
4690550895121146496	17.61774	-71.55801	13000±312	347±39	3.69±0.03	6.51	0.81
4690550998200337024	17.52473	-71.55514	17000±500	413±46	2.26±0.02	15.05	1.66
4690561306139945216	17.43771	-71.55480	14000±500	488±54	3.58±0.03	15.91	2.21

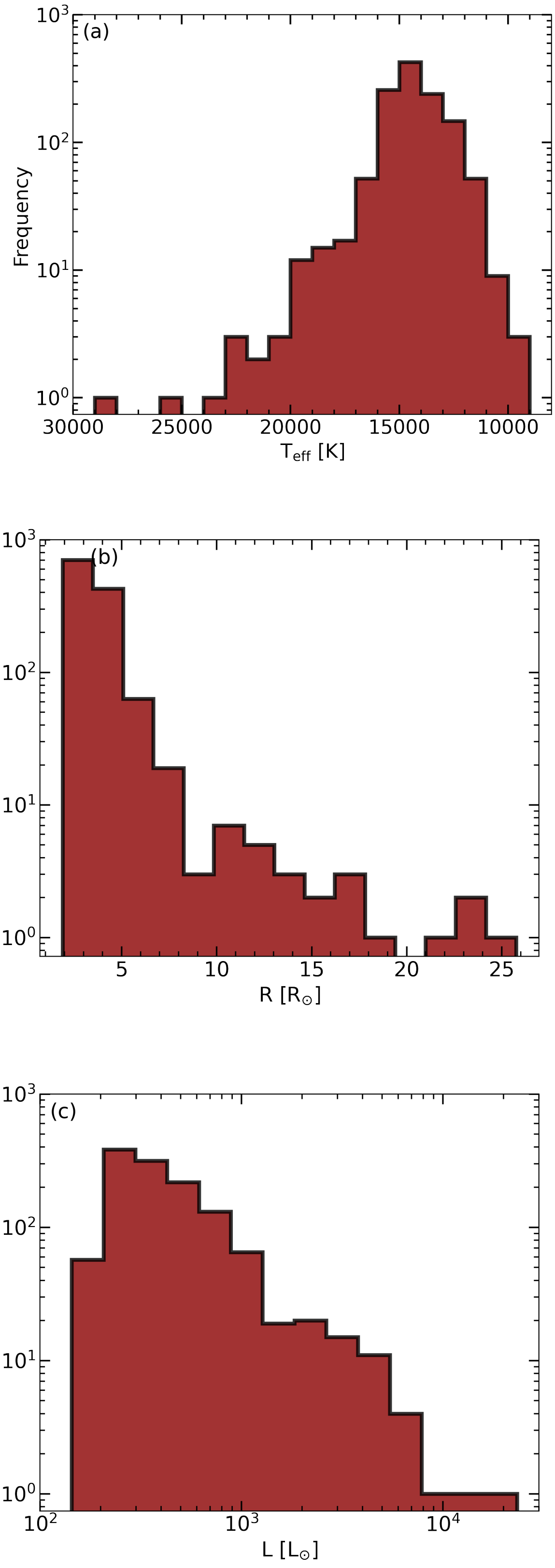

FIGURE 6.6: (a), (b), and (c) show the distribution of the stellar effective temperature (T_{eff}), radius (R), and luminosity (L), respectively.

6.4.1 Single Stars

By fitting single-component model to the observed SEDs, we identified 1242 stars that can be represented as single stars. Derived stellar parameters as well as the goodness of fit are provided in Table 6.1. These stars predominantly occupy the main sequence and the subgiant branch regions on the HR diagram as shown in Figure 6.5. Based on the location in the HR diagram, 1,213 are found to be main sequence and subgiant stars, including one late O-type star at ($\mathrm{T_{eff}}$, $\log(\mathrm{L/L_\odot})$)) = (29 kK and ∼4.22) with the majority being B-type and early A-type stars. The remaining 29 are giant stars of A- and F-spectral types.

To interpret their evolutionary stages, we overlaid an isochrone (PARSEC) from the Padova group (v2; Bressan et al. 2012) corresponding to an age of 30 Myr, assuming a metallicity of $Z = 0.002$ (Lemasle et al. 2017). In addition, we have also overlaid MIST stellar evolutionary tracks (version 1.2; Paxton et al. 2010; Dotter 2016; Choi et al. 2016) for stellar masses of 3, 4, 5, and 8 $\mathrm{M_\odot}$, adopting the same metallicity. These evolutionary tracks help in the interpretation of individual stellar positions on the HR diagram and provide context for the mass-dependent evolutionary paths of the sample. The color bar in Figure 6.5 denotes stellar radius, increasing from left to right. It can be inferred from the figure that the majority of stars are older than 30 Myr with photometric masses in the range of ∼3–8 $\mathrm{M_\odot}$. The brightest star in our HR diagram, positioned at ($\mathrm{T_{eff}}$, $\log(\mathrm{L/L_\odot})$) = (29 kK, ∼4.216), corresponds to a photometric mass estimate of ∼11 $\mathrm{M_\odot}$, placing it at the upper end of our mass distribution. In Figure 6.5, the error bars along the x-axis represent the median uncertainties in $\mathrm{T_{eff}}$, estimated within the bins of $\log(T_{\mathrm{eff}}) = [3.9, 4, 4.1, 4.2, 4.3, 4.5]$. Since the number of stars in the range , $\log(T_{\mathrm{eff}}) = 4.3$–$4.5$ is small, this interval is treated as a single bin. The error bars along the y-axis indicate the median spread in luminosity due to depth effects, computed within bins of $\log(L)$ from 2 to 4.5 in steps of 0.5.

Based on the $T_{\rm eff}$ distribution shown in Figure 6.6(a), we find a peak in $T_{\rm eff}$ between 13,000 and 15,000 K. The main sequence and subgiant stars exhibit $T_{\rm eff}$ values ranging from 10,000 K to 30,000 K, whereas the giant stars occupy a cooler range between 9,000 K and 15,000 K. Notably, a very bright post-main sequence star is present on the HR diagram at approximately ($T_{\rm eff}$, $\log(L/L_\odot)$) = (19 kK, $\sim$ 4.155), with a radius of $\sim$11 $R_\odot$. The radius distribution (Figure 6.6(b)) peaks between approximately 2 and 4 $R_\odot$. Main sequence stars and subgiants typically have radii ranging from 2 to 10 $R_\odot$, while giant stars span a larger range, from 10 to 26 $R_\odot$. The luminosity distribution (Figure 6.6(c)) shows a peak of $\log(L/L_\odot)$ = 2.3 and 2.6. Giant stars are significantly more luminous, with luminosities of $\log(L/L_\odot) = 3$ and 4, whereas main sequence and subgiant stars display a broader range of luminosity from $\log(L/L_\odot)$ = 2 to 4 .

6.4.2 Double/Binary Stars

We identified 85 stars that are well represented as a combination of two stellar models and Figure 6.7 presents their positions on the HR diagram. To interpret the evolutionary stages of these double components, we overlaid a Padova-PARSEC isochrone (v2.0 ; Bressan et al. 2012) of 30 Myr, and a metallicity of $Z = 0.002$ (Lemasle et al. 2017). In addition, we included MIST stellar evolutionary tracks (version 1.2, Paxton et al. 2010; Dotter 2016; Choi et al. 2016) for stellar masses of 2, 3, 4, 5, and 8 $M_\odot$ and a model of stripped stars by Götberg et al. (2018), considering the same metallicity, where the color bar indicates the mass of the stripped helium star in the model. The distribution of double components relative to these theoretical tracks suggests that the majority of systems are older than 30 Myr. All stars in these double systems have photometric masses exceeding 2 $M_\odot$.

For the double systems characterized in this study, the effective temperature ($T_{\rm eff}$) distributions show two distinct peaks for the cooler components, one in the range of 5–7 kK (F and G- spectral type) and another between 8000–1 kK (A and early B- spectral type). In contrast, the hotter components display a single dominant peak in their $T_{\rm eff}$ distribution at 18,000–22,000 K, as illustrated in Figure 6.8(a). The hotter components typically have $T_{\rm eff}$ values ranging approximately from 9 kK to 50 kK, while the cooler components fall within the 4 kK to 15 kK range. The radius distribution shows a strong concentration around 1–4 $R_\odot$ as shown in Figure 6.8(b). Hot components exhibit radii from 1 to 16 $R_\odot$, whereas their cooler counterparts span 2–70 $R_\odot$. In terms of luminosity, the distributions exhibit marked peaks: cooler stars peak near $\log(L/L_\odot)\sim$1.3-2.3, while hotter ones peak at $\log(L/L_\odot)=$ 2.3–3.3 (Figure 6.8(c)). Hotter components reach luminosities up to $\log(L/L_\odot)\sim$5.

We identify nine subgiant–giant double systems, represented as orange colored squares (hot components) and circles (cool components) in Figure 6.7. Their detailed stellar parameters are provided in Table 6.2. These double systems span a luminosity range of $\log(L/L_\odot)=$ 2.52-3.3. The effective temperatures of the cool and hot components lie in the ranges 4,750–5,750 K and 10,000–14,000 K, respectively. Based on their radii, the hot components are found to have sizes of $\approx$3–10 $R_\odot$, whereas the cool components exhibit significantly larger radii, between 30–70 $R_\odot$.

Notably, one double system (ID: 4690616114210976896) stands out as one of the component is found to be extremely hot and luminous, located at ($T_{\rm eff}$, $\log(L/L_\odot)$) = (50 kK, $\sim$3.87), while its other component appears to be a lower-mass subgiant star with ($T_{\rm eff}$, $\log(L/L_\odot)$) $\simeq$ (10.25 kK, $\sim$ 2.406). The hot and luminous component of the double system is also located on the bluer side of the main sequence branch and near the predicted location of stripped stars in the HR diagram, making it a candidate for a hot, compact helium star—possibly a product of binary mass transfer or envelope stripping. We note that out of 85, 18 double systems (shown as blue squares for hotter and blue circles for cooler companions in Figure 6.7) have hotter companions are likely to be stripped stars (including the hottest and bluest one, mentioned in the previous line), as these are located near the stripped star model (shown in gray gradient circles). As stripping requires interaction in a binary system, these 18 double systems are likely to be binary systems, and their details are provided in Table 6.3, with the hotter components likely to be stripped stars.

A recent study on the young open cluster NGC 663 by Nedhath et al. (2025) reported that 19 out of 23 Be stars in the cluster exhibited significant UV excess and were characterized as sdOB+Be binary systems. For comparison, we overlaid the HR diagram positions of 16 sdOB+Be binary systems of NGC 663 shown in black squares (hot) and black circles (cool) in Figure 6.7. We find that both the hot and cool components of 18 binary systems in our sample occupy similar temperature and luminosity ranges as those identified in the NGC 663 study, supporting their binary nature. From the model of stripped stars by Götberg et al. (2018), we note that the mass of the hot companions ranges from 0.5 to 3 $M_\odot$. Such objects play a role in binary evolution and may be precursors to type Ib/c supernovae, or even gravitational wave progenitors (Götberg et al. 2018; Karamehmetoglu et al. 2023; Hovis-Afflerbach et al. 2025). Spectroscopic follow-up would be essential to confirm their nature and further constrain their evolutionary states.

In Figure Figure 6.7, we have shown 20 double systems, where magenta squares indicate the hotter component, and circles represent the cooler component. The hotter stars are located close to the main sequence with masses of about $\geq$3 $M_\odot$, while the cooler companions are found to be slightly away from the main sequence with approximate masses near 2 $M_\odot$. The hotter components of these systems are found to be similar to the low luminous stripped stars found in this study (stars shown in blue squares), though slightly cooler. Similarly, the cooler components of these systems are similar to the cooler components of the stripped systems (stars shown in blue circles), though slightly less luminous. It is possible that there is an evolutionary link between these 20 double systems and the 18 double systems. Therefore, we designate these as 20 candidate binary systems. The detailed stellar parameters of these systems will be presented in the MRT table, following the same tabular format as used in Table 6.2 and Table 6.3 at https://drive.google.com/drive/folders/1I8RAzUTi9TYjpv36Qf5uIvxbvDp3jThO?usp=sharing.

As a next step, we have shown 38 double systems, where the hot components (shown as cyan squares) are predominantly located along the main sequence branch, with a smaller fraction positioned near the location of giant stars. The corresponding cool components (cyan circles) lie primarily in the relatively cooler part of the location for giants. Such configurations may represent a genuine binary system composed of a hot and a cool star, or, a single star surrounded by a circumstellar disk or a combination due to chance projection due to the depth of the SMC. The details of these systems are discussed later. The comprehensive stellar parameters of these systems will be listed in the MRT table, adopting the same tabular structure as Table 6.2 and Table 6.3 at https://drive.google.com/drive/folders/1I8RAzUTi9TYjpv36Qf5uIvxbvDp3jThO?usp=sharing.

From the spatial distribution of single and double stars shown in Figure 6.8(d), we observe that both populations are more or less evenly spread across the sampled region of the SMC Shell, with no prominent clustering or localized enhancement.

6.5 Discussion

In this section, we first discuss sources that are in common with previous studies and compare their derived properties. We cross-matched our single-star sample

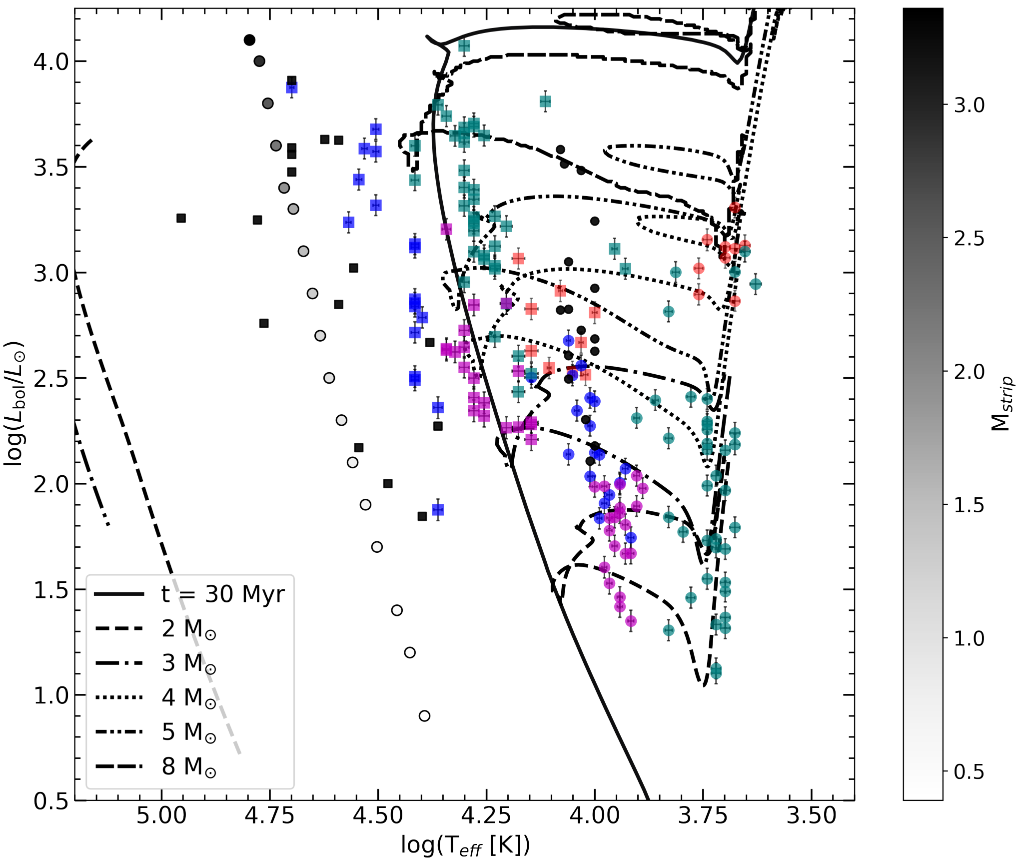

FIGURE 6.7: HR diagram of the double/binary systems, showing stellar luminosity versus effective temperature. Squares and circles denote the hot and cool components, respectively. Stripped binaries, giant–giant pairs, and candidate binaries are shown in blue, orange, and magenta, while systems that may represent either binaries or stars with disks are indicated in cyan. Overplotted are evolutionary references: a PARSEC (Padova v2) isochrone of 30 Myr with metallicity $Z = 0.002$, MIST stellar evolutionary tracks (v1.2) for stellar masses of 2, 3, 4, 5, and 8 $M_{\odot}$, and stripped-star models from Götberg et al. (2018), all at the same metallicity. The color bar indicates the stripped star's mass. Black markers represent the stripped binary systems in the young star cluster NGC 663, as reported by Nedhath et al. (2025).

with the OGLE-IV eclipsing binary catalog from Głowacki et al. (2024), identifying 23 common stars. A further cross-match with SIMBAD revealed additional classifications: two emission-line stars, three pulsating variables, four probable white dwarf candidates, and one object listed simply as a "star", all of which are shown in Figure 6.9(a). SIMBAD also provided eight more eclipsing binaries not

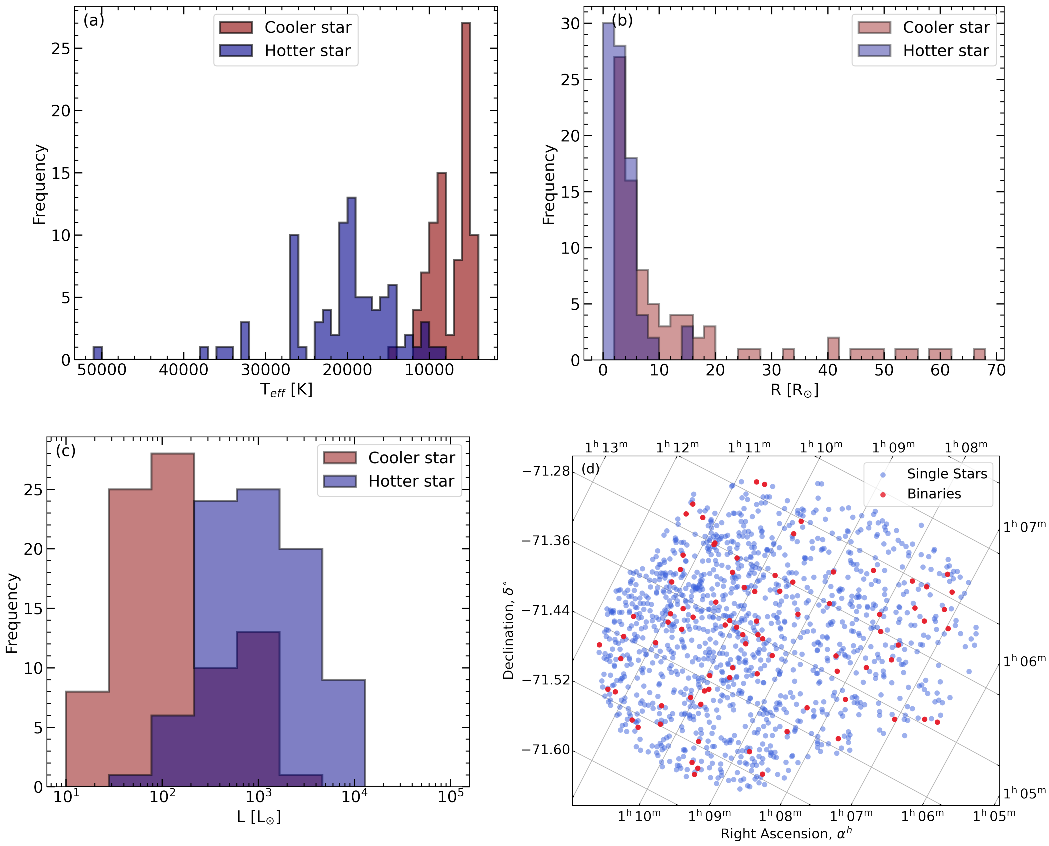

FIGURE 6.8: (a), (b), and (c) show the distribution of the stellar effective temperature (T_{eff}), radius (R), and luminosity (L), respectively, for both the components of the double systems. (d) Spatial distribution of the single and double systems.

included in the OGLE-IV catalog. The emission-line stars appear as luminous objects with effective temperatures of 18,000–19,000 K, while the four white dwarf candidates occupy positions consistent with low-luminosity main sequence stars. The object labeled as a generic star is likely a late B-type star based on its HR diagram location. Of the three pulsating variables, one is notably hotter and more luminous than the others. The eclipsing binaries lie along the main sequence with effective temperatures of 12,000–15,000 K and luminosities of about $\log(L/L_\odot)\sim$ 2.3 to 3. We note that the majority of these eclipsing systems are non-contact binaries with periods shorter than 5 days, while a smaller fraction have periods between 5 and 10 days, and only two systems exhibit longer periods of 40–50 days (Pawlak et al. 2013, 2016; Gaia Collaboration 2022). A total of 31 stars classified

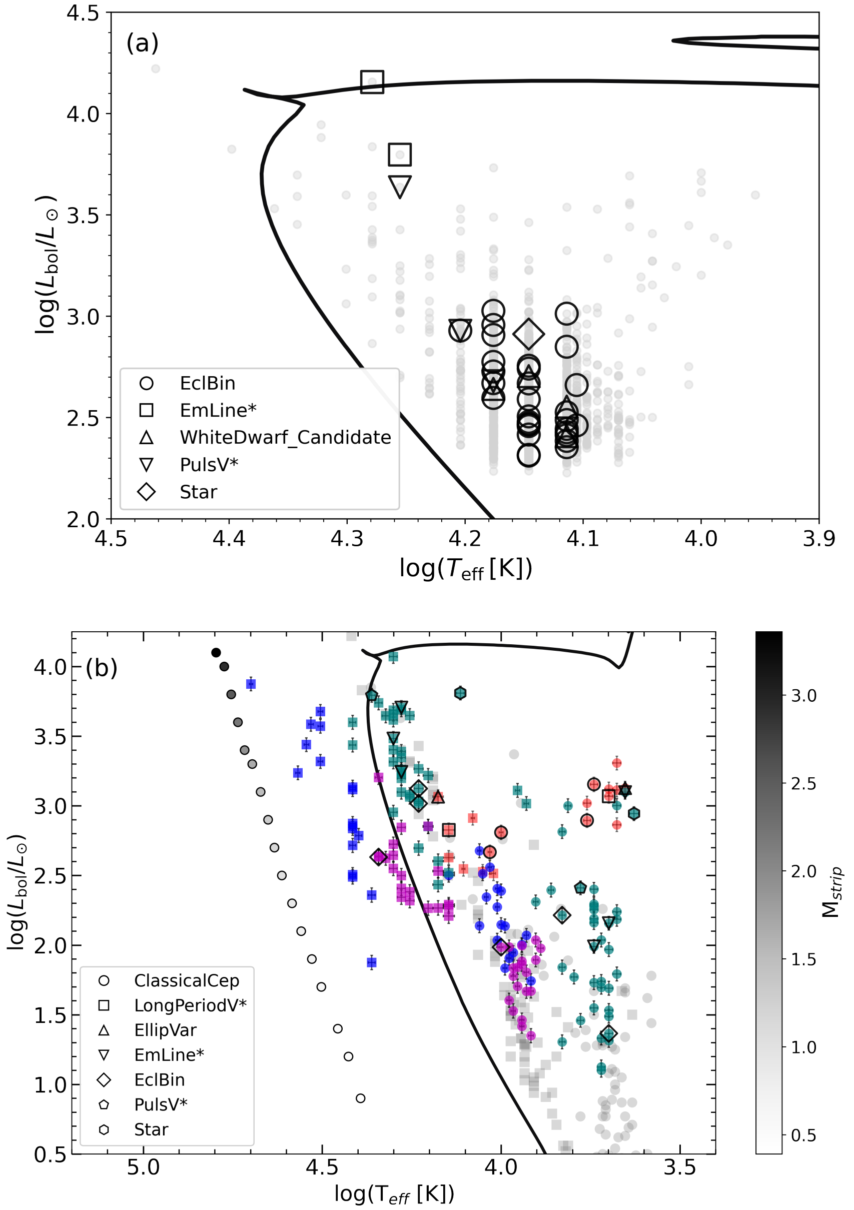

FIGURE 6.9: HRDs of the cross-matched single and binary systems are shown in panels (a) and (b), respectively. The black curve represents the 30 Myr Padova–PARSEC isochrone. Different marker shapes indicate various system types. (a) Gray points represent all single stars. (b) Stripped-star models with metallicity $Z = 0.002$ from Götberg et al. (2018) are shown as a grayscale colormap, where the color bar denotes the stripped-star mass. Colored markers follow the same scheme as in Figure 6.7. Gray squares and circles mark the hot and cool components of Algol-type eclipsing binaries from Giuricin et al. (1983).

Table 6.2: Stellar parameters derived from double-SED fitting of 9 subgiant-giant binary systems. Columns list the object name, coordinates (RA, Dec), binary component identifier, effective temperature ($T_{\rm eff}$), luminosity (L), radius (R), vgf and vgf$_{\rm b}$ fitting parameters.

Gaia DR3 ID	RA [deg]	DEC [deg]	Component	$T_{\rm eff}$ [K]	L [$L_\odot$]	R [$R_\odot$]	vgf	vgf$_{\rm b}$
4690566326946556928	17.11296	-71.45074	Hot	11250±125	337±39	4.7±0.04	11.85	1.98
			Cool	4750±125	2028±229	66.51±0.5		
4690567323379709312	17.48822	-71.43315	Hot	10000±125	645±77	8.21±0.06	26.73	1.62
			Cool	5500±125	1427±170	40.43±0.3		
4690657655117367808	17.86518	-71.41048	Cool	5750±125	786±91	27.56±0.21	24.17	2.49
			Hot	10750±125	465±54	5.95±0.04		
4690614705461743488	17.04936	-71.35181	Hot	12750±125	352±41	3.66±0.03	30.51	2.84
			Cool	4750±125	1297±147	53.18±0.4		
4690663152675448320	17.71166	-71.27854	Hot	14000±500	670±78	4.19±0.03	44.79	3.13
			Cool	5000±125	1172±133	45.97±0.35		
4690620065581050240	17.24513	-71.24103	Hot	10500±125	327±38	5.41±0.04	8.36	1.30
			Cool	4750±125	732±83	40.15±0.3		
4690563853045370112	17.73955	-71.42756	Hot	15000±500	1163±134	4.91±0.04	24.95	1.34
			Cool	4500±125	1341±152	60.89±0.46		
4690564883837503744	17.73314	-71.39664	Hot	14000±500	425±49	3.37±0.03	20.72	1.99
			Cool	5750±125	1046±118	32.66±0.25		
4690631576093401344	16.95455	-71.20382	Cool	5000±125	1321±150	48.58±0.37	9.79	0.97
			Hot	12000±125	817±94	6.49±0.05		

as eclipsing binaries in OGLE-IV or SIMBAD were not recognized as binaries in our analysis. This reflects the complementary nature of variability surveys and SED fitting techniques. Our method is most sensitive to systems with comparably bright components or strong multi-band flux contributions, but can miss binaries with faint companions or nearly equal-temperature stars that mimic single-star SEDs (Torres et al. 2011; Prša & Zwitter 2009; El-Badry & Rix 2021). These factors suggest that the 31 eclipsing binaries classified as single in our study are likely to be systems where the SED is dominated by the primary component and/or with similar multi-band flux contribution.

We cross-matched the double systems found in this study with SIMBAD and OGLE-IV catalogs (Figure 6.9(b)). This yielded three eclipsing binaries (two from OGLE-IV and one from SIMBAD), along with one ellipsoidal variable and

Table 6.3: Stellar parameters derived from double-SED fitting of 18 stripped star binary systems. Columns list the object name, coordinates (RA, Dec), binary component effective temperature ($T_{\rm eff}$), luminosity (L), radius (R), vgf and vgf$_{\rm b}$ fitting parameters.

Gaia DR3	RA [deg]	DEC [deg]	Component	$T_{\rm eff}$ [K]	L [L$_\odot$]	R [R$_\odot$]	vgf	vgf$_{\rm b}$
4690561546640027520	17.35959	-71.54599	Cool	8250±125	55 ±6	3.59±0.03	23.91	4.64
			Hot	23000±500	229 ±27	0.96±0.01		
4690562925322914688	17.57385	-71.51793	Cool	11000±125	221 ±25	3.96±0.03	42.75	2.39
			Hot	26000±500	1310 ±151	1.71±0.01		
4690568491600388992	17.42029	-71.37551	Cool	8750±125	101 ±12	4.24±0.03	73.02	3.29
			Hot	37000±500	1726 ±197	1 ±0.01		
4690661842707993088	17.78499	-71.32918	Cool	11500±125	138 ±16	2.91±0.02	21.62	1.32
			Hot	25000±500	612 ±71	1.29±0.01		
4690616114210976896	17.48419	-71.31043	Hot	50000±500	7498 ±845	1.15±0.01	80.71	3.23
			Cool	10250±125	255 ±29	4.95±0.04		
4690619030483415680	16.97133	-71.28030	Hot	26000±500	747 ±86	1.31±0.01	12.53	0.85
			Cool	9250±125	88 ±10	3.62±0.03		
4690616457808340096	17.44227	-71.27976	Hot	32000±500	2080 ±237	1.46±0.01	43.36	1.74
			Cool	8500±125	118 ±13	4.94±0.04		
4690551414820128000	17.82350	-71.50887	Cool	10750±125	362 ±41	5.38±0.04	49.98	2.01
			Hot	32000±500	4764 ±542	2.2±0.02		
4690563024129871872	17.60317	-71.49622	Cool	10250±125	108 ±13	3.24±0.02	18.29	1.31
			Hot	26000±500	520 ±60	1.09±0.01		
4690567495177634176	17.42234	-71.41060	Cool	14000±500	318 ±37	3 ±0.02	13.22	0.86
			Hot	23000±500	75 ±9	0.54±0.004		
4690567903213093120	17.70460	-71.37247	Cool	9750±125	137 ±16	3.96±0.03	36.18	3.06
			Hot	26000±500	321 ±38	0.83±0.01		
4690568525960116480	17.48265	-71.36184	Hot	26000±500	1361 ±156	1.76±0.01	45.35	1.89
			Cool	11250±125	325 ±37	4.62±0.03		
4690568697768450304	17.39422	-71.35772	Cool	10000±125	245 ±28	5.16±0.04	36.02	1.44
			Hot	34000±500	3855 ±438	1.77±0.01		
4690619069148475392	16.88405	-71.28496	Hot	26000±500	689 ±79	1.25±0.01	46.18	2.59
			Cool	9500±125	81 ±9	3.23±0.02		
4690611922322952704	16.75898	-71.37162	Cool	10000±125	140 ±16	3.84±0.03	47.06	2.92
			Hot	26000±500	715 ±83	1.25±0.01		
4690619412745838720	17.00641	-71.26144	Cool	10250±125	188 ±21	4.28±0.03	45.87	1.84
			Hot	35000±500	2748 ±313	1.41±0.01		
4690632160208733184	16.79635	-71.19230	Cool	11500±125	475 ±54	5.26±0.04	86.75	3.59
			Hot	32000±500	3731 ±426	1.92±0.01		
4690632297642107904	16.84528	-71.17474	Hot	26000±500	309 ±36	0.85±0.01	12.21	1.32
			Cool	9750±125	68 ±8	2.85±0.02		

one long-period variable. Both the ellipsoidal and long-period variables are located on subgiant–giant binary systems (orange markers). Two systems include classical Cepheids as the cooler components, paired with hotter subgiant companions. These Cepheids fall within the instability strip, consistent with the region shown in Figure 2 of Groenewegen (2025). In addition, we identify one pulsating binary system consisting of a main sequence–giant pair, where the hotter component is both luminous ($\log(L/L_\odot) \sim 3.75$) and hot (Teff $\sim 20,000$ K). Another system is simply listed as a “star” in SIMBAD. Three binaries are associated with emission-line stars. All of them lie on the main sequence and show similar effective temperatures and luminosities to the single emission-line stars identified from SIMBAD. Their cooler companions have $T_{\rm eff} \sim 5,000$ K. We identify 38 systems (cyan markers) in our sample of double systems where the hot component is highly luminous and the cool component appears faint. The nature of these systems is not fully constrained. One possibility is that they are single emission-line stars, similar to those we identified through SIMBAD cross-matching: in such cases, the stellar surface produces the hot component while a circumstellar disk contributes the apparent cool excess. Alternatively, they may be Algol-type binaries. To test this, we compared their locations in the HR diagram with the hot and cool components of known Algol systems from Giuricin et al. (1983) (gray squares and circles in Figure 6.9(b), respectively). We find that both components of these 38 systems lie in similar loci to Algol binaries. Notably, two eclipsing binaries in our sample also fall within this region. Their short orbital periods (¡5 days) and non-contact configurations strongly support an Algol-type interpretation (Pawlak et al. 2013, 2016; Gaia Collaboration 2022).

Drout et al. (2023) proposed theoretical predictions for stripped binary systems in the MCs by modelling a grid of hot, core-helium-burning stripped stars paired with main sequence companions. Their work showed that stripped stars should appear blueward of the ZAMS in UV–optical CMDs when the companion is either a low-mass main sequence star ($M \lesssim 8\ M_\odot$) or a compact object. Consistent with these predictions, we find that the hot companions in our identified stripped binaries are located on the blue side of the ZAMS, while their cool companions have masses ≤ 4 $M_\odot$. Ludwig et al. (2026) used 2,420 Swift-UVOT images of the LMC and SMC to construct a catalog of 734,869 sources in three UV filters, reaching to a depth of ∼20 Vega mag. They identified candidate stripped systems by selecting sources that lie blueward of the ZAMS in multiple UV–optical CMDs, after correcting for distance and extinction, and then applying quality cuts to ensure that the SEDs were consistent with stripped-star binaries while excluding spurious sources affected by poor photometry or systematics. From this procedure, they reported 298 candidate stripped stars in the SMC. In comparison, this study has identified 18 stripped binary systems. While this number is smaller, our detections are complementary to their study, as our sample probes the outskirts of the SMC, whereas their study covers the SMC main body. This suggests that stripped systems are present not only in the dense central regions but also in the less crowded outer parts of the SMC.

One limitation of our SED-fitting analysis is the assumption of a uniform distance for all stars. Given the intrinsic depth of the SMC, this simplification can introduce uncertainties in the derived stellar parameters, particularly luminosities. To quantify this effect, we propagated the depth as a distance uncertainty and examined its impact on the inferred luminosities. While this leads to moderate variations, the positions of the stars in the HR diagram remain consistent, suggesting that the stellar classifications are robust to distance uncertainties within the SMC's depth. A second caveat arises by considering the same extinction value for all stars, despite the spatial variations in extinction across the SMC (Gordon et al. 2024). However, since our sample is taken from a relatively compact region in the outer SMC, where extinction gradients are expected to be modest, the influence of spatially varying extinction on the derived parameters is likely to be minimal.

Recent studies have begun to constrain the BF of massive stars in the SMC across different evolutionary phases. Speckle imaging of massive young stellar objects (YSOs: M $\gtrsim$8 $M_{\odot}$) indicates a wide BF of $< 5\%$ (Kalari et al. 2024), significantly lower than the ∼15–60% wide BF reported in the MW, suggesting a role for metallicity and environment in shaping binary formation and survival. For more evolved populations, Dai et al. (2025) estimated a BF of $32.2 \pm 1\%$ for red supergiants in the SMC, while spectroscopic monitoring of 262 blue supergiants (BSG; B0–B3, I–II) revealed an observed fraction of $34 \pm 3\%$, consistent with an intrinsic fraction of $40 \pm 4\%$ (Britavskiy et al. 2025). The latter study also reported a decline in binary incidence for BSGs cooler than $T_{\rm eff} \sim$ 18kK, consistent with a transition toward post-main sequence evolution, and found no evidence for metallicity dependence compared to Galactic and LMC populations.

In our sample of 1,348 stars, we identified 85 double systems and 1,242 single stars, yielding an upper limit of BF of ∼6.3% (if all systems are considered as binaries) for stars with masses between 2–8 $M_{\odot}$ in an outer region of the SMC. This relatively low fraction likely reflects a combination of factors. First, our SED-fitting method is primarily sensitive to binaries with companions of comparable brightness with significantly differing in surface temperature, and may miss systems with faint or nearly identical-temperature secondaries. Indeed, upon cross-matching with OGLE-IV and SIMBAD, we identified 31 additional systems classified as eclipsing binaries that were not flagged as binaries in our analysis. Second, our strict sample selection—requiring flux measurements across 18 UV-to-NIR filters—may preferentially exclude stars with incomplete photometry, may introduce bias against certain binary configurations. Together, these effects contribute to the lower BF we measure compared to other studies.

We note that the advantage of this study is the coverage of data points in the UV region, thereby providing a better characterisation of SED for intermediate mass and high mass stars. This study also preferentially characterizes UV bright stars. Also, the coverage in the UV region has helped to detect and characterize the stripped binaries present in the region with good confidence. The characteristics of the stripped star binaries presented here can place important constraints on the formation and evolution of such systems. Upcoming LSST (Ivezić et al. 2019) and 4MOST (de Jong et al. 2019) data will provide the necessary variability, spectral, as well as orbital information to further probe their formation pathways. In the future, we shall extend this method to characterize UV stars across the SMC using the UV catalog of H24b.

6.6 Summary and Conclusions

In this study, we looked over a sample of 1348 UV bright stars located in the SMC's northeastern outskirts, the Shell, using UVIT (FUV and NUV bands), SMASH, Gaia, and VMC photometric data. Through SED fitting using VOSA, we derived key stellar parameters including effective temperature, luminosity, and radius. The main findings are summarized below:

- We identified 1,242 stars that are well described by single-component SEDs. These are predominantly B- and A-type main sequence and subgiant stars with masses of 3–8 $M_\odot$ and effective temperatures of 10,000–30,000 K, along with a small number of giants spanning T_{eff} ∼9,000–15,000 K and radii of 10–26 $R_\odot$.
- We identified 85 systems requiring two-component SED fits, which can be broadly classified into four categories: (1) stripped-star binaries, (2) subgiant–giant systems, (3) candidate binary systems with a possible evolutionary link to the stripped systems, and (4) systems that may represent either non-contact binaries or single stars with circumstellar disks or foreground stars.

- We found 18 stripped-star binaries, which contribute to our understanding of post-interaction binaries and their role as potential progenitors of exotic systems, such as type Ib/c supernovae or compact object binaries. Further spectroscopic studies are necessary to characterize them.

- Among the 85 double systems, 38 could be Algol-type eclipsing binaries, as suggested by their location in the HR diagram. Alternatively, they may represent stars with circumstellar disks, where the identified cool component corresponds to the circumstellar disk. A further possibility is that some of these systems arise from chance projections due to the depth of the SMC.

- In our sample, we identified 9 systems composed of subgiant–giant pairs, which are possible binary systems.

- 20 candidate binary systems were identified, which have hot companions similar to the low luminous stripped stars, but slightly cooler and hot companions similar to the low luminous cooler companions of the stripped stars. These require further studies to confirm their nature.

- The spatial distribution of both single and binary/double systems is broadly uniform across the Shell region, ruling out any clustered distribution.

- Cross-matching with OGLE-IV and SIMBAD catalogs revealed 31 eclipsing binaries that were not flagged as binaries in our SED analysis. These cases highlight an inherent limitation of photometric SED fitting, which may fail to resolve binaries where one component dominates the flux or where both stars have nearly identical temperatures.

- We estimated the binary/double fraction for stars with masses in the range of $\sim$2–8 $M_\odot$ to be $\approx$6.3%. This relatively low fraction may be partly attributable to our strict sample selection criteria, as well as intrinsic limitations of the SED-fitting method, which can fail to distinguish binary components when the stars have similar effective temperatures. This study has preferentially characterized UV bright and luminous stars and has helped to identify and characterize stripped star systems in this region.

This work underscores the utility of UV–optical–IR SED fitting in probing the physical properties and multiplicity of young intermediate and high mass stars in nearby low-metallicity environments. The combination of UVIT with deep optical and IR surveys offers a robust framework for identifying and characterizing both single and binary/double stellar populations. Future high-resolution spectroscopic follow-up of our candidate binaries can validate their nature, refine BFs, and offer insights into the impact of the environment on massive binary evolution in dwarf galaxies.

Chapter 7

Summary, Conclusions and Future Work

"Astronomy compels the soul to look upward, and leads us from this world to another." — Plato

7.1 Summary and Conclusions

This thesis has presented a comprehensive investigation of the SMC's young massive stars, examining their spatial distribution, kinematics, age-dating, and physical characteristics in the broader context of the galaxy's dynamical evolution. This is achieved using a multi-wavelength dataset that is constructed utilizing the superior spatial resolution of UVIT, in combination with complementary optical and NIR data from surveys such as Gaia, SMASH, and VMC. The primary motivation was to understand the imprints of the recent LMC-SMC interactions as traced by the massive stars as they form in the dynamically perturbed, low-metallicity environment of the galaxy. Conclusions from this study, based on the morphology, kinematics, age-dating, and characterization of single and double systems are presented below.

Construction of the first large-scale FUV catalog of the SMC

We produced a catalog of ~76,800 FUV stars in the main body and the Wing, cross-matched with Gaia and VMC catalogs. After careful foreground removal, ~62,900 stars were identified as probable members of the SMC through robust classification methods. This dataset provides a critical foundation for studying massive stars in metal-poor environments, as it includes 2,200 stars brighter than 15 mag in FUV, corresponding to a photometric mass of M > 8 $M_\odot$. This is a very valuable resource to study various types of massive stars in the SMC and their UV properties. This will serve as the input data to the future missions such as UVEX, INSIST etc.

Morphology and kinematics of the SMC

The FUV catalog traces the major stellar structures of the SMC, including the Wing, Bar, and shell. The morphology revealed clumpy stellar distributions, while the kinematic analysis showed evidence of sub-populations with distinct motions, particularly in stars younger than ~150 Myr. The results indicate that the latest encounter with the LMC has left imprints on the SMC's young massive stars. The kinematic details found in the young massive stars provide important constraints for the LMC-SMC interaction models.

Hierarchical star formation and fractal nature

Our study uncovered 236 young stellar structures with age ≤150 Myr and photometric mass of 5 to 40 $M_\odot$. Their sizes cover a broad range, from just a few parsecs to hundreds of parsecs. Their properties—sizes, surface densities, and number distributions—were shown to follow scaling relations characteristic of hierarchical star formation. The derived fractal and perimeter-area dimensions ($D_2 \sim$ 1.3–1.6,

$D_p \sim 1.46$) are consistent with those observed in other galaxies and with theoretical expectations from turbulence-driven star formation. These results provide compelling evidence that young massive stellar structures in the SMC inherit their fractal imprint from the turbulent ISM, with the hierarchical pattern persisting up to ages of ∼200 Myr in the SMC.

Mapping the northeastern Shell region

The first FUV map of the northeastern outskirts of the SMC, the SMC Shell, traced two extended features—an arm-like and an arc-like structure. Despite their prominence in stellar density maps, both features have similar kinematic properties with the control sample, suggesting that they are overdensities rather than tidally stripped or dynamically distinct substructures. The region has experienced multiple episodes of star formation over the last 400 Myr, including one around ∼260 Myr, likely linked to the Clouds' last close encounter, and another around ∼60 Myr, possibly triggered by the SMC's motion around the MW. The proper motions and velocity dispersions of young FUV stars of the Shell are similar to those of the main body, indicating no significant signs of tidal perturbation or disruption in this region. These findings establish that the Shell region, though located in the north-eastern outskirts, has been influenced by the recent interactions, resulting only in star formation with local densities. This provides important constraints to the LMC-SMC interaction models.

Physical properties and binarity of UV-bright stars

Through SED fitting of 1,348 stars of the sample region within the SMC Shell, we derived effective temperatures, luminosities, and radii. We identified 1242 single stars, mostly B- and A-type main sequence stars, along with a small population of giants, and 85 systems requiring two-component fits, including stripped-star binaries, subgiant–giant pairs, and candidate binary systems. Eighteen stripped-star binaries were recognized as potential progenitors of exotic systems such as type Ib/c supernovae. 38 double systems are found to be non-contact binaries or stars with circumstellar disks or foreground stars. The binary fraction was estimated at ∼6.3%, lower than expected, likely due to methodological and selection biases. These results highlight the effectiveness of UV–optical–IR SED fitting in identifying massive stellar populations and stripped binaries in low-metallicity environments, while also emphasizing the need for spectroscopic follow-up to refine binary properties and advance our understanding of massive star evolution in the SMC.

7.1.1 Utilization and Prospects of Thesis

The results of this thesis open multiple avenues for future research:

- Community resource: The FUV catalog (with better spatial resolution) of ∼76,800 sources, including ∼62,900 probable members, is a rich dataset for the community to study young and massive stars in the SMC. It can serve as a reference for young stellar population analyses, massive star catalogs, and preparations for future missions.
- Massive star evolution at low metallicity: The identified sample of stripped-star binaries and candidate massive binaries provides excellent targets for spectroscopic follow-up with ground-based telescopes to constrain evolutionary pathways toward supernovae and compact binaries.
- Kinematics and galaxy interactions: The evidence of perturbed proper motions among the youngest stars can be used in simulation, placing strong constraints on the dynamics of the recent LMC–SMC encounter and its role in shaping the SMC.

- Future UV missions: Upcoming UV space missions (e.g., ULTRASAT, INSIST, UVEX) can build upon the UVIT catalog to explore time variability, binarity, and massive star feedback at higher sensitivity and resolution.
- Synergy with JWST and Roman: While this thesis already combines UVIT, Gaia/SMASH, and VMC to cover the UV–optical–NIR regimes, the mid-infrared capabilities of JWST and Roman will extend this baseline, enabling full UV–to–mid-IR SEDs of young stars. This will provide tighter constraints on stellar ages, masses, and circumstellar environments, particularly for systems with dust or IR excesses that remain unconstrained in the current dataset.

7.2 Future Work

In future, we plan to extend this thesis work along several directions.

- In Chapter 6, strict sample selection criteria were applied, requiring stars to have flux measurements in all eight UVIT filters. While this ensured a robust dataset, it significantly reduced the sample size and may have contributed to the relatively low binary fraction derived. An immediate next step will be to relax these criteria, thereby adding new stars to the sample, and to examine the stellar properties and multiplicity fractions.
- In Chapter 3, our cross-match with the SIMBAD database revealed several intriguing classes of objects, including emission-line stars, eclipsing binaries, Classical Cepheids, and high-mass X-ray binaries. Building on the methods of Chapter 6, we aim to investigate the physical properties and evolutionary status of these sources in greater detail. We also plan to obtain spectroscopic follow-up of these sources along with light-curve analyses of the identified

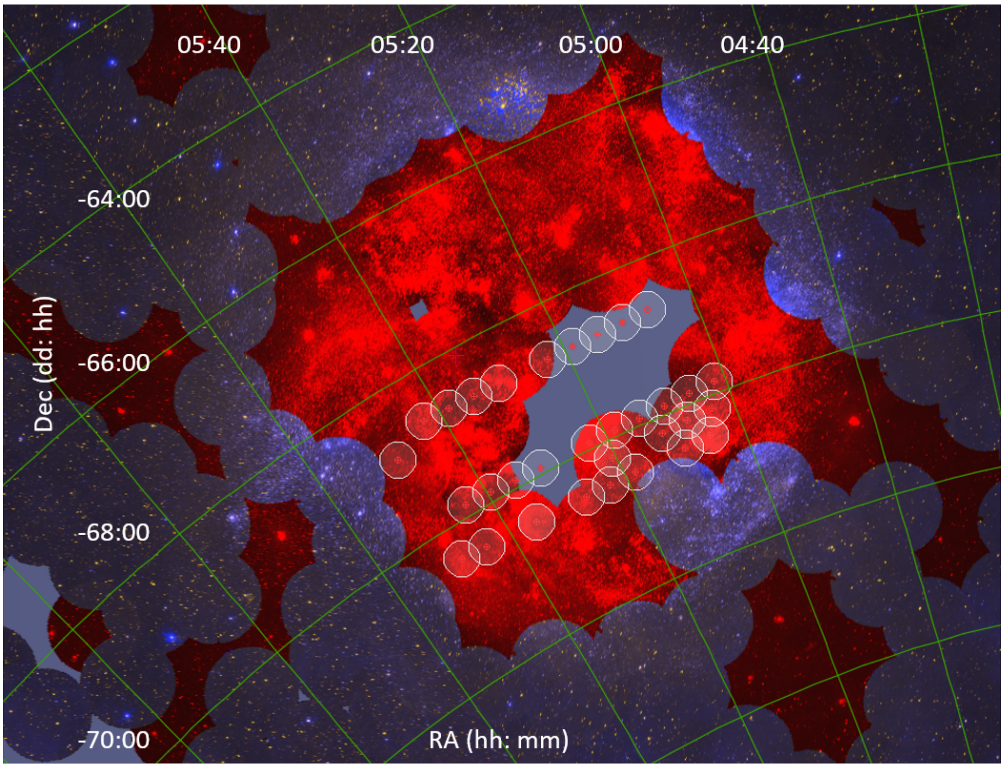

FIGURE 7.1: The UVIT-observed fields of the LMC are marked by white circles, overlaid on a GALEX background image. This background is a two-color composite, with blue indicating FUV data and red representing NUV data, incorporating both GR6 and GR7 releases (Bianchi et al. 2017).

variables, which will provide more direct constraints on binarity, stellar parameters, and evolutionary pathways.

- Looking ahead, we intend to extend the scope of this thesis to the LMC, where 32 UVIT fields have already been observed (Figure 7.1). As a first step, we will construct a FUV catalog of the observed regions (analogous to Chapter 3) and characterize the young massive stellar populations therein. We further aim to conduct kinematic studies of selected subregions in the LMC and compare them with those of the SMC, thereby probing how differences in interaction histories with the Milky Way and with each other shape the evolution of massive stars and their host environments.

Bibliography

Albers, H., MacGillivray, H. T., Beard, S. M., & Chromey, F. R. 1987, *Astron. Astrophys.*, 182, L8

Almeida, A., Majewski, S. R., Nidever, D. L., et al. 2024, *Mon. Not. Roy. Astron. Soc.*, 529, 3858, doi: 10.1093/mnras/stae373

Antwi-Danso, J., Barger, K. A., & Haffner, L. M. 2020, *Astrophys. J.*, 891, 176, doi: 10.3847/1538-4357/ab6ef9

Astropy Collaboration, Robitaille, T. P., Tollerud, E. J., et al. 2013, *Astron. Astrophys.*, 558, A33, doi: 10.1051/0004-6361/201322068

Astropy Collaboration, Price-Whelan, A. M., Sipőcz, B. M., et al. 2018, *Astron. J.*, 156, 123, doi: 10.3847/1538-3881/aabc4f

Astropy Collaboration, Price-Whelan, A. M., Lim, P. L., et al. 2022, *Astrophys. J.*, 935, 167, doi: 10.3847/1538-4357/ac7c74

Bally, J., & Zinnecker, H. 2005, *Astron. J.*, 129, 2281, doi: 10.1086/429098

Bastian, N., Ercolano, B., Gieles, M., et al. 2007, *Mon. Not. Roy. Astron. Soc.*, 379, 1302, doi: 10.1111/j.1365-2966.2007.12064.x

Bastian, N., Gieles, M., Ercolano, B., & Gutermuth, R. 2009, *Mon. Not. Roy. Astron. Soc.*, 392, 868, doi: 10.1111/j.1365-2966.2008.14107.x

Bate, M. R., Clarke, C. J., & McCaughrean, M. J. 1998, *Mon. Not. Roy. Astron. Soc.*, 297, 1163, doi: 10.1046/j.1365-8711.1998.01565.x

Battinelli, P. 1991, *Astron. Astrophys.*, 244, 69

Bayo, A., Rodrigo, C., Barrado Y Navascués, D., et al. 2008, *Astron. Astrophys.*, 492, 277, doi: 10.1051/0004-6361:200810395

Beech, M. 1987, *Astrophys. Space Sci.*, 133, 193, doi: 10.1007/BF00637432

Belcheva, M. K., Livanou, E., Kontizas, M., Nikolov, G. B., & Kontizas, E. 2011, *Astron. Astrophys.*, 527, A31, doi: 10.1051/0004-6361/201015835

Belokurov, V., Erkal, D., Deason, A. J., et al. 2017, *Mon. Not. Roy. Astron. Soc.*, 466, 4711, doi: 10.1093/mnras/stw3357

Belokurov, V. A., & Erkal, D. 2019, *Mon. Not. Roy. Astron. Soc.*, 482, L9, doi: 10.1093/mnrasl/sly178

Bergin, E. A., & Tafalla, M. 2007, *Ann. Rev. Astron. Astrophys.*, 45, 339, doi: 10.1146/annurev.astro.45.071206.100404

Bernard, E. J., Ferguson, A. M. N., Chapman, S. C., et al. 2015, *Mon. Not. Roy. Astron. Soc.*, 453, L113, doi: 10.1093/mnrasl/slv116

Bernard, E. J., Schultheis, M., Di Matteo, P., et al. 2018, *Mon. Not. Roy. Astron. Soc.*, 477, 3507, doi: 10.1093/mnras/sty902

Besla, G. 2015, arXiv e-prints, arXiv:1511.03346, doi: 10.48550/arXiv.1511.03346

Besla, G., Kallivayalil, N., Hernquist, L., et al. 2007, The Astrophysical Journal, 668, 949

Besla, G., Kallivayalil, N., Hernquist, L., et al. 2012, *Mon. Not. Roy. Astron. Soc.*, 421, 2109, doi: 10.1111/j.1365-2966.2012.20466.x

Bianchi, L., Shiao, B., & Thilker, D. 2017, *Astrophys. J. Suppl.*, 230, 24, doi: 10.3847/1538-4365/aa7053

Bica, E., Bonatto, C., Dutra, C. M., & Santos, J. F. C. 2008, *Mon. Not. Roy. Astron. Soc.*, 389, 678, doi: 10.1111/j.1365-2966.2008.13612.x

Bica, E., Westera, P., Kerber, L. d. O., et al. 2020, *Astron. J.*, 159, 82, doi: 10.3847/1538-3881/ab6595

Bodensteiner, J., Shenar, T., Sana, H., et al. 2025, *Astron. Astrophys.*, 698, A38, doi: 10.1051/0004-6361/202452623

Bonanos, A. Z., Lennon, D. J., Köhlinger, F., et al. 2010, *Astron. J.*, 140, 416, doi: 10.1088/0004-6256/140/2/416

Bonatto, C., & Bica, E. 2010, *Mon. Not. Roy. Astron. Soc.*, 403, 996, doi: 10.1111/j.1365-2966.2009.16177.x

Bonnarel, F., Fernique, P., Bienaymé, O., et al. 2000, *Astron. Astrophys. Suppl.*, 143, 33, doi: 10.1051/aas:2000331

Bot, C., Boulanger, F., Lagache, G., Cambrésy, L., & Egret, D. 2004, *Astron. Astrophys.*, 423, 567, doi: 10.1051/0004-6361:20035918

Bouret, J. C., Martins, F., Hillier, D. J., et al. 2021, *Astron. Astrophys.*, 647, A134, doi: 10.1051/0004-6361/202039890

Bower, R. G., Benson, A. J., Malbon, R., et al. 2006, *Mon. Not. Roy. Astron. Soc.*, 370, 645, doi: 10.1111/j.1365-2966.2006.10519.x

Bressan, A., Marigo, P., Girardi, L., et al. 2012, *Mon. Not. Roy. Astron. Soc.*, 427, 127, doi: 10.1111/j.1365-2966.2012.21948.x

Britavskiy, N., Mahy, L., Lennon, D. J., et al. 2025, *Astron. Astrophys.*, 698, A40, doi: 10.1051/0004-6361/202452963

Brueck, M. T., & Marsoglu, A. 1978, *Astron. Astrophys.*, 68, 193

Bullock, J. S., & Johnston, K. V. 2005, *Astrophys. J.*, 635, 931, doi: 10.1086/497422

Bustard, C., & Gronke, M. 2022, *Astrophys. J.*, 933, 120, doi: 10.3847/1538-4357/ac752b

Cakırlı, O., Hoyman, B., & Ozdarcan, O. 2023, *Mon. Not. Roy. Astron. Soc.*, 523, 1676, doi: 10.1093/mnras/stad1541

Calzetti, D., Lee, J. C., Sabbi, E., et al. 2015, *Astron. J.*, 149, 51, doi: 10.1088/0004-6256/149/2/51

Cardelli, J. A., Clayton, G. C., & Mathis, J. S. 1989, *Astrophys. J.*, 345, 245, doi: 10.1086/167900

Cartwright, A., & Whitworth, A. P. 2004, *Mon. Not. Roy. Astron. Soc.*, 348, 589, doi: 10.1111/j.1365-2966.2004.07360.x

Casetti-Dinescu, D. I., Moni Bidin, C., Girard, T. M., et al. 2014, *Astrophys. J. Lett.*, 784, L37, doi: 10.1088/2041-8205/784/2/L37

Castelli, F., Gratton, R. G., & Kurucz, R. L. 1997, *Astron. Astrophys.*, 318, 841

Castelli, F., & Kurucz, R. L. 2003, in IAU Symposium, Vol. 210, Modelling of Stellar Atmospheres, ed. N. Piskunov, W. W. Weiss, & D. F. Gray, A20, doi: `10.48550/arXiv.astro-ph/0405087`

Cautun, M., Benítez-Llambay, A., Deason, A. J., et al. 2020, *Mon. Not. Roy. Astron. Soc.*, 494, 4291, doi: `10.1093/mnras/staa1017`

Chandra, V., Naidu, R. P., Conroy, C., et al. 2023, *Astrophys. J.*, 956, 110, doi: `10.3847/1538-4357/acf7bf`

Choi, J., Dotter, A., Conroy, C., et al. 2016, The Astrophysical Journal, 823, 102, doi: `10.3847/0004-637X/823/2/102`

Choi, Y., Olsen, K. A. G., Besla, G., et al. 2022, *Astrophys. J.*, 927, 153, doi: `10.3847/1538-4357/ac4e90`

Choudhury, S., Subramaniam, A., Cole, A. A., & Sohn, Y. J. 2018, *Mon. Not. Roy. Astron. Soc.*, 475, 4279, doi: `10.1093/mnras/sty087`

Choudhury, S., de Grijs, R., Bekki, K., et al. 2021, *Mon. Not. Roy. Astron. Soc.*, 507, 4752, doi: `10.1093/mnras/stab2446`

Cioni, M. R. L., Habing, H. J., & Israel, F. P. 2000, *Astron. Astrophys.*, 358, L9, doi: `10.48550/arXiv.astro-ph/0005057`

Cioni, M. R. L., Clementini, G., Girardi, L., et al. 2011, *Astron. Astrophys.*, 527, A116, doi: `10.1051/0004-6361/201016137`

Cohen, M., Wheaton, W. A., & Megeath, S. T. 2003, *Astron. J.*, 126, 1090, doi: `10.1086/376474`

Cornett, R. H., Hill, J. K., Bohlin, R. C., et al. 1994, *Astrophys. J. Lett.*, 430, L117, doi: `10.1086/187452`

Cornett, R. H., Greason, M. R., Hill, J. K., et al. 1997, *Astron. J.*, 113, 1011, doi: `10.1086/118317`

Costa, E., Méndez, R. A., Pedreros, M. H., et al. 2009, *Astron. J.*, 137, 4339, doi: `10.1088/0004-6256/137/5/4339`

Cullinane, L. R., Mackey, A. D., Da Costa, G. S., Koposov, S. E., & Erkal, D. 2023, *Mon. Not. Roy. Astron. Soc.*, 518, L25, doi: `10.1093/mnrasl/slac129`

Dai, M., Wang, S., & Jiang, B. 2025, *Mon. Not. Roy. Astron. Soc.*, 539, 1220, doi: `10.1093/mnras/staf560`

de Grijs, R., & Bono, G. 2015, *Astron. J.*, 149, 179, doi: `10.1088/0004-6256/149/6/179`

de Grijs, R., Wicker, J. E., & Bono, G. 2014, *Astron. J.*, 147, 122, doi: `10.1088/0004-6256/147/5/122`

de Jong, R. S., Agertz, O., Berbel, A. A., et al. 2019, The Messenger, 175, 3, doi: `10.18727/0722-6691/5117`

De Leo, M., Carrera, R., Noël, N. E. D., et al. 2020, *Mon. Not. Roy. Astron. Soc.*, 495, 98, doi: `10.1093/mnras/staa1122`

De Marco, O., & Izzard, R. G. 2017, *Publications of the Astronomical Society of Australia*, 34, e001, doi: `10.1017/pasa.2016.52`

de Mink, S. E., Langer, N., Izzard, R. G., Sana, H., & de Koter, A. 2013, *Astrophys. J.*, 764, 166, doi: `10.1088/0004-637X/764/2/166`

de Vaucouleurs, G. 1954a, The Observatory, 74, 23

—. 1954b, The Observatory, 74, 158

—. 1955a, *Astron. J.*, 60, 126, doi: 10.1086/107173

—. 1955b, *Astron. J.*, 60, 219, doi: 10.1086/107218

—. 1957, *Astron. J.*, 62, 69, doi: 10.1086/107459

de Vaucouleurs, G., & Freeman, K. C. 1972, Vistas in Astronomy, 14, 163, doi: 10.1016/0083-6656(72)90026-8

Dennefeld, M. 2020, The Messenger, 181, 37, doi: 10.18727/0722-6691/5210

Devaraj, A., Joseph, P., Stalin, C. S., Tandon, S. N., & Ghosh, S. K. 2023, *Astrophys. J.*, 946, 65, doi: 10.3847/1538-4357/acba9c

Dhanush, S. R., Subramaniam, A., Nayak, P. K., & Subramanian, S. 2024, *Mon. Not. Roy. Astron. Soc.*, 528, 2274, doi: 10.1093/mnras/stae096

Dhanush, S. R., Subramaniam, A., & Subramanian, S. 2025, *Astrophys. J.*, 980, 73, doi: 10.3847/1538-4357/ada55f

Dias, B., Kerber, L., Barbuy, B., Bica, E., & Ortolani, S. 2016, *Astron. Astrophys.*, 591, A11, doi: 10.1051/0004-6361/201527558

Dias, B., Kerber, L. O., Barbuy, B., et al. 2014, *Astron. Astrophys.*, 561, A106, doi: 10.1051/0004-6361/201322092

Dias, B., Angelo, M. S., Oliveira, R. A. P., et al. 2021, *Astron. Astrophys.*, 647, L9, doi: 10.1051/0004-6361/202040015

Dias, B., Parisi, M. C., Angelo, M., et al. 2022, *Mon. Not. Roy. Astron. Soc.*, 512, 4334, doi: 10.1093/mnras/stac259

Diaz, J. D., & Bekki, K. 2012, *Astrophys. J.*, 750, 36, doi: 10.1088/0004-637X/750/1/36

Dickman, R. L., Horvath, M. A., & Margulis, M. 1990, *Astrophys. J.*, 365, 586, doi: 10.1086/169512

Dobbie, P. D., Cole, A. A., Subramaniam, A., & Keller, S. 2014a, *Mon. Not. Roy. Astron. Soc.*, 442, 1663, doi: 10.1093/mnras/stu910

—. 2014b, *Mon. Not. Roy. Astron. Soc.*, 442, 1680, doi: 10.1093/mnras/stu926

D'Onghia, E., & Fox, A. J. 2016, *Ann. Rev. Astron. Astrophys.*, 54, 363, doi: 10.1146/annurev-astro-081915-023251

Dotter, A. 2016, The Astrophysical Journal Supplement Series, 222, 8, doi: 10.3847/0067-0049/222/1/8

Drout, M. R., Götberg, Y., Ludwig, B. A., et al. 2023, Science, 382, 1287, doi: 10.1126/science.ade4970

Duchêne, G., Bouvier, J., Bontemps, S., André, P., & Motte, F. 2004, *Astron. Astrophys.*, 427, 651, doi: 10.1051/0004-6361:20041209

Efremov, Y. N. 2002, Astronomy Reports, 46, 791, doi: 10.1134/1.1515091

El-Badry, K., & Rix, H.-W. 2021, MNRAS, 506, 2269–

El Youssoufi, D., Cioni, M.-R. L., Bell, C. P. M., et al. 2019, *Mon. Not. Roy. Astron. Soc.*, 490, 1076, doi: 10.1093/mnras/stz2400

—. 2021, *Mon. Not. Roy. Astron. Soc.*, 505, 2020, doi: 10.1093/mnras/stab1075

El Youssoufi, D., Cioni, M.-R. L., Kacharov, N., et al. 2023, *Mon. Not. Roy. Astron. Soc.*, 523, 347, doi: 10.1093/mnras/stad1339

Elmegreen, B. G. 1993, *Astrophys. J. Lett.*, 419, L29, doi: 10.1086/187129

—. 2000, *Astrophys. J.*, 530, 277, doi: 10.1086/308361

—. 2011, *Astrophys. J.*, 731, 61, doi: 10.1088/0004-637X/731/1/61

Elmegreen, B. G., & Efremov, Y. N. 1996, *Astrophys. J.*, 466, 802, doi: 10.1086/177554

Elmegreen, B. G., & Elmegreen, D. M. 2001, *Astron. J.*, 121, 1507, doi: 10.1086/319416

Elmegreen, B. G., & Falgarone, E. 1996, *Astrophys. J.*, 471, 816, doi: 10.1086/178009

Elmegreen, B. G., Kim, S., & Staveley-Smith, L. 2001, *Astrophys. J.*, 548, 749, doi: 10.1086/319021

Elmegreen, B. G., & Scalo, J. 2004, *Ann. Rev. Astron. Astrophys.*, 42, 211, doi: 10.1146/annurev.astro.41.011802.094859

Elmegreen, D. M., & Elmegreen, B. G. 1980, *Astron. J.*, 85, 1325, doi: 10.1086/112802

Elmegreen, D. M., Elmegreen, B. G., Adamo, A., et al. 2014, *Astrophys. J. Lett.*, 787, L15, doi: 10.1088/2041-8205/787/1/L15

Evans, C. J., Lennon, D. J., Smartt, S. J., & Trundle, C. 2006, *Astron. Astrophys.*, 456, 623, doi: 10.1051/0004-6361:20064988

Falgarone, E., Phillips, T. G., & Walker, C. K. 1991, *Astrophys. J.*, 378, 186, doi: 10.1086/170419

Federrath, C., Roman-Duval, J., Klessen, R. S., Schmidt, W., & Mac Low, M. M. 2010, *Astron. Astrophys.*, 512, A81, doi: 10.1051/0004-6361/200912437

Feitzinger, J. V., & Galinski, T. 1987, *Astron. Astrophys.*, 179, 249

For, B.-Q., Staveley-Smith, L., & McClure-Griffiths, N. M. 2013, *Astrophys. J.*, 764, 74, doi: 10.1088/0004-637X/764/1/74

Fox, A. J., Wakker, B. P., Barger, K. A., et al. 2014, *Astrophys. J.*, 787, 147, doi: 10.1088/0004-637X/787/2/147

Fox, A. J., Barger, K. A., Wakker, B. P., et al. 2018, *Astrophys. J.*, 854, 142, doi: 10.3847/1538-4357/aaa9bb

Gaia Collaboration. 2022, VizieR Online Data Catalog: Gaia DR3 Part 4. Variability (Gaia Collaboration, 2022), VizieR On-line Data Catalog: I/358. Originally published in: 2023A&A...674A...1G

Gaia Collaboration, Prusti, T., de Bruijne, J. H. J., et al. 2016, *Astron. Astrophys.*, 595, A1, doi: 10.1051/0004-6361/201629272

Gaia Collaboration, Brown, A. G. A., Vallenari, A., et al. 2018a, *Astron. Astrophys.*, 616, A1, doi: 10.1051/0004-6361/201833051

Gaia Collaboration, Helmi, A., van Leeuwen, F., et al. 2018b, *Astron. Astrophys.*, 616, A12, doi: 10.1051/0004-6361/201832698

Gaia Collaboration, Luri, X., Chemin, L., et al. 2021a, *Astron. Astrophys.*, 649, A7, doi: 10.1051/0004-6361/202039588

Gaia Collaboration, Brown, A. G. A., Vallenari, A., et al. 2021b, *Astron. Astrophys.*, 649, A1, doi: 10.1051/0004-6361/202039657

Gaia Collaboration, Vallenari, A., Brown, A. G. A., et al. 2022, arXiv e-prints, arXiv:2208.00211, doi: 10.48550/arXiv.2208.00211

—. 2023, *Astron. Astrophys.*, 674, A1, doi: 10.1051/0004-6361/202243940

Gallagher, III, J. S., & Hunter, D. A. 1984, *Ann. Rev. Astron. Astrophys.*, 22, 37, doi: 10.1146/annurev.aa.22.090184.000345

García, B., & Mermilliod, J. C. 2001, *Astron. Astrophys.*, 368, 122, doi: 10.1051/0004-6361:20000528

Gardiner, L. T., & Noguchi, M. 1996, *Mon. Not. Roy. Astron. Soc.*, 278, 191, doi: 10.1093/mnras/278.1.191

Gardiner, L. T., Sawa, T., & Fujimoto, M. 1994, Monthly Notices of the Royal Astronomical Society, 266, 567, doi: 10.1093/mnras/266.3.567

Gardiner, L. T., Turfus, C., & Putman, M. E. 1998, *Astrophys. J. Lett.*, 507, L35, doi: 10.1086/311668

Gaustad, J. E., McCullough, P. R., Rosing, W., & Van Buren, D. 2001, *Pub. Astron. Soc. Pac.*, 113, 1326, doi: 10.1086/323969

Gehrels, N., Chincarini, G., Giommi, P., et al. 2004, The Astrophysical Journal, 611, 1005, doi: 10.1086/422091

Gieles, M., Bastian, N., & Ercolano, B. 2008, *Mon. Not. Roy. Astron. Soc.*, 391, L93, doi: 10.1111/j.1745-3933.2008.00563.x

Girardi, L., Dalcanton, J., Williams, B., et al. 2008, *Pub. Astron. Soc. Pac.*, 120, 583, doi: 10.1086/588526

Giuricin, G., Mardirossian, F., & Mezzetti, M. 1983, *Astrophys. J. Suppl.*, 52, 35, doi: 10.1086/190858

Glatt, K., Grebel, E. K., & Koch, A. 2010, *Astron. Astrophys.*, 517, A50, doi: 10.1051/0004-6361/201014187

Głowacki, M., Soszyński, I., Udalski, A., et al. 2024, *Acta Astronomica, 74, 241, doi: 10.32023/0001-5237/74.4.1*

Gonidakis, I., Livanou, E., Kontizas, E., et al. 2009, Astron. Astrophys., 496, 375, doi: 10.1051/0004-6361/200809828

Gonidakis, I., Livanou, E., Kontizas, E., et al. 2007, in IAU Symposium, Vol. 235, Galaxy Evolution across the Hubble Time, ed. F. Combes & J. Palouš, 311–311, doi: 10.1017/S1743921306006764

Gordon, K. D., Meixner, M., Meade, M. R., et al. 2011, Astron. J., 142, 102, doi: 10.1088/0004-6256/142/4/102

Gordon, K. D., Fitzpatrick, E. L., Massa, D., et al. 2024, Astrophys. J., 970, 51, doi: 10.3847/1538-4357/ad4be1

Goswami, S., Silva, L., Bressan, A., et al. 2022, Astron. Astrophys., 663, A1, doi: 10.1051/0004-6361/202142031

Götberg, Y., de Mink, S. E., Groh, J. H., et al. 2018, Astron. Astrophys., 615, A78, doi: 10.1051/0004-6361/201732274

Gouliermis, D. A., Hony, S., & Klessen, R. S. 2014, Mon. Not. Roy. Astron. Soc., 439, 3775, doi: 10.1093/mnras/stu228

Gouliermis, D. A., Schmeja, S., Klessen, R. S., de Blok, W. J. G., & Walter, F. 2010, Astrophys. J., 725, 1717, doi: 10.1088/0004-637X/725/2/1717

Gouliermis, D. A., Thilker, D., Elmegreen, B. G., et al. 2015, Mon. Not. Roy. Astron. Soc., 452, 3508, doi: 10.1093/mnras/stv1325

Gouliermis, D. A., Elmegreen, B. G., Elmegreen, D. M., et al. 2017, Mon. Not. Roy. Astron. Soc., 468, 509, doi: 10.1093/mnras/stx445

Graczyk, D., Pietrzyński, G., Thompson, I. B., et al. 2020, Astrophys. J., 904, 13, doi: 10.3847/1538-4357/abbb2b

Grasha, K., Calzetti, D., Adamo, A., et al. 2017, Astrophys. J., 840, 113, doi: 10.3847/1538-4357/aa6f15

Groenewegen, M. A. T. 2025, Astron. Astrophys., 699, A102, doi: 10.1051/0004-6361/202554369

Gusev, A. S. 2014, Mon. Not. Roy. Astron. Soc., 442, 3711, doi: 10.1093/mnras/stu1095

Haberl, F., & Sturm, R. 2016, Astron. Astrophys., 586, A81, doi: 10.1051/0004-6361/201527326

Hammer, F., Yang, Y. B., Flores, H., Puech, M., & Fouquet, S. 2015, Astrophys. J., 813, 110, doi: 10.1088/0004-637X/813/2/110

Harris, C. R., Millman, K. J., van der Walt, S. J., et al. 2020, Nature, 585, 357, doi: 10.1038/s41586-020-2649-2

Harris, J. 2007, Astrophys. J., 658, 345, doi: 10.1086/511816

Harris, J., & Zaritsky, D. 2001, Astrophys. J. Suppl., 136, 25, doi: 10.1086/321792

—. 2004, Astron. J., 127, 1531, doi: 10.1086/381953

—. 2009, Astron. J., 138, 1243, doi: 10.1088/0004-6256/138/5/1243

Haschke, R., Grebel, E. K., & Duffau, S. 2011, Astron. J., 141, 158, doi: 10.1088/0004-6256/141/5/158

Hetem, A., J., & Lepine, J. R. D. 1993, Astron. Astrophys., 270, 451

Hillier, D. J., & Miller, D. L. 1998, Astrophys. J., 496, 407, doi: 10.1086/305350

Hindman, J. V., Kerr, F. J., & McGee, R. X. 1963, Australian Journal of Physics, 16, 570, doi: 10.1071/PH630570

Hocdé, V., Smolec, R., Moskalik, P., Ziółkowska, O., & Singh Rathour, R. 2023, Astron. Astrophys., 671, A157, doi: 10.1051/0004-6361/202245038

Hodge, P. 1985, Pub. Astron. Soc. Pac., 97, 530, doi: 10.1086/131564

Hopkins, P. F., Kereš, D., Oñorbe, J., et al. 2014, Mon. Not. Roy. Astron. Soc., 445, 581, doi: 10.1093/mnras/stu1738

Hota, S., de Grijs, R., & Subramaniam, A. 2025, arXiv e-prints, arXiv:2506.08951, doi: 10.48550/arXiv.2506.08951

Hota, S., Subramaniam, A., Dhanush, S. R., Cioni, M.-R. L., & Subramanian, S. 2024a, Mon. Not. Roy. Astron. Soc., 532, 322, doi: 10.1093/mnras/stae1438

Hota, S., Subramaniam, A., Nayak, P. K., & Subramanian, S. 2024b, Astron. J., 168, 255, doi: 10.3847/1538-3881/ad7de2

Hovis-Afflerbach, B., Götberg, Y., Schootemeijer, A., et al. 2025, Astron. Astrophys., 697, A239, doi: 10.1051/0004-6361/202453185

Hubeny, I., & Lanz, T. 2011, TLUSTY: Stellar Atmospheres, Accretion Disks, and Spectroscopic Diagnostics, Astrophysics Source Code Library, record ascl:1109.021. http://ascl.net/1109.021

Hunter, I., Lennon, D. J., Dufton, P. L., et al. 2009, Erratum: The VLT-FLAMES survey of massive stars: atmospheric parameters and rotational velocity distributions for B-type stars in the Magellanic Clouds, EDP, doi: 10.1051/0004-6361/20078511e

Hunter, J. D. 2007, Computing in Science and Engineering, 9, 90, doi: 10.1109/MCSE.2007.55

Hutchings, J. B., Postma, J., Asquin, D., & Leahy, D. 2007, Pub. Astron. Soc. Pac., 119, 1152, doi: `10.1086/522635`

Ibata, R. A., Gilmore, G., & Irwin, M. J. 1995, Mon. Not. Roy. Astron. Soc., 277, 781, doi: `10.1093/mnras/277.3.781`

Indu, G., & Subramaniam, A. 2011, Astron. Astrophys., 535, A115, doi: `10.1051/0004-6361/201117298`

Irwin, M. J., Kunkel, W. E., & Demers, S. 1985, Nature, 318, 160, doi: `10.1038/318160a0`

Ivezić, Ž., Kahn, S. M., Tyson, J. A., et al. 2019, Astrophys. J., 873, 111, doi: `10.3847/1538-4357/ab042c`

Jadhav, V. V. 2025, Journal of Astrophysics and Astronomy, 46, 20, doi: `10.1007/s12036-025-10042-2`

James, D., Subramanian, S., Omkumar, A. O., et al. 2021, Mon. Not. Roy. Astron. Soc., 508, 5854, doi: `10.1093/mnras/stab2873`

Jiménez-Arranz, Ó., Romero-Gómez, M., Luri, X., & Masana, E. 2023, Astron. Astrophys., 672, A65, doi: `10.1051/0004-6361/202245720`

Joshi, Y. C., & Panchal, A. 2019, Astron. Astrophys., 628, A51, doi: `10.1051/0004-6361/201834574`

Joshi, Y. C., Prasad Mohanty, A., & Joshi, S. 2016, Research in Astronomy and Astrophysics, 16, 61, doi: `10.1088/1674-4527/16/4/061`

Kalari, V. M., Salinas, R., Zinnecker, H., et al. 2024, Astrophys. J., 972, 3, doi: `10.3847/1538-4357/ad5bd9`

Kallivayalil, N., van der Marel, R. P., & Alcock, C. 2006, Astrophys. J., 652, 1213, doi: `10.1086/508014`

Karamehmetoglu, E., Sollerman, J., Taddia, F., et al. 2023, Astron. Astrophys., 678, A87, doi: `10.1051/0004-6361/202245231`

Kennicutt, R. C. 2005, in IAU Symposium, Vol. 227, Massive Star Birth: A Crossroads of Astrophysics, ed. R. Cesaroni, M. Felli, E. Churchwell, & M. Walmsley, 3–11, doi: `10.1017/S1743921305004308`

Kennicutt, R. C., & Evans, N. J. 2012, Ann. Rev. Astron. Astrophys., 50, 531, doi: `10.1146/annurev-astro-081811-125610`

Kim, S., Staveley-Smith, L., Dopita, M. A., et al. 2003, Astrophys. J. Suppl., 148, 473, doi: `10.1086/376980`

Klessen, R. S. 2000, Astrophys. J., 535, 869, doi: `10.1086/308854`

Kobulnicky, H. A., Kiminki, D. C., Lundquist, M. J., et al. 2014, Astrophys. J. Suppl., 213, 34, doi: `10.1088/0067-0049/213/2/34`

Konstandin, L., Girichidis, P., Federrath, C., & Klessen, R. S. 2012, Astrophys. J., 761, 149, doi: `10.1088/0004-637X/761/2/149`

Kroupa, P. 2001, Mon. Not. Roy. Astron. Soc., 322, 231, doi: `10.1046/j.1365-8711.2001.04022.x`

Kroupa, P. 2002, in Astronomical Society of the Pacific Conference Series, Vol. 285, Modes of Star Formation and the Origin of Field Populations, ed. E. K. Grebel & W. Brandner, 86, doi: `10.48550/arXiv.astro-ph/0102155`

Krumholz, M. R., & Burkhart, B. 2016, Mon. Not. Roy. Astron. Soc., 458, 1671, doi: `10.1093/mnras/stw434`

Kulkarni, S. R., Harrison, F. A., Grefenstette, B. W., et al. 2021, arXiv e-prints, arXiv:2111.15608, doi: `10.48550/arXiv.2111.15608`

Kumar, A., Ghosh, S. K., Hutchings, J., et al. 2012, in Society of Photo-Optical Instrumentation Engineers (SPIE) Conference Series, Vol. 8443, Space Telescopes and Instrumentation 2012: Ultraviolet to Gamma Ray, ed. T. Takahashi, S. S. Murray, & J.-W. A. den Herder, 84431N, doi: `10.1117/12.924507`

Kurucz, R. 1993, Robert Kurucz CD-ROM, 13

Lada, C. J., & Lada, E. A. 2003, Ann. Rev. Astron. Astrophys., 41, 57, doi: `10.1146/annurev.astro.41.011802.094844`

Lamb, J. B., Oey, M. S., Segura-Cox, D. M., et al. 2016, Astrophys. J., 817, 113, doi: `10.3847/0004-637X/817/2/113`

Larson, R. B. 1995, Mon. Not. Roy. Astron. Soc., 272, 213, doi: `10.1093/mnras/272.1.213`

—. 2003, Reports on Progress in Physics, 66, 1651, doi: `10.1088/0034-4885/66/10/R03`

Lazarian, A., & Pogosyan, D. 2000, Astrophys. J., 537, 720, doi: `10.1086/309040`

Leahy, D. A., Postma, J., Chen, Y., & Buick, M. 2020, Astrophys. J. Suppl., 247, 47, doi: `10.3847/1538-4365/ab77a9`

Lee, Y., Li, D., Kim, Y. S., et al. 2016, Journal of Korean Astronomical Society, 49, 255, doi: `10.5303/JKAS.2016.49.6.255`

Lemasle, B., Groenewegen, M. A. T., Grebel, E. K., et al. 2017, Astron. Astrophys., 608, A85, doi: `10.1051/0004-6361/201731370`

Lin, D. N. C., Jones, B. F., & Klemola, A. R. 1995, Astrophys. J., 439, 652, doi: `10.1086/175205`

Lindegren, L., Hernández, J., Bombrun, A., et al. 2018, Astron. Astrophys., 616, A2, doi: `10.1051/0004-6361/201832727`

Liu, Y.-Z. 1992, Astron. Astrophys., 257, 505

Lombardi, M., Lada, C. J., & Alves, J. 2010, Astron. Astrophys., 512, A67, doi: `10.1051/0004-6361/200912670`

Lucchini, S. 2024, Astrophys. Space Sci., 369, 114, doi: `10.1007/s10509-024-04377-5`

Lucke, P. B., & Hodge, P. W. 1970, Astron. J., 75, 171, doi: `10.1086/110959`

Ludwig, B., Drout, M. R., Götberg, Y., Lang, D., & Laroche, A. 2026, Astrophys. J., 999, 73, doi: `10.3847/1538-4357/ae2d13`

Mandelbrot, B. B. 1983, The fractal geometry of nature (San Francisco, CA: Freeman)

Maragoudaki, F., Kontizas, M., Morgan, D. H., et al. 2001, Astron. Astrophys., 379, 864, doi: `10.1051/0004-6361:20011454`

Marchant, P., Langer, N., Podsiadlowski, P., et al. 2017, Astron. Astrophys., 604, A55, doi: `10.1051/0004-6361/201630188`

Martínez-Delgado, D., Vivas, A. K., Grebel, E. K., et al. 2019, Astron. Astrophys., 631, A98, doi: `10.1051/0004-6361/201936021`

Mason, B. D., Gies, D. R., Hartkopf, W. I., et al. 1998, Astron. J., 115, 821, doi: `10.1086/300234`

Massana, P., Noël, N. E. D., Nidever, D. L., et al. 2020, Mon. Not. Roy. Astron. Soc., 498, 1034, doi: `10.1093/mnras/staa2451`

Massana, P., Ruiz-Lara, T., Noël, N. E. D., et al. 2022, Mon. Not. Roy. Astron. Soc., 513, L40, doi: `10.1093/mnrasl/slac030`

Mastropietro, C., Moore, B., Mayer, L., Stadel, J., & Wadsley, J. 2004, in Astronomical Society of the Pacific Conference Series, Vol. 327, Satellites and Tidal Streams, ed. F. Prada, D. Martinez Delgado, & T. J. Mahoney, 234, doi: `10.48550/arXiv.astro-ph/0309244`

Mathewson, D. S. 1985, Publications of the Astronomical Society of Australia, 6, 104, doi: `10.1017/S1323358000026771`

Mathewson, D. S., Cleary, M. N., & Murray, J. D. 1974, Astrophys. J., 190, 291, doi: `10.1086/152875`

Mathewson, D. S., & Ford, V. L. 1984, in IAU Symposium, Vol. 1983, Structure and Evolution of the Magellanic Clouds, ed. S. van den Bergh & K. S. D. de Boer, 125–136, doi: `10.1017/S0074180900040092`

McClure-Griffiths, N. M., Staveley-Smith, L., Lockman, F. J., et al. 2008, Astrophys. J. Lett., 673, L143, doi: `10.1086/528683`

McClure-Griffiths, N. M., Dénes, H., Dickey, J. M., et al. 2018, Nature Astronomy, 2, 901, doi: `10.1038/s41550-018-0608-8`

Meena, B., Sabbi, E., Zeidler, P., et al. 2025, Astrophys. J., 987, 33, doi: `10.3847/1538-4357/add475`

Mellinger, A. 2009, Pub. Astron. Soc. Pac., 121, 1180, doi: `10.1086/648480`

Menon, S. H., Grasha, K., Elmegreen, B. G., et al. 2021, Mon. Not. Roy. Astron. Soc., 507, 5542, doi: `10.1093/mnras/stab2413`

Miller, A. E., Cioni, M.-R. L., de Grijs, R., et al. 2022, Mon. Not. Roy. Astron. Soc., 512, 1196, doi: `10.1093/mnras/stac508`

Miller, A. E., Slepian, Z., Lada, E. A., et al. 2024, arXiv e-prints, arXiv:2410.14186, doi: `10.48550/arXiv.2410.14186`

Moe, M., & Di Stefano, R. 2017, Astrophys. J. Suppl., 230, 15, doi: `10.3847/1538-4365/aa6fb6`

Mondal, C., Subramaniam, A., & George, K. 2019, Astron. J., 158, 229, doi: `10.3847/1538-3881/ab4ea1`

—. 2021a, Journal of Astrophysics and Astronomy, 42, 50, doi: `10.1007/s12036-021-09761-z`

Mondal, C., Subramaniam, A., George, K., et al. 2021b, Astrophys. J., 909, 203, doi: `10.3847/1538-4357/abe0b4`

Morrissey, P., Conrow, T., Barlow, T. A., et al. 2007, Astrophys. J. Suppl., 173, 682, doi: `10.1086/520512`

Muller, E., & Bekki, K. 2007, Mon. Not. Roy. Astron. Soc., 381, L11, doi: `10.1111/j.1745-3933.2007.00356.x`

Murray, C. E., Peek, J. E. G., Di Teodoro, E. M., et al. 2019, Astrophys. J., 887, 267, doi: `10.3847/1538-4357/ab510f`

Nakano, S., Tachihara, K., & Tamashiro, M. 2025, Astrophys. J. Suppl., 277, 62, doi: `10.3847/1538-4365/adb8de`

Nayak, P. K., Subramaniam, A., Choudhury, S., & Sagar, R. 2018, Astron. Astrophys., 616, A187, doi: `10.1051/0004-6361/201732227`

Nedhath, S., Rani, S., Subramaniam, A., & Pancino, E. 2025, Astron. Astrophys., 699, L1, doi: `10.1051/0004-6361/202555495`

Nestingen-Palm, D., Stanimirovic, S., Babler, B. L., et al. 2017, in American Astronomical Society Meeting Abstracts, Vol. 229, American Astronomical Society Meeting Abstracts #229, 435.05

Neugent, K. F., Massey, P., & Morrell, N. 2018, Astrophys. J., 863, 181, doi: 10.3847/1538-4357/aad17d

Nidever, D. L., Majewski, S. R., & Burton, W. B. 2008, The Astrophysical Journal, 679, 432–459, doi: 10.1086/587042

Nidever, D. L., Majewski, S. R., Butler Burton, W., & Nigra, L. 2010, Astrophys. J., 723, 1618, doi: 10.1088/0004-637X/723/2/1618

Nidever, D. L., Monachesi, A., Bell, E. F., et al. 2013, Astrophys. J., 779, 145, doi: 10.1088/0004-637X/779/2/145

Nidever, D. L., Olsen, K., Walker, A. R., et al. 2017, Astron. J., 154, 199, doi: 10.3847/1538-3881/aa8d1c

Nidever, D. L., Olsen, K., Choi, Y., et al. 2021, Astron. J., 161, 74, doi: 10.3847/1538-3881/abceb7

Niederhofer, F., Cioni, M.-R. L., Rubele, S., et al. 2021, Mon. Not. Roy. Astron. Soc., 502, 2859, doi: 10.1093/mnras/stab206

Noël, N. E. D., Aparicio, A., Gallart, C., et al. 2009, Astrophys. J., 705, 1260, doi: 10.1088/0004-637X/705/2/1260

Noël, N. E. D., Gallart, C., Costa, E., & Méndez, R. A. 2007, Astron. J., 133, 2037, doi: 10.1086/512668

O'Donnell, J. E. 1994, Astrophys. J., 422, 158, doi: 10.1086/173713

Oliveira, R. A. P., Maia, F. F. S., Barbuy, B., et al. 2023, Mon. Not. Roy. Astron. Soc., 524, 2244, doi: 10.1093/mnras/stad1827

Omkumar, A. O., Subramanian, S., Niederhofer, F., et al. 2021, Mon. Not. Roy. Astron. Soc., 500, 2757, doi: 10.1093/mnras/staa3085

Padoan, P., & Nordlund, Å. 2002, Astrophys. J., 576, 870, doi: 10.1086/341790

Padoan, P., Pan, L., Haugbølle, T., & Nordlund, Å. 2016, Astrophys. J., 822, 11, doi: 10.3847/0004-637X/822/1/11

pandas development team, T. 2020, pandas-dev/pandas: Pandas, Zenodo, doi: 10.5281/zenodo.3509134

Parisi, M. C., Oliveira, R. A. P., Angelo, M., et al. 2023, arXiv e-prints, arXiv:2312.09756, doi: 10.48550/arXiv.2312.09756

Parsons, T. N., Prinja, R. K., Bernini-Peron, M., et al. 2024, Mon. Not. Roy. Astron. Soc., 527, 11422, doi: 10.1093/mnras/stad3966

Patrick, L. R., Thilker, D., Lennon, D. J., et al. 2022, Mon. Not. Roy. Astron. Soc., 513, 5847, doi: 10.1093/mnras/stac1139

Patrick, L. R., Lennon, D. J., Najarro, F., et al. 2025, Astron. Astrophys., 698, A39, doi: 10.1051/0004-6361/202452949

Pawlak, M., Graczyk, D., Soszyński, I., et al. 2013, Acta Astronomica, 63, 323, doi: 10.48550/arXiv.1310.3272

Pawlak, M., Soszyński, I., Udalski, A., et al. 2016, Acta Astronomica, 66, 421, doi: 10.48550/arXiv.1612.06394

Paxton, B., Bildsten, L., Dotter, A., et al. 2010, The Astrophysical Journal Supplement Series, 192, 3, doi: 10.1088/0067-0049/192/1/3

Piatti, A. E. 2014, Mon. Not. Roy. Astron. Soc., 440, 3091, doi: 10.1093/mnras/stu534

—. 2022, Mon. Not. Roy. Astron. Soc., 509, 3462, doi: 10.1093/mnras/stab3190

Pieres, A., Santiago, B. X., Drlica-Wagner, A., et al. 2017, Mon. Not. Roy. Astron. Soc., 468, 1349, doi: 10.1093/mnras/stx507

Pietrzyński, G., Graczyk, D., Gallenne, A., et al. 2019, Nature, 567, 200, doi: 10.1038/s41586-019-0999-4

Pingel, N. M., Lee, M.-Y., Burkhart, B., & Stanimirović, S. 2018, Astrophys. J., 856, 136, doi: 10.3847/1538-4357/aab34b

Podsiadlowski, P., Joss, P. C., & Hsu, J. J. L. 1992, Astrophys. J., 391, 246, doi: 10.1086/171341

Postma, J., Hutchings, J. B., & Leahy, D. 2011, Pub. Astron. Soc. Pac., 123, 833, doi: 10.1086/661187

Postma, J. E., & Leahy, D. 2017, Pub. Astron. Soc. Pac., 129, 115002, doi: 10.1088/1538-3873/aa8800

—. 2021, Journal of Astrophysics and Astronomy, 42, 30, doi: 10.1007/s12036-020-09689-w

Prša, A., & Zwitter, T. 2009, ApJ, 696, 68–

Putman, M. E., Staveley-Smith, L., Freeman, K. C., Gibson, B. K., & Barnes, D. G. 2003, Astrophys. J., 586, 170, doi: 10.1086/344477

Putman, M. E., Gibson, B. K., Staveley-Smith, L., et al. 1998, Nature, 394, 752, doi: 10.1038/29466

Qin, C., Pang, X., Pasquato, M., Kouwenhoven, M. B. N., & Vallenari, A. 2025, Astron. Astrophys., 695, A22, doi: 10.1051/0004-6361/202452471

Ranasinghe, S., & Leahy, D. 2025, arXiv e-prints, arXiv:2503.05056, doi: 10.48550/arXiv.2503.05056

Rebassa-Mansergas, A., Parsons, S. G., Dhillon, V. S., et al. 2019, Nature Astronomy, 3, 553, doi: 10.1038/s41550-019-0746-7

Rebassa-Mansergas, A., Solano, E., Jiménez-Esteban, F. M., et al. 2021, Mon. Not. Roy. Astron. Soc., 506, 5201, doi: 10.1093/mnras/stab2039

Ripepi, V., Cioni, M.-R. L., Moretti, M. I., et al. 2017, Mon. Not. Roy. Astron. Soc., 472, 808, doi: 10.1093/mnras/stx2096

Rodrigo, C., & Solano, E. 2020, in XIV.0 Scientific Meeting (virtual) of the Spanish Astronomical Society, 182

Roman-Duval, J., Jackson, J. M., Heyer, M., Rathborne, J., & Simon, R. 2010, Astrophys. J., 723, 492, doi: 10.1088/0004-637X/723/1/492

Rubele, S., Girardi, L., Kerber, L., et al. 2015, Mon. Not. Roy. Astron. Soc., 449, 639, doi: 10.1093/mnras/stv141

Rubele, S., Pastorelli, G., Girardi, L., et al. 2018, Mon. Not. Roy. Astron. Soc., 478, 5017, doi: 10.1093/mnras/sty1279

Russell, S. C., & Dopita, M. A. 1990, Astrophys. J. Suppl., 74, 93, doi: 10.1086/191494

Sabbi, E., Gallagher, J. S., Tosi, M., et al. 2009, Astrophys. J., 703, 721, doi: 10.1088/0004-637X/703/1/721

Sabbi, E., Meena, B., Zeidler, P., et al. 2026, arXiv e-prints, arXiv:2603.06510, doi: `10.48550/arXiv.2603.06510`

Sakowska, J. D., Noël, N. E. D., Ruiz-Lara, T., et al. 2024, Mon. Not. Roy. Astron. Soc., 532, 4272, doi: `10.1093/mnras/stae1766`

Salem, M., Besla, G., Bryan, G., et al. 2015, Astrophys. J., 815, 77, doi: `10.1088/0004-637X/815/1/77`

Sana, H., de Mink, S. E., de Koter, A., et al. 2012, Science, 337, 444, doi: `10.1126/science.1223344`

Sana, H., Le Bouquin, J. B., Lacour, S., et al. 2014, Astrophys. J. Suppl., 215, 15, doi: `10.1088/0067-0049/215/1/15`

Sánchez, N., & Alfaro, E. J. 2008, Astrophys. J. Suppl., 178, 1, doi: `10.1086/589653`

Saroon, S., Dias, B., Tsujimoto, T., et al. 2023, Astron. Astrophys., 677, A35, doi: `10.1051/0004-6361/202346648`

Schlafly, E. F., & Finkbeiner, D. P. 2011, Astrophys. J., 737, 103, doi: `10.1088/0004-637X/737/2/103`

Schlegel, D. J., Finkbeiner, D. P., & Davis, M. 1998, Astrophys. J., 500, 525, doi: `10.1086/305772`

Schneider, F. R. N., Sana, H., Evans, C. J., et al. 2018, Science, 359, 69, doi: `10.1126/science.aan0106`

Schootemeijer, A., Langer, N., Lennon, D., et al. 2021, Astron. Astrophys., 646, A106, doi: `10.1051/0004-6361/202038789`

Scowcroft, V., Freedman, W. L., Madore, B. F., et al. 2016, Astrophys. J., 816, 49, doi: `10.3847/0004-637X/816/2/49`

Sewiło, M., Carlson, L. R., Seale, J. P., et al. 2013, Astrophys. J., 778, 15, doi: `10.1088/0004-637X/778/1/15`

Shapley, H. 1940, Harvard College Observatory Bulletin, 914, 8

Shashank, G., Subramanian, S., Muraleedharan, S., et al. 2025, Astron. Astrophys., 693, A188, doi: `10.1051/0004-6361/202451739`

Shenar, T., Bodensteiner, J., Sana, H., et al. 2024a, Astron. Astrophys., 690, A289, doi: `10.1051/0004-6361/202451586`

—. 2024b, arXiv e-prints, arXiv:2407.14593, doi: `10.48550/arXiv.2407.14593`

Shtykovskiy, P., & Gilfanov, M. 2005, Mon. Not. Roy. Astron. Soc., 362, 879, doi: `10.1111/j.1365-2966.2005.09320.x`

Simons, R., Thilker, D., Bianchi, L., & Wyder, T. 2014, Advances in Space Research, 53, 939, doi: `https://doi.org/10.1016/j.asr.2013.07.016`

Skowron, D. M., Skowron, J., Udalski, A., et al. 2021, Astrophys. J. Suppl., 252, 23, doi: `10.3847/1538-4365/abcb81`

Smithsonian Astrophysical Observatory. 2000, SAOImage DS9: A utility for displaying astronomical images in the X11 window environment, Astrophysics Source Code Library, record ascl:0003.002

Sriram, S., Valsan, V., Subramaniam, A., et al. 2023, Journal of Astrophysics and Astronomy, 44, 55, doi: `10.1007/s12036-023-09934-y`

Stanimirović, S., & Lazarian, A. 2001, Astrophys. J. Lett., 551, L53, doi: `10.1086/319837`

Stanimirovic, S., Staveley-Smith, L., Dickey, J. M., Sault, R. J., & Snowden, S. L. 1999, Mon. Not. Roy. Astron. Soc., 302, 417, doi: 10.1046/j.1365-8711.1999.02013.x

Stanimirović, S., Staveley-Smith, L., & Jones, P. A. 2004, Astrophys. J., 604, 176, doi: 10.1086/381869

Stanimirovic, S., Staveley-Smith, L., van der Hulst, J. M., et al. 2000, Mon. Not. Roy. Astron. Soc., 315, 791, doi: 10.1046/j.1365-8711.2000.03480.x

Stetson, P. B. 1987, Pub. Astron. Soc. Pac., 99, 191, doi: 10.1086/131977

Subramaniam, A. 2022, Journal of Astrophysics and Astronomy, 43, 80, doi: 10.1007/s12036-022-09870-3

Subramaniam, A., Tandon, S. N., Hutchings, J., et al. 2016a, in Space Telescopes and Instrumentation 2016: Ultraviolet to Gamma Ray, ed. J.-W. A. den Herder, T. Takahashi, & M. Bautz, Vol. 9905, International Society for Optics and Photonics (SPIE), 99051F, doi: 10.1117/12.2235271

Subramaniam, A., Sindhu, N., Tandon, S. N., et al. 2016b, The Astrophysical Journal Letters, 833, L27, doi: 10.3847/2041-8213/833/2/L27

Subramanian, S., & Subramaniam, A. 2012, Astrophys. J., 744, 128, doi: 10.1088/0004-637X/744/2/128

—. 2015, Astron. Astrophys., 573, A135, doi: 10.1051/0004-6361/201424248

Subramanian, S., Rubele, S., Sun, N.-C., et al. 2017, Mon. Not. Roy. Astron. Soc., 467, 2980, doi: 10.1093/mnras/stx205

Sun, N.-C., de Grijs, R., Subramanian, S., et al. 2017a, Astrophys. J., 849, 149, doi: 10.3847/1538-4357/aa911e

—. 2017b, Astrophys. J., 835, 171, doi: 10.3847/1538-4357/835/2/171

Sun, N.-C., de Grijs, R., Cioni, M.-R. L., et al. 2018, Astrophys. J., 858, 31, doi: 10.3847/1538-4357/aabc50

Tandon, S. N., Hutchings, J. B., Ghosh, S. K., et al. 2017a, Journal of Astrophysics and Astronomy, 38, 28, doi: 10.1007/s12036-017-9445-x

Tandon, S. N., Subramaniam, A., Girish, V., et al. 2017b, Astron. J., 154, 128, doi: 10.3847/1538-3881/aa8451

Tandon, S. N., Postma, J., Joseph, P., et al. 2020, Astron. J., 159, 158, doi: 10.3847/1538-3881/ab72a3

Tatton, B. L., van Loon, J. T., Cioni, M.-R. L., et al. 2021, Monthly Notices of the Royal Astronomical Society, 504, 2983, doi: 10.1093/mnras/staa3857

Taylor, M. 2011, TOPCAT: Tool for OPerations on Catalogues And Tables, Astrophysics Source Code Library, record ascl:1101.010

Tepper-García, T., Bland-Hawthorn, J., Pawlowski, M. S., & Fritz, T. K. 2019, Mon. Not. Roy. Astron. Soc., 488, 918, doi: 10.1093/mnras/stz1659

Thilker, D. A., Bianchi, L., Meurer, G., et al. 2007, Astrophys. J. Suppl., 173, 538, doi: 10.1086/523853

Tobias, C., & Santiago, H. 2020, arXiv e-prints, arXiv:2008.00037, doi: 10.48550/arXiv.2008.00037

Tody, D. 1986, in Society of Photo-Optical Instrumentation Engineers (SPIE) Conference Series, Vol. 627, Instrumentation in astronomy VI, ed. D. L. Crawford, 733, doi: 10.1117/12.968154

Tody, D. 1993, in Astronomical Society of the Pacific Conference Series, Vol. 52, Astronomical Data Analysis Software and Systems II, ed. R. J. Hanisch, R. J. V. Brissenden, & J. Barnes, 173

Torres, G., Andersen, J., & Giménez, A. 2011, Astronomy and Astrophysics Review, 18, 67

Trundle, C., Dufton, P. L., Hunter, I., et al. 2007, The VLT-FLAMES survey of massive stars: evolution of surface N abundances and effective temperature scales in the Galaxy and Magellanic Clouds, EDP, doi: 10.1051/0004-6361:20077838

van der Marel, R. P., & Cioni, M.-R. L. 2001, Astron. J., 122, 1807, doi: 10.1086/323099

van der Marel, R. P., & Kallivayalil, N. 2014, Astrophys. J., 781, 121, doi: 10.1088/0004-637X/781/2/121

van der Marel, R. P., & Sahlmann, J. 2016, Astrophys. J. Lett., 832, L23, doi: 10.3847/2041-8205/832/2/L23

Vasiliev, E. 2023, Monthly Notices of the Royal Astronomical Society, 527, 437, doi: 10.1093/mnras/stad2612

Vázquez-Semadeni, E., González-Samaniego, A., & Colín, P. 2017, Mon. Not. Roy. Astron. Soc., 467, 1313, doi: 10.1093/mnras/stw3229

Virtanen, P., Gommers, R., Oliphant, T. E., et al. 2020, Nature Methods, 17, 261, doi: 10.1038/s41592-019-0686-2

Vogelaar, M. G. R., & Wakker, B. P. 1994, Astron. Astrophys., 291, 557

Waskom, M. L. 2021, Journal of Open Source Software, 6, 3021, doi: 10.21105/joss.03021

Wes McKinney. 2010, in Proceedings of the 9th Python in Science Conference, ed. Stéfan van der Walt & Jarrod Millman, 56 – 61, doi: 10.25080/Majora-92bf1922-00a

Westmeier, T. 2018, Mon. Not. Roy. Astron. Soc., 474, 289, doi: 10.1093/mnras/stx2757

Zaritsky, D. 2004, Astrophys. J. Lett., 614, L37, doi: 10.1086/425312

Zaritsky, D., Harris, J., Grebel, E. K., & Thompson, I. B. 2000, Astrophys. J. Lett., 534, L53, doi: 10.1086/312649

Zinnecker, H., & Yorke, H. W. 2007, Ann. Rev. Astron. Astrophys., 45, 481, doi: 10.1146/annurev.astro.44.051905.092549

Zivick, P., Kallivayalil, N., & van der Marel, R. P. 2021, Astrophys. J., 910, 36, doi: 10.3847/1538-4357/abe1bb

Zivick, P., Kallivayalil, N., van der Marel, R. P., et al. 2018, Astrophys. J., 864, 55, doi: 10.3847/1538-4357/aad4b0

Zivick, P., Kallivayalil, N., Besla, G., et al. 2019, Astrophys. J., 874, 78, doi: 10.3847/1538-4357/ab0554